The POK2 Tail: A Versatile Connectivity Hub

Dissertation

der Mathematisch-Naturwissenschaftlichen Fakultät

der Eberhard Karls Universität Tübingen

zur Erlangung des Grades eines

Doktors der Naturwissenschaften

(Dr. rer. nat.)

vorgelegt von

Shu Yao Leong

aus Kuala Lumpur, Malaysia

Tübingen

2025

Gedruckt mit Genehmigung der Mathematisch-Naturwissenschaftlichen Fakultät der Eberhard Karls Universität Tübingen.

Tag der mündlichen Qualifikation:	02.06.2025
Dekan:	Prof. Dr. Thilo Stehle
1. Berichterstatter:	Prof. Dr. Erik Schäffer
2. Berichterstatter:	Prof. Dr. Klaus Harter

Abstract

Plants exist in a plethora of shapes and sizes. Plants achieve such diverse morphological feats through cell patterning, which is particularly challenging, as plant cells are rigidly bound to one another by their adjoining cell walls. Hence, the emergent morphology of the whole organism is determined at the level of cytokinesis, i.e. cell division. Consequently, cell division, particularly division plane positioning, is highly regulated in plants. Plant cells utilise chemical and mechanical signals to determine the division plane position and to mark this site with division plane marking proteins. To localise such proteins to the division site, a microtubule structure, known as the preprophase band, is constructed at the division plane and acts as a recruitment hub for division markers. One such division marker is the PHRAGMOPLAST ORIENTING KINESIN 2 (POK2). POK2 and its close homologue, POK1, are kinesins that reside at the division site to guide the microtubule-based cell division machinery, the phragmoplast, to the division site. *pok1/pok2* double mutants display cell patterning defects due to incorrect positioning of the phragmoplast. Importantly, *pok1/pok2* mutants do not exhibit cytokinetic defects, indicating that the POKs are important for spatial control of cytokinesis but not for function of cytokinesis itself. Reflective of its function, POK2 localises to the plasma membrane at the division site and also to the phragmoplast midzone. As a plus-end directed kinesin, POK2 is recruited to the phragmoplast midzone by way of the activity of its N-terminally located kinesin motor. Meanwhile, the C-terminal region of POK2, i.e. the POK2 tail is responsible for localisation to the division site. However, the mechanism of specific recruitment and retention at the division site was unclear. To uncover the mechanism of POK2 recruitment and residence at the division site, I purified the POK2 tail and performed *in vitro* characterisation of its intrinsic biochemical properties. *In vitro* experiments revealed that the POK2 tail is capable of direct binding to microtubules and anionic lipids. On microtubules, the POK2 tail is able to diffuse along the length of the microtubule. Microtubule binding assays with shorter POK2 tail constructs narrowed down the final $\sim$100 amino acid residues as important for the binding to microtubules and lipids. Additionally, reconstitution of previously reported *in vivo* interaction between the POK2 tail and the microtubule bundling protein, MAP65-3, revealed that MAP65-3 enhances POK2 tail microtubule binding. At the single molecule level, MAP65-3 and the POK2 tail are able to interact and co-diffuse at a slower rate than the POK2 tail diffusing alone. Interestingly, the final $\sim$100 amino acid residues also seem to be important for MAP65-3-based enhancement of POK2 tail microtubule binding. Overall, the ability of the POK2 tail to interact and bind several substrates insinuates a robust and possibly hierarchical accumulation at its *in vivo* sites.

Specifically, the *in vitro* results indicate that POK2 could be capable of directly binding preprophase band microtubules and the plasma membrane at the division site where interaction with MAP65-3 could confer further spatial and temporal specificity. In conclusion, this thesis work has revealed an aspect of the POK2 tail's biochemical capabilities, propounding the POK2 tail as a versatile interaction hub necessary for POK2's function in division plane guidance.

Zusammenfassung

Pflanzen existieren in einer Vielzahl von Formen und Großen. Sie erreichen diese vielfältigen morphologischen Ausprägungen durch Zellmusterung, die in Pflanzen insofern besonders ist, als dass Pflanzenzellen durch ihre aneinander grenzenden Zellwände fest miteinander verbunden sind. Die finale Morphologie des gesamten Organismus wird auf der Ebene der Zytokinese, d. h. der Zellteilung, determiniert. Aus diesem Grund ist die Zellteilung, insbesondere die Positionierung der Teilungsebene, in Pflanzen stark reguliert. Pflanzenzellen nutzen chemische und mechanische Signale, um die Position der Teilungsebene zu bestimmen, und markieren diese Stelle mit Proteinen. Um die Proteine zu lokalisieren, wird an der Teilungsebene mit dem so genannten Präprophasenband eine Mikrotubuli-Struktur aufgebaut, die als Rekrutierungszentrum fur Teilungsmarker dient. Ein solcher Teilungsmarker ist das PHRAGMOPLAST ORIENTING KINESIN 2 (POK2). POK2 und sein enges Homolog POK1 sind Kinesine, die sich am Teilungsort aufhalten, um die auf Mikrotubuli basierende Zellteilungsmaschinerie, den Phragmoplast, dorthin zu fuhren. *pok1/pok2*-Doppelmutanten weisen Zellmusterungsdefekte auf, die auf eine falsche Positionierung des Phragmoplasten zuruckzufuhren sind. Wichtig ist, dass *pok1/pok2*-Mutanten keine zytokinetischen Defekte aufweisen, was darauf hindeutet, dass die POKs zwar fur die raumliche Kontrolle der Zytokinese wichtig sind, aber nicht fur die Funktionalität der Zytokinese selbst. Entsprechend seiner Funktion befindet sich POK2 an der Teilungsebene zur Plasmamembran und zur Phragmoplast-Mittelzone. Als ein am Plus-Ende der Mikrotubuli ausgerichtetes Kinesin wird POK2 durch seine N-terminal gelegene Kinesin-Motoraktivitat in die Phragmoplast-Mittelzone rekrutiert. Der C-terminale Bereich von POK2, d. h. der POK2-Tail, ist hingegen fur die Lokalisierung am Teilungsort verantwortlich. Der Mechanismus der spezifischen Rekrutierung und des Verbleibs am Teilungsort war jedoch noch unklar. Um diesen Mechanismus aufzudecken, habe ich den POK2-Tail gereinigt und seine intrinsischen biochemischen Eigenschaften *in vitro* charakterisiert. *In-vitro*-Experimente zeigten, dass der POK2-Tail in der Lage ist, direkt an Mikrotubuli und anionische Lipide zu binden. An Mikrotubuli kann der POK2-Tail uber die gesamte Lange des Mikrotubulis diffundieren. Kurzere POK2-Tail-Konstrukte halfen dabei, die letzten etwa 100 Aminosaurenreste als wichtig fur die Bindung an Mikrotubuli und Lipide zu charakterisieren. Daruber hinaus ergab die Rekonstitution der zuvor berichteten *in-vivo*-Interaktion zwischen dem POK2-Tail und dem Mikrotubuli-Bundelungsprotein MAP65-3, dass MAP65-3 die Mikrotubuli-Bindung des POK2-Tailes verstarkt. Auf Ebene der Einzelmoleküle sind MAP65-3 und der POK2-Tail in der Lage, miteinander zu interagieren und gemeinsam mit einer langsameren Geschwindigkeit zu diffundieren

als der POK2-Tail allein. Interessanterweise scheinen die letzten etwa 100 Aminosaurenreste auch zentral fur die MAP65-3-basierte Verstarkung der POK2-Tail-Mikrotubuli-Bindung zu sein. Insgesamt deutet die Fahigkeit des POK2-Tailes, mit mehreren Substraten zu interagieren und diese zu binden, auf eine robuste und moglicherweise hierarchische Anhaufung an seinen *in-vivo*-Stellen hin. Insbesondere weisen die *in-vitro*-Ergebnisse darauf hin, dass POK2 in der Lage sein konnte, direkt an die Mikrotubuli der Praphase und die Plasmamembran am Teilungsort zu binden, wo die Interaktion mit MAP65-3 eine weitere raumliche und zeitliche Spezifitat verleihen konnte. Zusammenfassend lasst sich sagen, dass diese Arbeit eine biochemische Fahigkeit des POK2-Tailes aufgedeckt hat, welche den POK2-Tailes als vielseitiges Interaktionszentrum erscheinen lasst, der fur die Funktion von POK2 bei der Steuerung der Teilungsebene notwendig ist.

女人出门车要有油。

– 黄春来

Contents

Part I

Background

Chapter 1

Cell division

1.1 Cell division

Cell division is the process of dividing cell material into two or more daughter cells. Two major processes occur during cell division: division of genetic material (karyokinesis) and division of cellular material i.e. the cytoplasm (cytokinesis). Both processes are tightly controlled and coordinated such that the end of karyokinesis is coupled and occurs concurrently with the start of cytokinesis. Often, upstream signalling events proceed in tandem or are shared. Unsurprisingly, mitosis, meoisis, cell division have become blanket terms to refer to both processes. Nevertheless, it is not uncommon for karyokinesis and cytokinesis to be uncoupled, such as for synctia (multinucleate cells that form from dissolution of dividing cell membranes) and coenocytes (multinucleate cells that form as a result of multiple karyokineses without cytokinesis) which can be normal multinucleate stages of development in some organisms.

There are two types of cell division: symmetric (SCD, daughter cells have the same fate) and asymmetric cell division (ACD, daughter cells have differing fates). ACD is the basis of cell differentiation, where cell material is differentially segregated, such as for stem cells, where one daughter cell differentiates and the other maintains stem cell identity. The fate of a cell can be determined intrinsically, with polarised localisation of fate determining factors, or externally, from environmental input. In both SCD and ACD, it is important to position the division plane accurately relative to these signals. While ACD requires biased partitioning of materials, cells undergoing SCD have to divide equally such that materials and resources will be sufficient for the growth of the daughter cells. Accurate positioning of the cell division plane is thus of great importance.

1.2 What determines cell division plane?

Since the 1800s, naturalists have toyed with the idea of a basic deterministic law in which cells select a division plane in a geometrical and reductionist approach. Multiple theories emerged at the turn of the century, with hypotheses such as division perpendicular to the growth axis [126], the Rectangular Section theory [261] and the Principle of Minimal Area [19] enduring and still being cited to this day. The Principle of Minimal Area has been likened to a 'soap film' theory [244] in that cells would divide along a plane of minimal area just as a soap film with surface tension would minimise its area [83, 84] (Fig. 1.1). While Gottfried Berthold assigned his principle to be an absolute one, Léo Errera who made the theory famous thanks to his simple 'soap film' analogy actually had a nuanced approach. He considered that the 'soap film' theory identifies only a *relative* division plane (as highlighted in [21, 344]), and this was recapitulated to the modern probabilistic 'soap film' theory by computer modelling in the early 2010s [20]. This stipulates that the cell divides not along an area *minimum* but rather *one of the area minima*[1].

Figure 1.1: Soap films equilibrate to a surface minima.
Images are taken from [4]. Wired framed were dipped into soapy water and the soap films were left to equilibrate. The soap films consistently equilibrate to structures shown in order to minimise surface area.

The advent of mechanobiology: do cells sense geometry and if so how?

Theories like the Rectangular Section theory and Principle of Minimal Area are based on cell geometry [19, 83, 84, 261]. Underlying these parsimonious theories is the requirement for cells to actually sense its geometry, which beg the questions: Do cells sense geometry? What are the cellular processes involved in geometry sensing?

The 'soap film' theory asserts that the new cell plate would minimise its area as a soap film would when confined within a similar geometry. Flanders and colleagues experimentally drew this comparison to the position of the nucleus which is suspended by cytoplasmic strands in the vacuole center prior to mitosis (Fig. 1.2) [92]. This would suppose that the cytoplasmic strands respond similarly to soap

[1] These papers published in the 1800s were either in French or German and were not readily available as digital versions. Hence, I myself and many current-day reviewers have only read what others have written about these papers. Besson & Dumais [21] who are French themselves have probably delved directly into Léo Errera's French works as they quote even the PhD thesis of his student de Wildeman. It is a shame that such publications are no longer easily accessible as they are valuable and fun pieces of scientific history, but perhaps with AI tools, these will be translated and available once again?

films to minimise surface area. Adding credit to this, cytoplasmic strands have been shown to exert and experience tension through careful observations or laser ablation experiments [106, 112].

Both actin and microtubules have been found within cytoplasmic strands [15, 320]. However, as microtubules are stiffer than actin filaments with an intrinsic stiffness comparable to plexiglas [104], microtubules rather than actin have received greater attention as tension sensors. Additionally, microtubules in an *in vitro* gliding assay with immobilised Kinesin-1 on stretchable and compressable polydimethylsilane (PDMS) showed that microtubules align along the maximal tensile axis and against the maximal compression axis [133]. *In vivo*, mechanical stimulation such as wounding also reorients microtubule arrays along maximum stress [113]. Thus, a growing body of evidence points towards microtubules as potential major tension sensors in cells.

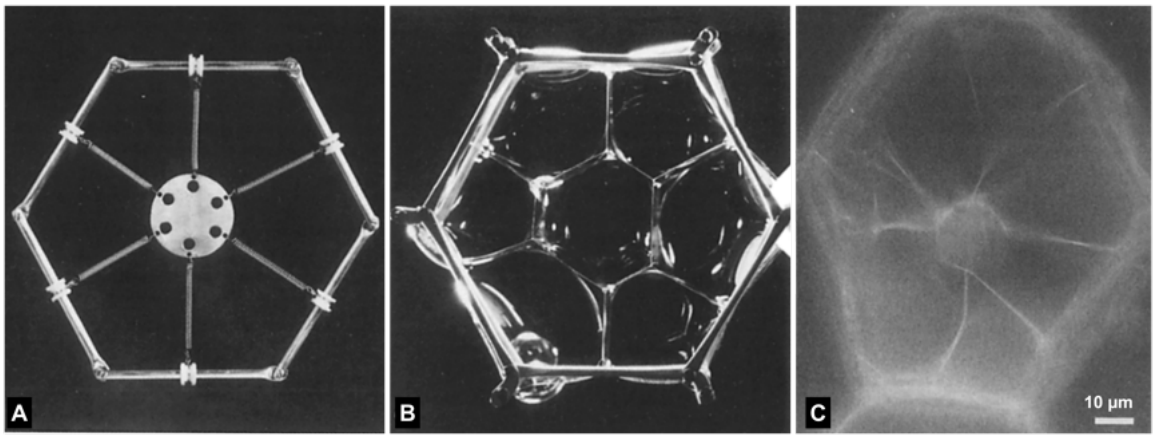

Figure 1.2: Soap films compared to plant cells.
(A) A flexible wired frame, to represent the rather rigid cell wall was attached springs capable of moving along the wires. **(B)** A hexagonal wired frame was dipped into soapy water to produce soap films that equilibrated into the structure seen. **(C)** A cross-section of *Tradescantia* leaf stained with rhodamine phalloidin. Images are modified from [92].

1.3 Plant cell division

Animal and yeast cells divide by way of an actomyosin contractile ring to physically separate the two daughter cells [242]. The actomyosin ring is capable of generating several hundred pN forces to induce fission [341], as demonstrated in the 1960s by the bending of an inserted microneedle into the cleavage furrow [250]. Conceptually, the actomyosin contractile ring works similarly to actin and myosin filaments in striated muscle sarcomeres, whereby myosin motors drive the sliding of actin filaments [242]. Unlike muscle sarcomeres however, the actomyosin contractile ring undergoes simultaneous disintegration as ingression proceeds [242].

In contrast to the outside-in contractile ring approach, land plants divide inside-out by building a new cross wall within the existing mother cell. As a result, plant cells are physically attached to one another and are biochemically connected via their plasmodesmata. Hence, even more so for plants, division plane selection is crucial for arrangement of cells within tissues and the organism as a whole. Concurrently, plants developed a number of plant-specific microtubule arrays such as the cortical

microtubule (CM) network which provides spatial information for cellulose deposition ([61, 352]), the preprophase band (PPB) and the phragmoplast [38]. The latter two are involved in cytokinesis, both of which are discussed in greater detailed in Sections 2.2.2 & 2.2.3.

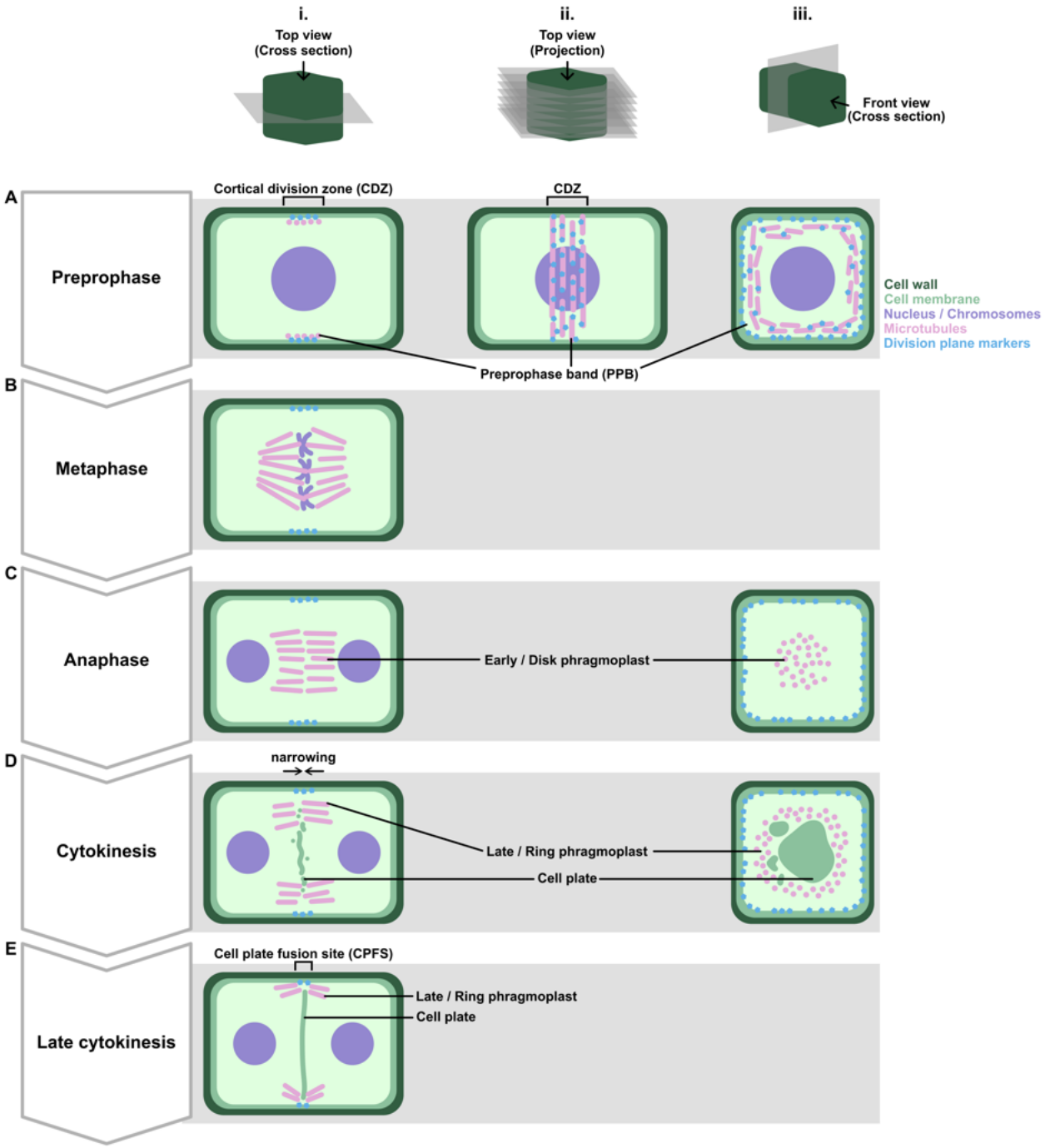

Figure 1.3: Schematic showing key processes in plant cell division.
(A-E) Key steps during plant mitosis and cell division. Division plane markers (blue pentagons) localise to the cortical division zone (CDZ) during preprophase band formation. Here, the representative marker is shown to localise throught mitosis and cell division. However, not all markers are long-term residents. *(Column i.) Top view* as a cross section through the middle of a cell where the mitotic spindle is visible as its eponymous spindle shape. *(Column ii.) Top view* but as a projection, where the microtubules of the preprophase band (PPB) are visible as bundles. *(Column iii.)* Right column shows the *front view* as a cross section through the middle of the cell, where the PPB is visible as a enrichment at the cell periphery, the phragmoplast in both its early/disk form and late/ring form.

The next chapters will go into detail on the players of plant cell division. Here, I provide only a brief

overview of the key processes involved. Plant cells select their division plane during the S/G2 phase. The nucleus migrates to its future division site and a ring of microtubules called the preprophase band (PPB) forms around the nucleus at the cell cortex (Fig. 1.3A, *column ii.*). In a cross-section of the plant cell, these microtubules are visible as an enrichment near the cell cortex. The area of enrichment is known as the cell division zone (CDZ) (Fig. 1.3A, *columns i. & iii.*). The PPB acts as a recruitment platform for division plane markers (light blue in Fig. 1.3) to the CDZ. The PPB dissassembles upon nuclear envelope breakdown while the division plane markers are retained at the CDZ and serve as positional landmarks for the division plane (Fig. 1.3B). The cell proceeds through mitosis with the division plane markers in place. After anaphase, the post-anaphase spindle microtubules are repurposed into the phragmoplast i.e. the cell division machinery in plants (Fig. 1.3C). Along these microtubules, vesicles containing cell plate building materials are transported to the midzone of the phragmoplast where they fuse to form a new cell plate (and eventually, the cross wall) (Fig. 1.3D). The phragmoplast expands centrifugally by depolymerising microtubules in its middle and nucleating microtubules on its edges. Thus, the phragmoplast adopts a ring shape (when viewing the division plane perpendicularly (Fig. 1.3D, *column iii.*)) which inner diameter grows to accomodate the growing cell plate. Concurrently, the localisation pattern of the division markers at the CDZ condenses into a narrow region called the cell plate fusion site (CPFS) (Fig. 1.3D & E). Phragmoplast expansion is guided to the CPFS and the cell plate eventually fuses at this site to the mother cell membrane and cell wall, thus completing plant cell division.

Chapter 2

Microtubules

2.1 Microtubules

Microtubules are macromolecular structures part of the cytoskeleton that provide structural integrity to the cell as well as provide means for intracellular transport. The latter is possible due to the presence of the motor proteins, such as kinesin and dynein, which carry intracellular cargo as they travel along microtubules. This is the basis for several cellular microtubule-based processes such as axonal transport, organelle positioning, mitosis, as well as some plant-speific processes like cell division and cell wall patterning.

Microtubules are made of ∼13 protofilaments associated laterally into a hollow cylinder of ∼25 nm diameter (Fig. 2.1), hence the name 'micro' - 'tubule'. The number of protofilaments vary depending on organism and cell type, with as few as 4 protofilaments in *Prosthecobacter* and as many as 40 in *Mantispa perla* [47]. Additionally, GMPCPP-stabilised microtubules mainly consist of 14 protofilaments [52, 337] whereas paclitaxel-stabilised microtubules have mainly 12 protofilaments [190][1]. The protofilaments themselves are made up of α-/β-tubulin heterodimers arranged end-to-end. This renders intrinsic polarity to the protofilaments that is subsequently conferred to the microtubule, with an α-tubulin protruding end, which is usually attached to a microtubule nucleator *in vivo*, and a β-tubulin protruding end, which is the *in vivo* growing end and *in vitro* faster growing end. This polarity confers directionality for the kinesins and dyneins that traverse the microtubule.

The binding of tubulin dimers to one another is GTP-dependent. Each tubulin monomer carries a

[1] The number of protofilaments in a microtubule affects of course the width, but also the helicity of the microtubule. 13 is the generally accepted number of protofilaments due to its prevalence across eukaryotes but also because of nucleation from γ-tubulin ring complexes necessitate 13 protofilaments. To accomodate 14 protofilaments, a supertwist is introduced such that the protofilaments no longer run straight along the microtubule axis as in Fig. 2.1. How the diversity of protofilament numbers affect cellular function is fascinating and is well reviewed in [47], but is far beyond the scope of this thesis, and thus not further discussed.

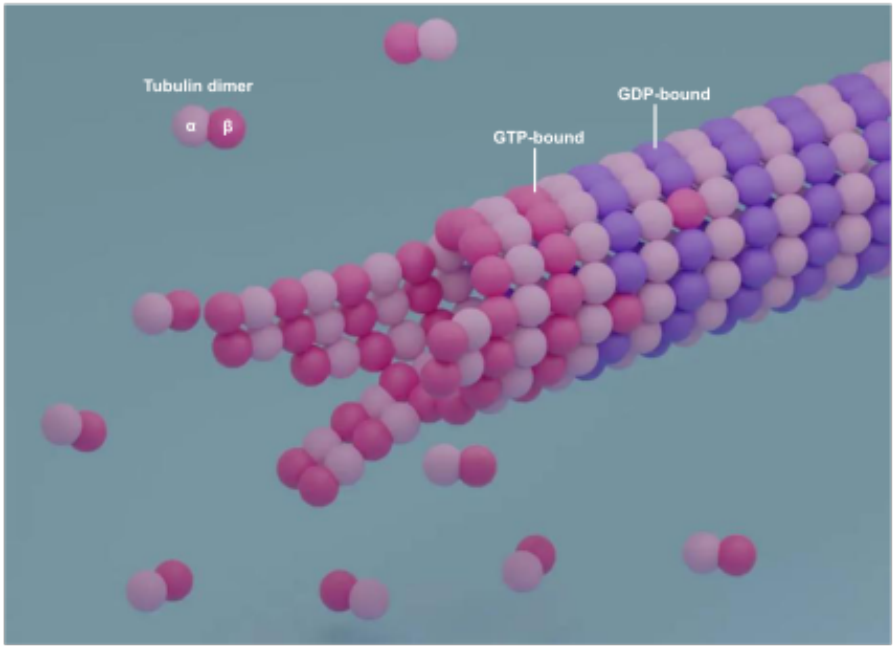

Figure 2.1: Cartoon of the growing end of a microtubule in 3D.
Tubulin dimers assemble end-to-end to form protofilaments, which in turn associate laterally to form a microtubule. Here, the microtubule end in question is the plus-end, with a protruding β-tubulin. Depicted is a microtubule with 13 protofilaments with a 3-start helix. Here the GTP-bound β-tubulin is coloured magenta, wheras the GDP-bound β-tubulin is coloured purple.

GTP binding site, but only the GTP on β-tubulin is readily accessible and therefore exchangeable [282]. As such, when mentioning GTP- or GDP-tubulin dimer, the GTP in question is referring to the nucleotide carried by β-tubulin. Microtubules are predominantly nucleated from GTP-tubulin dimer. GTP hydrolysis to GDP in β-tubulin changes the conformation of the tubulin dimer, causing it to pack more tightly [322]. Within the microtubule lattice, such a conformational change causes lateral tension between protofilaments and dimers, priming the microtubule for disassembly. The dynamic GTP hydrolysis cycle and molecular abundance of GTP and GDP underly microtubule dynamic instability. This dynamic instability is the rapid transition between growth and shrinkage of single microtubules [35]. Such a feature allows the microtubules to be broken down and remodeled quickly and effectively into a plethora of different function-specific microtubule arrays.

2.2 Plant microtubules and plant specific microtubule arrays

2.2.1 Plant tubulin and microtubules

Eukaryotic tubulins are part of the larger FtsZ/Tubulin superfamily, which includes the prokaryotic filamentous temperature-sensitive protein Z (FtsZ) [173]. Plant genomes have both FtsZ and tubulin genes, having inherited FtsZ from their plastidial genomes [32] where FtsZ is still used for plastidial division [184, 253]. Eukaryotic tubulins are incredibly well-conserved, sharing 72–95% amino acid identity for α-, β- and γ-tubulins across the eukaryotic lineage [32, 96] with majority of the divergence being in the C-terminal tail [316]. Consequently, *in vitro* microtubule experiments mainly utilise

porcine brain tubulin regardless of the organism source of the microtubule associated protein (MAP) being studied, as porcine brain tubulin is easy to purify due to the abundance of microtubules in neurons. For tubulin purification from organisms that do not have tissues with significant microtubule abundance, a TOG column can be used, which exploits the microtubule binding capability of the TOG domain to pull down tubulin [89, 350][2]. There has also been efforts to express recombinant tubulin in insect and human cells [201, 317], but is however a more challenging endeavour, often requiring considerable optimisation. While extremely useful for studies to investigate tubulin isotypes, different tubulin heterodimer makeup and post-translational modifications, purifying recombinant tubulin is highly technical. Issues include chaperon requirements and the balancing act of expressing α- and β-tubulin in complementary amounts [316]. Plant tubulins are particularly challenging to purify due to the presence of the vacuole and the lack of a specific organ so enriched in microtubules as the brain. Consequently, *in vitro* experiments for plant MAPs are also performed using porcine brain tubulin. While perhaps not entirely precise, the good conservation of eukaryotic tubulins enables experiments using porcine brain tubulin with non-porcine MAPs to yield contributive and insightful results.

Despite good conservation, plant tubulins still have 13–21% sequence difference from vertebrae tubulin [209] with alpha tubulins showing more divergence in particular [132, 208]. Accordingly, purified carrot microtubules were observed to be more dynamic than animal neuronal microtubules, with 10-fold faster depolymerising velocities, no rescue events, and shorter growth periods [205]. Moreover, plant microtubules are pharmocologically different from vertebrae microtubules. Colcichine, a potent vertebrae microtubule depolymeriser, binds poorly to plant microtubules [207] and are completely ineffective against plants that produce Colcichine themselves [162]. The divergence of plant tubulin may have occured concurrently with the emergence of plant-specific microtubule arrays.

2.2.2 Preprophase band (PPB)

The preprophase band (PPB) was first identified as an 'equatorial band' located *against* the cell periphery that appears shortly before entry into mitosis [241]. The PPB forms around the pre-mitotic nucleus by selective microtubule polymerisation, stabilisation and bundling with concomitant depolymerisation and clearing of the cortical microtubule (CM) array [166] (Fig. 1.3). The position of the PPB anticipates the future division plane with sub-micrometer precision [107]. However, the PPB disassembles upon entry into mitosis [241]. As such, the PPB has been suggested to initiate division plane specification [358]. This specification is remembered by proteins deposited at the cortical zone

[2] The tumour overexpression gene (TOG) domain is the hallmark domain of TOG-domain proteins, a family including XMAP215 and CLASP [89]. In 2012, Widlund et al. conjugated *E. coli* purified GST-TOG1-TOG2 from the *S. cerevisiae* Stu2 to a glutathione Sepharose column and used it to bind tubulin from various cell extracts. The tubulin was released from the TOG domains by 500 mM ammonium sulfate wash, which was reported to help retain nucleotide retention [60]. Interestingly, the TOG domains seem to bind tubulins that are free from post-translational modifications [331], making it useful to obtain 'clean' tubulin ready for *in vitro* post-translational modifications for study. Unfortunately, this means that using the TOG-column to purify native tubulins would not yield native post-translational modifications, which explains why Hotta et al. found that *Arabidopsis* tubulins were surprisingly free from post-translational modifications [128].

where the PPB forms [62, 166]. Thus, this zone is aptly called the cell division zone (CDZ)[3] (Fig. 1.3) [290, 325].

Evolutionarily, the PPB first appears in Zygnematophytes [38]. However, in spite of its purported role to 'decide' the division plane, not all land plants and not all cell types have a PPB [37, 198]. In vascular plants, the PPB is present in meristematic cells and absent in gametophytic cells, whereas the reverse is true for the moss *Physcomitrium patens* [34, 37]. To provide an explanation for this discrepancy, it was proposed that the PPB was needed for divisions that required more regulation, as the moss undergoes a 2D to 3D transition from sporophyte to gametophyte [76]. However, *Arabidopsis thaliana trm6,7,8* triple mutants, which lack PPBs but have an otherwise unperturbed CM network, experience only mild cytokinetic defects [269]. Hence, it became clear that the PPB may not be the deterministic factor of division plane position.

Early elegant centrifugation studies using black maidenhair fern (*Adiantum capillus-veneris L.*) showed that repositioning the nucleus repositions the PPB with it [217]. Additionally, polarised nuclear movement prior to asymmetric cell division (ACD) has long been known and can be actin or microtubule-dependent [10]. Recently, mispositioned PPBs were consistently observed in tandem with unpolarised nuclei in the stomata mother cells of mutants with defective linker of nucleoskeleton and cytoskeleton (LINC) complexes. The mispositioned PPBs led to mislocalised downstream division markers such as TANGLED1 (discussed in the next section) [10]. Thus, it is tempting to conclude that the nucleus rather than the PPB determines the division plane. Consequently, division plane specification can be thought to be nuclear dependent while the PPB reinforces this predetermined site [62]. This reinforcement comes in the form of stabilising nuclear position through cytoplasmic strands [92, 199, 288] and by recruitment of CDZ markers.

2.2.2.1 Remembering where to divide

In order to retain memory of the division plane that has been specified prior to mitosis, an ensemble of division plane markers are recruited to the cell division zone (CDZ) via the PPB. Despite the PPB having been observed since the 1960s, before TANGLED1 was discovered in 1996, only players that were depleted at the division zone were known. Actin [56] and the kinesin-14 KCA1 [329] are both characterised by their reduced abundance at the CDZ. As such, before positive markers were identified, the CDZ was also known as the actin depleted zone (ADZ).

Later, the first true CDZ marker, TANGLED1 (TAN1), was identified in *Zea mays* [294, 295] and found to localise to the CDZ from preprophase to end of cytokinesis. The identified maize *tan1* mutant had cytokinetic defects as a result of phragmoplast misalignment [55, 185]. The *Arabidopsis* homologue, *Arabidopsis* TANGLED (ATN)[4], was shortly found to localise similarly to the CDZ as

[3] The term cell division zone (CDZ) was first proposed in 2007 [325]. Terminology for plant cell division was only unified a decade later [290].

[4] Some papers directly refer to the *Arabidopsis* homologue by the TAN1 abbrieviation rather than ATN, usually

its maize counterpart [339]. However, the *Arabidopsis tan* mutant showed cytokinetic defects only in root tips[5]. This phenotype was considerably weaker than the maize *tan1* mutant phenotype, where the overall plant was shorter and severe aberrant cell patterning could be easily observed in the leaves. Eventually, it was shown that ATN functions redundantly with another microtubule bundling protein, *AUXIN INDUCED IN ROOTS9* (AIR9)[6] [202].

Since then, an ensemble of CDZ markers have been identified (Table 2.1). Of these, the kinesin-12 superfamily members PHRAGMOPLAST ORIENTING KINESIN 1 and 2 (POK1, POK2) were found through a yeast-two-hybrid screen against ATN [215]. The POKs, with POK2 in particular, is discussed in greater detail in Section 3.3.

Table 2.1: *Arabidopsis thaliana* proteins reported to associate with the CDZ.
CPFS denotes cell plate fusion site, which is the narrowed cell division zone (CDZ) at the time of cell plate insertion to the plasma membrane. The list only mentions the CDZ-related localisation but not if the protein localises elsewhere. For example, KCBP is also found on the anaphase spindle and phragmoplast distal zones [40]. Additionally, this list is not exhaustive. In particular, proteins involved in insertion of cell plate fusion at the end of cytokinesis, such as RSH and T-PLATE, are not mentioned. Please also note that MAP65-3, which strongly localises to the PPB does not remain at the CDZ upon PPB dissassemly, is also note listed here. Organisms: *Arabidopsis thaliana (At)*, *Zea mays (Zm)*.

Protein	Full name	CDZ persistance	Reference
AIR9	auxin induced in roots 9	Appears and disappears with PPB, reappears at CPFS	[39]
ATN	*Arabidopsis* TANGLED1	PPB to end	[339]
RanGAP1	Ran GTPase activating protein 1	PPB to end	[353]
PHGAP1, 2	pleckstrin homology GTPase activating protein 1 & 2	PPB to end	[303]
POK1, 2	phragmoplast orienting kinesin 1 & 2	PPB to end	[118, 167, 215]
MAP65-4	microtubule-associated protein 65 kda 4	PPB to end	[163]
IQD6, 8	IQ67 domain protein 6 & 8	PPB to end	[153]
KCBP	kinesin & calmodulin binding protein	PPB to end	[40]

2.2.2.2 PPB components

In addition to microtubules, the PPB is also enriched with actin [172, 198], endoplasmic reticulum [102, 198] and sees increased endocytosis activity [138]. Depending on the cell type, F-actin at the PPB can precede or succeed the microtubules and can disappear or remain after the microtubules have disassembled [198]. In some cases, F-actin appears to be instrumental to microtubule bundling at the PPB [196, 312]. Supporting this, proteins that bind both microtubules and actin such as KCBP are found to localise here [40, 172].

2.2.2.3 PPB assembly

PPB formation is controlled by dephosphorylation, as *ton* mutants, defective in protein phosphatase 2A (PP2A) function, are unable to produce PPBs [172]. γ-tubulin [76], MOR1 (the plant homologue

by researchers who work with both *Zea mays* and *Arabidopsis thaliana*. Perhaps the different nomenclature was distracting.

[5] There were three different mutants studied in [339]: *tan-csh*, *tan-mad*, and *tan-riken*. All three had insertions at the start of the gene and all three were morphologically normal with only cell patterning defects in the root tips. Their naming is related with their history of how and from where they were obtained. *tan-mad* was identified in a collaboration with University of Wisconsin, the *mad* indicating Madison. *csh* & *riken* indicates the research institute Cold Spring Harbour, USA and RIKEN, Japan, respectively.

[6] The *tan/air9* double mutant could be rescued by introducing TAN-YFP. This result validates the *tan* mutants (identified in [339]) as partial or total loss-of-function mutants.

of XMAP215) [50] and MACET4 [272] localise to the PPB, indicating that microtubule nucleation occurs here. At the same time, microtubules in the surrounding CM network are cleared, likely via the action of KATANIN, a microtubule severing protein, which is recruited here by MOR1 [50, 148]. Meanwhile CM network microtubules that are useful are selectively stabilised and bundled [68, 281, 335]. Unsurprisingly, several microtubule stabilising and bundling proteins such as SPIRAL2, MAP70 and several MAP65s (-1, -2, -3, -4 and -5) localise to the PPB [76]. A recent drug screen for cytokinetic drugs revealed the importance of MAP70 in reorganising the CM network into the PPB for mitotic entry [144] as PD-180970 treatment inhibits MAP70 phosphorylation and disrupts PPB formation. Additionally, MAP65-1 binding has been shown to inhibit KATANIN severing through microtubule bundling [36].

2.2.2.4 PPB disassembly

Phosphorylation appears to mediate PPB disassembly, as cyclin-dependent kinase A (CDKA), an *Arabidopsis* cdk1/2 homologue, was one of the earlier proteins identified to localise to the late PPB [57, 197]. Some PPB proteins have been identified to be phosphorylated, such as MAP65-1,-2, and -3 by the mitogen-activated protein kinase (MAPK) MPK4 [150, 264, 293]. MAP65-1 has been additionally shown to be phosphorylated by CDKs [267, 293], which affects its microtubule binding and bundling activity [293]. While *in vitro* results showed that MAP65-1 phosphorylation by CDK only mildly reduced microtubule bundling [267], proper meiotic localisation of MAP65-1, especially in prophase, was shown to be severely affect by CDKA activation [296]. These results suggest that a combination of MAP65 detachment from the microtubule and KATANIN-induced severing on unprotected microtubules leads to PPB disassembly.

2.2.3 Phragmoplast

The phragmoplast refers to the bipartite microtubule array at anaphase between the segregated daughter chromosomes (Fig. 1.3, C–E). Phragmoplast microtubules are repurposed from the post-anaphase mitotic spindle (Fig. 1.3) [276]. Consequently, they share a similar microtubule arrangement, with microtubule plus-ends facing the midzone and the minus-ends in the distal zone facing the daughter nuclei (Fig. 2.2) [86, 87]. The microtubules serve as tracks on which cell plate building materials are delivered to the midzone [189, 212], in particular to the cell plate assembly matrix (CPAM), a ribosome-free region (as identified by electron microscopy) $\sim$150 nm region around the cell plate where all cell plate growth events take place [11, 235, 276]. To accomodate the growing cell plate, microtubules depolymerise in the center [277] and nucleate new microtubules on its outer edge [218, 291]. Throughout its expansion, the phragmoplast is slowly guided to the site previously marked as the CDZ, which has narrowed to what is called the cell plate fusion site (CPFS) (Fig. 1.3E). Eventually the phragmoplast and growing cell plate reaches the mother cell periphery and fuses at the CPFS [166, 327], thereby completing cytokinesis.

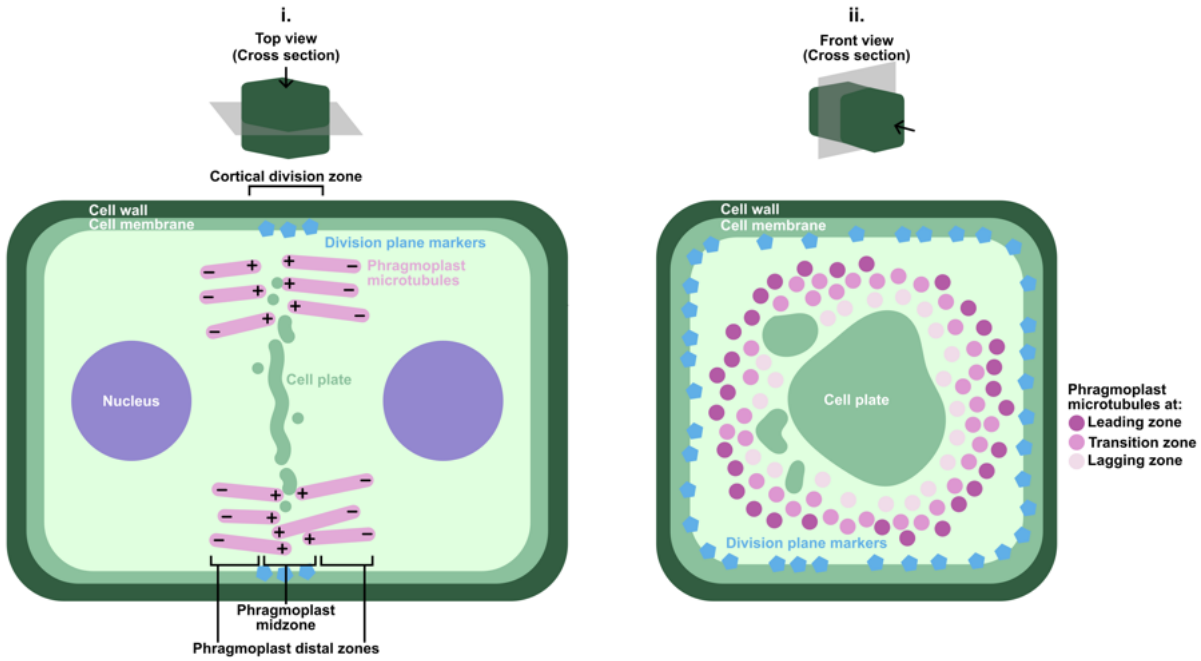

Figure 2.2: Simplified cartoon depicting ring-stage phragmoplast during cytokinesis.
The cartoon phragmoplast is depicted with only a few representative microtubules and without its associated proteins. Microtubule plus- and minus-ends are marked with + and - respectively. In the *front view* cross-section (right), which is taken in the division plane, the microtubules are viewed along their long axis and depicted as dots. Different hues of pink depict the three dynamic zones of the phragmoplast: leading (dark pink), transition (pink), lagging (light pink) zone.

2.2.3.1 Structure

A microtubule sandwich: minus-plus-plus-minus

When looking at the phragmoplast orthogonally to the division plane, a way to conceptually zone the phragmoplast becomes apparent: the distal zones (further away from the division plane) and the midzone (near the division plane) (Fig. 2.2, *i. Top view*). As the microtubules are inherited from the mitotic spindle and share the same arrangement in terms of microtubule polarity, the distal zones and midzone are enriched in microtubule minus- and plus-ends respectively. In the distal zones, the p60 subunit of katanin, KTN1 has been shown to localise here [237]. KTN1 seems to regulate phragmoplast microtubule length and plays a role in division plane orientation and phragmoplast expansion [148, 237].

Meanwhile, microtubule plus-ends are gathered at the midzone and may or may not interdigitate across the midzone. On one hand, cryo-electron microscopy experiments showed that microtubules did not interdigitate [11, 276]. Additionally, immunostaining with anti-tubulin or binding with *in vivo* microtubule marker, MAP4-GFP shows an unstained 'clear zone' in the phragmoplast midzone [214]. By contrast, the microtubule bundling protein, MAP65-3 was shown to directly decorate the phragmoplast in this 'clear zone' [214]. As MAP65-3 preferentially binds microtubule anti-parallel overlaps [123], it was taken to mean that microtubules must interdigitate across the midzone. This is

supported by electron micrographs in *Haemanthus* [116], *Physcomitrium patens* [122] and *Arabidopsis thaliana* [123] that showed microtubules interdigating across the phragmoplast midzone.

Three rings

The discrepancy, whether microtubules interdigitate or not, is purportedly due to different stages of phragmoplast maturity [291]. The early/disk phragmoplast having more interdigitation and the late/ring phragmoplast having less to none [11, 276]. Stepping back, it is crucial to note that the phragmoplast is a dynamic microtubule array that continually expands outwards. Hence, even within a specific stage, this dynamicity would result different zones of microtubule activity: a leading zone (high microtubule nucleation), a transition zone (stabilised microtubules where vesicles are actively being delivered) and a lagging zone (high microtubule depolymerisation) following the outer, middle and inner diameters of the ring-stage phragmoplast (Fig. 2.2, different hues of pink in *ii. Front view*). Thus, imaging the phragmoplast at different time points in different zones would result in differences in microtubule arrangement.

Accordingly, mutants defective in microtubule nucleators and microtubule branching nucleators γ-tubulin, GCP4, AUG3, AUG7 and MZT1 result in disorganised phragmoplasts, abnormal CD, and perturbed plant development [291]. Meanwhile, microtubules at the lagging zone are characterised by depolymerisation, brought on by the loss of MAP65 binding upon phosphorylation by the NACK-PQR MAPK cascade, Aurora kinases and cyclin-dependent kinases (CDKs) [27, 267, 293, 311]. Aside from nucleators and depolymerisers, microtubule stabilisers such as EB1, CLASP and SPIRAL1 are unsurprisingly also found at the phragmoplast [6, 22, 100, 147, 274]. Mutations in either CLASP or the microtubule dynamics enhancer, MOR1, result in smaller phragmoplasts [6, 140].

2.2.3.2 Regulation

Foundational experiments on phragmoplast regulation were performed in *Nicotiana tabacum* BY-2 cells, which uncovered the role of the NACK-PQR pathway in phragmoplast microtubule turnover. This pathway consists of the kinesin-7Cs NACK1/2 and the mitogen-activated protein kinases (MAPKs) NPK1, NQK1 and NRK1 [263] (Fig. 2.3). Later, the functionally analogous *Arabidopsis* pathway (kinesin-7Cs HINKEL and TETRASPORE and MAPKs ANP1–3, MKK6 and MPK4) was also identified [17]. All NACK-PQR pathway proteins localise to the spindle [299] and phragmoplast midzone [152, 225–227, 307, 310, 314]. However, both NACK1 and NPK1 are kept inactive by cyclin-dependent kinase (CDK) phosphorylation during early mitosis [268]. The proteins are then activated in cytokinesis by an unknown phosphatase, allowing them to interact and phosphorylate NQK1, which phosphorylates NRK1, which phosphorylates MAP65s in order to disassemble microtubules at the phragmoplast lagging zone [150, 264, 267, 293].

Recently, the TIO-Kinesin-12 pathway has been identified to function in parallel to the NACK-PQR pathway [232]. Two-in-one (TIO) is an *Arabidopsis* Ser/Thr kinase that localises to the phragmoplast

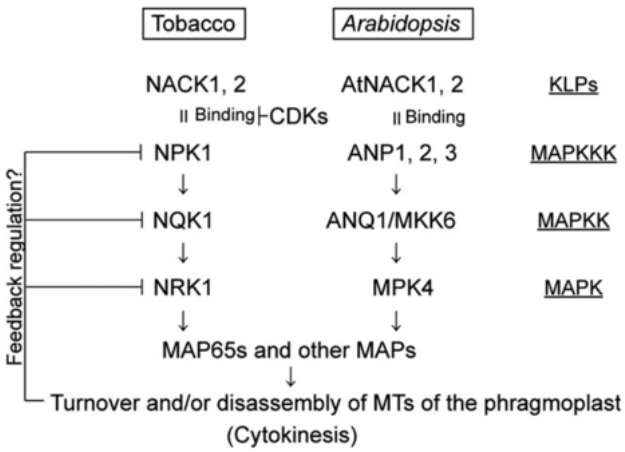

Figure 2.3: NACK-PQR pathway in tobacco and Arabidopsis.
Schematic is taken from [266]. Abbrieviations: *Arabidopsis* NPK1-related kinase (ANP), *Arabidopsis* NQK1-related kinase (ANQ1), cyclin-dependent kinase (CDK), kinesin-like protein (KLP), microtubule associated protein (MAP), microtubule associated protein 65 kDa (MAP65), mitogen-activated protein kinase (MAPK), mitogen-activated kinase kinase 6 (MKK6), mitogen-activated protein kinase 4 (MPK4), NPK1-activating kinesin (NACK), nucleus and phragmoplast localised kinase 1 (NPK1), N**Q**K and N**R**K are named following the alphabetical order after **P** as they are subsequently phosphorylated by N**P**K.

midzone [230]. Its name reflects its two N- and C-terminal kinase domains. TIO function is most apparent in male meiotic cytokinesis, but also seems to function in somatic cells as TIO RNAi lines exhibit multinucleate cells in shoot and root meristems [230]. The major phenotype of the *tio* mutant is enlarged pollen grains, which are occasionally multinucleated, and is inidicative of aborted cytokinesis. This phenotype is seen also in TIO overexpression lines, *pakrp1/pakrp1l* double mutants and *tetraspore* mutants [229]. Predictably, the kinesin-12/-15 family members, PAKRP1/kinesin-12A and PAKRP1L/kinesin-12B, bind to TIO [231]. Both kinesins localise to the phragmoplast midzone [160, 236] and are crucial for phragmoplast expansion [161]. TIO likely regulates the function of PAKRP1 and PAKRP1L by phosphorylation, however direct phosphorylation by TIO has not been shown. Recently, a drug screen identified 1-tert-Butyl-3-(4-chlorophenyl)-1H-pyrazolo[3,4-*d*]pyrimidin-4-amine (PP2) as a PAKRP1 phosphorylation inhibitor [144]. PAKRP1 and PAKRP1L failed to localise to the phragmoplast midzone in PP2 treated cells and phragmoplasts were subsequently incorrectly formed [144]. PP2 itself is a known Ser/Thr kinase inhibitor [115] and likely inhibits the TIO kinase upstream of PAKRP1 and PAKRP1L. Hence, phosphorylation of PAKRP1 and PAKRP1L, mostly probably by TIO kinase, is important for phragmoplast morphology.

The TIO-Kinesin-12 and NACK-PQR pathways cross-interact despite being separate cascades (Fig. 2.4). TIO was shown to interact with TETRASPORE in a yeast-two-hybrid assay [229], and the *tetraspore* mutants share the same enlarged pollen grain phenotype. Direct phosphorylation of TETRASPORE by TIO has not yet been experimentally proven but likely functions to prevent onset of phragmoplast disassembly by downstream MAP65-3 phosphorylation in the NACK-PQR pathway. On the other hand, PAKRP1 localisation to the phragmoplast midzone succeeds and depends on MAP65-3 [123]. The two pathways ultimately promotes opposing effects on phragmoplast organi-

sation: TIO-Kinesin-12 to stabilise and NACK-PQR to disassemble the phragmoplast. Hence, the cross-talk between the two pathways reflects the intricate coordination of microtubule dynamics in phragmoplast expansion.

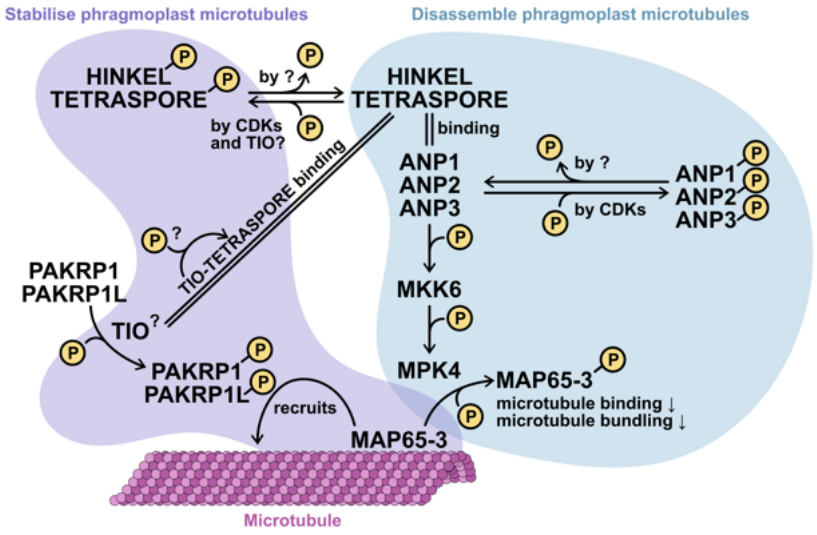

Figure 2.4: Convergence of NACK-PQR and TIO-KINESIN-12 pathways.
Arabidopsis thaliana protein names are used. The two pathways share some proteins, namely in the interactions between TIO kinase and kinesin-7 TETRASPORE and between PAKRP1 and PAKRP1L with MAP65-3. Question marks (?) indicate players or mechanisms that have yet to be empirically verified.

2.3 Microtubule associated proteins

'Microtubule associated protein' refers to any protein that interacts with microtubules. This umbrella term includes proteins that directly regulate microtubule morphology as well as proteins that use the microtubule as a substrate for other cellular activities. Proteins that regulate microtubule morphology include microtubule nucleating, stabilising, depolymerising, severing and bundling proteins as well as proteins that regulate the dynamicity of the growing microtubule ends.

Several MAPs and their respective functions have already been mentioned, such as: MOR1/XMAP215, ATN, AIR9, MAP65s, MAP70s, MACET4, KATANIN, SPIRAL2 and several kinesins. In the following section, I will discuss one particular MAP in more detail – MAP65.

2.3.1 MAP65/Ase1/PRC1

In 1993, Jiang & Sonobe isolated the first plant microtubule bundling protein when trying to pull down MAPs s from *Nicotiana tabacum* miniprotoplasts. They purified a 65 kDa protein that could bundle microtubules. This microtubule bundler was later found to be functionally and structurally analogous but not homologous in sequence to the yeast anaphase spindle elongation protein 1 (Ase1) and human protein regulator of cytokinesis (PRC1) [265]. Unlike the yeast and human proteins, which organisms have only one gene copy, plants have many MAP65s that have diverged in localisation and function. There are nine, eleven and five MAP65 paralogues in *Arabidopsis thaliana* [289], *Oryza sativa* [108]

and *Physcomitrium patens* [149] respectively. Interestingly, there is no known homologue of MAP65 in *Nicotiana benthamiana*, which makes the model organism particularly useful for MAP65 transient expression assays. The plant MAP65s are classed into 5 major clades [289] with seven of the nine *Arabidopsis* MAP65s represented in each group while the remaining two are grouped as orphans (Fig. 2.5). The *in vivo* localisation, *in vivo* and *in vitro* functions of *Arabidopsis* MAP65s and the phenotypes of reported MAP65 *Arabidopsis* mutants are listed in Table 2.3, Table 2.2 and Table 2.4 respectively.

There are many discrepancies to the localisation of MAP65s, owing to the different experimental techniques applied. *Arabidopsis* stable lines endogenously expressing tagged MAP65 under its native promoter in its respective mutant background is preferred but is more challenging to generate. In the absence of such stable lines, immunolocalisation experiments prove useful, especially since all reported antibodies against *Arabidopsis* MAP65s, except for anti-MAP65-1 which can also bind MAP65-2, are monospecific to their respective MAP65 [289]. In Table 2.2, experimental methods less likely to produce artefacts are prioritised and listed when available, while other sources with sometimes conflicting results are referenced. For instance, MAP65-4 has occasionally been reported to have perinuclear localisation either as dots or to microtubules [64], but is not reproduced in newer and more precise experiments.

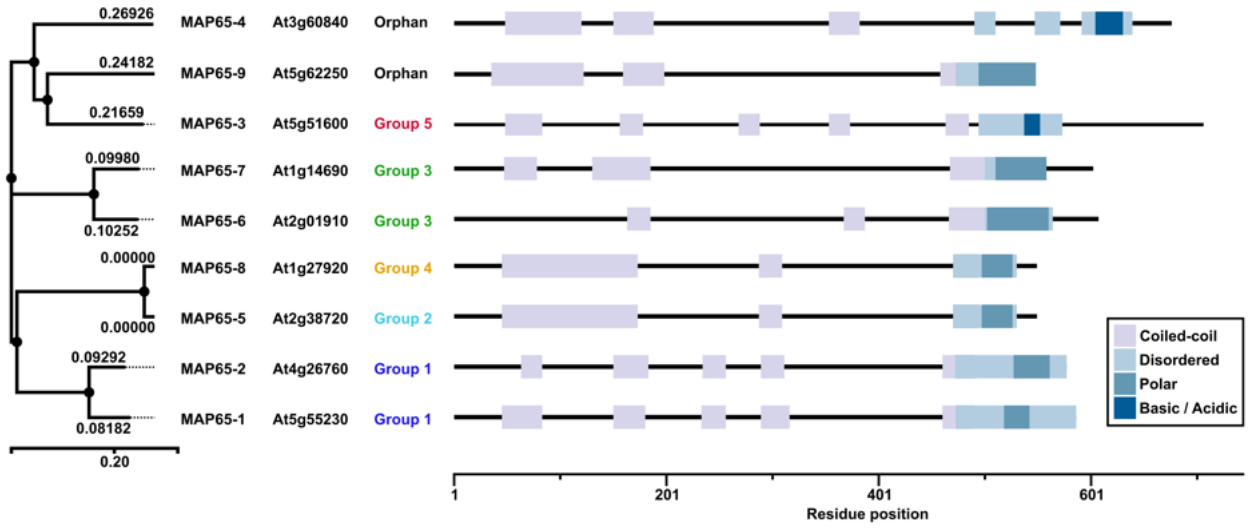

Figure 2.5: Protein domain and phylogeny predictions of *Arabidopsis* MAP65s.
Protein domain predictions are from UniProt. Phylogenetic estimations are predicted with ClustalW. Group numbers indicate subclades that were identified in [289] in a phylogenetic analysis of MAP65s across several plant species. MAP65-4 and -9 are orphans as they did not class into a clade with the other analysed MAP65s.

Table 2.2: Cellular localisation of *Arabidopsis* MAP65s.
Abbreviations: cortical microtubules (CMs), preprophase band (PPB), cell division zone (CDZ), mitotic spindle (MS), phragmoplast (PP), cell plate (CP), microtubule (MT), promoter (pro), not available (n.a.). ✔ high signal overlap with microtubules in the respective microtubule array, ✘ indicates no localisation. Here I make a distinction between midzone and midline localisation to differentiate between the more broad localisation of MAP65-1 and -2 to the phragmoplast compared to MAP65-3 and -5. Elsewhere, I simply refer to the localisation as a midzone localisation.

Protein	Localisation						Details	Method & Reference	Other reports
	CMs	PPB	CDZ	MS	PP	CP			
MAP65-1	✔	✔	✘	✔	✔	✘	PP midzone	GFP tag, native pro, in *map65-1/2* [177]	[64, 264, 289, 292]
MAP65-2	✔	✔	✘	✔	✔	✘	PP midzone	mCherry tag, native pro, in *map65-1/2* [177]	[164]
MAP65-3	✘	✔	✘	✔	✔	✘	late anaphase spindle midzone, PP midline	GFP tag, native pro, in *map65-3*[66]	[64, 123, 214, 264, 289, 330]
MAP65-4	✘	✔	✔	✔	✔	✔	diffuse around PPB, late anaphase spindle midzone, PP midline and distal ends	GFP tag, native pro, in *map65-4* [163]	[64, 88, 289]
MAP65-5	✔	✔	✘	✔	✔	✔	MS & PP midline, also to perinuclear MTs	Immunolocalisation [289]	[64]
MAP65-6	✔	✘	✘	✔	✔	✘	CM subset, diffuse around MS and PP, also to mitochondria	GFP tag, native pro, in wild-type [175]	[289]
MAP65-7	✔	n.a.	n.a.	n.a.	n.a.	n.a.	CM subset	GFP tag, native pro, in wild-type [175]	n.a.
MAP65-8	✔	✘	✘	✔	✔	✘	punctate on CMs, spindle poles, interpolar MTs, PP distal zones	GFP tag, 35s pro, *Nt* BY-2 [64]	Others
MAP65-9	✘	✘	✘	✘	✘	✘		Immunolocalisation [289]	n.a.

Table 2.3: Reported functions of *Arabidopsis* MAP65s.
Question mark (?) indicates suggested putative *in vivo* functions baesd on localisation. There are no reported functions for MAP65-7 and -9. Abbreviation: microtubule (MT).

Protein	Function		Other comments
	in vivo	*in vitro*	
MAP65-1	axial cell elongation [177, 178, 264] axial cell proliferation [177, 178, 264] salt stress MT reorganisation [361] gravity response MT reorganisation [297] pathogen induced MT reorganisation [109]	MT bundling [292] ➥ preference for antiparallel MTs [98] ➥ contact-angle dependence [321] ➥ salt dependence [48] bundled MT dynamicity regulation [304] phase separation [48, 98] bent MT stabilisation [247] MT stabilisation at 10°C but not on ice [164, 182] antagonist of kinesin-1-based MT sliding [248]	phosphorylated by MPK4 [264] phosphorylated by AUR1 [27] interacts TRAPII [301] interacts HopE1 [109] binds phosphatidic acid [245, 359] monomeric in solution [98]
MAP65-2	axial cell elongation [177, 178, 264] axial cell proliferation [177, 178, 264]	MT bundling [164] MT catastrophe reduction on ice [164]	phosphorylated by MPK4 [264]
MAP65-3	phragmoplast MT stabilisation [214]	antiparallel MT bundling [123]	phosphorylated by MPK4 [264] phosphorylated by AUR1 [66] dephosphorylated by SAC9 [157] interacts POK2 [118] interacts TRAPII [301] interacts PAKRP1, PAKRP1L [123]
MAP65-4	phragmoplat MT stabilisation [163]	MT bundling [88] ➥ increases rescue, reduces catastrophe [88]	
MAP65-5	plasmodesmata formation ? [64]	antiparallel MT bundling [98]	monomeric in solution [98] binds phosphatidic acid [359]
MAP65-6	mitochondria positioning ? [182]	weak MT bundling [182] no MT stabilisation at 10°C [182]	binds phosphatidic acid [359]
MAP65-8	MT minus end targeting ? [64]		binds phosphatidic acid [359]

Table 2.4: Phenotypes of *Arabidopsis* MAP65 mutants.
$^{+/-}$ and $^{-/-}$ indicate heterozygous and homozygous for the mutant allele respectively. In the main body of this thesis, mutants mentioned are homozygous for the mutant allele unless stated otherwise. Double mutants here are separated by semicolon (;), whereas elsewhere it is a forward slash (/). There are two types of MAP65-3 mutant alleles, the *pleaide (ple)* [216] alleles and the *dyc283* [44] allele identified in separate genetic screens. They all show the same phenotype and is thus collectively referred to as *map65-3*$^{-/-}$ here. Mutant phenotypes for MAP65-5 to -9 have not been reported.
*There are two *map65-4* listed to indicate that an extra copy of wild-type MAP65-4 was introduced into the *Arabidopsis* genome in an experiment to test if MAP65-4 could compensate for MAP65-3 loss.

At mutant	Phenotype	Reference
map65-1$^{-/-}$	no phenotype	[264]
map65-2$^{-/-}$	no phenotype	[264]
map65-3$^{-/-}$	stunted growth, enlarged multinucleate cells, wall stubs	[64, 214]
map65-4$^{-/-}$	no phenotype	[163]
map65-1$^{-/-}$*;map65-2*$^{-/-}$	no phenotype	[264]
map65-1$^{-/-}$*;map65-3*$^{-/-}$	exacerbates *map65-3*$^{-/-}$ phenotype	[264]
map65-2$^{-/-}$*;map65-3*$^{-/-}$	exacerbates *map65-3*$^{-/-}$ phenotype	[264]
map65-4$^{+/-}$*;map65-3*$^{-/-}$	exacerbates *map65-3*$^{-/-}$ phenotype	[163]
map65-4$^{-/-}$*;map65-3*$^{-/-}$	synthetic lethal	[163]
**map65-4*$^{+/+}$*;map65-4*$^{+/-}$*;map65-3*$^{-/-}$	rescues *map65-3*$^{-/-}$ phenotype	[163]

2.3.2 MAP65-3

2.3.2.1 *In vivo* function

Of the nine MAP65s, MAP65-3 is especially interesting, on account of its strong mutant phenotype in *map65-3* mutants. Unlike *map65-1*, *map65-2* or *map65-4* single mutants, *map65-3* plants are overall smaller and exhibit cellular patterning defects (Table 2.4). *map65-3* mutants have incomplete cross-walls, evidenced by the presence of wall stubs, indicating a failure to complete cytokinesis [44, 123, 214]. MAP65-1, -2 and -4, which all localise ot the phragmoplast as well (Table 2.2), have been shown to function somewhat redundantly with MAP65-3 as double mutants display more severe growth and cytokinetic defects [163, 264]. Moreover, *map65-3/-4* mutants are synthetic lethal [163] (Table 2.4).

2.3.2.2 *In vivo* localisation

MAP65-3 is a mitosis specific MAP as it only localises to the preprophase band (PPB) and phragmoplast (Table 2.2). Its PPB localisation has been consistently reported in immunolocalisation experiments [123, 214, 289] and GFP-tagged exogenous expression in tobacco BY-2 cells under a dextran inducible promoter [264]. The best and latest localisation experiment for MAP65-3 is with an *Arabidopsis* stable line expressing GFP-MAP65-3 under its native promoter in the *map65-3* mutant background [66]. This latest report confirms the late anaphase spindle and phragmoplast midzone localisation of MAP65-3, but does not comment on its preprophase band (PPB) localisaiton. It is likely that the authors chose not to comment on the PPB localisation since it is well-established and beyond the focus of their paper in particular. Moreover, although not as precise as stablie line expression, the earlier

immunolocalisation experiments that showed PPB localisation was performed using a monospecific anti-MAP65-3 antibody [289]. Altogether, MAP65-3 localises to the PPB, dissapears with it, reappears in late anaphase at the spindle midzone and remains targeted to the phragmoplast midzone [66, 123, 214, 289, 330].

2.3.2.3 Regulation

Details on MAP65-3 specific recruitment to and function at the PPB is unclear, as *map65-3* mutants still produce functional PPBs [214, 216]. Meanwhile, MAP65-3 functions at the phragmoplast midzone to cross-link and stabilise antiparallel microtubule overlaps [123, 214]. *map65-3* mutants have widened 'clear zones', a region where the microtubule binding domain (MBD) of MAP4 cannot bind in the phragmoplast. Consequently, *map65-3* mutants fail to properly fuse cell plate materials and do not form proper cross-walls [123, 214].

2.3.2.3.1 Restriction by kinases The restriction of MAP65-3 to the midzone of the late anaphase spindle and phragmoplast and away from the distal zones is controlled by the group α Aurora kinases, Aurora 1 and 2 (AUR1, 2) [66] (Fig. 2.6). Aurora 1 and 2 (AUR1, 2) are two functionally redundant *Arabidopsis* Ser/Thr kinases involved in cytokinesis and are part of the larger Aurora family kinases that regulate mitosis in eukaryotes [158, 326][7]. AUR1, 2 localises to perinuclear microtubules during preprophase, to spindle poles, to interpolar microtubules and to the phragmoplast distal zone with AUR1 additionally also found at the cell plate [28, 66, 139]. At these regions, MAP65-3 is actively excluded due to Aurora phosphorylation at Ser-528 and Ser-570 [66]. Notably, in contrast to MAP65-3 localisation, AUR1 is excluded from the midzone of the spindle and phragmoplast, but appears on the phragmoplast midzone in the lagging zone, seemingly on the cell plate [66]. Consequently, MAP65-3 is prematurely recruited to the mitotic spindle and loses its midzone specificity in *aur1/aur2* double mutants [66].

In vivo, the inability to phosphorylate MAP65-3 in *aur1/2* mutants is manifested as increased MAP65-3 lifetime on microtubule arrays [66]. MAP65-3^{AA} (a non-phosphorylatable variant) and MAP65-3^{DD} (a phosphomimetic variant) show much slower and slightly faster turnovers on phragmoplast microtubules respectively compared to wild-type MAP65-3 [66]. The inability to phosphorylate and remove MAP65-3 from the phragmoplast results in aberrantly long phragmoplasts that appear wonky and increases the time needed to expand the phragmoplast [66]. Nevertheless, cytokinesis itself is not aborted, like in *map65-3* mutants, indicating that other factors come into play to remove MAP65-3 from the phragmoplast, albeit at a later stage. A possible player is MPK4, which is also cell plate localised and is the final MAPKKK of the *Arabidopsis* NACK-PQR cascade (Fig. 2.4). MAP65-3 has also been shown to be phosphorylated by MPK4 [150].

[7] There are three aurora kinases that are classed into two groups in *Arabidopsis thaliana.* AUR1, 2 form group α and AUR3 forms group β [326].

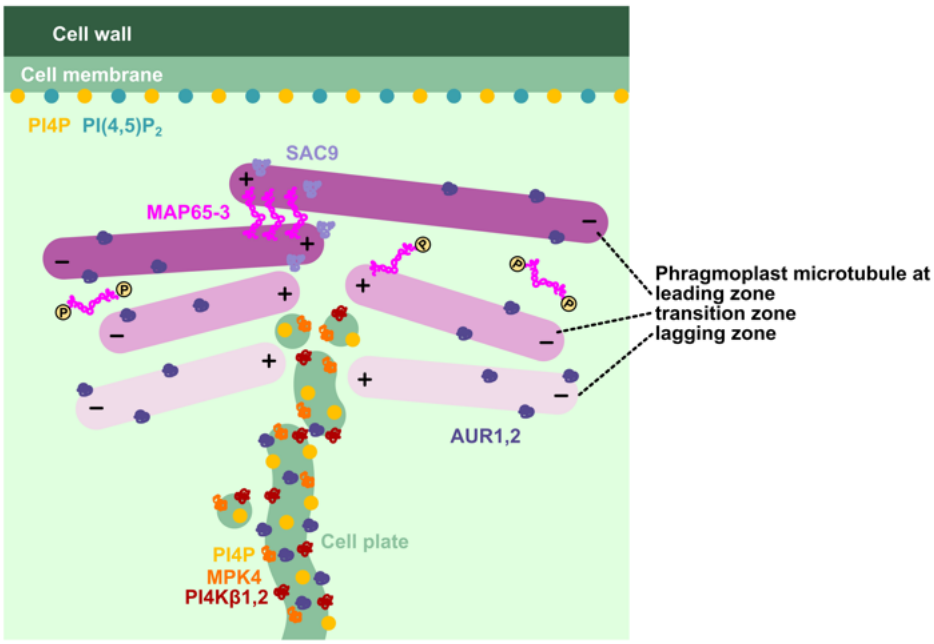

Figure 2.6: MAP65-3 regulation at the phragmoplast.
MAP65-3 is restricted in localisation and function directly through dephosphorylation by kinases, MPK4 and AUR1, 2. MAP65-3 restriction is also dependent on accurate PI4P accumulation at the cell plate. PI4P formation at the cell plate is regulated synergistically by PI4Kβ1, 2, MPK4 and SAC9, while PI(4,5)P_2 is actively removed from the cell plate by SAC9. Please note that other than MAP65-3, which is a known microtubule binding protein, the mechanism of localisation of other proteins at the phragmoplast is not completely elucidated. Here, SAC9 is depicted to sit on the microtubule, but it is not known if it co-localises with MAP65-3 because it is a microtubule binding protein or if it is binding MAP65-3 or other proteins or structures here. Similarly, the mechanism of AUR1, 2, MPK4 and PI4Kβ1, 2 localisations are also not completely clear.

2.3.2.3.2 Restriction by PI4P Lipid signatures have been known to a play a role in controlling cytokinesis. For instance, the human OCRL phosphatase converts the phosphoinositol phosphate (PIP) PI(4,5)P_2 into PI4P at the division site on the plasma membrane, creating a PI4P only zone [63], which is important to clear F-actin from the intercytokinetic bridge [69, 334]. PI4P and PI(4,5)P_2 also play cytokinetic roles in plants, but do not differentially mark the cell division zone (CDZ). Interestingly, PI4P localises to the plasma membrane and cell plate [286, 333] whereas PI(4,5)P_2 localises also to the plasma membrane but is actively excluded from the cell plate until cell plate fusion [157, 287]. PI4P accumulation at the cell plate is synergistically mediated by the kinases MPK4 and PI4P kinase β 1 and 2 (PI4Kβ1, 2) [165]. Meanwhile, PI(4,5)P_2 is actively cleared from the cell plate by the phosphatase SAC9, which converts it to PI4P [157]. In regards to this, MPK4, PI4Kβ1 and 2 are localised to the cell plate [150, 165, 333] while SAC9 co-localises with MAP65-3 at the phragmoplast leading zone [157] (Fig. 2.6), however the exact mechanism for their localisations is not clear.

The retention of PI4P and clearing of PI(4,5)P_2 at the cell plate is required for accurate restriction of MAP65-3 to the leading zone of the phragmoplast. In *pi4kβ1/pi4kβ2* double mutants and *sac9* mutants, MAP65-3 mislocalises to the phragmoplast midzone but without regard to the leading or lagging edge [157, 165]. Full homozygous *pi4kβ1/pi4kβ2/mpk4* plants are synthetically lethal [165],

whereas heterozygous plants show more severe cytokinetic defects. The phragmoplasts generated by ectopic MAP65-3 localisation experience prolonged phragmoplast expansion, inability to mature into the ring-shape and discontinuous cell plate formation. Hence, the anionic lipid signature of the cell plate is crucial in the timely and proper localisation and function of MAP65-3 for coordinated phragmoplast expansion and cell plate formation.

2.3.2.4 Biochemistry

MAP65-3 exhibits a similar protein domain arrangement to that of its animal and yeast counterparts. (Fig. 2.7, 2.8). Its N-terminal consists of a coiled-coil (CC) dimerisation domain followed by a conserved spectrin-fold domain that binds microtubules (Fig. 2.7)[8]. The region after the microtubule binding domain (MBD) is unstructured.

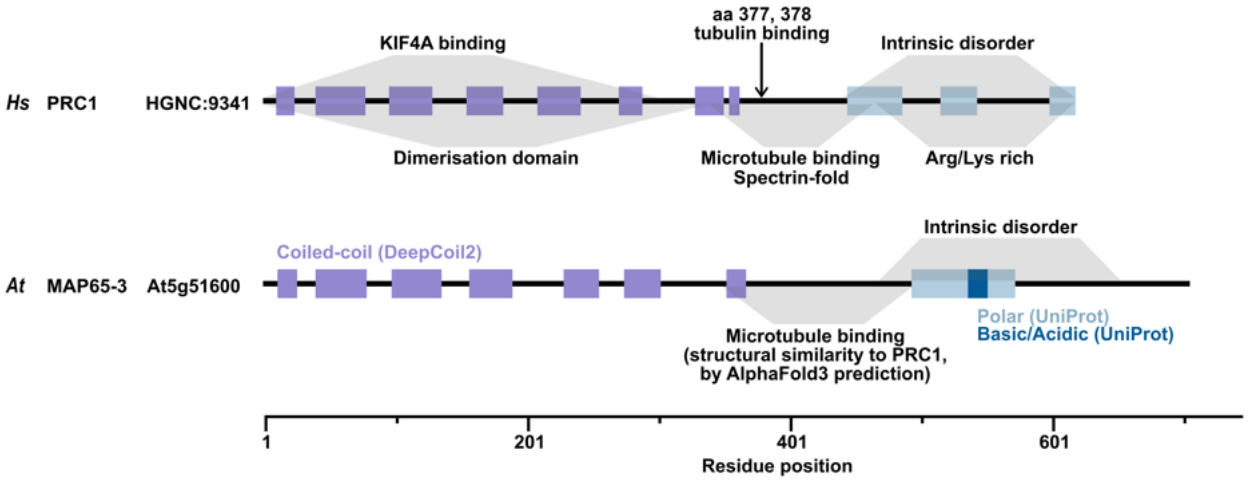

Figure 2.7: Protein domain annotation of *Hs*PRC1 and *At*MAP65-3.
Coiled-coil predictions are from DeepCoil2. Intrinsic disorder predictions are from AIUpred. The PRC1 microtubule binding domain has been confirmed with X-ray crystallography and contains a spectrin-fold. This same spectrin-fold is present in MAP65-3 (predicted by AlphaFold3, Fig. 2.8) and the corresponding region is marked on MAP65-3.

At the microtubule binding site, two alanines (A409 & A420 in MAP65-1) have been shown to be well conserved and essential for microtubule binding and bundling [292]. The corresponding A420V in MAP65-3 is the point mutation in the *ple-4* mutant that lacks a functional MAP65-3 [292]. Interestingly, A409 in MAP65-8 is naturally substituted with a valine [292], which might reflect the differential microtubule array preference of the two MAP65s (Table 2.2).

Unlike the MAP65-1 and -5 which purifies cleanly and appears monomeric in solution [98], MAP65-3 is dimeric in solution [123]. *In vitro*, MAP65-3 has been shown to retain the antiparallel microtubule bundling activities of its yeast and animal counterparts [123].

[8] All nine *Arabidopsis* MAP65s have their microtubule binding domain previously predicted [164].

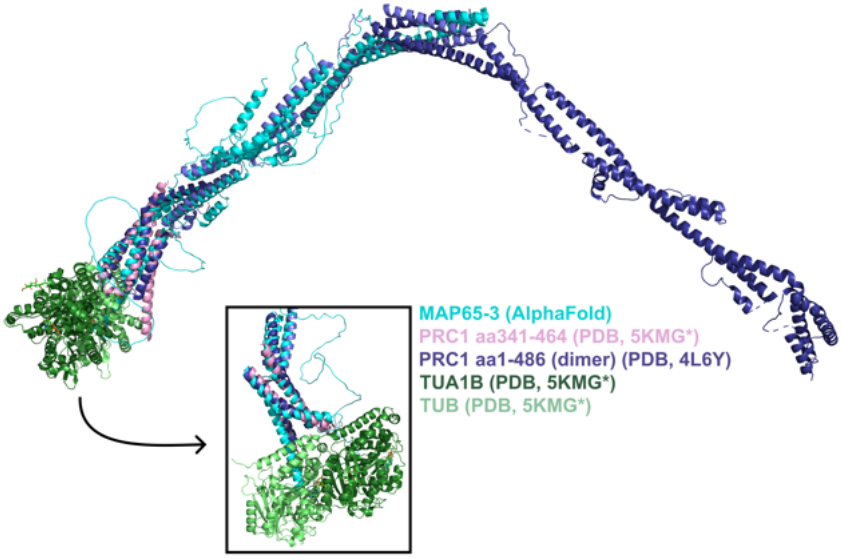

sequences to align		RMSD	aligned atoms
PRC1 aa341-464 (PDB, 5KMG*)	PRC1 aa1-486 (dimer) (PDB, 4L6Y)	2.351	678
MAP65-3 (AlphaFold)	PRC1 aa1-486 (dimer) (PDB, 4L6Y)	5.336	1993

*structure is of PRC1 bound to tubulin dimer

Figure 2.8: Structures of PRC1, MAP65-3 and a tubulin dimer.
Two PDB structures of PRC1 are shown here: 5KMG which has aa 341-464 of PRC1 (pink) bound to the tubulin dimer (green) and 4L6Y which has aa 1-486 of PRC1 (lilac) as a dimer. Not shown is the unstructured C-terminal region of PRC1 (aa 487-620), which is analogous to the unstructured C-terminal region visible for MAP65-3 (cyan).

Chapter 3

Kinesins

3.1 Kinesins

Kinesins are a superfamily of proteins first discovered observed in the 1980s [2, 30], identified as molecular machines that translocate along the microtubule from giant squid axons [324] and dubbed 'kinesin' (from Greek 'kinein', meaning 'to move'). The kinesin's ability to bind to and translocate along microtubules underpins its function in transporting and positioning cargo and organelles within the cell. As such, kinesins play essential roles in many microtubule-based processes such as mitosis, meiosis, axonal and intraflagellar transport, as well as cell wall patterning and cytokinesis in plants. In humans, defects in kinesins are often manifested as motor neuron diseases such as amyotrophic lateral sclerosis (ALS) [224], hereditary spastic paraplegia (HSP) [97], microcephaly [246] and encephalopathy [85] and have also been implicated in Parkinson's [220] and Alzheimer's diease [75]. Additionally, viruses can hijack kinesins to efficiently colonise their hosts [256].

Since its discovery, numerous kinesins have been identified across various kingdoms, requiring a classification system of its own and nomenclature standardisation [156]. As several decades passed after the initial kinesin discovery before a naming consensus was reached, there are understandably many kinesins whose names make historical sense but relate little to their superfamily. For example, the *Homo sapien* KIF5s (KIF initially stood for Kinesin Family) are kinesin-1s. Interestingly, the kinesin of this thesis - *Arabidopsis thaliana* kinesin-12D/POK2 is a member of the kinesin-15 superfamily, which was originally part of the monophyletic kinesin-12 superfamily. The term 'kinesin-12' should supposedly be deprecated because the superfamily was resolved into the kinesin-15 and -16 superfamilies, which respectively contain the *Hs* KIF15 and KIF16 [348]. Nevertheless, these naming conventions have yet to gain widespread adoption within the plant community, calling this superfamily 'kinesin-12' is still convention. More recently some publications have begun referring to this family as Kinesin-12/15 to include both the plant and larger kinesin community conventions [176].

The most recent comprehensive analysis classes the kinesins into 17 superfamilies [349] and follows conventions laid out at the 2003 American Society for Cell Biology meeting [156]. In particular, phylogenetic classification compares only the kinesin motor domain and sequences have to be found in at least two kingdoms [156], otherwise it is classed as an 'orphan kinesin'. This classification was also used in a recent phylogenetic analysis carried out for plant kinesins [176]. Classification of kinesins based on only the motor domain is sufficient for functional correlations within superfamilies across several species. Interestingly, classification of kinesins using the entire protein sequence generates the same clades and superfamilies [176], suggesting co-evolution of the motor domain and its auxiliary domains. A brief but not exhaustive overview of all kinesin superfamilies, key members, some reported functions and notable features are listed in Table 3.1. Despite the name 'kinesin' to denote movement, not all kinesins translocate along the microtubule, such as the kinesin-13 superfamily of microtubule depolymerisers which only diffuse along the microtubule.

3.1.1 Directionality

Historically, kinesins were separated into three groups based on the location of the kinesin motor domain: N- or C-kinesins when the kinesin motor domain was located at the N- or C- terminal of protein primary sequence, and M- or I-kinesins (standing for 'middle' or 'internal') when the motor domain was in the center of the protein sequence [121, 193, 323]. This grouping correlated misleadingly well with translocation directionality of the kinesin on the microtubule [186, 342]. N-kinesins were plus-end directed (e.g., kinesin-15 superfamily), C-kinesins were minus-end directed (e.g., kinesin-14 superfamily), and M-kinesins were diffusive and did not translocate on the microtubule (e.g., kinesin-13 superfamily). With this neat correlation of motor domain position and directionality, it was tempting to speculate a direct casual connection.

Although a very useful mnemonic, this is however, untrue. Rather than merely the position of the motor domain in the protein sequence, it was the neck or stalk domains, adjacent to the motor, that were variable in sequence and length across superfamilies, that determined directionality. For example, the *Hs*KIF18A/kinesin-8 neck linker docks along the motor domain towards the plus-end [239], thus tilting the connected stalk towards the plus-end, creating probabilistic positioning for the next binding event towards the plus-end [9, 254]. Similarly, this tilt was shown with laser-trap single molecule assays for the stalk of *Drosophila melanogaster* Ncd/kinesin-14 towards the microtubule minus-end [79]. Mutations on the stalk domain of *Dm*Ncd/kinesin-14 reversed directionality [260]. Additionally, an unstable Ncd mutant lost directional specificity and could switch directions [79]. Other kinesins have also been shown to switch directionality under specific conditions [33, 77, 93, 101, 258].

The presence of the neck/stalk domains is not solely deterministic of translocation directionality. For example, a single point mutation in the stalk of *Dm* Ncd/kinesin-14 led to a reversal of direction [79]. Moreover, unlike the rest of the minus-end directed kinesin-14s, *Arabidopsis thaliana* kinesin-14D1/MDKIN2 was recently shown to be plus-end directed, despite having the conserved 'neck helix'

Table 3.1: Kinesin superfamilies, reported functions and notable features.
Most of the information were gathered from previous reviews [94, 192] and is not exhaustive for family members, functions or features. As of 2020, there is no data on kinesin-17, 18, 19, 20 superfamilies other than the initial phylogenetic classification and are represented only in a few species [349]. A few famous plant kinesins are listed here, but will be discussed to greater detail in Table 3.3. Abbreviations: *Hs, Homo sapiens; Ce, Caenorhabditis elegans; At, Arabidopsis thaliana; Sc, Saccharomyces cerevisiae; Dm, Drosophila melanogaster; Sp, Saccharomyces pombe; Cr, Chlamydomonas reinhardtii; Xl, Xenopus laevis; Pp, Physcomitrium patens.*

Superfamily	Representative family members	Reported functions	Notable features	References
Kinesin-1	*Hs*KIF5A, B, C	vesicle transport	consists of a heavy and light chain	[192]
Kinesin-2	*Hs*KIF17, *Hs*KIF3A/B	vesicle intraflagellar transport	the former is homodimeric, the latter is heterotrimeric	[114, 192]
Kinesin-3	*Ce*UNC-104	organelle transport	monomeric	[192]
Kinesin-4	*Hs*KIF4A/Chromokinesin, *Hs*KIF21A/B, *At*FRA1	organelle transport, chromosome movement	includes previously Kinesin-10 family members	[192]
Kinesin-5	*Hs*Eg5/KIF11, *Sc*Cin8, *An*BimC	bipolar spindle formation	homotetrameric, bidirectional translocation	[192]
Kinesin-6	*Hs*KIF23/MKLP1, *Ce*ZEN-4	cytokinesis, spindle polarity		[192]
Kinesin-7	*Hs*CENP-E, *Sc*Kip2	kinetochore microtubule attachment	homodimers	[143, 192]
Kinesin-8	*Sc*Kip3, *Dm*KLP67A, *Hs*KIF18A/B, *Hs*KIF19	plus-end directed motor, variety of microtubule dynamic regulation	homodimer, but *Sp*KLP5/6 is a heterodimer	[170, 192]
Kinesin-9	*Hs*KIF9, *Hs*KIF6, *Cr*KLP1	not uniform across species; *Hs*KIF9 has mitotic function in HeLa cells and regulates podosome number and function of macrophages; *Cr*KLP1 localises to axonemes	only in flagellated / cilia possessing species	[7, 18, 58, 348]
Kinesin-10			now kinesin-4	
Kinesin-11			previous members *Hs*KIF26A, *Sc*SMY1 are now orphan kinesins	[348]
Kinesin-12			now kinesin-15/-16	
Kinesin-13	*Hs*KIF2C/MCAK, *Dm*KLP10A, *Dm*KLP59C, *Xl*KCM1, *Ce*KLP7	microtubule depolymeriser	central motor domain	[347]
Kinesin-14	*Sc*KAR3, *Dm*Ncd, *Hs*HSET	minus-end directed motor, microtubule crosslinkers	C-terminal motor domain	[31]
Kinesin-15	*Hs*KIF15, *At*POK1, POK2, *Pp*KINID1a,b	plus-end directed motors	homodimers/tetramers	[71]
Kinesin-16	*Hs*KIF12	possible role in axoneme function or building	only in flagellated / cilia possessing species	[1, 349]
Kinesin-17			only in flagellated / cilia possessing species	[348, 349]
Kinesin-18, -19, 20				[349]

(see Section 3.1.2.2) of the kinesin-14 superfamily [110]. Thus, the specific sequence of the neck and stalk domains adjacent to the motor domain is also very important.

3.1.2 Structure

The founding member of the kinesin superfamily – kinesin-1 – is a heterotetramer of a dimer of two heavy chains (kinesin heavy chain, KHC) and a dimer of two light chains (kinesin light chain, KLC). The KHC has a globular motor domain, which is the catalytic core that binds and releases microtubules

in an ATP-dependent manner, connected to a stalk domain via a neck linker, followed by a C-terminal tail that interacts with the KLC. The KLC acts an adaptor that couples the KHC to cargo for transport. Apart from the kinesin-1 superfamily, other kinesins are usually homodimers with some exceptions (see Table 3.1). The monomer structure of the homodimeric kinesin is similar to that of the KHC dimer, where the tail takes over the role of the KLC and mediates direct binding to cargo or additional adaptor proteins.

3.1.2.1 Motor domain

The kinesin motor domain is the catalytic nucleotide-hydrolysing core of the protein. All kinesin motors share the same basic structure: a β-sheet sandwiched between two sets of three α-helices. The helices are numbered 1 to 6 in order of their appearance in their primary amino acid sequence, from the N- to C-terminus. Helices-α4 to 6 face the microtubule lattice. The microtubule binding surface consists thus of some of these helices and nearby loops. Meanwhile, the ATP binding site is located on the P-loop between β-strand 3 and helix α2 [186]. ATP binding, hydrolysis and release of ADP + P_i causes changes in conformation of elements within the motor domain around the P-loop (the switch-1 and switch-2 motifs) which is amplified as large-scale conformational changes in the motor domain as a whole [186].

3.1.2.2 Neck

Neck linker: The neck or neck linker is a sequence of 12–18 residues immediately after the motor domain in N-terminal motor kinesins [240] and is essential for the function of the kinesin motor domain. In structural experiments, the neck linker is found to be either docked against the motor domain, forming a β-sheet that interacts with the β-sheet in the motor domain, or is unstructured and therefore not visible [120]. In addition to directionality, the neck linker is also thought to modulate processivity of translocative kinesins. In particular, kinesin-1 (neck length, 14 residues) is more processive than kinesin-2 (neck length, 17 residues) [125, 280]. The longer neck is thought to aid obstacle navigation.

Neck helix: The kinesin-14 superfamily is a family of C-kinesins, where their motor domain is at the C-terminus (except for *Arabidopsis thaliana* Kinesin-14 subclass D–G (Fig. 3.1)). In the superfamily, there is no neck linker between the motor domain and the stalk, and so the first helix of the stalk is a 'pseudo-neck' domain, called the 'neck helix' to distinguish it from the neck linker of N-kinesins. In addition to directionality, the neck helix is also thought to modulate microtubule binding affinity [169].

3.1.2.3 Stalk

The stalk is a coiled-coil (CC) region in the middle of the kinesin after the motor and neck domain and before the tail region. The CCs serve as dimerisation modules of the kinesin. Morever, they also amplify conformational changes from the neck and motor domain, as well as conformational changes in the tail to the neck and motor domain [46]. In some kinesins (e.g., kinesin-1, kinesin-3) there exist a

long unstructured domain between the CC regions that acts as a 'hinge' between rigid CCs. These hinges allow the kinesin to fold back on itself, where the tail interacts with the motor domain and auto-inhibits its interaction with microtubules. This auto-inhibition is lifted when the tail domain is bound by a specific cargo or phosphorylated [332] and functions to regulate kinesin activity. More recently it was shown that other shorter unstructured domains between CCs serve as smaller hinges, where the auto-inhibitory folding is multi-phasic in order to pack the kinesin into an inactive state [313].

3.1.2.4 Binding interfaces

Other than kinesin-1s, most kinesins bind their cargo directly through their tail domain. As such several binding interfaces have been identified in the tail and directly relate to the cellular processes the kinesin is involved in. For instance, several members of the kinesin-4/10 superfamily have DNA binding domains in their tails, and are thus also known as 'Chromokinesins' [3]. There is also a variety of protein binding interfaces found across kingdoms (e.g. forkhead associated (FHA) domain in *Hs*KIF1A/kinesin-3 and *Ce*UNC-104/kinesin-3) and specific to kingdoms (e.g. Aramdillo repeat motifs (ARM) in *At*ARK/kinesin-19B) [255]. Of great interest is the plant kinesin-14 family member KCBP/Zwichel which contains a plant-specific Calmodulin binding domain (CaM) in the C-terminus, just downstream of the C-terminal motor domain (Fig. 3.1). The CaM modulates microtubule binding of the motor domain where microtubule binding is lost in the presence of Ca^{2+} [219].

Additional microtubule binding Except for kinesin-2, the basic functional unit of a kinesin is a dimer. Hence, kinesin dimers contain two motor microtubule binding domain (MBD)s. Some kinesins possess additional MBDs in their tail domain. In many cases, the second MBD acts like a cargo binding domain with the cargo in question being another microtubule. This is the case for kinesin-1/*Hs*KIF5B [111, 221, 275, 305] and kinesin-14 [91, 136, 204, 219, 233, 318].

However, in the case of tetramers such as kinesin-5/Eg5/BimC [302, 346] and kinesin-12/15/KIF15 [308], their second motor dimer pair is essentially the 'cargo binding' domain where it binds another microtubule. Furthermore, both kinesins possess second non-motor MBDs in their tails, effectively giving the tetratmer 8 MBDs. For Eg5, this second MBD helps to keep the kinesins tethered to the microtubule during antiparallel sliding as the motor domain binds microtubules only weakly [346]. Meanwhile, the second MBD of KIF15 overlaps its auto-inhibitory domain, and only releases the kinesin motor domain when bound to another microtubule [308]. This allows for selectivity, such that only KIF15s bound to microtubule bundles would be active and is a proposed mechanism for selective localisation of KIF15 to kinetochore fibers [308].

Lipid binding Many of the cargo transported by kinesins are membrane-bound. For example, *Hs*KIF5B/kinesin-1 transports mitochondria in the neurons via adaptor proteins MIRO and TRAK [42]. Additionally, Anton et al. showed that longer KLCs sometimes carry an amphiphatic helix (AH) that is capable of phosphoinositol phosphate (PIP) binding [8]. In addition to lipid binding

via adaptor proteins and KLCs, the C-terminal tail of *Hs*KIF5B/kinesin-1 heavy chain directly binds PA, PI(3,4,5)P_3 and PI(4,5)P_2, with the binding largely mediated through a positively charged 10-residue stretch (residues 901–909) [343]. The kinesin-3 family of long-range transporters [283] have also several members with lipid binding motifs, such as the START/lipid sterol-binding domain in mammalian KIF16A [319], the phox homology (PX) domain in mammalian KIF16B [23, 124] and the pleckstin homology (PH) domains in mammalian KIF1A and KIF1B [354] and *Ce*Unc-104 [146].

3.2 Plant kinesins

Kinesins were initially isolated from a plethora of organisms (squid optic lobe (1985), mammalian neurons (1985), sea urchin eggs (1985), slime mold (1989), fruit flies (1988), with *Arabidopsis thaliana* following not far behind in 1993. In 1993, Mitsui et al. isolated the first 5 of 61 *At*kinesins, which they termed kinesin of *Arabidopsis thaliana* (KAT), alphabetically assigned (A–E) to distinguish between the five identified kinesins [203]. These KATs were cloned by PCR amplification of *At* gDNA using primers targeting the conserved ATP-binding and microtubule binding regions of the kinesin motor domain [203]. Since then, many more plant kinesins across the plant kingdom have been identified and investigated, particularly for their specialised roles in plants. A brief summary of what has been discovered on the 61 *At* kinesins are listed in Table 3.3. Their protein domain annotations are depicted in Fig. 3.1. Please note that many reports are also available for rice, maize, cotton, *Nicotiana*, liverwort and moss but are not discussed in this thesis.

3.2.1 Diversity of plant kinesins

The main body of kinesin research is based on animal or yeast kinesins. Yeast poses an excellent model organism for kinesin studies, as there are only six kinesins in *S. cerevisiae* and nine in *S. pombe* (Table 3.2). Meanwhile, kinesins in plants have expanded in number (both in number of families and number of family members) and diverged in function [176, 180, 255, 362] (Table 3.2). Even the earliest diverged plants such as *C. reinhardtii* and *M. polymorpha* have 39 and 29 kinesins respectively, a comparable number to the 45 kinesins in humans [45, 81] and 25 in fruit flies [105]. The Californian poplar tree *Populus trichocarpa* has a staggering 86 kinesins [176].

The expansion of kinesin number and number of kinesin superfamilies (i.e., repertoire) has occurred in tandem with the emergence of plant-specific microtubule arrays [222, 273]. Whole genome and protein coding gene duplication events have driven the expansion of kinesin number and diversity [176]. In particular, the kinesin-7 and -14 superfamilies have greatly expanded. The plant kinesin-7s are further subdivided into three classes, kinesin-7A, B and C where the kinesin-7A classes together with the human and yeast kinesin-7s [176]. On the other hand, kinesin-7C is unique to the plant kingdom. The reports on the few plant kinesin-7s studied have revealed that they largely retain mitotic and cytokinetic functions and are thematically similar to their opisthokont counterparts [307, 310, 314, 315, 356]. Meanwhile, the kinesin-14s are a family of kinesins known for their C-terminally

Table 3.2: Number of known kinesins in common model organisms.

Kingdom	Species	Number of kinesins	References
Fungi	*Schizosaccharomyces cerevisiae*	6	Yeastgenome.org
	Schizosaccharomyces pombe	9	*pombe* GeneDB
Animalia	*Drosophila melanogaster*	25	[105]
	Homo sapiens	45	[45, 81]
	Caenorhabditis elegans	19	[283]
Plantae	*Chlamydomonas reinhardtii*	39	[176]
	Marchantia polymorpha	29	[176]
	Physcomitrium patens	72	[194]
	Arabidopsis thaliana	61	[251]
	Oryza sativa japonica cv. *nipponbare*	41	[255]
	Oryza sativa indica cv. *9311*	45	[255]
	Zea mays	76	[176]

located kinesin motor domain and minus-end directed microtubule motility [31]. As such, it has often been proposed that the kinesin-14 superfamily of plants expanded to compensate for dynein loss [355]. However, the plant kinesin-14 superfamily is subdivided into 7 subfamilies, where only kinesin-14A and B contain C-terminally located motor domains and are therefore the only groups correlated with minus-end directed motility required to compensate for dynein loss (See 3.1 for *Arabidopsis* kinesin domain architecture). Moreover, the expansion of the kinesin-14A and B subfamilies do not coincide with the loss of cytoplasmic dynein in the plant lineage [176].

Interestingly, certain families do not see significant expansion in family member number. For instance, kinesin-1, -2, -3 and -16 usually contained only a single member in most plant genomes [176]. For *Arabidopsis thaliana*, the kinesin-1, 4/10B, 6, 8 and 13 families are quite conservative (Fig. 3.1). Copy number variation (CNV) in the plant kingdom has usually been linked to advantageous traits [13], whereas in opisthokonts it generally not favoured as it can lead to reduced fitness [134, 257]. Negative selection might have also occured in these minimally expanded families. With little genetic 'wiggle-room', these families would theoretically retain ancestral functions and resemble their opisthokont counterparts more faithfully in structure and function.

3.2.2 A confusing trajectory of plant kinesin nomenclature

Conventionally, proteins and genes are named after phenotypes or mutants that originally allowed for their identification. A good example are the genes MUTE, SPEECHLESS (SPCH) and TOO MANY MOUTHS (TMM) which regulate stomatal guard cell differentiation, identified from mutants that produced none or too many stomatas [338]. Similary in the kinesin field, names like RADIALLY SWOLLEN 7 (RSW7) for the kinesin-5 KRP125c/RSW7 evokes the radially swollen roots of the respective *rsw7* mutant [351]. Such names are very useful in quickly informing the reader of the gene or protein function.

However, as more kinesins were identified, so too grew the need for standardised nomenclature. Thus a set of naming and classification conventions were set by the wider kinesin community [156]. Hence, in addition to historic names, kinesins were also given names that reflect their superfamily. For instance, MCAK was given the additional name *Hs*Kinesin-13C, to represent its membership in kinesin-13 superfamily. The inclusion of plant kinesins into this convention was difficult, as there were much more plant kinesins in terms of superfamilies as well as family members within each group. For instance, in *Arabidopsis*, there are 22 kinesin-14s and 15 kinesin-7s, which necessitates their classification into subfamilies. Due to difficulty in directly comparing kinesin superfamilies between the plant and other kingdoms, kinesin naming reflected the diverse preferences and interpretations of the researchers studying them.

There are many discrepancies even when discussing only *Arabidopsis* kinesins, of which there are 61 proteins. For the most part, naming is logical and reflects either function or domain constitution. For instance, the kinesin-19Bs ARK1–3 all contain Armadillo-repeats (hence, Armadillo-repeat kinesin); the kinesin-14B KCBP is named after its calmodulin binding domain (hence, kinesin CB protein)[1]; MDKIN1 and 2 are named after their malectin-binding domains (MDs).

Occasionally the renaming of kinesins can, at best, be considered unnecessary and, at worst, misleading and confusing. For example, the founding members of the kinesin-7B, mitochondria-targeted kinesin related protein 1 and 2 (MKRP1, 2) were named after their N-terminal mitochondria targeting signal sequence [135]. Later, a study of all five *Arabidopsis* kinesin-7B members renamed the kinesins to Kin7.1–5 according to the chromosomes they were located on, coincidentally chromsomes 1–5 [210]. Both naming systems are not very useful, as they do not reflect phylogeny or domain conservation. Specifically, Kin7.2 and Kin7.4/MKRP2 share a RING domain and rightly forms a subclade, Kin7.3 and Kin7.5 forming another (Fig. 3.1) [210].

Another example that breeds confusion is in the renaming of the kinesin-14D superfamily, which has three members. The first members studied were malectin-binding domain kinesin 1 and 2 (MDKIN1, 2) [99]. Later, a study that looked at all three kinesin-14Ds renamed them logically as simply kinesin-14D1, 2 and 3 [110]. However, the order was flipped such that kinesin-14D1 was MDKIN2 and kinesin-14D2 was MDKIN1 [110]. The order change is not only confusing but also nontrivial, since kinesin-14D1/MDKIN2 and kinesin-14D2/MDKIN1 have slight differences in localisation [110].

Plant kinesins, especially in their specific microtubule-based motility and effects on the microtubule, are often compared directly to their counterpart kinesins of other kingdoms. Despite this, updates in classifications and naming are not carried over into the plant field. Although phylogeneticists in the broader kinesin field have long united the kinesin-4/-10 family, split the kinesin-12 family into

[1] KCBP's historic name is ZWICHEL(ZWI) from the *zwichel* mutant identified to have trichomes with abnormally long branches and short stalks [130]. However, I am not sure what *zwichel* means in german, maybe something like 'little in between'?

the kinesin-15 and -16 families and identified the new kinesin-18, -19, and -20 families [348, 349]. Kinesins previously thought to be orphan kinesins (belonging to only one kingdom) have families now, but several plant kinesin phylogenetic papers overlook these updates [222, 342]. Thankfully, the most recent phylogenetic study of plant kinesins includes these updates and rightly classes the orphan kinesins into the new kinesin-18 and 19 families [176].

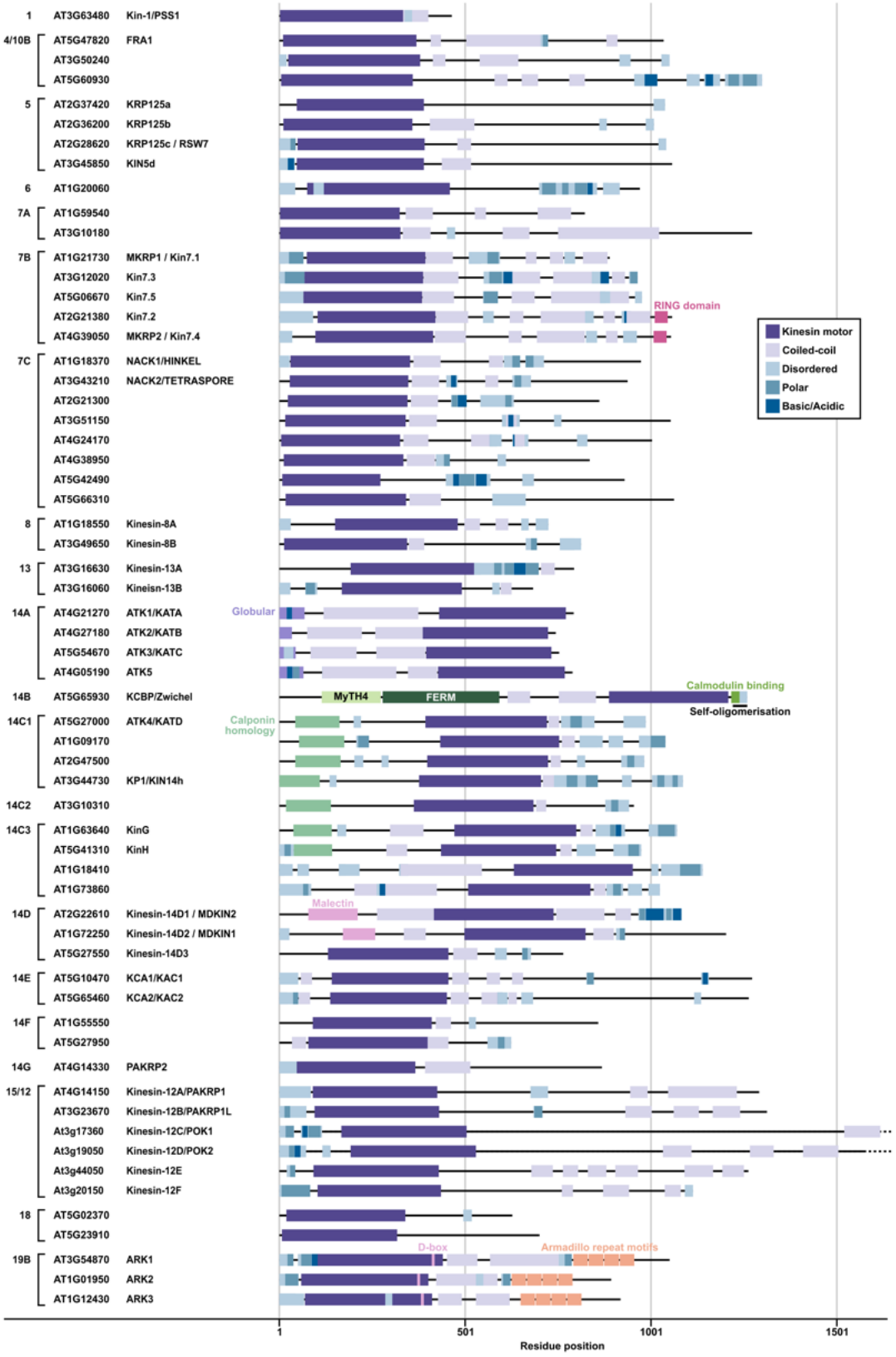

Figure 3.1: Protein domains of *Arabidopsis thaliana* kinesins.
Domain annotations follow predictions in UniProt. Superfamilies are classed according to [176], where the kinesin-14 superfamily is subclassed according to [110]. In this case, kinesin-14G/PAKRP2 (AT4G14330) was not given a name in [110], but was assigned kinesin-14D in [176] where it is grouped with the *Physcomitrium patens* KINID1a and KINID1b. Since kinesin-14D was used already to refer to the MDKIN1, 2 and Kinesin-14D3 in [110], I assigned PAKRP2 with the next available alphabet, kinesin-14G. The sequence length of kinesin-12C/POK1 (AT3G17360) and kinesin-12D/POK2 (AT3G19050) are 2066 and 2771 residues respectively and not fully shown here. To see their entire length, see Fig. 3.3.

Table 3.3: Plant kinesins reported functions and notable features. Abbreviations: amiprophos-methly (APM) – microtubule depolymerising drug, cell division zone (CDZ), cortical microtubules (CMs), cell plate (CP), Separase EXTRA SPINDLE POLES (ESP), *Gossypium herbaceum (Gh)*, kinetochore (kc), kinesin/separase complex (KISC), microtubule (MT), *Nicotiana tabacum (Nt)*, *Oryza sativa (Os)*, plasma membrane (PM), preprophase band (PPB), SHOOT-ROOT (SHR) transcription factor.

Superfamily	TAIR ID	Other name	Localisation	Function
1	AT3G63480	Kin-1/PSS1		role in female gametophytic division [340]
4/10B	AT5G47820	FRA1	CMs [360]	cellulose microfibril patterning [360]
	AT5G60930			
	AT3G50240			
5	AT2G37420	KRP125a		
	AT2G36200	KRP125b	nucleus, cytoplasmic [306]	*in vitro* assays show plus-end directed motility [306]
	AT2G28620	KRP125c / RSW7	CMs, PPB, spindle, phragmoplast [16]	spindle and phragmoplast organisation [16]
	AT3G45850	KIN5d		
6	AT1G20060			
7A	AT3G10180	KAK1	kc [315]	chromosome congression, interacts BUB3.3 and acts downstream [315]
	AT1G59540			
7B	AT1G21730	MKRP1 / Kin7.1	contains mitochondria-targeting sequence [135]	interacts Kin7.1, Kin7.5, ESP [210], redundant with Kin7.3 and Kin7.5 [210], triple mutants are hypersensitive to APM
	AT2G21380	Kin7.2		
	AT3G12020	Kin7.3		part of KISC, interacts Kin7.1, Kin7.5, ESP [210], MT plus-end stabiliser [210], redundant with Kin7.1 and Kin7.5 [210], triple mutants are hypersensitive to APM
	AT4G39050	MKRP2 / Kin7.4	contains mitochondria-targeting sequence [135]	
	AT5G06670	Kin7.5		interacts Kin7.1, Kin7.3, ESP [210], redundant with Kin7.1 and Kin7.5 [210], triple mutants are hypersensitive to APM
7C	AT1G18370	NACK1/HINKEL	phragmoplast [227, 307, 310]	cell plate formation in male gametogenesis [227, 307], phragmoplasts in *hinkel* mutants never enter ring-stage [307]
	AT3G43210	NACK2/TETRASPORE	phragmoplast [227, 310]	tetrad formation in male gametogenesis [227, 356]
	AT2G21300			
	AT4G24170			
	AT4G38950			
	AT5G42490			
	AT3G51150			
	AT5G66310			
8	AT1G18550	Kinesin-8A		
	AT3G49650	Kinesin-8B		
13	AT3G16630	Kinesin-13A	CMs in the presence of MIDD1 co-expression [228], punctae that colocalises with Golgi [174]	trichome morphogenesis [174], xylem pit formation under ROP GTPase signalling cascade [228]
	AT3G16060	Kineisn-13B		trichome morphogenesis [174]
14A	AT4G21270	ATK1/KATA	CMs [168], PPB [168, 183], spindle [49, 168, 183], phragmoplast [168], nucleus [128]	interacts ATK5 [128], *atk1* mutants displace AUG3 [128], male sterility [49, 183], non-processive minus-end directed motility [183]
	AT4G27180	ATK2/KATB		increased expression during mitosis [203]
	AT5G54670	ATK3/KATC		increased expression during mitosis [203]
	AT4G05190	ATK5	CMs, spindle, phragmoplast [5]	spindle assembly [103], spindle pole organisation [5], interacts ATK1/KATA [128], *atk1/atk5* is synthetic lethal [249]
14B	AT5G65930	KCBP/Zwichel	CMs [187, 234], PPB, CDZ [40], spindle, phragmoplast [29, 336]	MT organisation, trichome morphogenesis [65, 252, 298], chloroplast transport [103], has two extra MBDs [318], bundles MTs *in vitro* [137]
14C1	AT5G27000	ATK4/KATD		homolog of *Os*KCH and *Gh*KCH
	AT3G44730	KP1/KIN14h	CMs [223, 357]	respiration regulation during seed germination [223, 357], mitochondrial transport [103]
	AT2G47500			
	AT1G09170			
14C2	AT3G10310			
14C3	AT1G63640	KinG	colocalises as foci on MTs and actin [300]	CH domain interacts SIEL proteins [300],*kinG;kinH* mutant has impaired SHR cell-cell movement [300]
	AT5G41310	KinH		*kinG;kinH* mutant has impaired SHR cell-cell movement [300]
	AT1G18410			
	AT1G73860			
14D	AT2G22610	Kinesin-14D1 / MDKIN2	nuclear during interphase, kc during mitosis [99, 110], phragmoplast midzone [110]	pollen/seed development [99], hypersensitive to oryzalin treatment [110], *in vitro* plus-end directed motility [110], spindle shape lost in *mdkin2* mutant [110], rigor mutant mislocalises to spindle poles [110]
	AT1G72250	Kinesin-14D2 / MDKIN1	nuclear during interphase, kc during mitosis but more diffuse than MDKIN2 [99, 110], phragmoplast midzone [110]	pollen/seed development [99]
	AT5G27550	Kinesin-14D3	diffuse around spindle, kc during mitosis and gets progressively more diffuse, cell plate [110]	
14E	AT5G10470	KCA1/KAC1	CMs [309], diffuse around PPB, spindle, phragmoplast [328], even PM decoration during interphase, depleted at CDZ, then enriched on CP [329]	actin-based chloroplast movement [309, 328]
	AT5G65460	KCA2/KAC2		actin-based chloroplast movement [309, 328]
14F	AT5G27950			homologue of *Nt* TBK5
	AT1G55550			
14G	AT4G14330	PAKRP2	phragmoplast midzone [159], mislocalises to entire phragmoplast in *map65-3* mutants [123]	phragmoplast organisation [159]
15/12	AT4G14150	Kinesin-12A/PAKRP1	see Table 3.5	see Table 3.4
	ATG23670	Kinesin-12B/PAKRP1L		
	AT3G17360	Kinesin-12C/POK1		
	AT3G19050	Kinesin-12D/POK2		
	AT3G44050	Kinesin-12E		
	AT3G20150	Kinesin-12F		
18	AT5G23910			
	AT5G02370			
19B	AT3G54870	ARK1	CMs [262], PPB spindle, phragmoplast [80]	promotes catastrophe and tracks MT plus-ends in root hair cells [80], *ark1* mutant does not display mitotic or cytokinetic defects [80]
	AT1G01950	ARK2	CMs [155, 262]	MT plus-end stabilisation [155], MT bundling to some extent [155], *ark2* mutants have root twisting phenotype [262], essential for MT reorientation in light response [154]
	AT1G12430	ARK3/KINUa	CMs, PPB [181]	has D-box motif [181], RNAi lines not obtainable suggesting lethality [181]

3.3 Kinesin-12/15

While there is only one kinesin-12/15 member in *homo sapiens* (KIF15/KLP2), this superfamily is expanded to 6 members in *Arabidopsis thaliana* [213] and 20 in *Physcomitrium patens* [194]. The six *Arabidopsis* kinesin-12/15s are grouped into two clades, with kinesin-12A/PAKRP1, kinesin-12B/PAKRP1L[2] and kinesin-12F grouped into Class II and kinesin-12C/POK1, kinesin-12D/POK2 and kinesin-12E grouped into Class I based on their phylogenetic divergence (Fig. 3.2). The functions of all *At*kinesin-12/15s except for kinesin-12F have been reported and are summarised in Table 3.4.

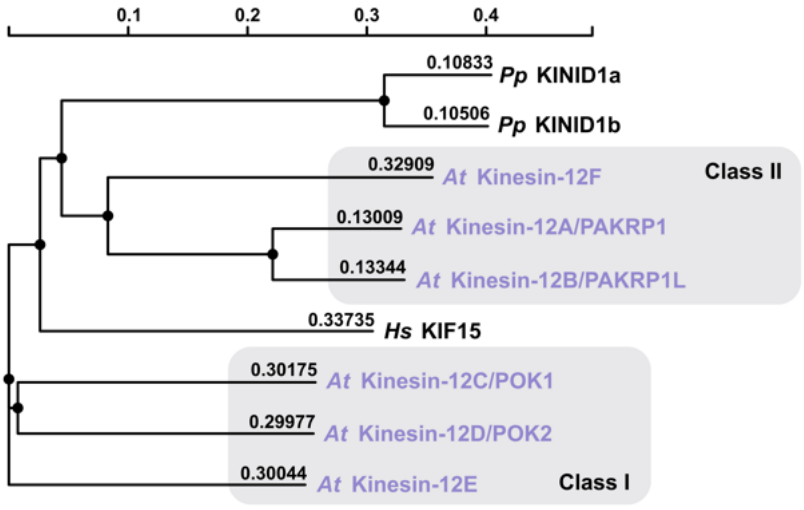

Figure 3.2: Phylogeny of kinesin-12/15 proteins.
Phylogenetic tree was generated with Clustal Omega [179] using entire protein sequences. This analysis groups the kinesins into the same clade as in [213]. Numbers indicate branching distance. The *Physcomitrium patens (Pp)* KINID1s are orphan kinesins not part of the kinesin-12/-15 superfamily, rather it is grouped into kinesin-14G with PAKRP2 (see Fig. 3.1). and are used as an outgroup. The *Arabidopsis thaliana (At)* kinesins are highlighted in lavender. Other abbreviation: *Homo sapiens (Hs)*.

Of the six *Arabidopsis* kinesin-12/15s, kinesin-12E is most similar to *Hs*KIF15. Human KIF15 has been shown to function in promoting metaphase spindle bipolarity in a manner distinct from that of the kinesin-5 KIF11/Eg5 [71]. Unlike Eg5 that localises to the spindle midzone and slides microtubules in an antiparallel fashion, KIF15 is primarily kinetochore (kc) localised during mitosis [71]. KIF15 tracks microtubule plus-ends of kinetochore-fiber (k-fiber) where it probably bundles and protects the ends from catastrophe [71]. Meanwhile, the *Arabidopsis* kinesin-12E also binds and stabilises k-fibers [119] (Table 3.5). Prometa- and metaphase duration in *kin12e* mutants are prolonged due to delayed kc congression and stability [119] (Table 3.6).

Interestingly, despite kinesin-12E also localising to the phragmoplast midzone, *kin12e* mutants do not display cytokinetic defects [119] (Table 3.6). This could be due to the redundant functions of the other *Arabidopsis* kinesin-12/15 family members, all of which localise to the phragmoplast midzone as well (except kinesin-12F, which is unreported, Table 3.5). Of these kinesins, kinesin-12A/PAKRP1

[2] There is a similarly named *Arabidopsis* kinesin, PAKRP2 which is an un-subclassed kinesin-14 in [110] that I have designated kinesin-14G (Fig. 3.1. It shares a similar name as it was first identified to associate with phragmoplasts, like PAKRP1 [159]. The *Physcomitrium patens* phragmoplast associated KINID1a and KINID1b [122] are also members of kinesin-14G [176], where previously it was designated an orphan kinesin [194].

Table 3.4: Reported functions of *Arabidopsis* kinesin-12/15s.
As kinesins, all proteins are expected to bind microtubules. Nevertheless, direct evidence of microtubule binding is valued and listed below. Abbreviations: kinetochore fiber (k-fiber), microtubule (MT), N-terminal (N-ter), phragmoplast (PP), 1-tert-Butyl-3-(4-chlorophenyl)-1H-pyrazolo[3,4-*d*]pyrimidin-4-amine (PP2).

Protein	Function		Other comments
	in vivo	*in vitro*	
Kinesin-12A/PAKRP1	PP formation in microspores [161]	MT binding [160]	phosphorylated by TIO [231] inhibited by drug PP2 [144] functionally redundant with PAKRP1L [161]
Kinesin-12B/PARKP1L	PP formation in microspores [161]	n.a.	functionally redundant with PAKRP1 [161]
Kinesin-12C/POK1	PP guidance [215]	plus-end directed motility [54]	interacts ATN [167, 215] tail interacts IQD6, 7, 8 [153] tail interacts PHGAP1, 2 [303] functionally redundant with POK2 [215]
Kinesin-12D/POK2	PP guidance [215] PP expansion [118]	plus-end directed motility [53]	tail interacts MAP65-1, -3, -5 [118] tail interacts IQD8 [153] unstructured N-ter extension interacts MAP65-3 [118] PP guidance but not expansion redundant with POK1 [215]
Kinesin-12E	k-fiber stability [119]	n.a.	velocity of 7.02 ± 2.52 μm/min [119]
Kinesin-12F	n.a.	n.a.	

Table 3.5: Cellular localisation of *Arabidopsis* kinesin-12/15s.
There is currently no report on Kinesin-12F. Abbreviations: cell division zone (CDZ), preprophase band (PPB).

Protein	Cellular localisation	Comments
Kinesin-12A/PAKRP1	phragmoplast midzone [160]	MAP65-3 dependent [123] PAKRP1L independent [236]
Kinesin-12B/PAKRP1L	phragmoplast midzone [236]	PAKRP1 independent [236]
Kinesin-12C/POK1	PPB, CDZ [167]	PPB localisation is MT dependent
Kinesin-12D/POK2	PPB, CDZ [118]	tail-suifficient [118] PPB localisation is MT dependent [118]
	phragmoplast midzone [118]	motor-sufficient [118]
Kinesin-12E	perinuclear region, spindle midzone [119]	tail-sufficient [119] perinuclear localisation is MT-independent [119]
	phragmoplast midzone [119]	motor-sufficient [119]
Kinesin-12F	n.a.	n.a.

and kinesin-12B/PAKRP1L function redundantly in phragmoplast formation in microspores [161]. Meanwhile, kinesin-12C/POK1 and kinesin-12D/POK2 marks the division site and guides the phragmoplast to it [118, 167, 215]. POK2 additionally plays a role in phragmoplast expansion, as *pok2* single mutants also show prolonged phragmoplast duration [118].

As N-terminal motor kinesins (Fig. 3.3), the *At*kinesin-12/15s are expected to have plus-end directed motility like their opisthokont counterparts [71]. All reported *At*kinesin-12/15s localise to the phragmoplast midzone, which is where the microtubule plus-ends are localised. Furthermore, the motor

Table 3.6: Phenotypes of *Arabidopsis* kinesin-12/15 mutants.
All mutants are homozygous for the mutant allele. Note: There are three reported *pok1/pok2* double mutants: *pok1-1;pok2-1*, *pok1-2;pok2-2* [215] and *pok1-1;pok2-3* [167]. The *pok1-1;pok2-3* was generated in a EMS screen in the *pok1-1* background, which generated plants with cytokinetic defects more severe the two previously identified double mutants [167]. Additionally, the *pok2* single mutant phenotypes listed below are for *pok2-1* and *pok2-2*, as *pok2-3* was not analysed [167].

Mutant	Phenotype	Reference
pakrp1	no phenotype	[236]
pakrp1l	no phenotype	[236]
pakrp1/pakrp1l	fertile but seed number reduced defective microspores impaired phragmoplast formation in defective microscpores absent of cell plates in defective microspores	[161]
pok1	no phenotype	[215]
pok2	no obvious phenotype prolonged phragmoplast expansion	[118, 167, 215]
pok1/pok2	dwarfed plant with all organs present but miniaturised fertile but seed number reduced disordered cell patterning slightly misoriented PPBs misoriented phragmoplast increased proportion of tilted preprophase bands (PPBs) prolonged phragmoplast expansion	[118, 215]
kin12e	increased prometa- & metaphase duration delayed kinetochore congression increased kinetochore prometa- & metaphas dynamicity reduced kinetochore-fiber distance overall smaller spindle sparse spindle (microtubules) reduced spindle flux rate	[119]

dead versions of POK2 and kinesin-12E are unable to restrict to the phragmoplast midzone, instead covering the entire phragmoplast, indicating *in vivo* plus-end motility [118, 119]. Additionally, *in vitro* assays with motor only countructs of POK1 and POK2 show that they translocate towards the plus-end [53, 54].

Despite the ability to translocate directedly towards microtubule plus-ends, the *At*kinesin-12/15s do not appear to be transport kinesins. *In vivo*, there is no evidence of any role of the *Arabidopsis* kinesin-12/15 in vesicle trafficking [213]. This is reminiscent of *Hs*KIF15 function on the metaphase spindle. However, whether or not the *At*kinesin-12/15s are able to track microtubule plus-ends, bundle microtubules or influence microtubule dynamics, as have been seen for *Hs*KIF15 [72], remains to be investigated.

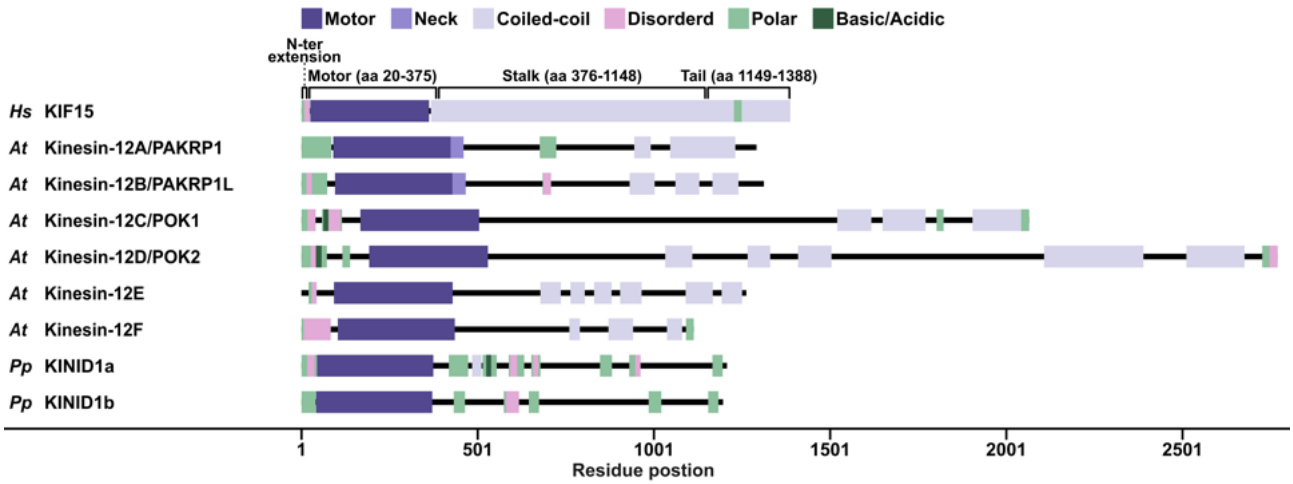

Figure 3.3: Protein domains of kinesin-12/15 superfamily members as predicted by UniProt. See Fig. 3.1 for accession numbers of *Arabidopsis* kinesin-12s. The *Physcomitrium patens (Pp)* KINID1s are not part of the kinesin-12/-15 superfamily and are considered orphan kinesins [194] or classed into kinesin-14D [176] but localise to the phragmoplast midzone and are important for phragmoplast interdigitation in moss [194]. Additionally for *Homo sapiens* KIF15, which biochemistry is well studied, regions corresponding to the N-terminal (N-ter) extension, motor, stalk and tail determined experimentally are also marked [71].

3.4 PHRAGMOPLAST ORIENTING KINESINS (POKs)

Kinesin-12C and -D, more commonly known as phragmoplast orienting kinesin 1 (POK1) and phragmoplast orienting kinesin 2 (POK2) were first identified in a yeast-two-hybrid screen against *Arabidopsis* TANGLED (ATN) [215]. Like ATN, POK1 and 2 localise to the preprophase band (PPB) and then to the cell division zone (CDZ) until cell plate fusion [119, 167, 339]. POK1 CDZ retention is dependent on the combined presence of ATN and auxin induced in roots9 (AIR9) [195]. In turn, the CDZ retention of ATN, Ran GTPase activating protein 1 (RanGAP1) and pleckstrin homology GTPase activating protein 1 and 2 (PHGAP1, 2) depends on POK1 and 2 as these proteins are absent from the CDZ in *pok1/pok2* double mutants [303, 339, 353]. On the other hand, how POK2 localises to the PPB and CDZ has not been directly investigated but has been shown to be dependent on its tail region (Fig. 3.4). Meanwhile, the motor region of POK2 is reponsible for an additional localisation to the phragmoplast midzone [118] (Fig. 3.4).

3.4.1 POK2 but not POK1 stabilises the phragmoplast and localises to the phragmoplast midzone

In addition to its PPB and CDZ localisation, POK2 is also found at the phragmoplast midzone [118]. POK2 purportedly stabilises the phragmoplast as *pok2* single mutants have increased phragmoplast expansion duration [118]. *In vivo*, POK2 localises to the phragmoplast midzone by way of its plus-end directed kinesin motor [53, 118]. Expression of a motor-containing N-terminal truncation construct, POK2$^{1–589}$, is sufficient for phragmoplast midzone localisation (Fig. 3.4) [118]. However, POK2$^{1–589}$ phragmoplast midzone restriction is looser than for the full-length POK2 (POK2-FL) and is completely abolished in *map65-3* mutants [118]. Interestingly, MAP65-3 is able to recruit both POK2$^{1–589}$

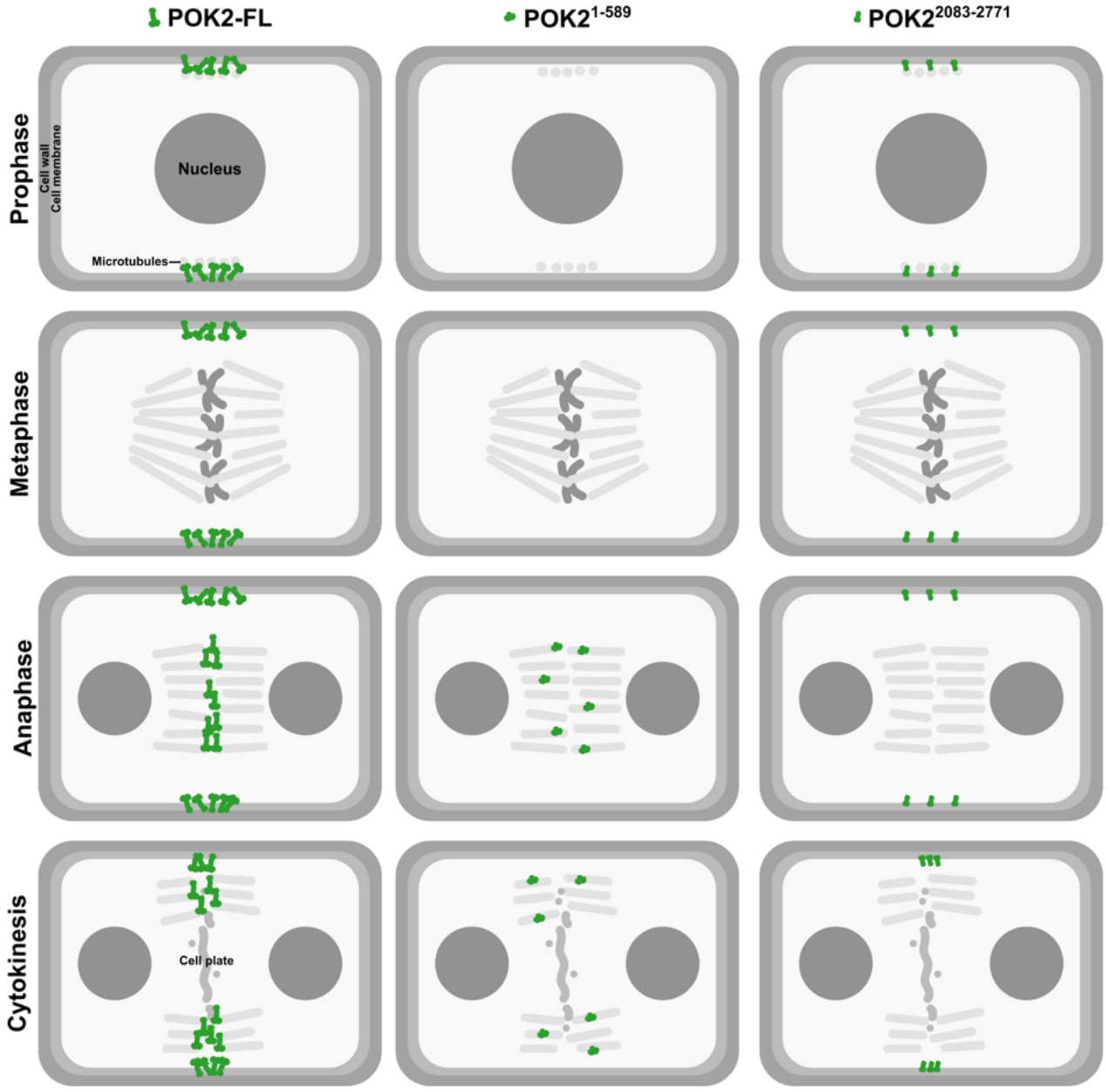

Figure 3.4: Summary of POK2 cellular localisation.
Full-length POK2 (POK2-FL) localises to the preprophase band (PPB), cell division zone (CDZ) and to the phragmoplast midzone. The N-terminal truncated POK2 construct containing the kinesin motor domain, POK2$^{1–589}$ localises only to the phragmoplast midzone. The C-terminal truncated POK2 construct localises to the PPB and CDZ. Note that the abundance of POK2$^{1–589}$ and POK2$^{2083–2771}$ is reduced compared to POK2-FL. Moreover, POK2$^{1–589}$ phragmoplast midzone localisation is broader than POK2-FL. Localisations are from [118] in the *pok1/pok2* mutant background to exclude effects of endogenous POK1 and 2. The cartoon of the cells are grayscaled versions of Fig. 1.3 for visualisation of the POK2 constructs. Please refer to Fig. 1.3 for details on cell division. Depictions here at not to scale.

and a shorter N-terminal construct lacking the motor domain, POK2$^{1–189}$, to microtubules when expressed exogenously in *N. benthamiana* [118]. Hence, MAP65-3 likely helps to restrict POK2 to the phragmoplast midzone through an interaction in the region upstream of the motor domain. Additionally, MAP65-3 has also been shown to interact with a POK2 C-terminal truncation construct, POK2$^{2083–2771}$, in yeast split ubiquitin assays and exogenous expression in *N. benthamiana* [118].

These results would imply that in addition to N-terminal interaction site, MAP65-3 is also able to utilise a C-terminal interaction site to restrict POK2 to the phragmoplast midzone.

On the contrary, unlike for POK2$^{1\text{-}589}$, POK2-FL phragmoplast midzone localisation is retained in *map65-3* mutants [118]. This suggests that regions outside the first 1-589 residues, e.g. the POK2 tail, somehow mediate phragmoplast midzone localisation of the POK2-FL. However, it is important to note that POK2$^{2083–2771}$ does not localise to the phragmoplast midzone in a background where MAP65-3 is still present here [118]. Hence, this mediation of POK2 midzone localisation by the POK2 tail occurs independently of MAP65-3, despite the fact that MAP65-3 can interact with the POK2$^{2083–2771}$. The mechanisms that specify MAP65-3 to the N-terminal region but not the tail *in vivo* is still ambiguous.

The phragmoplast expansion phenotype found in *pok2* but not *pok1* single mutants reflects the difference in their localisation, as POK1 is detected only at the PPB and CDZ while POK2 localises additionally to the phragmoplast midzone [118, 167]. Interestingly, POK1 mislocalised to the phragmoplast midzone in *atn* mutants and completely relocalised here from the CDZ in *atn/air9* double mutants [195]. This indicates that POK1 has the potential to be phragmoplast midzone-localised but is specifically kept from the phragmoplast midzone by CDZ resident proteins. Whether or not mislocalised POK1 serves any function, compensative or adverse to POK2, remains to be investigated.

3.4.2 POKs localise to the division site for phragmoplast guidance

POK1 and 2 primarily function to guide the phragmoplast to the predetermined cell division site [118, 167, 215]. These two kinesins are functionally redundant in this regard, with *pok1/pok2* mutants exhibiting cell patterning defects, while their single mutants do not [215]. Specfically, *pok1/pok2* mutants do not display wall stubs, which is a feature of incomplete cross-wall formation and aborted cytokinesis [215]. Hence, POK1 and POK2 do not play a role in phragmoplast establishment or function itself.

A key aspect to their function in phragmoplast guidance is the localisation of POK1 and 2 to the CDZ. However, it is not clear how POK1 and POK2 are recruited to and maintained the CDZ. Initial deposition of both proteins to the CDZ is PPB microtubule dependent [118]. Given that both proteins are kinesins, the most plausible scenario would involve direct binding to PPB microtubules through their N-terminal kinesin motor domains. However, the POK2$^{2083–2771}$, which lacks the kinesin motor domain, is necessary and sufficient for both CDZ targeting and retention [118]. How exactly the POK2 tail is able to target and remain at the CDZ is unclear. Meanwhile, POK1 CDZ targeting and residence seems to require the combined presence of AIR9 and ATN [195], where ATN has been shown to interact with POK1 via its tail [167]. Whether or not POK2 localisation to the CDZ also rely on AIR9 and ATN has not been investigated.

As previously mentioned, POK2 interacts MAP65-3 via two interactions regions, residues 1–189

and 2083–2771 [118] (Fig. 3.5). Additionally, the C-terminal truncation construct POK2$^{2083–2771}$ also binds MAP65-1 and -5 [118]. All three MAP65s bind to the PPB and phragmoplast midzone (Table 2.2). Hence, the initial PPB recruitment of POK2 could be mediated by MAP65-1, -3 and/or -5. However, all three MAP65s do not remain at the CDZ after PPB disassembly. Hence, CDZ residence of POK2 cannot be mediated by MAP65-1, -3 or -5, but could be mediated by other CDZ resident proteins that remain here up to the end of cytokinesis (Table 2.1). For instance, the POK2 tail has been shown to interact the scaffolding protein IQD8 in a yeast-two-hybrid assay [153]. However the region decorated by IQD8 at the plasma membrane is significantly broader than that of POK2. Thus, more research is still required to uncover the precise mechanism of POK2 tail localisation and maintenance at the CDZ.

3.4.3 POK2 uses its kinesin motor to push phragmoplast microtubules into place

Despite the necessity and sufficiency of POK2$^{1–589}$ and POK2$^{2083–2771}$ to localise POK2 to the phragmoplast midzone and the division site respectively, neither construct is sufficient to rescue the phragmoplast misorientation phenotype in the *pok1/pok2* double mutant[3]. Hence, proper phragmoplast guidance either requires the entire full-length protein or at least both the N- and C-terminal regions responsible for its dual localisation.

This has prompted researchers to develop a model for POK2 in phragmoplast guidance [53, 118]. In brief, this model entails that POK2 at the CDZ would capture phragmoplast microtubules as they approach the cell periphery. POK2 would then walk itself to the microtubule plus-end, consequently positioning the midline of the phragmoplast relative to itself. The POK2 already present at the phragmoplast midzone would meet the POK2 at the CDZ, although subsequent interactions between them remain unclear.

Contigent to this model is POK2's ability to walk processively to the microtubule plus-end. *In vitro*, the POK2$^{1–589}$ construct is dimeric and walks processively towards the microtubule plus-end [53]. The directed movement is however interspersed with bouts of diffusive motion where the POK2$^{1–589}$ spends ∼62% of the time in the directed mode [53]. Consequently, this construct was not reported to track the microtubule ends, unlike the *Hs*KIF15 [72]. This explains why the same POK2$^{1-589}$ construct localises to a broader midzone region on the phragmoplast as compared to the POK2-FL, as the motor could sometimes exist in its diffusive mode rather than solely processive, which prevents end-tracking. Interestingly, removal of the N-terminal unstructured region upstream of the motor domain results in a construct , POK2$^{183–589}$, that is purely diffusive [53]. This suggests that the N-terminal unstructured region functions to modulate the microtubule binding affinity of the kinesin motor domain. Since MAP65-3 has been shown to interact with this unstructured region, this presents a scenario where

[3] A construct lacking the central domain, POK2$^{\Delta 590–2082}$ is able to localise similarly as POK2-FL with lower abundance [118]. However, the phenotype of this construct introgressed into the *pok1/pok2* double mutant has not been reported.

MAP65-3 is able to modify POK2 kinesin activity, possibly by inducing conformational changes that favour processive motion in the motor domain. This also raises the question of what the influence the rest of the POK2 protein would have on the motor domain. Some kinesins are known to have auto-inhibitory domains in their tail which bind the motor and keep it inactive until certain conditions are met (see Section 3.1.2.3). Perhaps the POK2 tail could also serve the same function to inactivate the motor domain when the protein reaches the microtubule plus-end in the phragmoplast midzone. To investigate for such a possibility, the POK2 tail would first have to be studied thoroughly.

Remarkably, force measurements using optical tweezers revealed the POK2$^{1–589}$ construct to be a weak motor, reaching only average maximal forces of ∼0.34 pN for a single molecule [53]. Such forces would be too weak to meaningfully move microtubules extending out from the growing phragmoplast. These forces are also in contrast to forces recorded for *Hs*KIF15, which detaches at loads between 1.5∼3.5 pN [73]. These forces were, however, measured for the full-length *Hs*KIF15, which is a homotetramer under physiological conditions[4]. Indeed, forces for the POK1$^{1\text{-}589}$ did exceed 1 pN in multi-molecule conditions [53]. In this regard, POK2 could potentially form larger oligomers in order to generate large enough forces to guide phragmoplast microtubules. Whether or not the POK2 tail is able to mediate further oligomerisation of the POK2 protein and other influences the POK2 tail would have on force generation of the motor domain would require a first extensive study of the POK2 tail.

3.4.4 Every answer begets a quest for more

POK2 and POK1 are undoubtedly crucial for proper phragmoplast guidance and downstream cell patterning [215]. POK2 is additionally important for phragmoplast stabilisation [118]. These functions require the presence of both N- and C-terminal regions of POK2, if not the entire protein, despite the specific localisations to the phragmoplast midzone and division site being attributed separately to the N- and C-terminal regions respectively.

How does POK2 restricts itself to the phragmoplast midzone and what exactly does it do here?
Interaction with MAP65-3 for both N- and C-terminal regions have uncovered a role for MAP65-3 in fine-tuning POK2 restriction to the phragmoplast midzone, but does not fully explain initial recruitment here. The POK2 tail is clearly involved in a MAP65-3 independent manner, as the full-length but not the N-terminal region of POK2 is able to localise to the phragmoplast midzone in the absence of MAP65-3 but in the presence of wild-type POK2 [118]. How then, does the POK2 tail mediate this localisation, given that it does not localise here on its own?

How can POK2, which does not track plus-ends, stabilise the phragmoplast?
In vitro investigation on the N-terminal motor-containing region of POK2 has revealed it to be a plus-end directed motor capable of switching between procesive and diffusive modes [53]. As it is

[4] *Hs*KIF15 has been shown to form dimers at ionic strengths >300 mN and tetramers at 25–225 mN [71]. Interestingly, the homotetramers are expected to tetramerise in parallel with all the motor heads on one end, unlike the dumbbell antiparallel tetramerisation of the kinesin-5 KIF11/Eg5, according to cross-linking mass spectrometry [131].

incapable of staying entirely in directed motility, this construct was not reported to track microtubule plus-ends, which would be required in order to have an effect on microtubule plus-end dynamics. The N-terminal unstructured region upstream of the motor was revealed to modulate the mode switching. However, removal of this region results in a fully diffusive motor, suggesting that the microtubule binding capacity of the motor domain alone is insufficient for processivity. What then would increase the microtubule binding capacity of the motor? Since the full-length protein is capable of maintaining its phragmoplast midzone restriction, would the answer lie in the rest of the protein?

How can POK2 be so weak?

Curiously, the single motor is remarkably weak [53], and theoretically incapable of directing phragmoplast microtubules anywhere. Multiple motors would be able to theoretically generate sufficient forces for phragmoplast guidance. Multimerisation might depend on interactions with other proteins or direct higher oligomerisation through the POK2 tail. The N-terminal motor-containing region makes up less than one-third of the entire protein (Fig. 3.5) with the rest of the protein consisting largely of coiled-coils (Fig. 3.6) which could potentiate multimerisation. Multimerisation might also directly increase the microtubule binding capacity of the protein by simply increasing the number of binding sites per molecule, in turn also increasing processivity. Would the POK2 tail be able to mediate multimerisation? Or would the POK2 tail induce conformational changes in the motor domain that results in higher force generation and/or higher microtubule binding capacity when bound to specific cargo?

How does POK2 get to the division site and then stay there?

POK2 initial recruitment to the preprophase band and subsequent retention at the division site is dependent on its tail. The POK2 tail is predicted to consist of coiled-coils interspersed with disordered regions, terminating with a final short unstructured region ($\sim$100 aa) (Fig. 3.5). There is no other specific motif or structure predicted in the POK2 tail [54] (Fig. 3.5, 3.6). Reported interactions with MAP65-3 and IQD8 [118, 153] provide possible but incomplete scenarios for the division site residence of POK2. Thus, the question of how the POK2 tail localises to and maintains at the division site, remains unanswered.

All these questions point towards the necessity to investigate the POK2 tail in detail and is the focus of this thesis. In this doctoral research, I cloned, expressed and purified the POK2 C-terminal region and studied its biochemical properties *in vitro* using single molecule and bulk TIRF assays. I found that the POK2 tail was capable of interacting directly with microtubules and anionic lipids. I also reconstituted the interaction of the POK2 tail with MAP65-3. With shorter constructs, I narrowed down the interaction sites and found the final $\sim$100 aa to be particular important for interactions with microtubules, anionic lipids, as well as MAP65-3. The overlapping interaction sites for different binding partners potentiates a regulatory mechanism that could be exploited *in vivo* for spatiotemporal

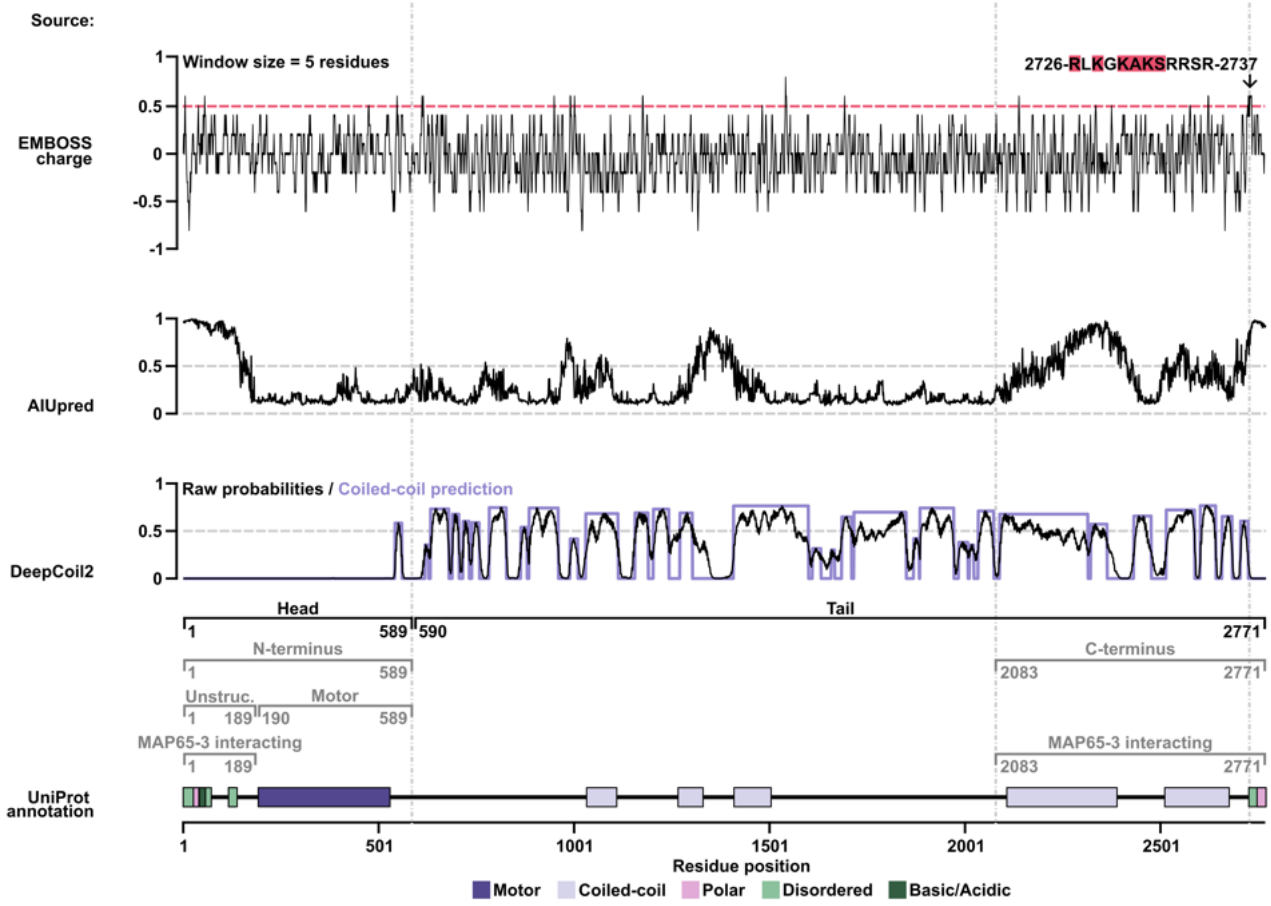

Figure 3.5: Domain, structural and feature prediction of kinesin-12D/POK2.
Prediction or annotation tools are listed on the left. All predictions were performed with default parameters. According to DeepCoil2 predictions, there are 31 coiled-coils (CCs) which cover 54.1% of the entire protein, where the first CC is usually required for dimerisation of the kinesin motor domain. The POK2 tail (aa 590–2771) is 67.9% covered in CCs. The window size used for charge prediction (EMBOSS charge) is calculated with a window size of 5 residues. The positively charged residues are marked in red. The regions designated as N- and C-terminus, Unstructured, Motor and MAP65-3 interacting (regions marked in gray) follows [53, 118]. In this thesis, I refer to the region aa 1–589 as the head, the region downstream of the head (aa 590–2771) as the tail (regions marked in black). I use the term POK2 tail loosely, and it may refer to the entire stretch aa 590–2771 or a portion of it. When referring to a specific region, I indicate the amino acids (aa) directly in text.

coordination. Overall, this doctoral research revealed important intrinsic capabilities of the POK2 tail, providing further insights on the function of the POK2 protein in entirety in phragmoplast guidance and expansion.

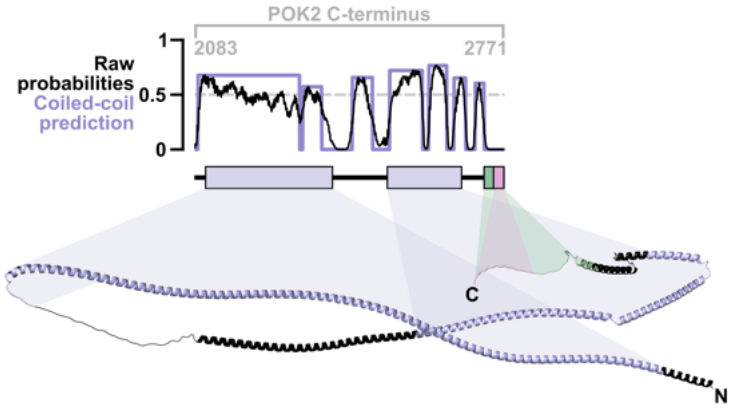

Figure 3.6: The C-terminus of POK2 consists mostly of coiled-coils.
Coiled-coils were predicted with DeepCoil2. Structure was predicted with AlphaFold 3.0. Both predictions were performed using default parameters. Protein domain annotations follow UniProt assignments. For more predictions, see Fig. 3.5.

Part II

Methods

Chapter 4

Materials & Methods

The three main steps necessary in preparing a protein are cloning, protein expression and protein purification. Before starting, decisions have to be made on the type of purification method, the expression system and what type of buffers to use.

4.1 Cloning

Theory

Before expressing proteins, the protein coding sequence has to be cloned into an expression vector specific to its desired protein expression system. In our lab, we used the baculovirus-insect cell ExpiSf Protein Production kit (Gibco, 15829126) which utilises the *Spodoptera frugiperda 9* (Sf9) clone line of a Sf21 continuous cell line originally developed in the United States. For this expression system, I used a modified version of pFastBac1 in which I have already added an N-terminal eGFP for in-frame insertion of desired protein sequences (Fig. 4.1, Table 7.3).

To prepare the plasmids, I used the HiFi assembly (NEB, E2621L) cloning technique. This is another name for InFusion cloning technique developed by TaKaRa, which exploits 15 to 20 bp complementary regions to promote homologous recombination events at the ends of dsDNA fragments, thus joining them precisely. The benefit of HiFi assembly over conventional restriction enzyme-mediated cloning is the absence of restriction enzyme footprints and accuracy of plasmid design. For higher efficiency, the ratio of fragments should be 1:2 = vector:insert in molecular concentration, of which can be verified by NanoDrop Spectrophotometer (Peqlab, ND-1000) and by UV illumination of the PCR fragment after gel electrophoresis.

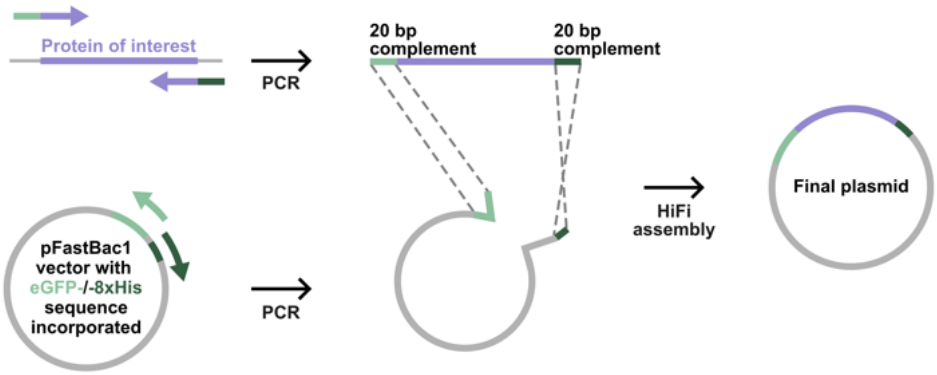

Figure 4.1: Cloning strategy of desired expression vector.
Plasmids were prepared by HiFi assembly (NEB, E2621L) where desired sequences are amplified by PCR with complementary overhangs that are used as homologous recombination sites. The final plasmid will contain the coding sequence of the protein of interest (lilac), the desired fluorophore (light green) and purification tag (dark green) in the pFastBac1 vector backbone.

Protocol

The protein coding sequence of POK2 (aa 2083-2771, bp 6247-8313 of the POK2 CDS) was cloned from a plasmid already containing the POK2 CDS, which was gifted by Dr. Pantelis Livanos and Dr. Sabine Müller. The sequence was amplified by polymerase chain reaction (PCR) (Table 7.2). Simultaneously, the vector pFastBac1 was linearised by PCR (Table 7.2). The resulting PCR products were verified by their predicted sizes in 1% agarose gel electrophoresis. The PCR products were then cleaned-up by FastDigest DpnI (Fisher Scientific, 10819410) treatment (37°C, 30 min) followed by gel extraction (NEB, T1120) and verified again by 1% agarose gel electrophoresis. The concentration of the cleaned PCR product was estimated with a NanoDrop Spectrophotometer. Then, the cleaned PCR products of the vector and insert are mixed in a 1:2 ratio, and mixed again in a 1:1 ratio with 2x HiFi Master Mix (NEB, E2621L) to a total volume of 3 μl, incubated at 50°C for 40 min and then 80°C for 5 min to deactivate the recombinase. This final reaction mix was transformed into 50 μl chemically competent DH5a *E. coli* (NEB, C2987H) (prepared in-house by the Inoue method) and then plated on LB (drug+) plates (drugs specific to each plasmid is listed in Table 7.3) and cultured at 37°C. Colonies that appeared were checked first by colony PCR with an internal (within the insert) and external (on the vector) forward/reverse primer pair. Colonies that were positive were then amplified in a liquid culture (drug+) and their DNA were extracted (Monarch Spin Miniprep Kit (NEB, T1110S)) and sent for sequencing to verify that their protein coding regions were correct.

Similar design and cloning strategies were used for the shorter POK2 tail constructs (#S62, 64, 66, Table 7.3). The same design was also used for MAP65-3-mCherry-8xHis (#S102, Table 7.3), however as I did not have the cDNA of this protein, I ordered the full plasmid in the pFastBac1 vector directly from GenScript and had it codon-optimised for insect cell expression. See Table 7.2 for primers.

A note on the choice of fluorophores

mCherry is a fluorescent protein, that at the time of cloning, was one of the best general purpose red fluorophore due to its high photostability compared to other red fluorophores. However, for single molecule experiments it is lacking. It bleaches twice as fast and is two-fold dimmer than eGFP [279]. Hence, while single molecules of eGFP-POK2$^{2083\text{-}2771}$ can be easily viewed at 5% 488 nm, single molecule of mCherry proteins can only be viewed at 10% 561 nm laser power and then bleaches twice as fast (maximum laser output = 80 mW). When trying to actively avoid bleaching, assays had to be performed at 1% 561 nm laser power at the cost of not detecting single molecules. However to account for this, single molecule assays could be performed at 10% 561 nm laser. For most assays in this thesis, the laser power was 1% 561 nm laser, unless stated otherwise. For assays using the 561 nm, the setup *Shenlong* was used, which 561 nm laser has an output power of 80 mW (See Section 4.5.1 for details).

Similarly, eGFP was at the time of cloning a good choice of fluorophore. More importantly, eGFP was chosen as initial cloning experiments were performed to reproduce previous purification and experimental results where the previous construct used eGFP as the fluorophore. However, I have now found that mNeonGreen is both brighter and less prone to dimerise than eGFP and would use this construct for future constructs. Nevertheless, for my experiments, eGFP was a serviceable fluorophore and that produced nice single molecule traces without much bleaching at 5% 488 nm laser power (maximum on *Shenlong*, 80 mW; maximum on *Aalo*, 100 mW). This was the standard laser power unless stated otherwise.

4.2 Protein expression

Proteins can be expressed through a variety of methods. Most commonly, *E. coli* expression is favoured due to accessibility and ease of up-scaling. However, a prokaryotic system like *E. coli* is sometimes too simplistic as it lacks the post-translational modifications and protein folding chaperones that may be required for more sophisticated eukaryotic proteins. In this respect, yeast, insect cell, human, plant and even *in vitro* eukaryotic expression systems have been developed.

In the case of the POK2 tail, the expression was initially attempted in yeast (*Saccharomyces cerevisiae*) in Dr. Sabine Müller's lab due to convenient availability of the yeast. However, expression and subsequent protein extraction was not reproducible in this system. POK2 tail expression was also attempted with the Cell Free Protein Expression System: ALiCE for Research Kit (LenioBio, AL00000001) to some degree of success (Fig. 5.2) and also with insect cells from the ExpiSf Protein Production kit. Expression and protein extraction from insect cells was the most successful and reproducible. As a result all experiments were performed with insect cell expressed proteins and the protocols for this expression are outlined in this thesis.

4.2.1 Preparing the bacmid

Theory

The key point of the baculovirus-insect cell expression system is actually the baculovirus used to transfect the insect cells. To do this, a bacmid which contains the baculovirus genome is incorporated with the coding sequence of our protein of interest. This resulting bacmid is then transfected into the insect cells, where the virus will hijack its host cells to self-replicate and in doing so, drive expression of our protein of interest.

Bacmid incorporation with the Bac-to-Bac system (Invitrogen) exploits the high specificity and transposition frequency of the Tn7 transposase. The pFastBac1 vector has Tn7 sites (Fig. 4.2A) that are used for tranposition of this region into the bacmid, where Tn7 sites are also present (Fig. 4.2B). The bacmid (bMON14272, Kan^R) and a helper plasmid (pMON7142, Tet^R) containing the coding sequence of the Tn7 transposase are already present in the DH10Bac *E. coli* (Gibco, 10361012) strain.

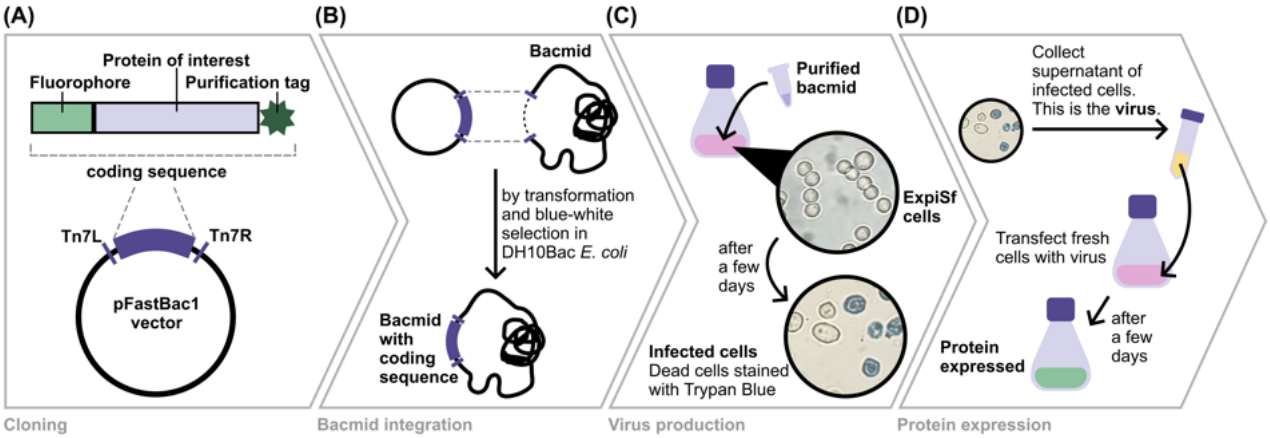

Figure 4.2: Scheme depicting the main steps in cloning and protein expression with the ExpiSf system. **(A)** Cloning of the coding sequence of the protein of interest with appropriate tags into the pFastBac1 vector. **(B)** Integration of the coding sequence into the bacmid via Tn7 transposon sites. The bacmid is already in the DH10Bac *E. coli*. **(C)** Transfection of healthy ExpiSf cells with purified bacmid. The cells are cultured until 60–70% confluency. Death rate is assessed using Trypan Blue (Gibco, 15250-061). **(D)** Expression of the protein of interest in healthy ExpiSf cells by transfection with virus. The virus is the supernatant collected from transfected cells from (C). The cells are cultured for 3–5 days and is assessed by how green (if eGFP tagged) or pink (if mCherry tagged) the culture becomes if using a fluorophore or by the degree of infection.

Protocol

100-150 ng purified and verified plasmids containing the coding sequence of desired recombinant proteins in the pFastBac1 vector backbone were transformed into 50 μl of chemically-competent DH10Bac *E. coli* cells in which Tn7 transposition takes place to transpose the coding sequence into the bacmid by heat shock. The transformed *E. coli* were then mixed with 900 μl SOB media (2% (w/v) tryptone, 0.5% (w/v) yeast extract, 8.56 mM NaCl, 2.5 mM KCl, 10 mM $MgCl_2$, 10 mM $MgSO_4$, 20 mM glucose) and incubated at 37°C at 200 rpm for 3–5 h. The solution was then centrifuged at 1 krcf for 2 min to pellet the cells. 850 μl supernatant was discarded, and the pellet was resuspended in the remaining supernatant. This was then plated unto freshly made Blue-White plates (Table 4.1) and cultured for 48 h at 37°C. Then, at least 3 white colonies (desired) were restreaked onto fresh

Blue-White plates and cultured overnight at 37°C. The white colonies were then inoculated in a 25 ml liquid culture (LB (Kan+, Tet+, Gen+), concentrations as in Table 4.1) and cultured overnight at 37°C with shaking at 200 rpm in baffled and sterile erlenmeyer flasks. The bacmid was then extracted from this liquid culture (Monarch Spin Miniprep Kit (NEB, T1110S)) where the final alcohol precipitation steps were carried out in the clean bench to prevent contamination. The bacmids were verified that they successfully incorporated the desired sequence by PCR using the standard M13F/M13R primer pair. Concentrations were estimated with the NanoDrop Spectrophotometer.

Table 4.1: Recipe for Blue-White plates.
Water, LB and agar-agar are mixed first, autoclaved and cooled to touch. Then the other ingredients (marked with asterisks) are added, mixed well and poured into 10-cm diameter culture plates. This recipes makes 25 plates. Note: the X-gal is light sensitive, so shield the plates from light. Additionally, X-gal is only stable for two weeks, so plates should be made fresh.

Component	Amount	Final concentration
Deionised water	up to 400 ml	
LB (Carl Roth, X968.2)	10 g	2.5 % (w/v)
Agar-agar (Sigma Aldrich, A7002)	6 g	1.5% (w/v)
50 mg/ml Kanamycin* (Gibco, 15160-054)	400 μl	50 μg/ml
50 mg/ml Gentamycin* (Gibco, 15750-060)	56 μl	7 μg/ml
10 mg/ml Tetracyclin* (Sigma Aldrich, T7660)	400 μl	10 μg/ml
20 mg/ml X-Gal* (Invitrogen, 15520034)	400 μl	20 μg/ml
200 mg/ml IPTG* (Sigma Aldrich, I5502-10G)	80 μl	40 μg/ml

4.2.2 Producing a viral stock

13 μg purified bacmid was transformed into 25 ml healthy ExpiSf cells (2.5 x 10^6 cells/ml) following standard ExpiSf protocols from Gibco (ExpiSf Protein Production kit). The culture was grown at 27°C shaking at 130 rpm until cells reach a death rate of 30–40%, assessed using Trypan Blue (Gibco, 15250-061) (Fig. 4.2C). The culture was then centrifuged at 300–500 rcf for 5 min at room temperature. The supernatant was transfered to a new sterile falcon and stored at 4°C shielded from light until ready for use. This was the P0 virus stock.

If it took more than 6 days for death rate to reach 30–40%, then a second passage to make P1 virus stock was carried out. To do this, 3 ml of the P0 virus stock was added to 25 ml healthy ExpiSf cells (1 x 10^6 cells/ml) and grown at 27°C shaking at 130 rpm until cells reach a death rate of 30–40% and collected as above.

4.2.3 Protein expression

Healthy ExpiSf cells were seeded to a 30 ml culture with fresh CD media (Gibco, 15889116) at 5 x 10^6 cells/ml and grown overnight at 27°C shaking at 130 rpm. The next day, 1 ml of the virus stock was added to the seeded cells (Fig. 4.2D). The culture was grown until it turned green or pink, depending on whether the attached fluorophore was eGFP or mCherry (Fig. 4.2D). The cells were pelleted at 500 rcf for 5 min at room temperature and resuspended in 5 ml 1x PBS (phosphate buffered saline,

Sigma Aldrich, P5493). It was pelleted down again and the pellet was flash frozen in liquid nitrogen and stored at -80°C until ready for use.

4.3 Protein Purification

In this thesis, the proteins were all purified by metal affinity chromatography followed by desalting purification using the Aekta pure chromatography system (Cytiva) (Fig. 4.3). Additionally, since the proteins were all expressed from insect cells, very harsh lysis conditions were not necessary. However, addition of DNAses such as Benzonase nuclease (Sigma Aldrich, E1014) was important to reduce viscosity of the lysate due to presence of DNA and RNA. Moreover, the clarification step (Fig. 4.3, last step) need not necessarily be done with an ultracentrifuge, especially since the metal affinity chromatography column I used was a crude column (HiTrap TALON crude column (Cytiva, 28953766)), which allows application of a dirtier lysate while retaining high purity and protein concentration.

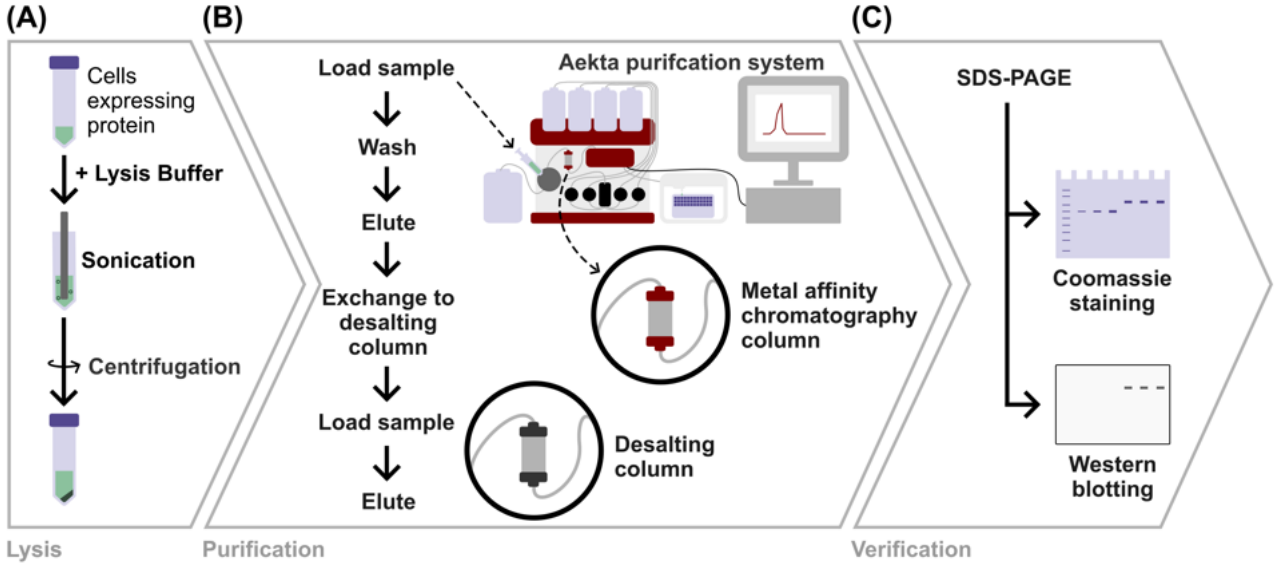

Figure 4.3: Scheme depicting the main protein purification steps used in this thesis.
(A) Lysis of the insect cells expressing the desired recombinant protein by sonication. The lysed cells are then clarified by centrifugation. **(B)** Protein purification using the Aekta pure chromatography system with a metal affinity column (HiTrap TALON crude column (Cytiva, 28953766)) and followed by a desalting column (HiTrap Desalting Sephadex G-25 columns (Cytiva, 29048684)). The Aekta pure chromatography system has an attached UV-Vis spectrophotometer which allows for real-time monitoring of the elution profile. The final eluates are collected in a fraction collector. **(C)** The fractions from the purification in step (B) are run in an SDS-PAGE for verification. The resulting gel can be stained with Coomassie or treated for western blotting with antibodies specific to the fluorophore or purification tag.

4.3.1 Purifying POK2 constructs: S59, 62, 64, 66

-80°C stock of 30 ml transfected ExpiSf cells expressing the protein of interest was thawed on ice for ~1 h, then resuspended in 10 ml cold POK2 Lysis Buffer (50 mM sodium phosphate buffer [pH 7.5], 300 mM KCl, 1 mM $MgCl_2$, 10% glycerol, 10 mM imidazole, 0.1 mM ATP, 5 mM β-mercaptoethanol, 1 mM PMSF (Thermo Scientific, 36978), 1x cOmplete EDTA-free Protease Inhibitor Cocktail (Roche, 5056489001), 25 U/ml Universal Nuclease for Cell Lysis (Thermo Scientific, 88700)) and sonicated at

75% power, 10 pulses for a total of 5 min with 40 s pause time in between pulses (Active Motif, 53057). Lysed cells were clarified by 7800 rpm 4°C 20 min centrifugation. The supernatant was passed through a 0.22 μm MCE filter membrane (Millipore, GSWP02500) and loaded unto a 5 ml HiTrap TALON crude column (Cytiva, 28953766) using the Aekta pure chromatography system (Cytiva). The column was then washed with 20 ml POK2 Wash Buffer (POK2 Lysis Buffer, but without nuclease) and 50 ml POK2 Desalting Buffer (POK2 Lysis Buffer, but without PMSF, protein inhibitors, nuclease)). The sample was eluted as fractions with the attached fraction collector with 100 (10 ml), 300 (15 ml) and finally 500 (30 ml) mM imidazole in POK2 Desalting Buffer. 1.5 ml of the greenest fractions were pooled and loaded onto a 5 ml HiTrap Desalting Sephadex G-25 columns (Cytiva, 29048684) and eluted using 15 ml POK2 Desalting Buffer. Proteins were verified by SDS-PAGE followed by Coomassie staining and western blotting with anti-GFP mouse antibody (Roche, 11814460001) and anti-His mouse antibody (Invitrogen, MA1-21315).

4.3.2 Purifying MAP65-3 constructs: S102

-80°C stock of 15 ml transfected ExpiSf cells expressing MAP65-3-mCherry-8xHis was thawed on ice for $\sim$1 h and then resuspend in 10 ml MAP65-3 Lysis Buffer (50 mM sodium phosphate buffer [pH 7.5], 100 mM NaCl, 0.5% Triton X-100, 30 mM imidazole, 0.1 mM ATP, 5 mM β-mercaptoethanol, 1 mM PMSF (Thermo Scientific, 36978), 1x cOmplete EDTA-free Protease Inhibitor Cocktail (Roche, 5056489001), 25 U/ml Universal Nuclease for Cell Lysis (Thermo Scientific, 88700)) and sonicated at 75% power, 10 pulses for a total of 5 min with 40 s pause time in between pulses (Active Motif, 53057). The supernatant was then pass through a 0.8 μm cellulose acetate membrane (Whatman, FP30/0.8 10462240) and loaded onto a 1 ml HisTrap HP column (Cytiva, 17524701) using the Aekta pure chromatography system. The column was washed with 20 ml MAP65-3 Wash Buffer (Lysis Buffer, but without PMSF or Triton X-100) and then eluted using 150 (5 ml), 300 (5 ml), and 500 (10 ml) mM imidazole in MAP65-3 Desalting Buffer (Lysis Buffer, but without PMSF or Triton X-100 and with 5% glycerol). 1.5 ml of the pinkest fractions were pooled and loaded unto a 5 ml HiTrap Desalting Sephadex G-25 columns (Cytiva, 29048684) and eluted using 15 ml MAP65-3 Desalting Buffer. The sample was verified by SDS-PAGE followed by Coomassie staining and western blotting with anti-RFP mouse antibody (Chromotek, 6g6-100) and anti-His mouse antibody (Invitrogen, MA1-21315).

4.3.3 Protein verification by SDS-PAGE

Theory

Sodium dodecyl sulfate-polyacrylamide gel electrophoresis (SDS-PAGE) is a gel-based technique to resolve proteins of different sizes. In contrast to Native-PAGE, samples are first denatured by boiling either with or without a reducing agent in the sample buffer. The sample buffer contains bromophenol blue, which is a pH indicator (yellow below pH 3.5, blue above pH 4.6) but in this case is used more for its color to ease sample loading and assessment of protein migration in the gel. The pH indication of bromophenol blue is nonetheless also useful to ensure that the pH of the samples and the gel is within expectation. The sample buffer also contains sodium dodecyl sulfate (SDS), which is an anionic

surfactant that helps to denature proteins and also binds to proteins at one SDS molecule for every two amino acid residues. This allows the proteins to travel electrophoretically through the SDS-PAGE gel and also renders the same mass-charge ratio to all proteins. Thus the migration distance of the protein would theoretically only be dependent on the mass of the proteins. Larger proteins are longer when denatured and will therefore take longer to travel through the acrylamide matrix. This is the basis of SDS-PAGE.

Protocol

Samples were mixed in correct proportions with dithiothreitol (DTT)-containing 3x Protein loading dye (New England Biolabs, B7703S), boiled at 90°C for 7 min, before loading directly into the wells of a 4-20% gradient Mini-PROTEAN TGX Precast protein gel (Bio-Rad, 4561035). 10 μl Prestained broad range protein ladder (New England Biolabs, P7719S) was usually loaded into either the right-most and/or left-most lane. Gels were then run at 200 V until the dye front reached the bottom.

4.3.3.1 Staining an SDS-PAGE gel

Theory

SDS-PAGE gels are usually stained with Coomassie Brilliant Blue (CBB), which is a type of triphenylmethane dye that binds electrostatically with the amino and carboxyl groups on amino acids. The binding stabilises the anionic form of the dye, whereas free CBB molecules are usually cationic in solution [51]. This is the basis of the Bradford assay (not used in this thesis), since the cation-to-anion shift causes also a 465 to 595 nm shift in wavelength. There are two types of Coomassie: G-250 which is greenish and R-250 which is reddish. In the case where even higher sensitivity is needed, silver staining can be used (not used in this thesis).

Protocol

The gels were then washed three times in deionised water (5 min, gently shaking at room temperature) before staining with Imperial protein stain (Thermo Scientific, 24615) for 1 h (room temperature, gently shaking). The gel is then destained with deionised water for at least 1 h until the background is sufficiently destained. The gel is then imaged with the Typhoon Scanner (GE Healthcare, FLA 9500) with the 635 nm laser and LP filter at 600 V (with the Photon Multiplier Tube) with 100 μm pixel size.

4.3.3.2 Protein concentration assessment

Protein concentration can be measured using a NanoDrop spectrophotometer or by comparing the band intensities in a stained SDS-PAGE gel with BSA mass standards. For spectrophotometry, 2 μl of the protein sample wasw measured at 280 nm wavelength against a blank control while taking into account the extinction coefficient (estimated from the primary sequence) and the molecular weight of the protein. The spectrophotometric measurement was confirmed by then running an SDS-PAGE gel with the desired protein samples and BSA at known amounts (stock is 2 mg/ml from Bovine serum

albumin (BSA) standard (Thermo Scientific, 23210)) (Fig. 4.4A). The SDS-PAGE was run, stained and destained as usual. The intensity of the bands were then analysed in FIJI [271]. A box was drawn around the lanes of interest to obtain an intensity profile (Fig. 4.4B). The area under the intensity profile is obtained. To correct for the background, an intensity profile of the same size box in the background was obtained and the area under this graph was also obtain (Fig. 4.4B, C). Another way to subtract the background was to directly draw a line at the base of each band peak in the intensity profile, and measuring only the area under the peak. The background subtracted area versus known mass of the BSA mass standards were plotted to obtain a regression line, with which the mass of the protein of interest was calculated (Fig. 4.4C). Take note, for accuracy, it is essential that the intensity of the band of the protein of interest has to be within the regression line plotted for the BSA mass standards. Hence, it is good to use the initial spectrophotometric measurements to estimate how much protein to load to remain within this range of the BSA mass standards.

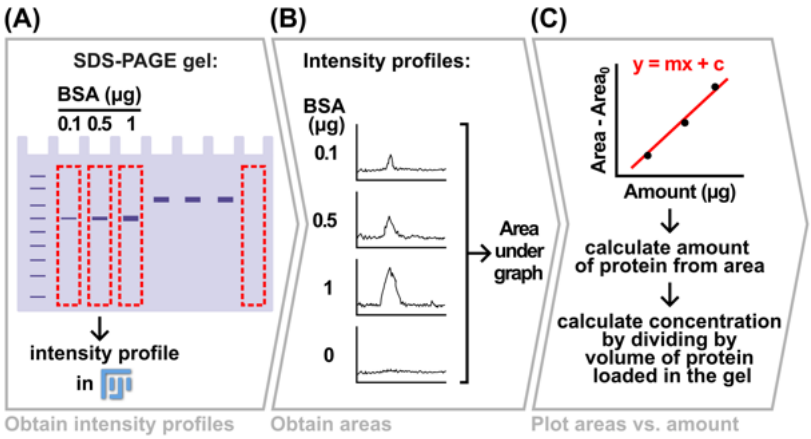

Figure 4.4: Schematic showing key steps to measure protein concentration by a BSA standard in SDS-PAGE. **(A)** BSA of known amounts are loaded and run in an SDS-PAGE gel. Several dilutions of the protein to be assessed is loaded in the same gel. The gel is stained and destained. Then imaged and analysed in FIJI [271]. Boxes around the lanes are drawn and intensity profiles are obtained using the built-in gel analysis function. **(B)** The area under the intensity profiles are obtained and plotted in a graph as in (C). **(C)** The graph of area versus known amounts of BSA is plotted and fitted with a linear regression. Using the formular of the linear regression, the amounts of the protein desired can be calculated by measuring also the area of the proteins as in (A). The concentration can then be calculated by dividing the mass amount (μg) with the volume amount (μl) of protein loaded into the gel.

4.3.3.3 Western blotting

Theory

Western blotting is a technique used to detect the presence and amount of proteins using antibodies. In this regard, it is also known as immunoblotting. The 'blot' part of the name refers to the transfer of proteins unto a solid substrate. For western blotting, this is done after an SDS-PAGE run where the resolved proteins are transferred unto a nitrocellulose or polyvinylidene fluoride (PVDF) (in the case of this thesis) membrane. Once on this solid substrate, the proteins are incubated with primary and secondary antibodies for detection. The secondary antibody is used for signal amplification and is conjugated to horse radish peroxidase (HRP). Horse radish peroxidase (HRP) catalyses the oxidation of luminol, which exhibits chemiluminescence when oxidised.

Protocol

After SDS-PAGE, the gel was placed on top of a stack of blotting papers (Trans-Blot Turbo Mini 0.2 μm 7 x 8.5 cm PVDF Transfer Packs (Bio-Rad, 1704156)) on the bottom electroplate of Trans-Blot Turbo Transfer System (Bio-Rad, 1704150). Then, a PVDF membrane and another stack of blotting papers were placed on top (Trans-Blot Turbo Mini 0.2 μm 7 x 8.5 cm PVDF Transfer Packs) of the gel with the PVDF membrane facing the gel. Air bubbles were gently rolled out. The top electroplate was fastened on the stack and the whole cassette was inserted into the Trans-Blot Turbo Transfer System. Transfer was carried out at 2.5 A and 25 V for 3 min. Then, the membrane was transferred with the protein side up (similar to Fig. 4.6B) into a 50 ml falcon tube and washed once with 1x Wash Buffer (SuperSignal West Pico mouse Fast Western kit (Pierce, 35060)). The usual blocking step is omitted when using the SuperSignal West Pico mouse Fast Western kit (Pierce, 35060). The membrane was then immediately incubated in 1:2000 anti-GFP mouse antibody (Roche, 11814460001), 1:4000 anti-RFP mouse antibody (Chromotek, 6g6-100) or 1:800 anti-His mouse antibody (Invitrogen, MA1-21315) in Antibody diluent solution (Pierce, 35060) for 1.5 h. Then membrane was then washed three times with 1x Wash Buffer for 5 min each. Then, the membrane was incubated in 1:20 anti-mouse HRP-conjugated antibody (Pierce, 35060) for 1 h and was washed again in 1x Wash Buffer three times for 5 min each. Finally, 3 ml premixed luminol and peroxide solutions (Pierce, 35060) was dropped onto a clean plastic sheet. Using tweezers, the membrane was placed unto the droplet protein-side-down and left to incubate for 3 min at room temperature. The membrane was then imaged with the Fusion Fx7 Imaging System (Vilber).

4.4 Biochemical assays

4.4.1 Sedimentation assay

In this thesis, a sedimentation assay at 20 krcf was used to investigate the large clusters seen in POK2 tail microtubule binding experiments (Fig. 5.6). Proteins were first diluted to 100 nM in POK2 Storage Buffer (the buffer POK2 is stored, in this case, the POK2 Desalting Buffer.). This pre-diluted protein was then further diluted into a PEM20 (PEM buffer but with 20 mM PIPES instead)-based Motility buffer (0.16 mg/ml casein, 20 mM D-glucose, 20 μg/ml glucose oxidase, 8 μg/ml catalase, 1 mM ATP, 5 mM DTT in PEM20) (at $\sim$130 mN ionic strength) and incubated at room temperature for 10 min (Fig. 4.5A). The mix was then centrifuged for 20 min at 20 krcf at 4°C. The supernatant and pellet were separated. 0.25x volumes of 100% trichloroacetic acid (TCA) (Sigma Aldrich, T8657) was mixed with input, supernatant and pellet samples and centrifuged at 20 kcrf for 30 min at 4°C (Fig. 4.5B). The pellets were washed with 200 μl cold acetone and centrifuged again at 20 krcf for 30 min at 4°C (Fig. 4.5C). Finally, the pellets were dried in the dessicator under vacuum for 10 min (Fig. 4.5D). The dried pellets were resuspended in Protein loading dye (New England Biolabs, B7703S), boiled at 90°C, then all loaded into a 4-20% Mini-PROTEAN TGX Precast protein gel (Bio-Rad, 4561035) and run at 200 V for 30 min (Fig. 4.5E). The gel was then stained with Imperial protein stain (Thermo Scientific, 24615) and destained according to manufacturer instructions.

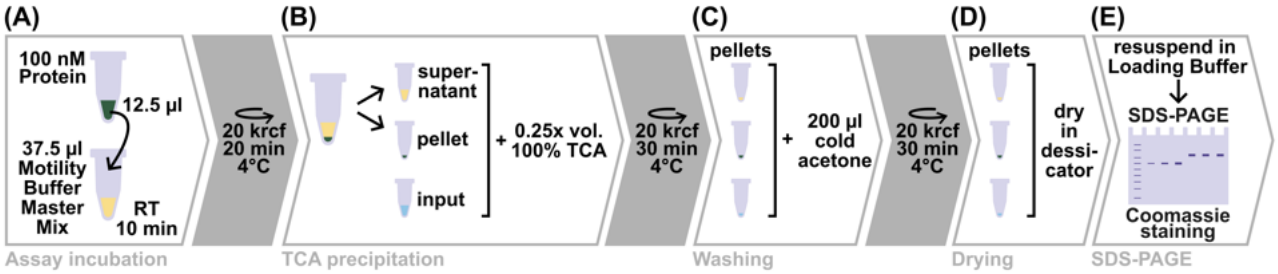

Figure 4.5: Schematic showing key steps of the POK2 sedimentation assay.
(A) 12.5 μl 100 nM protein is mixed with 37.5 μl Motility Buffer Master Mix such that the final reaction mix consists of the Motility Buffer with 25 nM protein. This reaction mix is then incubated at RT for 10 min then centrifuged. **(B)** The supernatant and pellet of the centrifuged mix from (A) are separated. Together with the input, the supernatant and pellet are precipitated using TCA, then centrifuged. **(C)** The precipitates are washed with acetone and centrifuged again. **(D)** The final precipitates are dried under vacuum in a dessicator for 10 min. **(E)** The precipitates are resuspended in protein loading dye and loaded into a 4–20% polyacrylamide gel for SDS-PAGE analysis.

4.4.2 Lipid blot assay

Phosphoinositols (PIs) are a class of lipids made of a phosphate group, two fatty acid chains, one inositol molecule, and can be phosphorylated with up to 3 phosphates. PIs and their phosphorylated versions, phosphoinositol phosphates (PIPs), are phospholipid components of cell membranes. As a method to screen for potential interactions with specific lipids, several lipids are dotted onto a nitrocellulose membrane with 100 pmol per spot (according to Echelon Bioscience, P-6002 and P-6001).

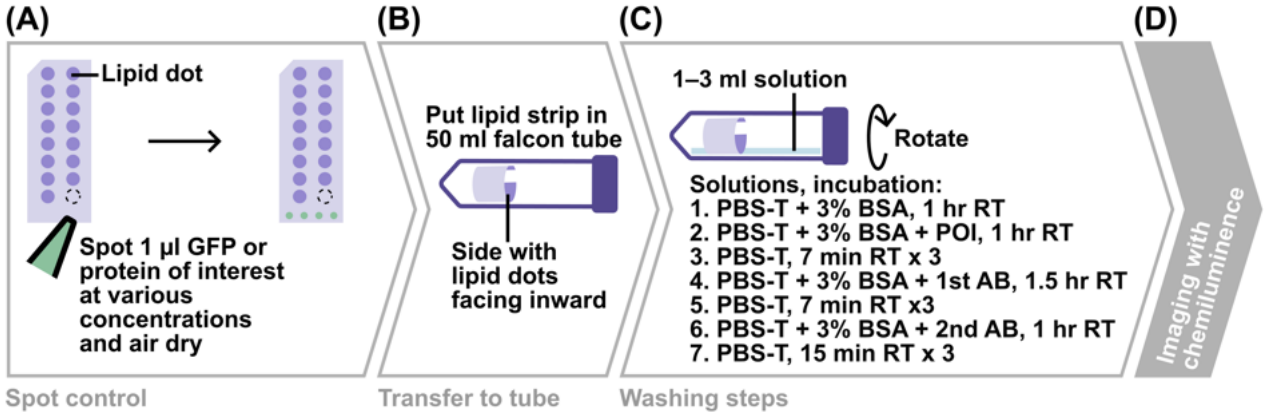

Figure 4.6: Schematic showing key steps of the lipid strip assay.
(A) Controls are spotted at the bottom of the lipid strip and allowed to air dry. **(B)** The lipid strip is then carefully placed into a 50 ml falcon with the lipid dots facing inward. **(C)** Using a 50 ml falcon allows the use of just 1-3 ml solution during washing steps to reduce the amount of protein used. The incubation is done on a roller at room temperature. Acronyms: PBS-T, phosphate buffered saline with 0.1% (w/v) Tween-20 at pH 7.2; BSA, bovine serum albumn; AB, antibody; RT, room temperature.

Protocol

First, the lipid strip (Membrane lipid strips (Echelon Biosciences, P-6001/P-6002)) were spotted on the bottom with 1 μl controls (55, 20, 2, 0.2 ng/μl eGFP-POK2$^{2083\text{-}2771}$) and allowed to air-dry (Fig. 4.6A). Using tweezers, the strip is gently transferred into a 50 ml falcon tube with the lipid side facing

away from the walls (Fig. 4.6B). 3 ml PBS-T + 3% Bovine serum albumin (BSA) (Carl Roth, 0052.2) (which is fatty acid free) was added gently to the tube without disturbing the strip and incubated for 1 h. All the incubation steps were performed by rolling the closed tube on a tilt/roller mixer (Phoenix Instruments, RS-TR05 at room temperature. The strip was then subsequently incubated in 0.2 mg/ml of our protein of interest in PBS-T + 3% BSA for 1 h, 1:2000 anti-GFP mouse antibody (Roche, 11814460001) in PBS-T + 3% BSA for 1.5 h and finally in 1:20 anti-mouse HRP-conjugated antibody (SuperSignal West Pico mouse Fast Western kit (Pierce, 35060)) for 1 h. In between these steps, the strip was incubated three times with PBS-T for 5 min to wash the strips before the next step. After the last incubation step, the strip was also washed three times with PBS-T, this time for 15 min each. Finally, 3 ml premixed luminol and peroxide solutions (SuperSignal West Pico mouse Fast Western kit (Pierce, 35060)) was dropped onto a clean plastic sheet. With tweezers, the strip was placed unto the droplet with the lipid-/protein-side-down and incubated for 3 min at room temperature. The membrane was then imaged with Fusion Fx7 Imaging System (Vilber).

Note on ordering and storage

The lipid strips were ordered from Echelon Bioscience through its German distributor MoBiTec, with each strip costing ∼80 euros/strip. The lipid strips come in a zip-loc bag, but it is important to touch the strips as little as possible, even through the plastic. Even during transfers and use, I used tweezers to grab the edges and avoided touching the strips with my hands. I kept the lipid strips in a hard plastic box at 4°C to prevent touching the lipid strips directly.

Analysis

FIJI was used to analyse the image of the lipid strip. Raw integrated intensities were obtained by drawing circles around the lipid dots and corrected by subtracting the intensity from a nearby background region of the same circle size. In order to compare the intensities between strips, the controls at the bottom of the strip were also measured. Since the 0.2 ng eGFP-POK2$^{2083\text{-}2771}$-8xHis spot had the best intensity without saturation, this was used as the control. The final relative gray value (a.u.) in Fig. 5.32 was the intensity relative to the 0.2 ng control.

4.4.3 GUV assays

A liposome is a small spherical vesicle with at least one lipid bilayer. There are different classes of liposomes depending on their size and number of bilayers (Table 4.2). There are two general methods to prepare liposomes: electroformation (reviewed in [25]) and gentle hydration. While electroformation can have better yield, it more difficult to do and requires specific devices[206]. Gentle hydration techniques such as gel-assisted swelling [238, 345] is simpler and faster. In this thesis, I used polyvinyl alcohol (PVA)-assisted swelling.

Table 4.2: Liposome are classed depending on their size and number of bilayers.
Data is compiled from [211].

Class	Abbrev.	Bilayers (n)	diameter (nm)
Small Unilamellar Vesicle	GUV	1	20-40
Medium Unilamellar Vesicle	GUV	1	40-100
Large Unilamellar Vesicle	GUV	1	>100
Giant Unilamellar Vesicle	GUV	1	>1000
Oligolamellar Vesicle	OLV	2-5	>100-1000
Multilamellar Vesicle	MLV	>5	>500
Multivesicular Vesicle	MVV	1	>5000

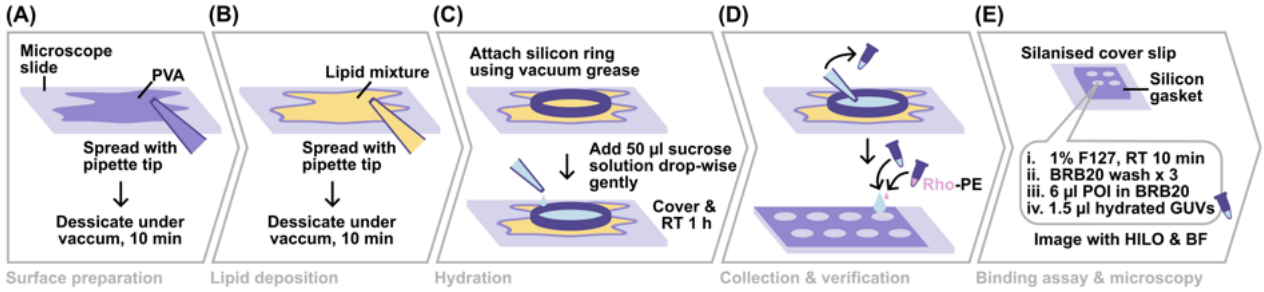

Figure 4.7: Schematic showing key steps of the GUV assay.
(A) 1% PVA was spread on a clean microscope slide and dried in the dessicator for 10 min. **(B)** A premixed lipid mixture in chloroform is then spread on top of the PVA-dried microscope slide and also dessicated for 10 min. **(C)** A silicon ring is attached onto the microscope slide with vacuum grease. Then, 50 µl sucrose solution is added drop-wise gently to promote hydration of the lipids into GUVs. The hydration is left to take place at room temperature for 1 h. **(D)** The hydrated GUVs are collected in a fresh 1.5 ml tube. Formation of GUVs are checked by epifluorescence microscopy by spotting 5 μl of the hydrated GUVs on to a microscope slide with reaction wells. To visualise the GUVs, trace amounts rhodamine-PE is spiked into the droplet on the slide. **(E)** The GUV assay takes place inside the wells of a silicon gasket mounted on a silanised cover slip (Section 4.5.6, Fig. 4.8). The surface is first incubated with 1% Pluronic F-127 (Sigma Aldrich, P2443) for 10 min at room temperature, and then this is washed away using PEM20 (PEM buffer but with 20 mM PIPES instead). The assay is then visualised with HILO and BF microscopy. Acronyms: polyvinyl alcohol (PVA), room temperature (RT), rhodamine (Rho), phosphatidylethanolamine (PE), highly inclined and laminated optical sheet (HILO), bright field (BF).

Protocol

Lipid mixtures of 10, 50, 75 and 100% (mol) phosphatidic acid (PA) or Cardiolipin (CL) (Avanti, 840012P) were prepared in remaining % (mol) of DOPC (Avanti, 850375) to a total lipid concentration of 1 mg/ml in Chloroform (Sigma Aldrich, 288306). 20 μl 1% polyvinyl alcohol (PVA) (Sigma Aldrich, 341584) was spread on a microscope slide and dessicated under vacuum for 10 min (Fig. 4.7A). Then, 10 μl of the lipid mixture was spread over the PVA-coated surface and dessicated under vacuum for another 10 min (Fig. 4.7B). Silicon rings of 15 mm inner diameter were sealed unto the lipid-PVA surface with vacuum grease. This has to be done carefully to ensure no leakage of solutions in the next step (Fig. 4.7C, top). Then 50 μl 450 mM sucrose solution (sotonic to the final reaction buffer containing PEM20 buffer and protein of interest) was gently added over the lipids and incubated at room temperature for 1 h to allow GUVs to form by gentle hydration (Fig. 4.7C, bottom). Hydrated GUVs were then collected in a clean 1.5 ml tube (Fig. 4.7D). To check if GUVs succesfully formed, 5 μl of the collected GUV solution is pipetted onto a well of a

microscope slide with reaction wells (Marienfeld Superior, 1216333) and spotted with trace amounts of rhodamine-conjugated phosphatidylethanolamine (PE) (Fig. 4.7D, bottom) and visualised with epifluorescence and phase-contrast light microscopy. To prepare a sample for a GUV binding assay, a pre-cut 4x4-well reusable CultureWell gaskets (Grace Bio-Labs, 103250) was placed on a 22 x 22 mm silanised glass cover slip (see Section 4.5.6). 5 μl of 1% Pluronic F-127 (Sigma Aldrich, P2443) was added into the gasket wells and incubated for 10 min at room temperature to block the surface. The Pluronic F-127 was washed away thrice using PEM20 buffer. The sample is first set on the microscope to find the surface, and then 6 μl 2.5 nM eGFP-POK2$^{2083\text{-}2771}$ in PEM20 buffer was added to the well. Immediately after, 1.5 μl hydrated GUVs were added. The sample was then visualised using highly inclined and laminated optical sheet (HILO) microscopy (Section 4.5.1.2) for the protein and bright field (BF) for the GUVs. The GUVs were also detectable with HILO microscopy, when they illuminated by reflections off fluorescent contaminations in the sample.

4.5 Microscopy assays

4.5.1 Microscopy techniques

4.5.1.1 Total internal reflection fluorescence (TIRF) microscopy

microscopy In order to visualise proteins interacting with microtubules at single molecule resolution, we use total internal reflection fluorescence (TIRF), which exploits the excitation from an evanescent wave generated at the solid-liquid interface when the excitation light is totally internally reflected in the solid medium. The evanescent wave is actually an electromagnetic field that has the same frequency of the excitation light and is only about 200 nm range from the solid-liquid interface. In our assays, our microtubules (themselves only 25 nm in diameter) are attached to the surface and fluorescently-tagged microtubule-interacting proteins are mixed into the liquid medium. As the evanescent wave is only about 200 nm high, only proteins that interact with the microtubule would be excited and visible, whereas the proteins that are floating in the liquid medium would not be excited, thus providing the high signal-to-noise ratio required for single-molecule precision.

4.5.1.2 Highly inclined and laminated optical sheet (HILO) microscopy

The signal-to-noise ratio achieved with TIRF is highly sought after. However, TIRF becomes inappropriate in situations where the sample is further than 200 nm from the glass surface. Meanwhile, epifluorescence imaging, where collimated light illuminates the sample, encountering the glass sample interface straight-on, results in everything within the light column to be excited. By contrast, epifluorescence imaging has much lower signal-to-noise ratio. Between these two extremes is HILO imaging, where the collimated light is directed at near critical angles to the glass-sample interface, which allows a smaller volume of the sample to be illuminated. Although signal-to-noise ratio is not as high as for TIRF microscopy, it is far better than epifluorescence imaging.

4.5.1.3 Interference reflection microscopy (IRM)

Interference reflection microscopy (IRM) is a label-free imaging technique that takes advantage of the phase difference between the light reflected by objects in the liquid medium and the light reflected at the solid-liquid interface. To be able to detect a phase difference, we have to use linearly polarised light of a specific wavelength. Depending on the distance of the object from the solid-liquid interface, the phase difference can be (1) half a wavelength, (2) smaller than half a wavelength, and (3) none when the objects are (1) directly at the solid-liquid interface, (2) deeper in the liquid medium, and (3) when there is no object to reflect the light. When the phase difference is half a wavelength as in scenario (1), the light waves are superimposed such that they cancel each out completely, producing a dark pixel in the final image. In scenario (2), where the phase difference is less than half a wavelength, the light waves do not completely cancel out, and will produce a wave of different amplitude and thus a brighter pixel in the final image. As you can imagine, for scenario (3), if there is no interference at all, then the reflected light will produce a bright pixel in the final image. In our assays, we use IRM to visualise label-free microtubules which we attach to the glass surface. However, as IRM is only able to detect the proximity of an object to the solid-liquid interface, we are unable to tell for example whether or not a single protein is binding to the microtubule, especially if it is perpendicular to the glass surface on top of the microtubule.

Note
TIRF microscopy and IRM were performed on the custom-built setups - single-color TIRF/IRM setup *Aalo* [270] and dual-color TIRF/IRM setup *Shenlong* [117], which was built similarly and functions conceptually in a similar manner as another setup *Gleipnir* [285]. Camera exposure time was always 100 ms. On *Aalo*, 488 nm laser power was set at 10–20% whereas on *Shenlong* it was 5% unless stated otherwise. 561 nm laser power on Shenlong was either 1% or 10% and is mentioned directly in the Results section. The lasers on *Aalo* had a maximum output of 100 mW whereas the lasers on *Shenlong* had a maximum output of 80 mW. Images were acquired at 100 ms time intervals unless stated otherwise.

4.5.1.4 Mass photometry

Mass photometry is an imaging-based technique that uses the principles of IRM and interferometric scattering microscopy to measure the molecular mass of small molecules. Experiments were performed using the OneMP system (Refeyn Inc.) in the lab of Dr. John Weir (Friedrich-Miescher Laboratory, Max Planck Institute for Biology, Tübingen). The technique exploits the phenomenon that molecules scatter light proportionally to their mass [141, 142]. By calculating the ratio between the amount of light reflected at the glass-sample interface and the light scattered by the molecules in the sample (i.e., ratiometric contrast values) and correlating this to a mass standard, the ratiometric contrast of molecules of unknown mass can be inferred. This technique is powerful as it requires only a small sample volume (10 μl) and can be performed in solution. In this thesis, mass photometry was used sparingly to obtain preliminary impressions of the oligomeric species of the POK2 tail and MAP65-3-mCherry constructs.

The experiments were performed as described in [141, 142] in the PEM20 buffer-based Motility buffer (0.16 mg/ml casein, 20 mM D-glucose, 20 μg/ml glucose oxidase, 8 μg/ml catalase, 1 mM ATP, 5 mM DTT in PEM20). Analysis was performed using a custom Python script written by Dr. Maria Kharlamova [141, 142].

4.5.2 Tubulin purification

While it is ideal to use plant tubulin when studying plant microtubule interacting proteins, producing useful quantities of plant tubulin has proven experimentally challenging and time-consuming. On the other hand, 700 mg of tubulin is easily obtainable from 12 porcine brains by several rounds of cold (depolymerisation) and warm (polymerisation) incubations. Hence, I take advantage of the rather faithful conservation of tubulins across eukaryotes and use porcine brain tubulin for the microtubule assays in this thesis.

Protocol

While preparing porcine brain tubulin is efficient, it is still a labour-intensive effort, and was thus together by everyone in the lab. The purification protocol exploits how microtubules depolymerise in the cold and polymerises in the warmth and consists of multiple rounds of cold-warm incubation and centrifugation steps.

First we removed the blood vessels from the brain hemisphere and homogenised the brains in Depolymerisation buffer (50 mM MES [pH 6.6], 1 mM $CaCl_2$). As the suspension is already chilled, we proceeded directly to the first cold centrifugation step for 1 h at 25 kcf at 4°C. The supernatant was passed through a linen sheet and mixed with equal volume HMPB buffer (high-molarity PIPES buffer: 1 M PIPES [pH 6.9], 10 mM $MgCl_2$, 20 mM EGTA) and equal volume glycerol supplemented with fresh ATP and GTP to final concentrations of 5 mM. Next, we polymerised the microtubules for the first time by incubation in a 37°C water bath for 1 h followed by centrifugation at 160 krcf for 30 min at 37°C. The pelleted polymerised microtubules are recovered in Depolymerisation buffer and subjected to a second cold incubation-centrifugation step, this time at 80 kcrf. The supernatant was then mixed again with HMPB buffer, glycerol and fresh ATP and GTP for a second polymerisation incubation-centrifugation step. The pellet was resuspend in a small volume of PEM buffer (80 mM PIPES [pH 6.9], 1 mM EGTA, and 1 mM $MgCl_2$) for the third and final cold incubation-centrifugation step, this time at 100 krcf. The supernatant was then collected, portioned to 1 ml aliquots, snap frozen in liquid nitrogen and stored at -140°C.

4.5.3 Tubulin cycling

Before use, the tubulin has to be cycled once more to get rid of any remaining inactive tubulin. Quite simply, the -140°C frozen tubulin from the previous step were thawed on ice, resuspended in equal volume 2x Polymerisation buffer (2x PEM, 30% glycerol, 1 mM GTP, 4 mM $MgCl_2$), and incubated at

37°C for 1 hr. The polymerised microtubule suspension was then centrifuged through a 60% glycerol cushion (in PEM buffer) at 180 krcf for 20 min at 37°C. The pellet was first rinsed with warm PEM buffer without disturbing it and then resuspended into cold PEM buffer. The suspension was incubated on ice for 30 min and then centrifuged at 180 krcf for 20 min at 4°C. The supernatant was measured for its concentration, diluted to a final concentration of 6 mg/ml (i.e. 60 μM), portioned into 5 μl aliquots, snap frozen in liquid nitrogen and stored at -80°C.

4.5.4 Tubulin labelling

Tubulin can be conjugated to functional groups or dyes such as rhodamine, Atto488 or biotin via NHS-esterification. In general, it is good to use 10–20x molar excess of the dye or functional group relative to tubulin. However, in our lab's experience, 20x molar excess of atto565 can be inhibitory to polymerisation of microtubules. Hence, caution must be exercised regarding how the functional groups and dyes adversely affect microtubule dynamicity, especially if the labelling protocol has not yet been tested in the lab.

Protocol

In this thesis, I occasionally used rhodamine labelled tubulin, so here I explain labelling steps which I performed with Dr. Serapion Pyrpassopoulos. Essentially, the steps are the same as for tubulin cycling, with an extra step for labelling.

A -140°C aliquot of purified but uncycled tubulin was thawed on ice, diluted to 20 mg/ml (i.e. 0.2 mM) with PEM buffer and supplemented with 30% glycerol, 1 mM GTP, 4 mM $MgCl_2$. This resuspended tubulin was incubated at 37°C for 1 h to polymerise into microtubules. To the polymerised microtubules, we added 4 mM NHS-Rhodamine (Thermo Fisher Scientific, 46406, pre-dissolved in dimethylsulphoxide (DMSO)), vortexed to mix and incubated at 37°C for another 20 min. To quench the reaction, 1/40-th volume K-glutamate of the entire solution was mixed in and incubated for a further 5 min at 37°C. The labelled, polymerised microtubules were sedimented at 55 krpm (TLA-55 fixed angle rotor (Beckman Coulter) for 1 h at 37°C through a 60% glycerol cushion (in PEM buffer). From here, the steps are the same as for tubulin cycling.

4.5.5 Microtubule polymerisation

0.3 mg/ml i.e., 3 μM cycled unlabelled tubulin or 10% rhodamine-labelled tubulin was mixed with 1 mM non-hydrolysable analog of GTP (GMPCPP) (Jena Bioscience, NU-405S) and 1 mM $MgCl_2$ in PEM buffer and incubated on ice for 5 min to ensure that all the tubulin is depolymerised. The mixture was then incubated at 37°C on a heat-block for 1 h to polymerise microtubules. The microtubules were collected by centrifugation at 20 krcf for 20 min at 37°C. The pellet was carefully resuspended with a cut-200μl-tip (to reduce shearing) into PEM-Tx buffer (10 μM paclitaxel in PEM buffer).

To check if the microtubules were polymerised, 2 μl of the final resuspension was sandwiched between two 22 x 22 mm glass cover slips (Marienfeld Superior, 0102052). This sandwich was mounted on the TIRF/IRM setup and observed with either TIRF (when fluorescently labelled) or IRM (when label-free) for microtubules.

Note

These microtubules were double-stabilised (i.e. GMPCPP and paclitaxel) and, in my experience, stable for more than a week. However, I would not rely on data using microtubules more than a week old. Additionally, as microtubules degrade over time even if stored at 37°C, if the microtubules were not prepared fresh for same-day use, then the microtubules were centrifuged again to remove free and/or inactive tubulin.

4.5.6 Silanisation of glass cover slips

Microtubules are attached to the glass surface using anti-β-tubulin mouse antibody (Sigma Aldrich, T7816). To attach the antibodies, the surface of the glass surface is silanised with hexamethyldisilane (HMDS) to be hydrophobic, which allows antibodies to adsorb onto the surface more stably through its hydrophobic groups.

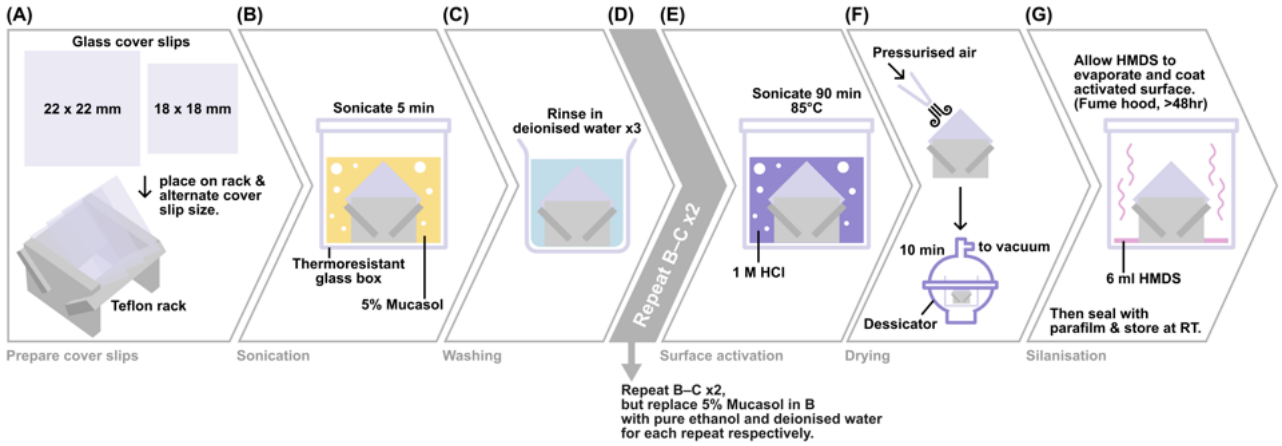

Figure 4.8: Schematic showing key steps in preparing HMDS silanised glass cover slips.
(A) Cover slips were arranged on a teflon rack alternating between 22 x 22 and 18 x 18 mm size cover slips. **(B)** The rack was placed in a thermoresistant glass box and filled with 5% Mucasol and sonicated for 5 min. **(C)** The solution in the glass box was replaced with deionised water to rinse the cover slips thrice. **(D)** Steps (B–C) were repeated with 100% ethanol and deionised water. **(E)** The solution in the glass box was replaced with 1 M HCl and sonicated for 90 min at 85°C. **(F)** The cover slips were dried by presssured air until no large water droplets could be seen and was then further dried by dessication for 10 min. **(G)** The dried cleaned cover slips were placed in a clean dry glass box and 6 ml hexamethyldisilane (HMDS) was added to the bottom of the glass box. The box was then sealed with parafilm and left in the fume hood where the HMDS would evaporate and coat the cover slips.

Protocol

18 x 18 mm glass cover slip #1.5 (Menzel Glaeser, 630-1842) and 22 x 22 mm glass cover slip #1.5 (Marienfeld Superior, 0102052) were alternately arranged on teflon racks and placed in glass boxes (Fig. 4.8A) filled with solutions for the following sonication steps. The cover slips were cleaned by sonication in 5% Mucasol (Carl Roth, 1A3L.2), 100% ethanol and deionised water for 5 min each (Fig.

4.8B–D) . In between each solution, the cover slips were rinsed with deionised water by submerging them in deionised water and gently wriggling the racks with tweezers while submerged. The rinse was repeated three times. Next, the coverslips were surface-activated by sonication in 1 M hydrochloric acid (HCl) at 85°C for 90 min (Fig. 4.8E). The cover slips were dried with pressurised air to get rid of excess water. To ensure that the cover slips were completely dry, the cover slips were placed in a cleaned room-temperature glass box and dessicated together for an additional 10–20 min under vacuum (Fig. 4.8F) . Then in the fume hood, 6 ml HMDS was added to a corner at the bottom of the glass box without directly touching the cover slips. The glass box was sealed with parafilm and the HMDS was left to evaporate and coat the cover slips for 2 d under the fume hood (Fig. 4.8G) .

4.5.7 Building a simple *in vitro* two-channel flow cell

Using ethanol-cleaned scissors and tweezers, a piece of double-sided waterproof sticky tape (KlebeShop24, KS DC 3702-9) ∼25 mm long was cut into 3 strips. The strips of tape were stuck on to a 22 x 22 mm silanised cover slip to create two channels of ∼1 mm width (Fig. 4.9A). The sides of the tape strips which were cut should face the channels. The protective seal on the other side of the strip was removed and a 18 x 18 mm cover slip was stuck on by aligning one edge of the cover slip first, and then letting it fall unto the rest of the tape. The top coverslip was gently pressed with a gloved-thumb to encourage sealing. Next, excess parts of the tape are cut off with an ethanol-cleaned scalpel while avoiding the entry points of the channels (Fig. 4.9B). In this manner, solutions could be easily introduced using a pipette and 200 μl pipette tip. However as the channels were thin and the surface was hydrophobic, a vacuum was used first to form a liquid column through the channel. After a liquid column was formed, solutions could then be encouraged through the channel either using a filter paper or a vacuum on the other side (Fig. 4.9C).

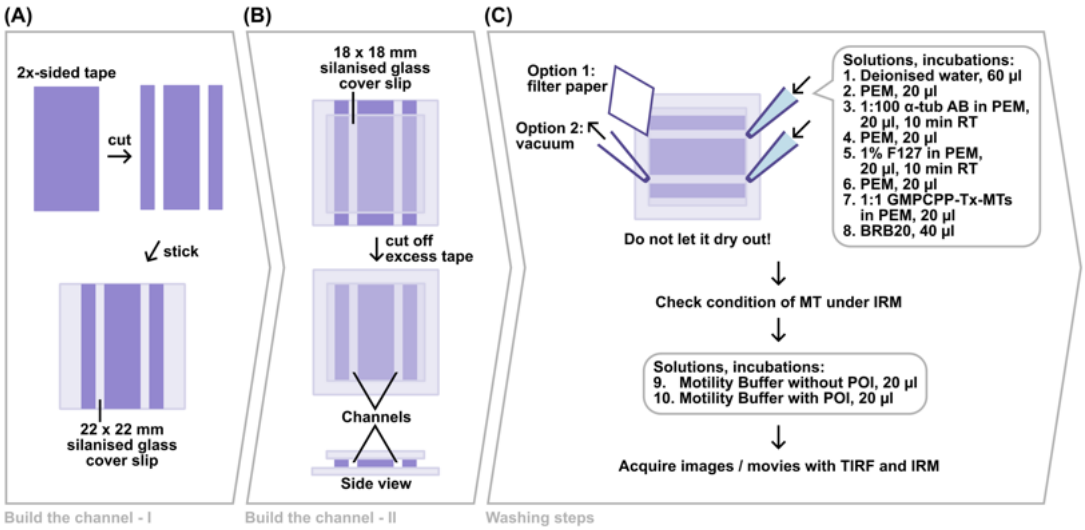

Figure 4.9: Schematic showing key steps in building a two-channel flow cell.
(A) Double-sided sticky tape was cut into three strips and stuck unto a 22 x 22 mm silanised glass cover slip. **(B)** An 18 x 18 mm silanised glass cover slip was placed on top and the excess tape was cut off. **(C)** Washing steps to prepare the channel for *in vitro* microtubule assays. See Section 4.5.8 for details. Abbreviations: microtubule (MT), antibody (AB), room temperature (RT), total internal reflection fluorescence (TIRF), interference reflection microscopy (IRM).

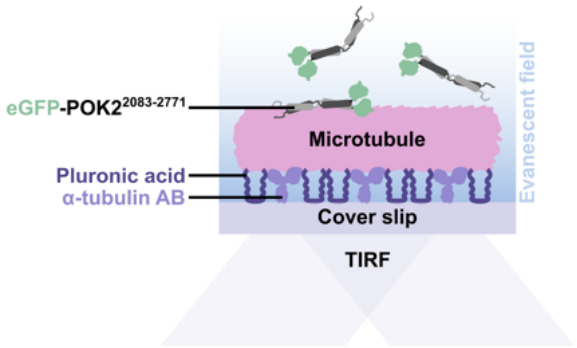

Figure 4.10: *In vitro* microtubule binding assay setup inside a channel.
The cartoon shows how the polymerised microtubules (pink) are immobilised to a glass cover slip by anti-β-tubulin mouse antibody (lilac) binding. The surface is further blocked from non-specific binding with Pluronic F-127 (dark violet). The channel here is also flushed with some eGFP-POK2$^{2083-2771}$ (green-grey) which would bind the microtubules or remain floating in the solution. The evansecent field generated when the laser hits the glass surface at the TIRF angle allows that only signal near the surface are visible. Floating protein signals would be less visible. Abbreviations: antibody (AB), total internal reflection fluorescence (TIRF), interference reflection microscopy (IRM).

4.5.8 *In vitro* microtubule binding assay - bulk

To wash the channels of a flow cell, at least 60 μl deionised water was passed through using a vacuum (Fig. 4.9C, Option 2). Then, 20 μl PEM buffer was passed through before passing in 20 μl of 1:100 anti-β-tubulin mouse antibody (Sigma Aldrich, T7816) in PEM buffer and left to incubate for 3 min to promote adhesion. Then, the channel was washed by passing in 20 μl PEM buffer. To block the surface from non-specific binding, 20 μl 1% Pluronic F-127 was passed through and incubated for 10 min. The channel was washed again with PEM buffer before finally introducing 20 μl double-stabilised microtubules (further diluted 1:1 = microtubules from Section 4.5.5 : PEM-Tx buffer). The microtubules were immediately washed out with PEM buffer (Fig. 4.9C). The binding of microtubules were checked with either TIRF or IRM before continuing.

If the microtubules were good and at a density that was satisfactory, then the Motility buffer was prepared at 10x concentration. For eGFP-POK2$^{2083-2771}$, the protein was also pre-diluted to 4x the final concentration in its -80°C POK2 Storage Buffer (the buffer POK2 is stored, in this case, the POK2 Desalting Buffer.). Since the POK2 Storage Buffer has glycerol, the 4x pre-dilutions were then snap frozen in liquid nitrogen and kept in liquid nitrogen until ready to use. For MAP65-3-mCherry, a similar pre-dilution 4x the final concentration was also prepared in MAP65-3 Desalting Buffer (Lysis Buffer, but without PMSF or Triton X-100 and with 5% glycerol), which also contains glycerol.

The flow cell with microtubules was mounted on either the *Shenlong* or *Aalo* setups and the TIRF plane was focussed. The channel was pre-equilibrated with 20 μl 1x Motility buffer and imaged as a control. Then, the final reaction mix (1x Motility buffer and 1x protein to 20 μl with PEM20 buffer, Table 4.3, 4.4) was prepared, mixed by pipetting and passed into the channel. To encourage the solution to pass

through the channel, a piece of filter paper was used at the exit point of the channel to create a capillary pull. The assay was thus set up as shown in Fig. 4.10. The sample was then immediately imaged for reference. For uniformity, the protein was allowed to bind microtubules for 10 min on the setup. After which, at least 10 images were acquired at 100 ms camera exposure and 5 % laser power for the 488 nm laser and and 1% for the 561 nm laser on *Shenlong* or 10% laser power on *Aalo*.

Table 4.3: Final reaction mix of *in vitro* microtubule binding assay with the POK2 tail.
The same recipe was used for all POK2 tail constructs, including the shorter POK2 tail constructs. The ionic strength of this recipe is ∼130 mN.

10x Motility buffer	2 μl
4x pre-diluted POK2 tail constructs in POK2 Storage Buffer	5 μl
PEM20 buffer	up to 20 μl
Total volume	20 μl

Table 4.4: Final reaction mix of *in vitro* microtubule binding assay with the POK2 tail and MAP65-3.
The same recipe was used for all POK2 tail constructs, including the shorter POK2 tail constructs. The ionic strength is estimated to be ∼170 mN.

10x Motility buffer	2 μl
4x pre-diluted POK2 tail construct in POK2 Storage Buffer	5 μl
4x pre-diluted MAP65-3-mCherry in MAP65-3 Desalting Buffer	5 μl
PEM20 buffer	up to 20 μl
Total volume	20 μl

4.5.9 *In vitro* microtubule binding assay - single molecule

Single molecule *in vitro* microtubule assays are similarly performed as for bulk assays. The only difference is the concentration of protein used. For eGFP-POK2$^{2083\text{-}2771}$, single molecule concentrations are around 1–5 nM. For experiments where only eGFP-POK2$^{2083\text{-}2771}$ was used, the protein was pre-diluted to 4x the final desired concentration in its own POK2 Storage Buffer before mixing to a final 1x concentration in Motility buffer as for bulk assays (Table 4.3). Time-lapse imaging was sampled at 100 ms unless stated otherwise.

For experiments with both eGFP-POK2$^{2083\text{-}2771}$ and MAP65-3-mCherry at single molecule conditions, both proteins were pre-diluted to 20x the final concentrations in POK2 Storage Buffer and MAP65-3 Desalting Buffer respectively. The proteins were mixed into the PEM20 buffer-based Motility buffer as in Table 4.5. For experiments which varied ionic strength, potassium chloride (KCl) was used as in Table 4.5.

4.5.10 Analyses

All initial measurements used to analyse the microscopy images and movies from *in vitro* microtubule assays were performed in FIJI [271] using macros I wrote. Measurements were then exported and post-processed in R, Python or Origin (Pro) (OriginLab Corp. USA). The following analyses were performed for the *in vitro* microtubule binding assays in bulk or single molecule conditions. The analysis performed for which type of assay is listed in the titles.

Table 4.5: Final reaction mix of *in vitro* microtubule binding assay with the POK2 tail at MAP65-3 single molecule conditions.
0.4, 0.6 or 0.8 μl 3 M KCl was used to obtain a final additional KCl concentration of 60, 90 and 120 mM. The resulting ionic strength of the buffer was then ∼130, 160, 190 mN respectively, where the buffer without additional KCl was at ∼70 mN ionic strength.

10x Motility buffer	2 μl
20x pre-diluted eGFP-POK2$^{2083\text{-}2771}$ in POK2 Storage Buffer	1 μl
20x pre-diluted MAP65-3-mCherry in MAP65-3 Desalting Buffer	1 μl
3 M KCl in deionised water	0, 0.4, 0.6 or 0.8 μl
PEM20 buffer	up to 20 μl
Total volume	20 μl

4.5.10.1 Microtubule binding rate - bulk

Using FIJI, segemented lines were drawn along the length of microtubules and saved as region of interests (ROIs). Microtubule ends, bundles or cross-overs were avoided. The raw integrated intensity of these lines were obtained. Then, these ROIs were moved to a nearby microtubule-absent region, where the raw integrated intensities of these lines were obtained as the background value. This background value is subtracted from the intensity values obtained along the microtubules. The background subtracted values are then divided against their respective lengths of microtubule measured. Protein binding to microtubule is thus defined as background subtracted intensity / microtubule length.

4.5.10.2 Landing rate - single molecule

First, kymographs were obtained by drawing segmented lines along the lengths of microtubules. In this case, lines were carefully traced from end-to-end along single microtubules that were not bundled with or crossing any other microtubule. Diffusive, stationary and mixed events that landed during the duration of the kymograph were marked with the point-tool in FIJI and saved as ROIs. Events that landed before the start of the kymograph were ignored. The number of diffusive, stationary or mixed traces was thus obtained and divided by the length of microtubule analysed, i.e. the width of the kymograph (in this case, the width is the distance axis, whereas the height is the time axis). Landing rate is thus defined as the number of traces / microtubule length.

To obtain the landing rate of the 'background', kymographs were obtained from lines drawn randomly in the background where microtubules are not present. Here, only immotile events where molecules stick to the surface could be observed. The number of events were thus marked and counted as before.

4.5.10.3 Interaction time - single molecule

Kymographs were drawn as for the landing rate analysis. In the kymographs, entire traces were traced manually using segmented lines. Lines were drawn carefully only for traces where the molecule appeared and disappeared, i.e. associated and dissociated from the microtubule within the kymograph, i.e. within the imaging duration. Hence, the interaction time analysis is inevitably an underestimation.

To account for short and long interaction times, time-lapse movies were sampled at 0.1, 0.5 and 1.0 s for a duration of 1, 5 and 10 min respectively (where every movie was imaged for a total of 600 frames). Since only the time is needed, it was not as important to trace the entire traces so carefully. It was however very important to mark the start and end of the traces accurately. The resulting (x,y) coordinates along the entire length of the trace was then exported and analysed using R, where the difference in the y axis (= time) was calculated as interaction time. In order ensure that only traces that associated and dissociated during the kymograph duration, traces were filtered such that ymin > 3 pixels and ymax < 600 pixels. Pixels were converted to time depending on the sampling intervals of 0.1, 0.5 or 1 s. The interaction times were then plotted in a survival plot and fitted with the sum of two exponentials in Origin (Pro) (OriginLab Corp. USA) by Dr. Serapion Pyrpassopoulos.

4.5.10.4 Intensity - single molecule

This analysis was done by Dr. Hauke Drechsler. Similarly to interaction time, diffusive and stationary traces in kymographs along entire microtubule lengths were traced, this time very carefully and faithfully. As occasionally, photobleaching of the traces occured, the different intensities were determined by eye as separate regions and traced separately. The background subtracted intensities were obtained as in Section 4.5.10.1. The distribution of the resulting mean background subtracted intensities (total intensity / number of pixels) were then plotted and fitted with multiple Gaussians using Origin (Pro) (OriginLab Corp. USA).

4.5.10.5 Photobleaching probability - single molecule

To account for photobleaching effects, kymographs from randomly chosen microtubules were drawn. All traces diffusive or stationary or mixed in the kymographs were traced, regardless of whether they associated or dissociated within or outside the duration of the kymograph to obtain the total interaction time. The number of bleaching events observed for these traces were counted and divded by the total interaction time. Bleaching probability was thus defined as the number of bleaching events / total interaction time (in frames).

4.5.10.6 Diffusion coefficient - single molecule

Single molecules in time-lapse imaging sampled at 100 ms were automatically tracked using FIESTA [259] with parameters listed in Table 4.6. The resulting tracks were then manually checked and edited for continuity (i.e., that single traces were joined by single tracks and not multiple tracks) and obvious mistakes (i.e., that fluorescent dirt flying too close was not tracked instead of the actual trace).

The (x,y) coordinates of the tracks were then exported and further analysed using R and Python. The traces were interpolated (necessary as some points were manually deleted when erroneously traced or when two tracks were joined as they belonged to the same trace, but FIESTA could not identify the connection). The traces were then rotated horizontal based on a linear region of the (x,y) points. This is possible because we assume one-dimensional diffusion, as the single molecules travel along

Table 4.6: Parameters used in FIESTA single particle tracking.

Parameters		Values
Tracking		Only Molecules
Threshold		Constant Intensity
	Height	0
	Fit(CoD)	0
	FWHM(Est.)	244 nm
	Border Margin	0 pixel
Filter for thresholding		average before
Tracking options		Molecules
Connecting	max. Velocity	1500 nm/s
	Verification Steps	2
	Weights	Position: 40%
		Direction: 40%
		Speed: 20%
	Use intensity to connect	Yes
Tracks	min. Length	4 frames
	max. Break	3 frames
	max. Angle	45°
Model		Symmetric 2D-Gaussian
	max. Number of functions	4
	Parameter	16

the microtubule, which at the diffraction limited resolution appears as a one-dimensional line. Hence, by rotating the (x,y) horizontal such that x is the displacement along the microtubule, then y is the tracking precision, and in principle this value should be very close to 0. The displacement steps for the x values are then calculated for different lag times, $\tau = 0.1$ to 2.0 s for eGFP-POK2$^{2083\text{-}2771}$ data and $\tau = 0.1$ to 1.0 s for eGFP-POK2$^{2083\text{-}2771}$ and MAP65-3-mCherry data. The displacement steps are then plotted as a distribution. The distributions were then fitted using Gaussian Mixture Models with K-means clustering for initialisation in a custom Python script written by Laura Muras. To assess the goodness of fit and decide on the optimal number of Gaussians, the Akaike and Bayesian information criteria (AIC, BIC) were used. The largest drop in IC values were used to settle on the number of Gaussians to fit the data with. The resulting variances of the Gaussians were plotted against lag time, τ to obtain mean squared displacement (MSD) plots. The data could then be fitted with a regression line, described by the one-dimensional diffusion equation $MSD = 2D\tau + \varepsilon^2$ where D is diffusion coefficient and ε is tracking precision [26]. Diffusion coefficient, D is thus calculated from the half-slope of the regression line.

Part III

Results & Discussion

Chapter 5

Results

5.1 The POK2 tail is difficult to express and purify.

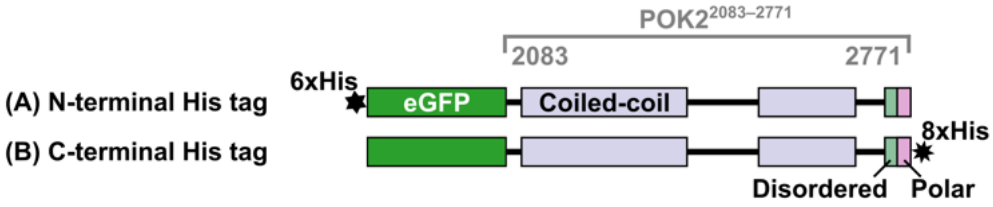

Figure 5.1: Scheme depicting POK2 tail constructs.
POK2$^{2083\text{-}2771}$ was tagged N-terminally with eGFP **(A)** and C-terminally **(B)** with His-tags. Protein domain annotations are from UniProt. For EMBOSS charge, AIUpred and DeepCoil2 predictions, see Fig. 3.5.

In order to investigate the mechanism of cell division zone (CDZ) recruitment and subsequent maintenance, the tail of the phragmoplast orienting kinesin 2 (POK2) was purified for *in vitro* studies. Since the aa2083–2771 region of POK2 was sufficient for *in vivo* CDZ localisation and retention [118], this same region was used for purification and *in vitro* experiments. A construct with an N-terminal 6xHis and eGFP tag, 6xHis-eGFP-POK2$^{2083\text{-}2771}$ (Fig. 5.1A), was initially designed and expressed in *Saccharomyces cerevisiae* THY.AP5 cells by Dr. Arvid Herrmann and purified by Dr. Mayank Chugh [54] for preliminary experiments. The expression of this construct however was not reliable and resulted in sequestration of the protein into inclusion bodies. Although efforts to optimise the cell lysis procedure helped retain some protein in the supernatant, the yield remained less than promising (Figure 5.2A).

Proteins in inclusion bodies can be recovered by unfolding and refolding experiments, however as the function of the POK2 tail was not yet known, I would not have been able to assess protein functionality if I were to denature and refold the protein. Hence, I decided to try several other protein expression systems simultaneously hoping one of them have improved solubility. One system was the *in vitro* cell free protein expression (CFPE) system (cell free protein expression) that uses evacuolated *Nicotania*

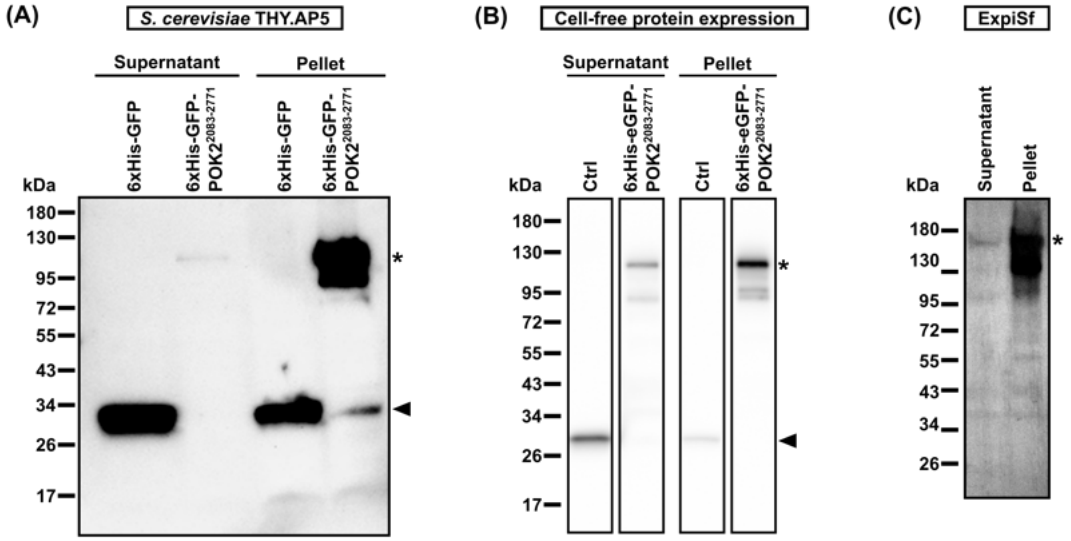

Figure 5.2: Western blots with anti-GFP of 6xHis-eGFP-POK2$^{2083\text{-}2771}$ from different expression systems. 6xHis-eGFP-POK2$^{2083\text{-}2771}$ was expressed and lysed from from **(A)** yeast *Saccharomyces cerevisiae* THY.AP5 cells, **(B)** the *in vitro* cell-free protein expression system and **(C)** the baculovirus/ExpiSf expression system. Samples were clarified by centrifugation after lysis. The resulting supernatant and pellet fractions were separately loaded into an SDS-PAGE gel. Asterisks, predicted 6xHis-eGFP-POK2$^{2083\text{-}2771}$ sized at around 110 kDa; arrowheads, predicted size of GFP at around 26.9 kDa.

tobaccum BY-2 cell lysates, and the other was the baculovirus/ExpiSf insect cell system (Gibco, 15829126).

Expression with the CFPE system was quite promising as preliminary experiments estimate better protein retention in the supernatant (Fig. 5.2B, C), as compared with yeast expresion. While CFPE actually produced the most soluble protein, the baculovirus/ExpiSf system was the easiest to replicate, upscale and, therefore, reproduce. Hence, I went ahead to use and optimise the baculoviurs/ExpiSf system.

When the 6xHis-eGFP-POK2$^{2083\text{-}2771}$ construct (Table 7.3 plasmid #S42, 5.1A) was expressed in the baculovirus/ExpiSf system, it produced several degradation products (indicated as *d* in Fig. 5.3A). To reduce the presence of such degradation products, a construct with a C-terminal 8xHis tag was instead prepared (Table 7.3 plasmid #S59, Fig. 5.1B). Indeed, this construct retained less degradation products (Fig. 5.3B). This eGFP-POK2$^{2083\text{-}2771}$-8xHis construct, used in all following experiments, was expressed and extracted from ExpiSf insect cells, purified with Cobalt-His affinity chromatography and cleaned by desalting. The predicted size of the protein is 110 kDa, but runs higher in SDS-PAGE at slighly less than 130 kDa (Fig. 5.3B, asterisk). The protein was verified further with anti-GFP and anti-His western blotting (Fig. 5.4) and mass spectrometry (performed by Dr. Katharina Zittlau, Fig. 5.5). However, yield of the protein was low and only had 100 μg purified protein per 30 ml of insect cell culture at a concentration ranging between 500–800 nM. Attempts to concentrate the protein using Amicon Ultra-15 Centrifugal Filter Units (Merck, UFC910008) were unsuccessful as the the

protein stuck to the filter membrane. Nevertheless, the concentrations of eGFP-POK2$^{2083–2771}$-8xHis (hereafter simply eGFP-POK2$^{2083–2771}$) after purification were sufficient for subsequent assays.

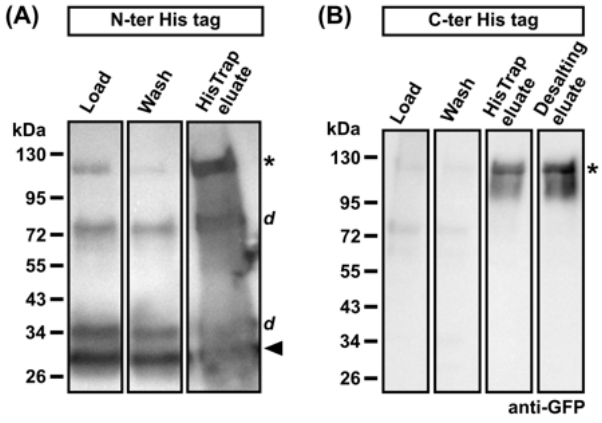

Figure 5.3: Western blots of POK2 tail constructs expressed from the baculovirus/ExpiSf system.
N- **(A)** and C-terminally **(B)** His-tagged eGFP-POK2$^{2083-2771}$ load (flow-through of the supernant loaded onto the column after lysis and clarification), wash (flow-through when washing the column to remove unspecific binding) and eluate (final elution product from either anti-His affinity chromatography or desalting). Design of constructs follow Fig. 5.1.

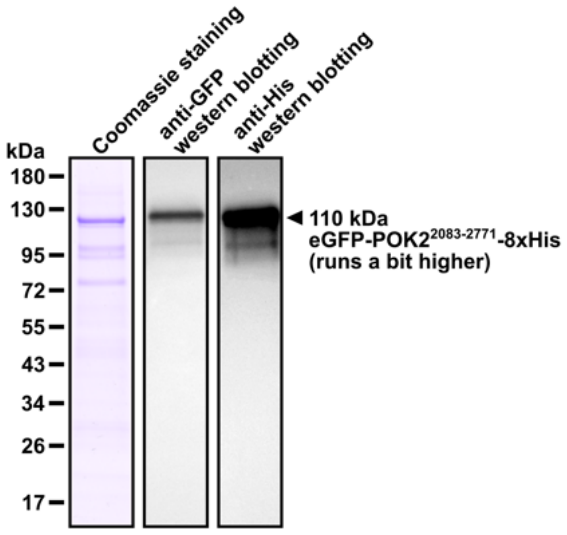

Figure 5.4: Coomassie staining and western blotting of purified eGFP-POK2$^{2083-2771}$ -8xHis with anti-GFP and anti-His.
eGFP-POK2$^{2083-2771}$-8xHis was purified by Cobalt-His affinity chromatography followed by desalting. The predicted size of the protein is 110 kDa, but runs a bit higher (arrowhead).

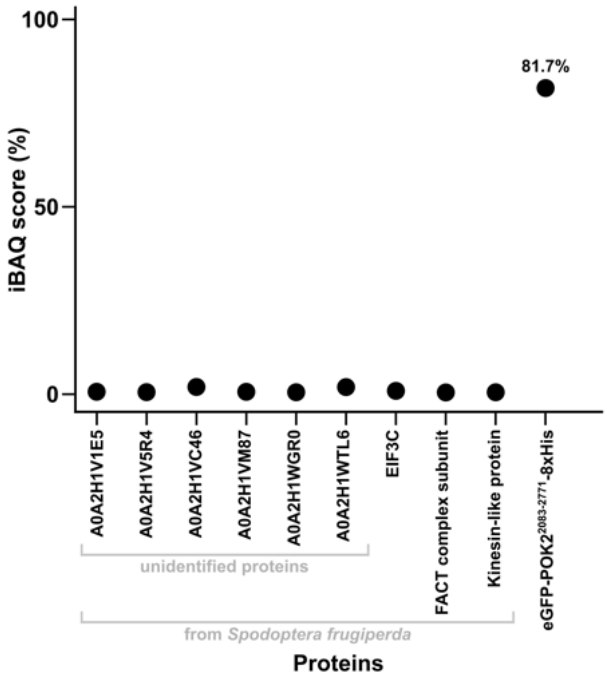

Figure 5.5: Protein iBAQ score for purified POK2 tail from mass spectrometry.
Graph showing iBAQ (intensity-based absolute quantification) score normalised against total iBAQ values from mass spectrometric analysis of eGFP-POK2$^{2083–2771}$-8xHis. iBAQ is the sum of all peptide abundances divided by the number of theoretically obtainable peptides by Trypsin digest. The mass spectrometry was performed by Dr. Katharina Zittlau from the Proteome Centre from a sample ran shortly (5 min) in an SDS-PAGE gel. The proteins shown are those only with a iBAQ score $>$ 0.5 %. The mass spectrometry data was then screened against the protein sequence of recombinant eGFP-POK2$^{2083–2771}$-8xHis and the *Arabidopsis thaliana* and *Spodoptera frugiperda* databases. The purified protein was found with 81.7% iBAQ score and determined to be the desired recombinant eGFP-POK2$^{2083–2771}$-8xHis protein.

5.2 The POK2 tail binds microtubule *in vitro*.

The region aa2083–2771 of the POK2 tail has been shown to be sufficient and necessary for CDZ deposition and residence [118]. However, initial deposition is a preprophase band (PPB) microtubule-dependent process [118]. Since the canonical microtubule binding site of POK2 lies in its N-terminal region, i.e. its kinesin motor domain, it was unclear how the POK2 tail could be recruited by the PPB. Several kinesins have been shown to possess secondary microtubule binding sites in their tails (see Section 3.1.2.4), which raises the possibility of the POK2 tail doing the same for PPB microtubule recruitment.

To test if the POK2 tail could also bind microtubules, microtubule binding assays at the mid-nanomolar range with the purified eGFP-POK2$^{2083\text{-}2771}$ were performed. As the protein was purified in a high salt buffer but had low yield, a lower salt PEM20 buffer was used in the Motility Buffer rather than the conventional BRB80, i.e. PEM buffer. Even with these adjustments, the highest concentration of eGFP-POK2$^{2083\text{-}2771}$ usable was 200 nM at $\sim$130 mN ionic strength.

0 to 200 nM eGFP-POK2$^{2083\text{-}2771}$ were mixed with surface-immobilised GMPCPP- and paclitaxel-

stabilised rhodamine-labelled microtubules and imaged with a single-color TIRF microscopy (Fig. 5.6). Both the eGFP and rhodamine were excited by the 488 nm laser on the *Aalo* setup, which unfortunately does not have a band pass filter and results in some bleed-through from the green to the red channel but not vice versa (especially at 150 and 200 nM, Fig. 5.6, two bottom-most rows). As the concentration of eGFP-POK2$^{2083\text{-}2771}$ increased, the eGFP signals started to resemble lines. These lines correlated with microtubules visualised in the rhodamine channel, suggesting that the POK2 tail binds microtubules on its own in a concentration-dependent manner.

As a readout of microtubule binding, the intensity of eGFP signals along the length of the microtubules were measured and plotted against the eGFP-POK2$^{2083\text{-}2771}$ concentrations used (Fig. 5.7). The data was fitted with a Hill equation with a Hill coefficient, $n_H = 4.6 \pm 0.8$ and dissociation constant, $K_d = 106 \pm 4$ nM. The $n_H > 1$ suggests that eGFP-POK2$^{2083\text{-}2771}$ binds microtubules in a cooperative manner. However, even at 50 nM, eGFP-POK2$^{2083\text{-}2771}$ large clusters were visible and seen to bind microtubules as well. The measurements for microtublue binding includes these large clusters. Hence, the n_H is an overestimation of the binding cooperativity of eGFP-POK2$^{2083\text{-}2771}$. Nevertheless, these results show that the POK2 tail is capable of binding microtubules on its own.

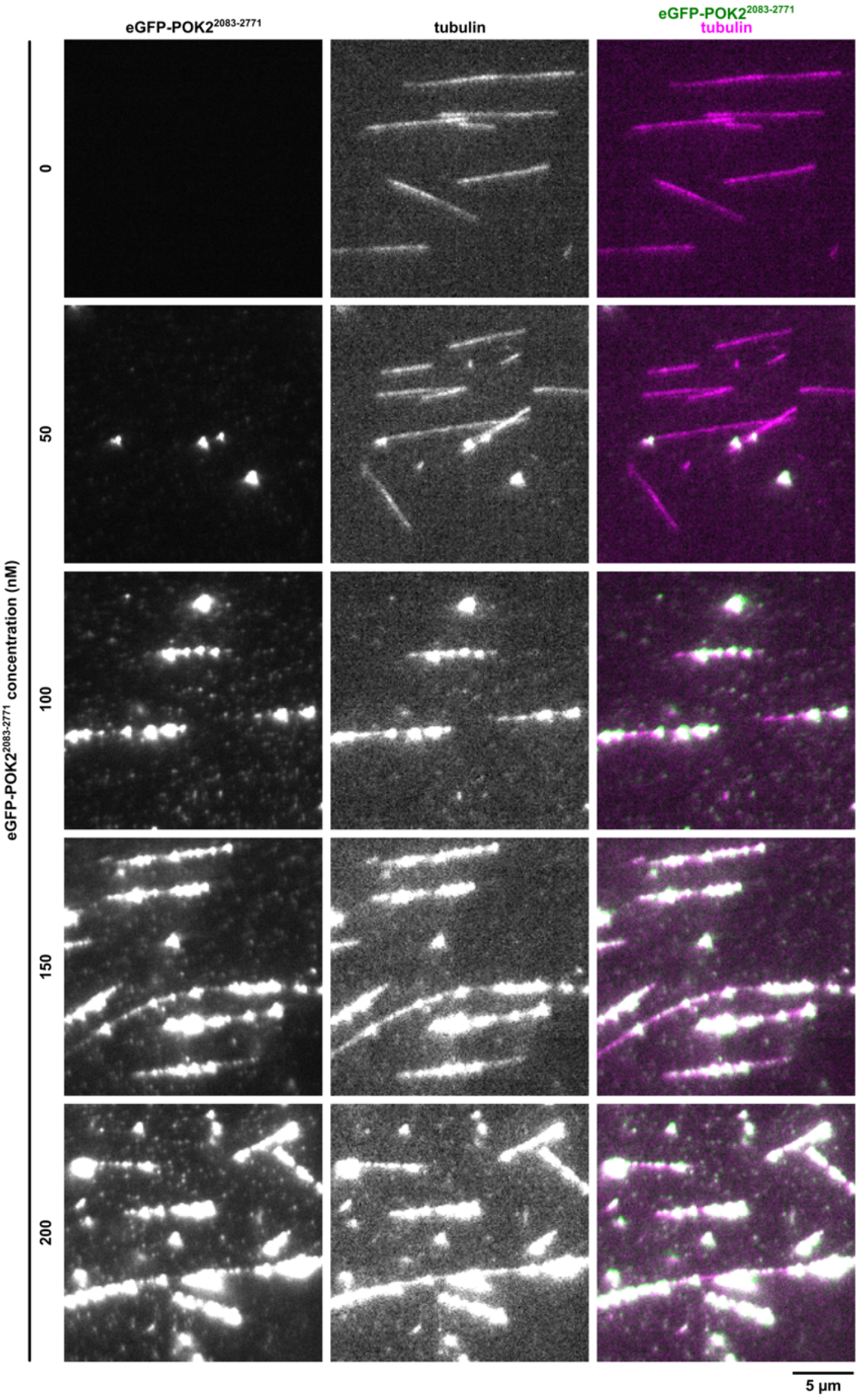

Figure 5.6: The POK2 tail binds microtubules directly.
TIRF microscopy image of eGFP-POK2$^{2083-2771}$-8xHis of different concentrations binding to double-stabilised rhodamine labelled microtubules. Note the bleed-through of eGFP signal into the rhodamine channel especially at 150 and 200 nM.

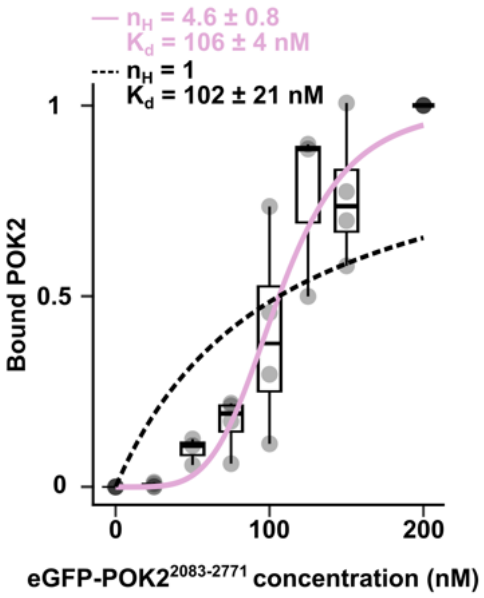

Figure 5.7: Graph of POK2 tail microtubule binding against concentration.
Background subtracted intensities of eGFP signals along the length of microtubules are plotted against concentration of eGFP-POK2$^{2083-2771}$. The data is normalised to the highest intensity value for each experimental repeat for easier comparison. The data altogether is then fitted with a Hill-equation (pink line) with a Hill coefficient, n_H of 4.6 $\pm$ 0.8 and dissociation constant of K_d = 106 $\pm$ 4 nM. For reference is a fit with a Michaelis-Menten equation (black dotted line) which is a Hill-equation of n_H = 1 which gives a K_d = 102 $\pm$ 21 nM. Each point, mean value from a single independent experimental repeat; horizontal line in boxplot, median; boxplot whiskers, 1.5 IQR.

5.2.1 The POK2 tail forms large clusters in a concentration dependent manner.

Since large clusters of eGFP-POK2$^{2083-2771}$ could be seen to bind microtubules especially at concentrations above 100 nM, the nature of these clusters were assessed with a sedimentation assay. eGFP-POK2$^{2083-2771}$ was allowed to incubate at room temperature for 10 min in the same buffer used in the *in vitro* microtubule binding assays, and then centrifuged at 20 krcf for 20 min to obtain the pellet and supernatant fractions. The input, supernatant and pellet fractions were then resolved with an SDS-PAGE gel (Fig. 5.8). Interestingly, eGFP-POK2$^{2083-2771}$ was always present in both the supernatant and pellet fractions with a slight increase in the pellet fraction as the concentration of eGFP-POK2$^{2083-2771}$ increased. As 20 krcf would allow large aggregates to sediment, these species of eGFP-POK2$^{2083-2771}$ in the pellet are likely large aggregates. This would indicate that there are aggregates of eGFP-POK2$^{2083-2771}$ present. On the other hand, the results also indicate that there is definitely a soluble fraction of eGFP-POK2$^{2083-2771}$ also present in the solution. However, it is not possible to conclude whether or not these aggregates are able to bind microtubules as well and whether these large aggregates are necessarily the large clusters seen to bind microtubules in Fig. 5.6.

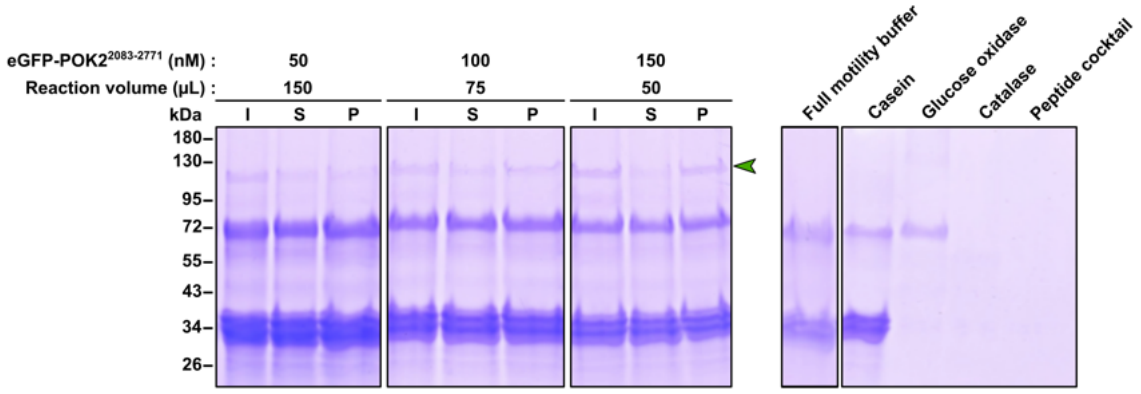

Figure 5.8: The POK2 tail forms large clusters.
Image of Coomassie stained SDS-PAGE gel of input (I), supernatant (S) and pellet (P) fractions from a sedimentation assay. The amount of eGFP-POK2$^{2083-2771}$ used was constant in the different conditions, but concentation was varied by varying the reaction volume. All of the protein was loaded into an SDS-PAGE gel after TCA precipitation. The components of the buffer used, i.e. the motility buffer, were also loaded separately (right) to easily distinguish the eGFP-POK2$^{2083-2771}$ band from the bands from the motility buffer. Green arrowhead, predicted band size of eGFP-POK2$^{2083-2771}$.

5.3 Single POK2 tail molecules diffuse on the microtubule.

The sedimentation assays and *in vitro* microtubule binding assays hint at a tendency for increased clustering as concentrations of eGFP-POK2$^{2083-2771}$ increases. Hence, to further investigate the microtubule binding activity of eGFP-POK2$^{2083-2771}$ without the influence of these clusters, *in vitro* microtubule binding assays with eGFP-POK2$^{2083-2771}$ at single molecule conditions were performed. The single molecule concentration is manually determined by trial-and-error, using a dilution series until a concentration where single, discernible and traceable signals on the microtubule could be obtained. The landing rate can be subject to great variation due to pipetting errors or variations between aliquots of proteins or variabilities in buffer components, which become significant when using single molecule concentrations. For eGFP-POK2$^{2083–2771}$, single molecule concentrations were around 1 to 5 nM in a PEM20-based buffer of ∼130 mN ionic strength. This single molecule concentration value could also be subject to change depending the protein purification batch and the researcher performing the experiment. Nonetheless, for the following analysis shown in this section, all experiments were performed using 2 nM eGFP-POK2$^{2083–2771}$.

5.3.1 Landing rate

In order to better assess the behaviour of eGFP-POK2$^{2083-2771}$ on microtubules, lines along the length of the microtubule were drawn and kymographs of these lines were obtained using FIJI [271] (Fig. 5.9A). From the kymographs, immotile traces and traces that moves back and forth indicating stationary and diffusive movement respectively could be observed. About 4% of these traces were mixed and switched between diffusive and stationary modes (Fig. 5.9A, white arrowhead; Fig. 5.9C). The landing rate of diffusive events, which were the most often seen type of landing event on microtubules, were 0.16 ± 0.01 $\mu m^{-1} \cdot min^{-1}$ (mean ± SE) (Fig. 5.9B).

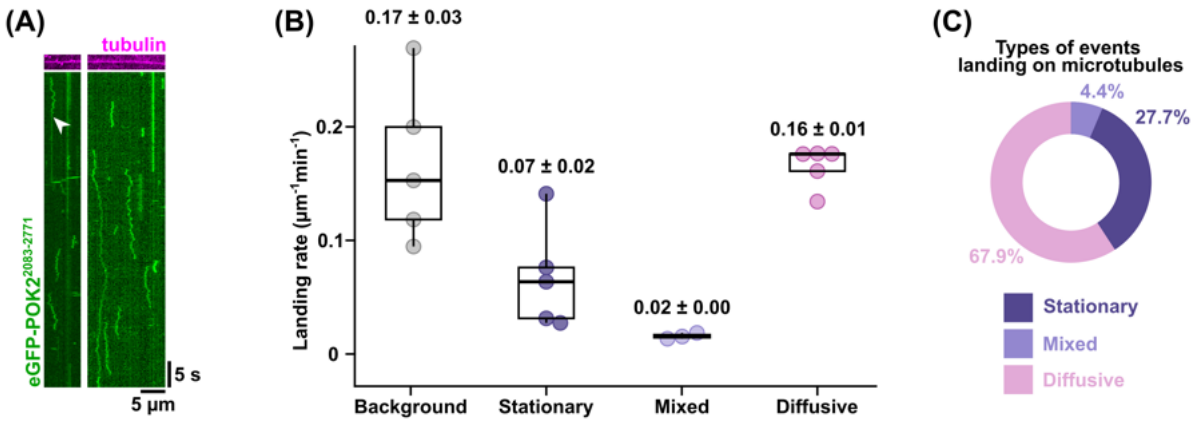

Figure 5.9: POK2 tail diffuses on microtubules.
(A) Kymograph of TIRF time-lapse imaging sampled at 0.1 s of single molecule (2 nM) eGFP-POK2$^{2083–2771}$ (green) interaction on 10% rhodamine-labelled double-stabilised microtubules (magenta). Diffusive and stationary traces are observed. White arrowhead, mixed diffusive and stationary behaviour. **(B)** Landing rate of eGFP-POK2$^{2083–2771}$ (2 nM) events on the microtubule as in (A) (colored data points). Background landing rate are events counted from kymographs drawn from lines in areas without microtubules. Data points are mean values of experimental repeats, with each experiment consisting of at least 10 randomly chosen kymographs along microtubules or in the background. Horizontal lines in boxplot, median; whiskers, 1.5 IQR. **(C)** Percentage of each type of landing event that were observed to land on microtubules. Data is from (B).

5.3.2 Interaction time

Next, to obtain the duration of eGFP-POK2$^{2083–2771}$ binding events on microtubules, time-lapse movies were sampled at 0.1, 0.5 and 1 s for a duration of 1, 5 and 10 min respectively. The different sampling time intervals and recording durations were varied to account for short and long binding events. Using FIJI [271], binding events that landed and dissociated within a kymograph were manually tracked. As a control, kymographs drawn from randomly selected areas where there were no microtubules were tracked. In these kymographs, there were only stationary traces, where eGFP-POK2$^{2083–2771}$ or fluorescent dirt landed on the surface. As mixed traces only account for $< 5\%$ (Fig. 5.9C) of the traces, there were insufficient statistics to obtain interaction times for mixed traces and were omitted from the analysis.

Diffusive traces

The survival plots of the interaction times of diffusive eGFP-POK2$^{2083–2771}$ traces were plotted and fitted with the help of Dr. Serapion Pyrpassopoulous with the sum of two exponential fits (Fig. 5.10). Each exponential fit had two time constants, t_1 and t_2. By keeping certain time constants fixed while performing the fitting, three time constants were obtained overall = $\sim$ 0.9, 5.2, 42 s (Table 5.1).

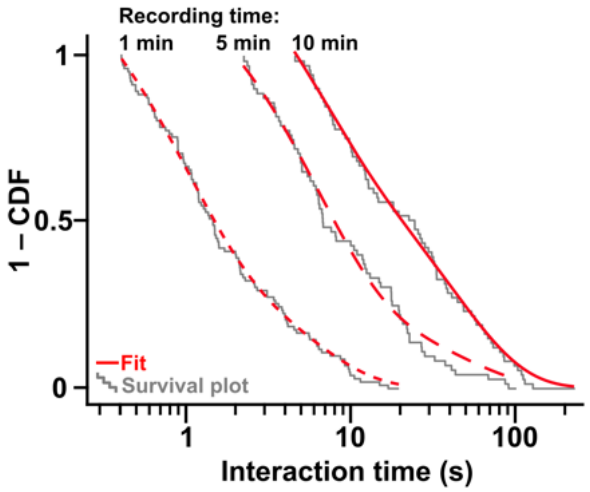

Figure 5.10: Interaction times of the diffusive POK2 tail.
Survival plots (gray lines) of the interaction times of diffusive eGFP-POK2$^{2083\text{-}2771}$ traces measured from time-lapse movies sampled at 0.1, 0.5 and 1 s for 1, 5 and 10 min respectively. The survival curves were fitted with a sum of two exponentials (red lines), given by the equation: $A_1 e^{-\frac{x-t_0}{t_1}} + A_2 e^{-\frac{x-t_0}{t_2}}$, where A is amplitude, t are time constants, with t_0 denoting the respective smallest time interval. Each fitting resulted in two time constants, with an overall three time constants. Please see Table 5.1 for details.

Table 5.1: Interaction times of single molecule POK2 diffusive events.
Survival plots of interaction time of diffusive eGFP-POK2$^{2083–2771}$ traces (Fig. 5.10) were fitted with a sum of two exponentials. The fitting equation is given as: $A_1 e^{-\frac{x-t_0}{t_1}} + A_2 e^{-\frac{x-t_0}{t_2}}$, where A is amplitude, t are time constants, with t_0 denoting the respective smallest time interval. Overall, three time constants, $t_{a,b,c}$ were obtained with two time constants per recording time and time interval. Additionally in the table, t_{total} denotes recording time, Δt denotes time interval, N is the number of traces, R^2 is the R-squared value of the fitting. Asterisk indicates time constants that were fixed during fitting. Time constants and amplitudes are given ± SE.

t_{total}	Δt	N	R^2	t_a	A_a	t_b	A_b	t_c	A_c
1 min	0.1 s	103	0.997	0.8 ± 0.05 s	0.58 ± 0.03	5.2 ± 0.4 s	0.40 ± 0.21		
5 min	0.5 s	73	0.990			6.0 ± 0.3 s	0.70 ± 0.02	*42.7 s	0.30 ± 0.02
10 min	1.0 s	74	0.996			*5.3 s	0.30 ± 0.02	42 ± 1 s	0.70 ± 0.01

Stationary and background traces

Meanwhile the distribution of interaction times of stationary traces were not distinguishable from that of background traces (Fig. S5.11). Please be reminded that background traces are stationary events that were tracked from kymographs from randomly drawn lines in areas without microtubules. Stationary traces are immotile binding events tracked from kymographs from lines drawn along randomly chosen microtubules. The fact that stationary and background traces were indistinguishable by their landing rate suggests that eGFP-POK2$^{2083\text{-}2771}$ interacted with microtubules to the same degree as to the surface. Hence, the events seen from kymographs along microtubules could only be on the surface, just in proximity of the measured microtubule. With the current data, it is not possible to reliably conclude whether or not eGFP-POK2$^{2083–2771}$ binds microtubules in a stationary manner.

A note on bleaching probability

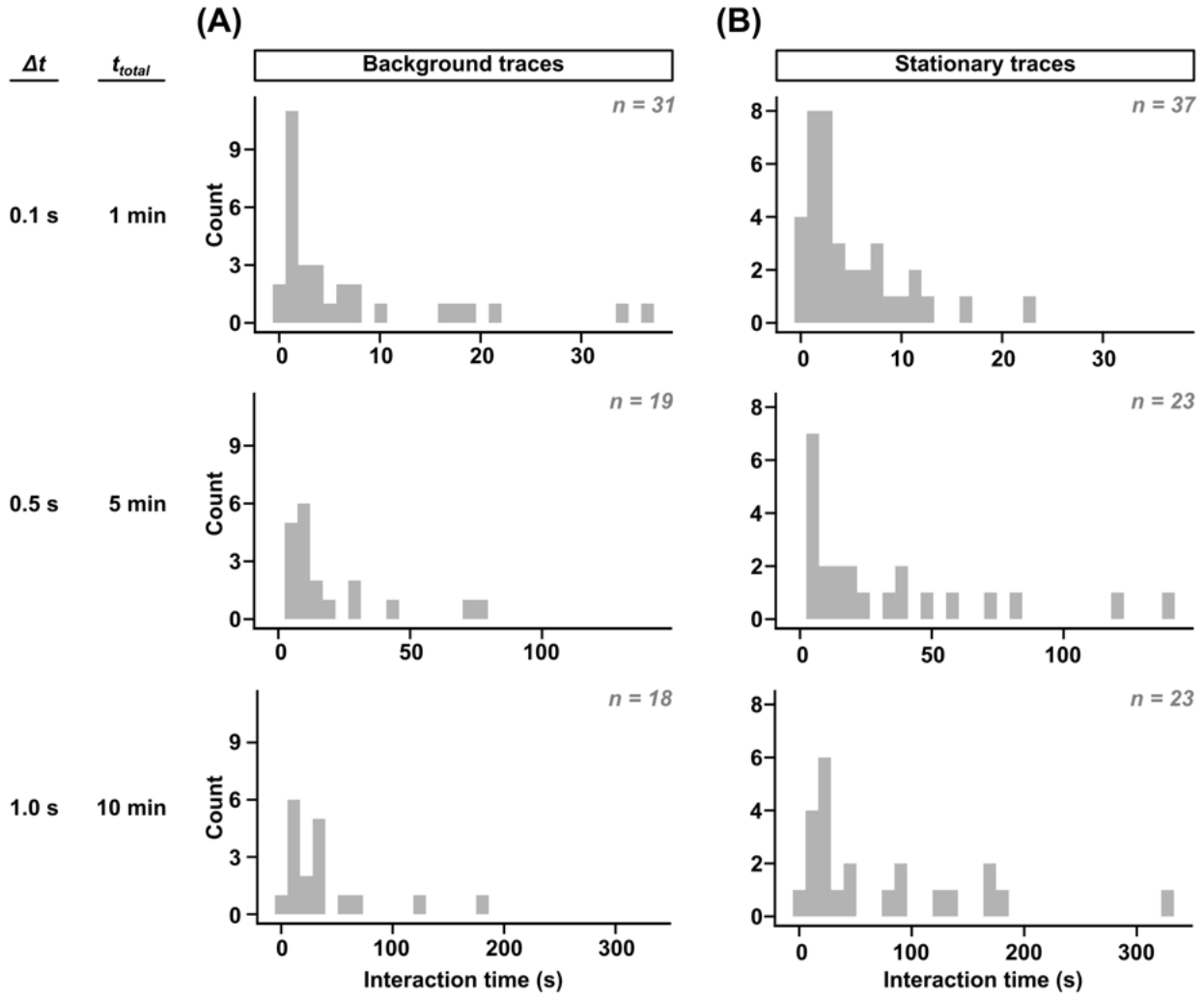

Figure 5.11: Interaction times of background and stationary traces are indistinguishable.
Distribution of interaction times of background **(A)** and stationary **(B)** events. Background events are stationary events tracked from kymographs from lines randomly drawn in an area absent of microtubules. Stationary events are stationary events tracked from kymographs from lines drawn along randomly chosen microtubules. Δt, sampling time interval; t_{total}, total recording time.

In the assay, anti-fade (glucose oxidase, catalase, D-glucose) is included to reduce photobleaching. Nevertheless, during time-lapse imaging, bleaching events do occasionally occur and would be impossible to distinguish from true dissociation events. The bleaching probability was estimated by dividing the number of times a bleaching event was observed over the total interaction time. The total interaction was measured for diffusive and stationary traces on all observable microtubules in a time-lapse movie and was irrespective of whether the molecules associated or dissociated during the movie. From this analysis, it was estimated that one bleaching event occurs on average after $\sim$670 frames, while each time-lapse movie comprises of only 600 frames. Additionally, interaction time in Fig. 5.10 & 5.11 was measured only from traces that landed on and dissociated from the microtubule within the time-lapse movie, thus these traces were always less than 600 frames long. Hence interaction time is unlikely to be influenced heavily by photobleaching.

5.3.3 Diffusion coefficient

While the stationary traces are difficult to reliably consider as true binding events, the diffusive traces can only be true events as diffusion of eGFP-POK2$^{2083–2771}$ in a straight line only ever occurs on a microtubule. Diffusion of eGFP-POK2$^{2083–2771}$ in the background where there are no microtubules does occur, but never in a straight line.

To determine the extent of diffusive ability, the diffusive traces were tracked automatically with FIESTA [259]. The resulting traces' (x, y) coordinates were exported for post-processing using R and Python (see Materials & Methods, Section 4.5.10.6 for details). As an internal control, stationary traces were also tracked and expected to produce a diffusion coefficient of 0. From the (x, y) coordinates, displacement steps for lag times, τ = 0.1–2.0 s at 0.1 s increments were calculated. Akaike and Bayesian information criterions (AIC, BIC) were used to determine the number of Gaussians that best fit the distributions for each lag time. The best improvement in AIC and BIC was from one to two Gaussians (Fig. 5.12A), indicating that two Gaussians best described the distribution. Subsequently, each displacement step distribution for each τ was fitted with two Gaussians (Fig. 5.12B, S7.1). The variances of the Gaussians were plotted against their respective lag times, τ (Fig. 5.12C). The larger and smaller variances were fitted with a regression line assuming two-dimensional diffusion, *variance* = $2D\tau + \varepsilon^2$, where D is the diffusion coefficient and ε is the tracking precision. The half-slope of the regression lines gives the diffusion coefficients, $D = 0.03 \pm 0.00\ \mu m^2 \cdot s^{-1}$ and $0.000 \pm 0.000\ \mu m^2 \cdot s^{-1}$. The former D value represents the diffusive portion and the latter D is the internal control value for the stationary traces. The Gaussian fitting and information criteria estimations were performed in Python, with a custom script written by Laura Muras.

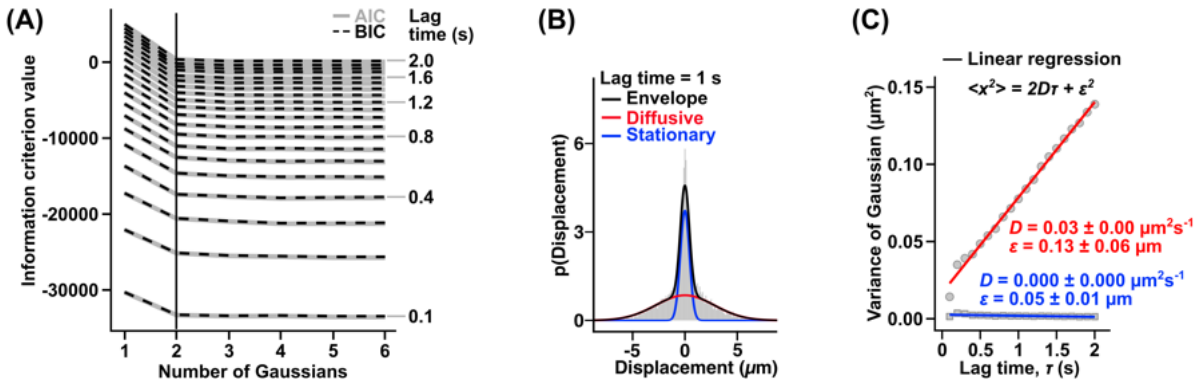

Figure 5.12: Diffusion coefficient of the POK2 tail.
(A) Akaike and Bayesin information criterions (AIC in gray lines, BIC in black dashed lines) calculated for one to six Gaussians fitted to distribution of displacement steps for lag times, τ = 0.1 to 2.0 s for every 0.1 s. The distributions are shown in Fig. S7.1. The largest drop in ICs is from one to two Gaussians (vertical black line). **(B)** Distribution of displacment step of a representative lag time, τ = 1.0 s fitted with two Gaussians. The assignment of diffusive and stationary populations are based on (B). **(C)** Graph of the variance, i.e. the squared standard deviation of individual Gaussians versus the lag time, τ. The larger and smaller variance values are fitted separately with regression lines, *variance* = $2D\tau + \varepsilon^2$, where D is the diffusion coefficient, when assuming 2-dimensional diffusion. ε denotes the tracking precision. The respective values for D and ε is given ± SE.

5.3.4 Intensity and oligomeric state

Single molecule TIRF assays

Dr. Hauke Drechsler analysed the diffusive and stationary traces on microtubules for their intensities and plotted their distributions (Fig. 5.13). The intensity distributions were described by two Gaussians, with peaks at 21 ± 1 and 50 ± 3 a.u.. The former and latter values likely correspond to monomeric and dimeric fluorescence intensities, suggesting that eGFP-POK2$^{2083–2771}$ exists at least as a dimer on the microtubule at single molecule concentrations. Occasionally trimeric and tetrameric species were observed (Fig. 5.14A, *top right*), but were not frequent enough to constitute a significant peak in the distribution. Moreover, fluorescence intensity loss of photobleaching events indicated that photobleaching step size corresponds roughly to the intensity of the first peak in the intensity distribution (Fig. 5.13, 5.14B), further supporting the 21 ± 1 a.u. peak as the intensity of a single eGFP.

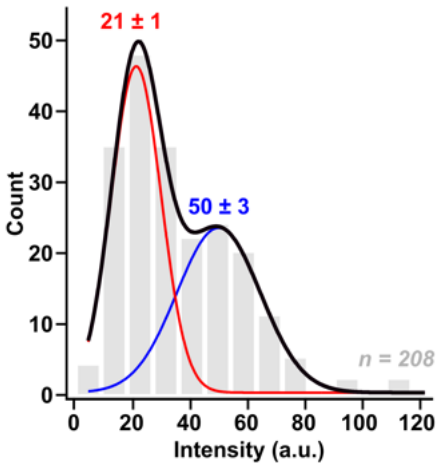

Figure 5.13: The POK2 tail is likely dimeric.
(A) Distribution of mean intensities of diffusive and stationary traces from kymographs of single molecule eGFP-POK2$^{2083-2771}$. Red and blue, Gaussian fits; Black line, envelope; red and blue numbers indicate mean peak intensity values ± SE. **(B)** Fluosresence loss during photobleaching of eGFP-POK2$^{2083-2771}$ diffusive and stationary particles. Square, mean; whiskers, 1.5 IQR. Compare with (A), see also Fig. 5.14.

Mass photometry

Another method to obtain information on the oligomeric state of proteins in single molecule conditions is with mass photometry. This method leverages the phenomenon where proteins scatter light proportionally to their mass. Using a mass standard to calibrate the scattered light, the mass of a protein or protein species can then be back-calculated using the light it scatters. For these experiments, the mass photometry system, OneMP (Refeyn Inc.) in the research group of Dr. John Weir at the Friedrich Miescher Laboratory at the Max Planck Institute of Biology, Tübingen was used.

Unfortunately, measurements with this purification of eGFP-POK2$^{2083–2771}$ was not reliable. Peaks that roughly correspond to the predicted monomeric and dimeric eGFP-POK2$^{2083–2771}$ size, ∼110 and 220 kDa respectively, were observed for 10 and 20 nM eGFP-POK2$^{2083–2771}$ diluted in PEM buffer (Fig. 5.15). However, as a control, the POK2 Storage Buffer was also measured and produced peaks at 60 and 110 kDa as well. This is especially concerning and this 60 and 110 kDa overlaps exactly the

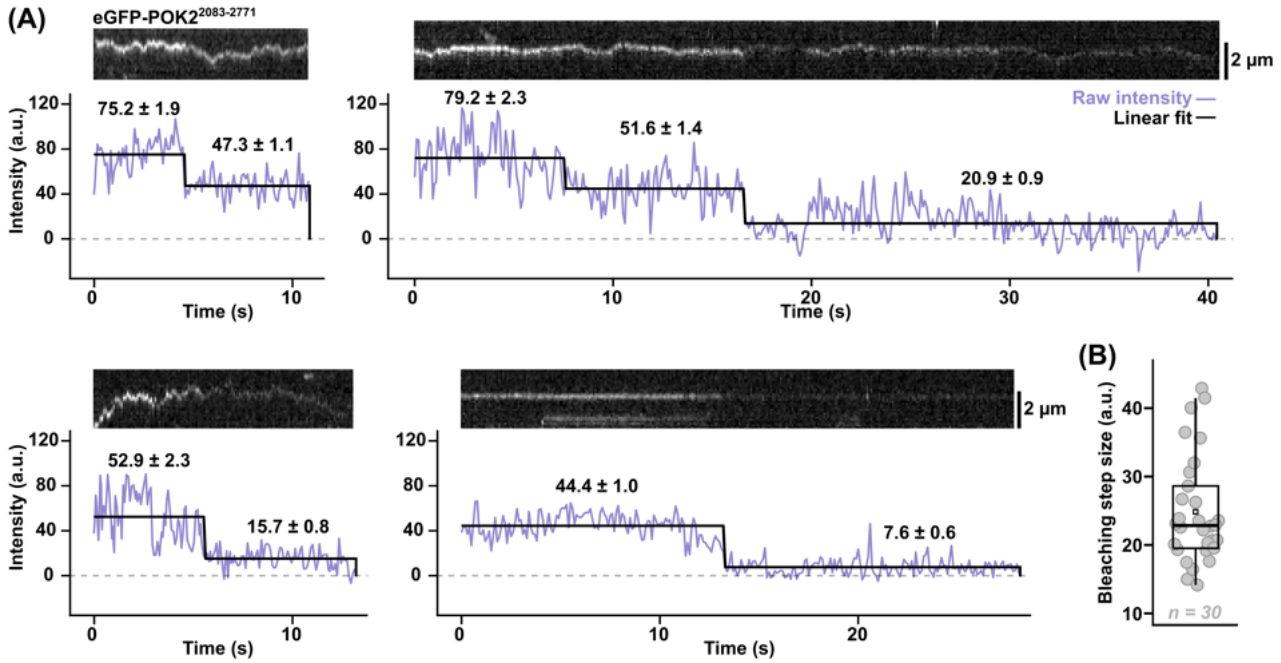

Figure 5.14: The POK2 tail is likely dimeric.
(A) Example intensities of diffusive and stationary eGFP-POK2$^{2083-2771}$ that underwent photobleaching. Lilac lines, background subtracted raw values; black lines, sections of the data sectioned by eye, fitted with a linear regression with slope = 0; mean values are given ± SE. **(B)** Fluoresence loss during photobleaching of eGFP-POK2$^{2083-2771}$ diffusive and stationary particles. Square, mean; whiskers, 1.5 IQR. Compare with Fig. 5.13.

110 kDa monomeric peak expected for eGFP-POK2$^{2083–2771}$. Hence, from these experiments it was not possible to reliably conclude anything for the eGFP-POK2$^{2083–2771}$ measurements, as the internal control itself had concerning peaks.

While having a separate independent technique to verify the oligomeric state of eGFP-POK2$^{2083–2771}$ would have been valuable, the intensity analysis of the single molecule eGFP-POK2$^{2083–2771}$ traces from *in vitro* microtubule binding experiments with TIRF were nonetheless sufficient to conclude that the POK2 tail exists at least as dimeric species.

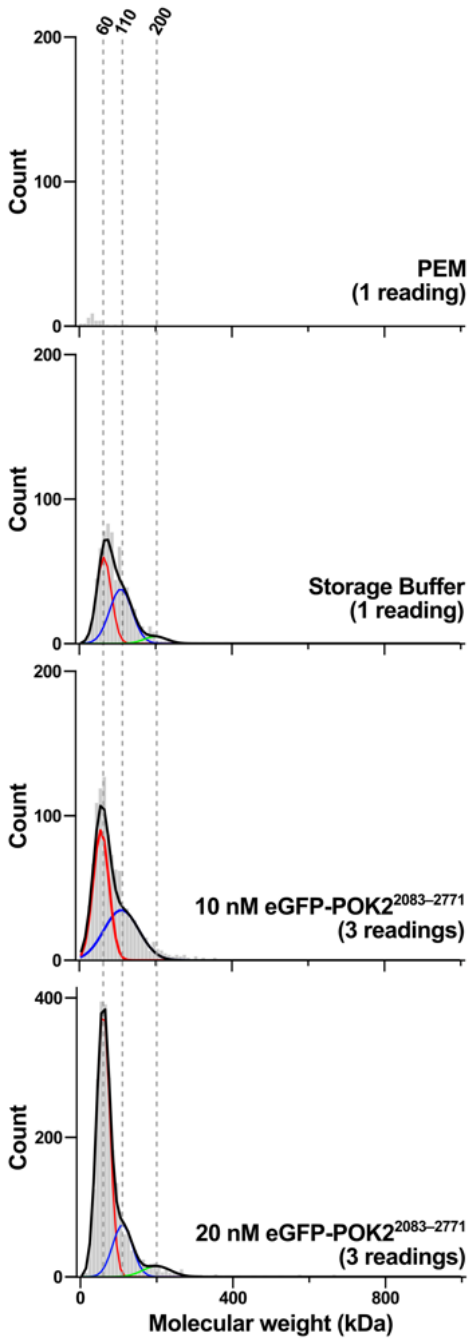

Figure 5.15: Preliminary mass photometry measurements with POK2 tail.
Measurements were performed in PEM buffer, which produces very little signal (top graph). As a control, the POK2 Storage Buffer was also measured, but produced a peak that resembles the peaks with 10 and 20 nM eGFP-POK2$^{2083–2771}$. For PEM buffer and POK2 Storage Buffer measurements, only one measurement reading was taken and plotted. For 10 and 20 nM eGFP-POK2$^{2083–2771}$, three measurement readings were taken and are plotted together in the graph. Black lines, Gaussian envelope; colour lines, individual Gaussians; dashed vertical lines, reference lines at 60, 110, and 200 kDa. Analysis was performed in a custom script written by Dr. Maria Kharlamova [141, 142].

5.4 The final ∼100 residues of POK2 are critical for microtubule binding.

The microtubule binding experiments strongly indicated that the POK2 tail binds microtubules on its own. To narrow down the region responsible for microtubule binding within the aa2083–2771 region, three shorter tail constructs based on predicted features of the POK2 tail were prepared.

The region aa2083–2771 of the POK2 tail largely consists of coiled-coils (CCs) (7 CCs comprising 68.5% of the region aa2083–2771) interspersed with unstructured domains (Fig. 3.5). These CCs can be roughly grouped into two parts based on proximity. From this grouping, two constructs, eGFP-POK2$^{2083\text{-}2440}$-8xHis (plasmid #S62, Fig. 5.16A, Table S7.3) and eGFP-POK2$^{2510\text{-}2771}$-8xHis (plasmid #S64, Fig. 5.16B, Table S7.3), were designed, cloned, expressed and purified following the same protocol as for eGFP-POK2$^{2083\text{-}2771}$ (Fig. 5.17). Hereafter the constructs will be referred to without -8xHis.

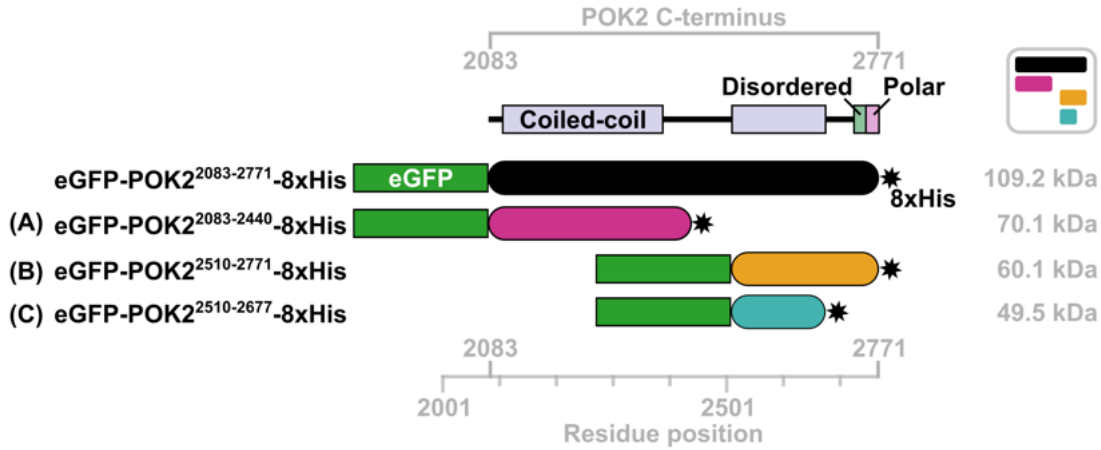

Figure 5.16: Design of shorter POK2 tail constructs.
Shorter POK2 tail constructs were designed according to protein domain predictions (UniProt). One containing the first extended coiled-coil (CC) region **(A)**, another construct containing the second CC region **(B)** and finally a construct similar to (B) but without the final unstructured region **(C)**. For easy reference, a cartoon icon was designed to represent the protein constructs with color codes corresponding to each construct, dark pink for (A), sunset orange for (B), turqoise for (C) and black for the previously mentioned POK2 tail construct, eGFP-POK2$^{2083–2771}$. This icon is used in later figures where multiple shorter POK2 tail constructs are shown together for easy referral.

At the very end of the protein is an intrinsically disordered region (IDR) predicted both by AIUpred and UniProt (Fig. 3.5). This same region is predicted to be polar by UniProt. To study if this region has any effect on microtubule binding, another construct, eGFP-POK2$^{2510\text{-}2677}$-8xHis (plasmid #S66, Fig. 5.16C, Table S7.3), was also designed, cloned, expressed and purified in the same procedure (Fig. 5.17). Four other constructs were also designed, cloned and expressed, with their protein-expressed cell pellets stored in -80°C (Fig. 7.2). However, due to time constraints, I focussed on these three constructs (Fig. 5.16) as they were of greater interest.

To test for microtubule binding activity, the same microtubule binding assay was performed using these

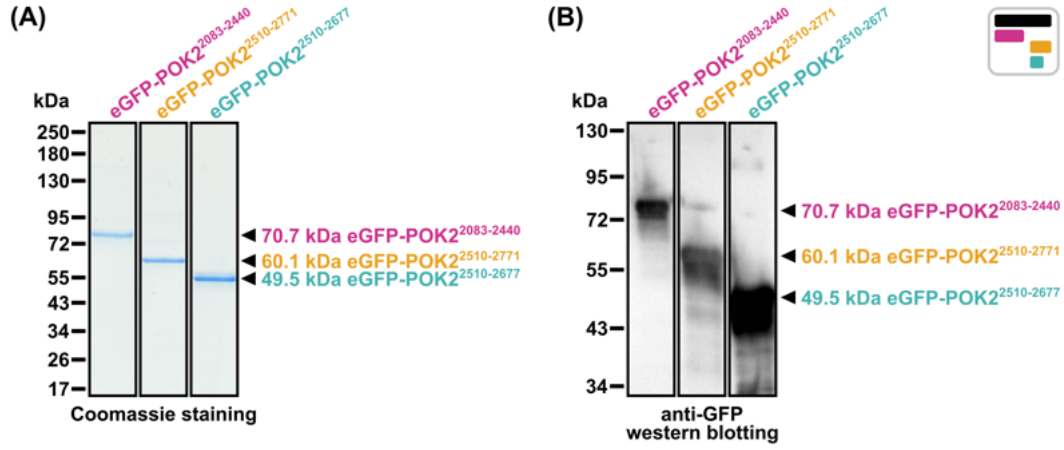

Figure 5.17: Purification of shorter POK2 C-terminus constructs used in this thesis.
(A) Coomassie stain and **(B)** western blot of SDS-PAGE gels with purified shorter POK2 C-terminus constructs. Arrowheads indicate predicted band sizes of the constructs. Cartoon icon represents recombinant protein constructs with colours corresponding to Fig. 5.16.

constructs, also using a PEM20-based buffer at ~130 mN ionic strength. Unlike eGFP-POK2$^{2083–2771}$, the shorter constructs purified well and consequently higher concentrations could be achieved in the microtubule binding assay. Like for eGFP-POK2$^{2083-2771}$, with increasing concentrations, eGFP signals appeared as lines that corresponded to microtubules in the rhodamine channel (Fig. 5.18). This was apparent for all three shorter constructs, suggesting that all three shorter constructs retained microtubule binding activity.

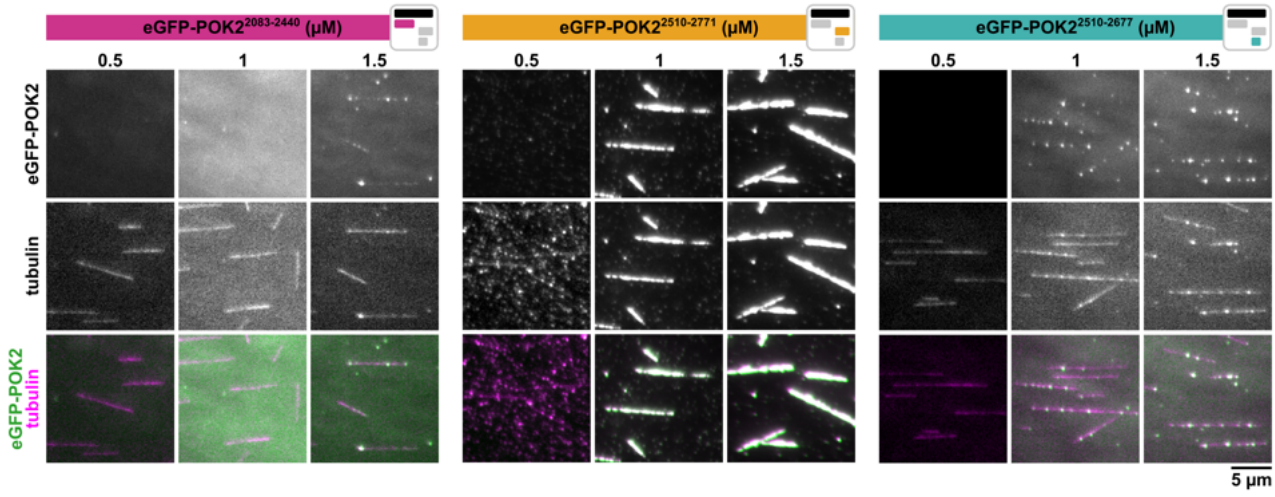

Figure 5.18: Shorter POK2 tail constructs bind microtubules in the mid-nanomolar range.
TIRF microscopy images showing eGFP- and -8xHis tagged shorter POK2 tail constructs binding double-stabilised rhodamine-labelled microtubules. Cartoon icon represents recombinant protein constructs with colours corresponding to Fig. 5.16.

However, significant microtubule binding activity was only observed at concentrations above 500 nM, several folds higher than for eGFP-POK2$^{2083–2771}$ (Fig. 5.19). Overall, eGFP-POK2$^{2083-2440}$ bound microtubules the least, suggesting that the more terminal region of the tail (aa2510-2771) played a larger role in microtubule binding. Between the other two constructs, the construct that still contained

the IDR and polar residues, eGFP-POK2$^{2510\text{-}2771}$, had 200-fold higher microtubule binding affinity compared to the construct without. Altogether, the data suggests that the final ∼100 residues of POK2 are important for microtubule binding, while the longer CC regions play lesser roles in enhancing microtubule binding.

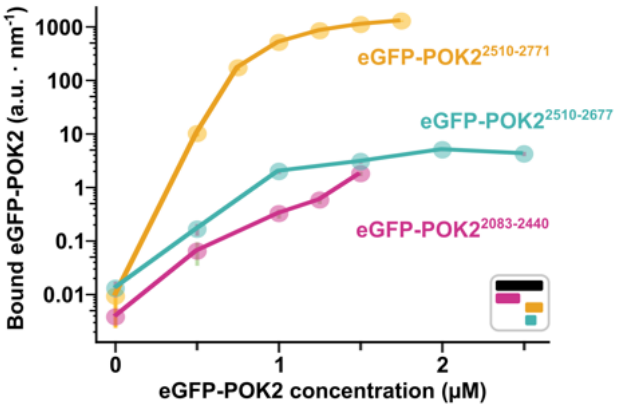

Figure 5.19: Graph of shoter POK2 tail constructs microtubule binding against concentration. Background subtracted eGFP signals of eGFP-POK2$^{2083–2440}$ (pink), eGFP-POK2$^{2510–2771}$ (orange) and eGFP-POK2$^{2510–2677}$ (turquoise) along microtubules were plotted against concentration of POK2. The maximum usable concentration for each respective construct depending on their purification yield was used. Unlike for eGFP-POK2$^{2083–2771}$ (Fig. 5.7), none of the shorter constructs reached saturating amounts and therefore were not fitted with a binding rate equation. Cartoon icon represents recombinant protein constructs with colours corresponding to Fig. 5.16. Data points are mean ± SE of experimental repeats.

5.5 MAP65-3 enhances POK2 tail microtubule binding.

The data so far strongly indicates that the POK2 tail is capable of binding microtubules on its own. However, its intrinsic microtubule binding ability still does not explain how the POK2 tail is recruited specifically to PPB microtubules during preprophase and not other microtubule structures. Previously, it was suggested that MAP65-1, -3 or -5 could mediate this specificity [118], as all three proteins localises to the PPB (Table 2.2) and was shown to interact with the POK2 tail [118]. Despite this, the localisation of POK2 to the CDZ in *ple-2* mutants that lack functional MAP65-3 was not altered, indicating that the recruitment mechanism is more complicated.

To further investigate the previously reported interaction between MAP65-3 and the POK2 tail, I purified the full-length MAP65-3 to reconstitute it with the POK2 tail in *in vitro* microtubule assays. Previous reports on MAP65-3 purification with an N-terminally tagged fluorophore indicated that the fluorophore detached from the protein, but could not be removed by size-exclusion chromatography as MAP65-3 purifies as a dimer [123]. In an attempt to circumvent this detachment, I attached the an mCherry fluorophore to the C-terminus of MAP65-3 instead and also included the 8xHis tag for affinity purification at this end. Expression and purification of this MAP65-3-mCherry-8xHis construct (hereafter, simply MAP65-3-mCherry) was successful and had a high yield (Fig. 5.20). Unfortunately, the C-terminally tagged mCherry fluorophore also detached from MAP65-3 to some extent. Similarly the tagless MAP65-3 could not be separated from the MAP65-3-mCherry-8xHis species due to its

dimerisation. Nevertheless, since my goal was to characterise the activity of the POK2 tail in the presence of MAP65-3, the presence of tagless MAP65-3 was not too concerning and I proceeded with more experiments.

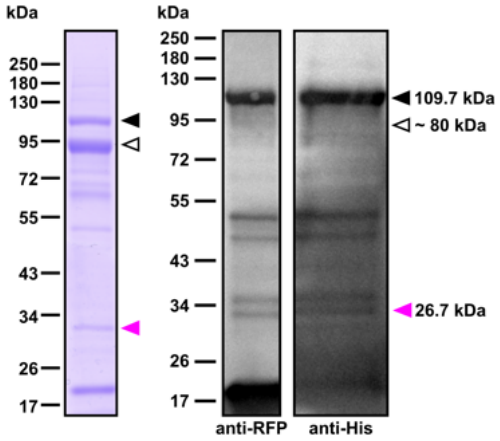

Figure 5.20: Coomassie stain and western blot of purified MAP65-3-mCherry in an SDS-PAGE gel.
Black arrow head, predicted MAP65-3-mCherry size; open arrow head, predicted sized of untagged MAP65-3 without mCherry-8xHis; magenta arrow head, predicted size of mCherry. There is quite a bit of degradation but this resembles the band patterns from previous publications even after size-exclusion chromatography [123]. Additionally, it is not possible to remove the untagged MAP65-3 as MAP65-3 are dimeric in solution and cannot be removed by methods such as size exclusion chromatography.

As a first look into the interaction between MAP65-3 and the POK2 tail, *in vitro* microtubule binding assays with non-single molecule conditions were performed. 20 nM eGFP-POK2$^{2083–2771}$ was mixed with varying concentrations of MAP65-3-mCherry (0, 0.1, 1, 10, 20 nM) in a PEM20-based Motility buffer and introduced into a flow-cell with immobilised unlabelled double-stabilised microtubules (Fig. 5.21, 5.22A, B). eGFP-POK2$^{2083–2771}$, which binds microtubules at 20 nM in a non-saturating manner, increased microtubule binding with increasing concentrations MAP65-3-mCherry. Thus, the interaction between MAP65-3 and the POK2 tail was successfully reproduced *in vitro*, which allows for further detailed investigations.

The experiments for these assays were performed in an ionic strength of ∼170 mN (see Table 4.4 for recipe), which is slightly higher than the previous ∼130 mN used for bulk binding assays of eGFP-POK2$^{2083\text{-}2771}$ alone. This was not a huge issue, as 20 nM eGFP-POK2$^{2083\text{-}2771}$ bound microtubules to a similar degree (compare images from Fig. 5.6 and 5.21). Nevertheless, to check if the same interaction would be possible at lower ionic strengths, the assays were repeated at 70 mN ionic strength (Fig. 5.22C, D). Overall, the trend of microtuble binding increase by eGFP-POK2$^{2083\text{-}2771}$ with increasing MAP65-3-mCherry concentration was reproduced. This suggests that the interaction between eGFP-POK2$^{2083\text{-}2771}$ and MAP65-3-mCherry themselves are not largely effected by ionic strength.

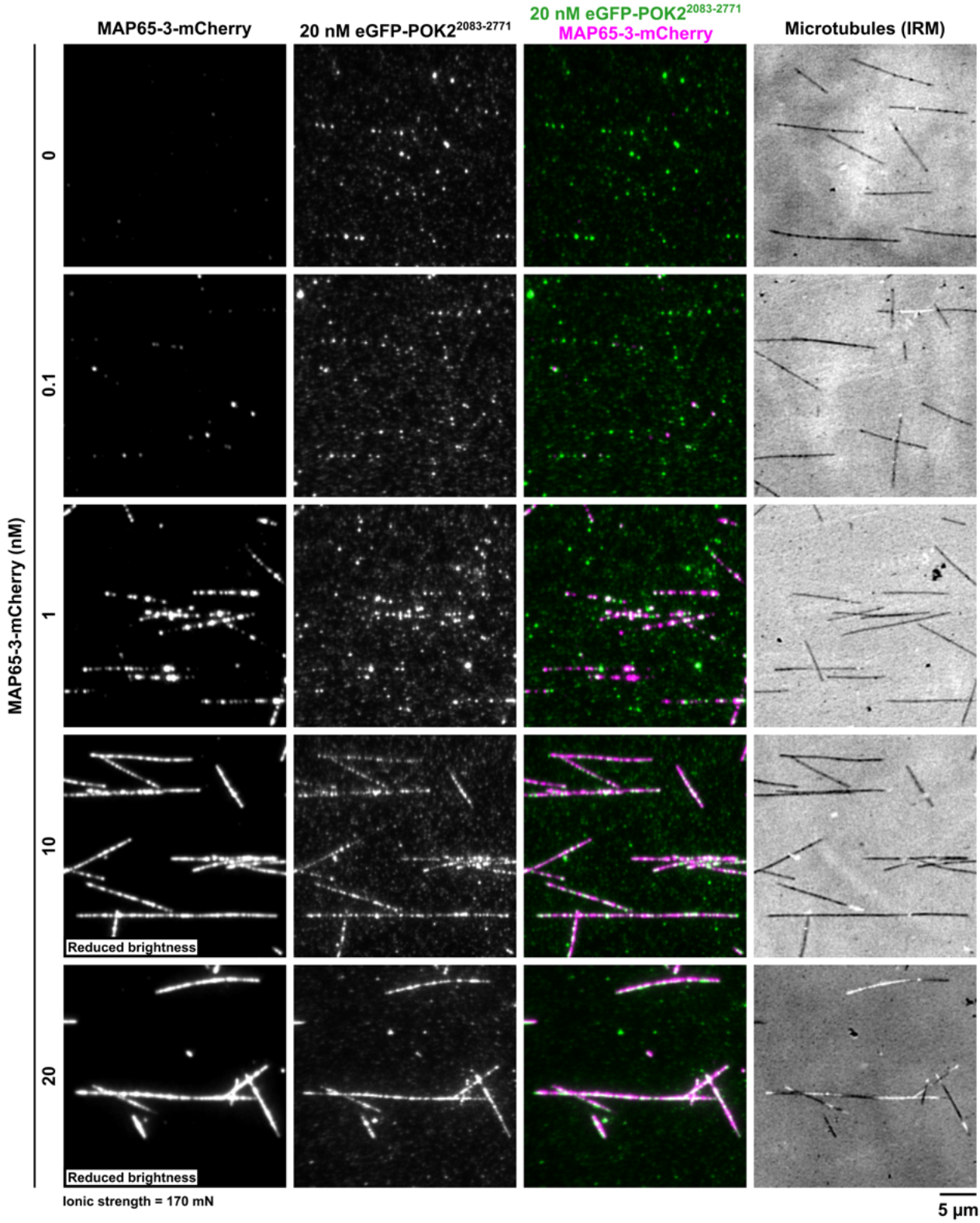

Figure 5.21: MAP65-3-mCherry enhances microtubule binding of eGFP-POK2$^{2083-2771}$.
TIRF microscopy images of MAP65-3-mCherry at various concentrations and 20 nM eGFP-POK2$^{2083-2771}$ binding to microtubules. Microtubules were unlabelled and visualised using IRM. At 10 and 20 nM MAP65-3-mCherry, the mCherry (magenta) signal was saturated and therefore brightness was reduced in these images. For all other images, the brightness and contrast levels were the same. Note that all these experiments were performed at an ionic strength of 170 mN.

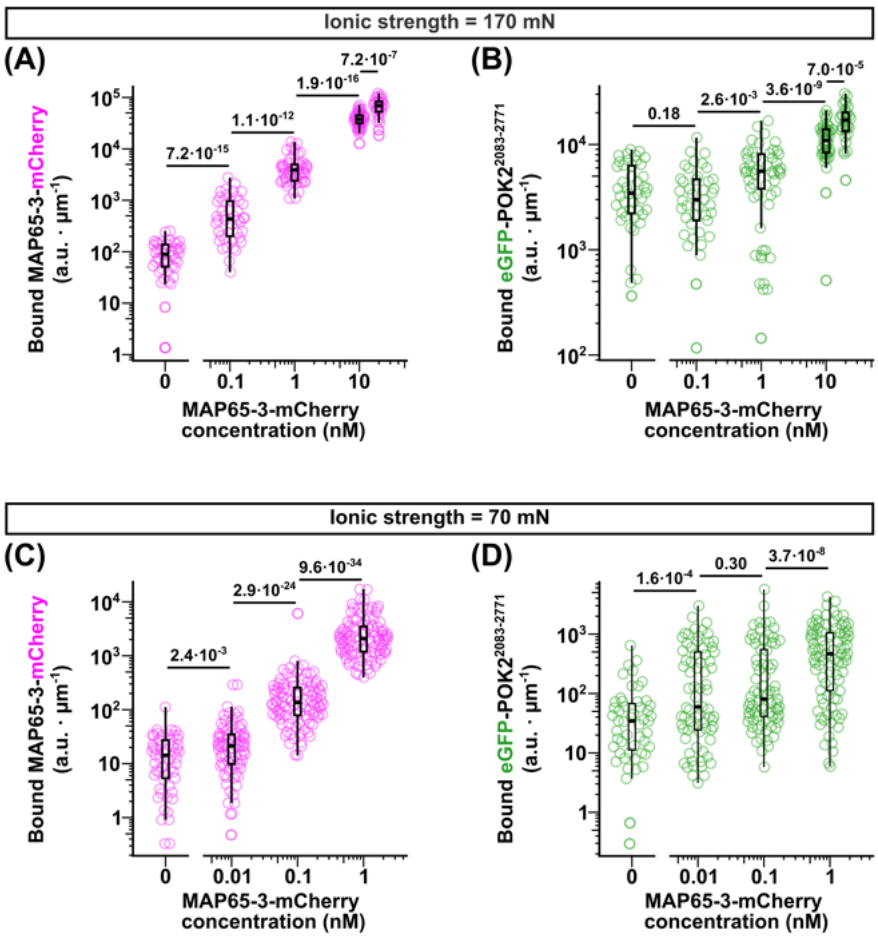

Figure 5.22: MAP65-3 enhances POK2 tail microtubule binding at different ionic strengths.
Microtubule binding of MAP65-3-mCherry and 20 nM eGFP-POK2$^{2083–2771}$ with different concentrations of MAP65-3-mCherry at an ionic strength of 170 mN (A, B) and 70 mN (C, D). Box plots, maxima, median, minima; whiskers, 1.5 IQR; points are individual intensity measurements.

5.6 MAP65-3 interacts with the POK2 tail through the final ∼100 residues.

To narrow down the region of the POK2 tail which is important for this enhancement of microtubule binding by MAP65-3, the same *in vitro* microtubule binding assay was performed with 20 nM MAP65-3-mCherry and 20 nM of the shorter POK2 tail constructs (Fig. 5.23). With 20 nM POK2 tail proteins and at 170 mN ionic strength, none of the shorter tail constructs significantly bound the microtubule on their own. However, with the addition of 20 nM MAP65-3-mCherry, eGFP-POK2$^{2510–2771}$ significantly increased its microtubule binding. At these concentrations, the other two shorter POK2 tail constructs did not increase microtubule binding in the presence of 20 nM MAP65-3-mCherry.

Of the three shorter POK2 tail constructs, eGFP-POK2$^{2510–2771}$ has the higher microtubule binding affinity (Fig. 5.19). Since the POK2 tail is able to bind microtubules on its own, it becomes difficult to distinguish if MAP65-3 is truly recruiting POK2 tail constructs from solution on to the microtubule or

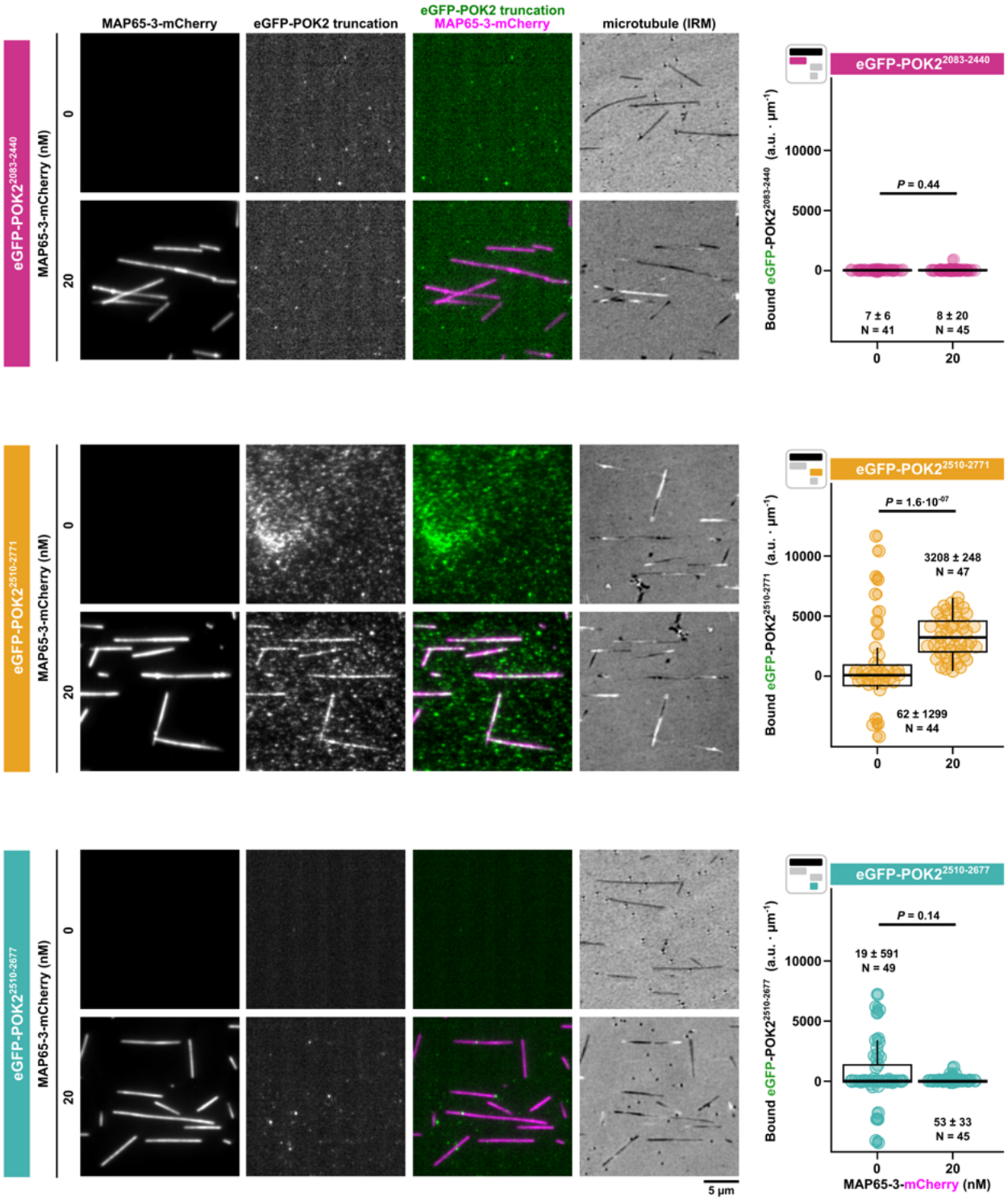

Figure 5.23: MAP65-3-mCherry likely interacts with the C-terminus of POK2 via its final ∼100 amino amino acids.
Snapshots of shorter POK2 tail constructs (20 nM) and MAP65-3-mCherry (0 and 20 nM) interaction with unlabelled double-stabilised microtubules at 170 mN ionic strength. On the right are corresponding background subtracted intensities plotted against MAP65-3-mCherry concentration. Colors and cartoon icon correspond the shorter POK2 tail constructs following Fig. 5.16. Horizontal line in box plot is median; whiskers are 1.5 IQR; data points are individual microtubule measurements, mean binding is given ± SE, *p*-values were calculated with a Mann-Whitney-Wilcoxon test.

it was simply increasing the intrinsic microtubule binding capabilities of the protein. To investigate this distinction, the *in vitro* microtubule binding assay was repeated with 500 nM of the other two shorter POK2 tail constructs (Fig. 5.24). Interestingly, eGFP-POK2$^{2510\text{-}2677}$ increased microtubule binding in the presence of 20 nM MAP65-3-mCherry while there was no difference to microtubule binding of eGFP-POK2$^{2083\text{-}2440}$. Note that single molecule concentrations of eGFP-POK2$^{2083\text{-}2440}$ is around 100 nM at 130 mN ionic strength (data not shown here). Hence, eGFP-POK2$^{2083\text{-}2440}$ is able to bind microtubules on its own even at 500 nM, although without fully saturating the microtubule. However, the presence of saturating amounts of MAP65-3-mCherry does not enhance its microtubule binding. Altogether, these data indicate that MAP65-3-mCherry interacts with the final ∼100 residues of POK2 to recruit it to the microtubule. The interaction region may reach further upstream, as eGFP-POK2$^{2510\text{-}2771}$ also saw its microtubule binding increased in the presence of MAP65-3-mCherry. However, as the effect was most apparent for eGFP-POK2$^{2510\text{-}2677}$, the further upstream regions may not be as critical as the final ∼100 residues.

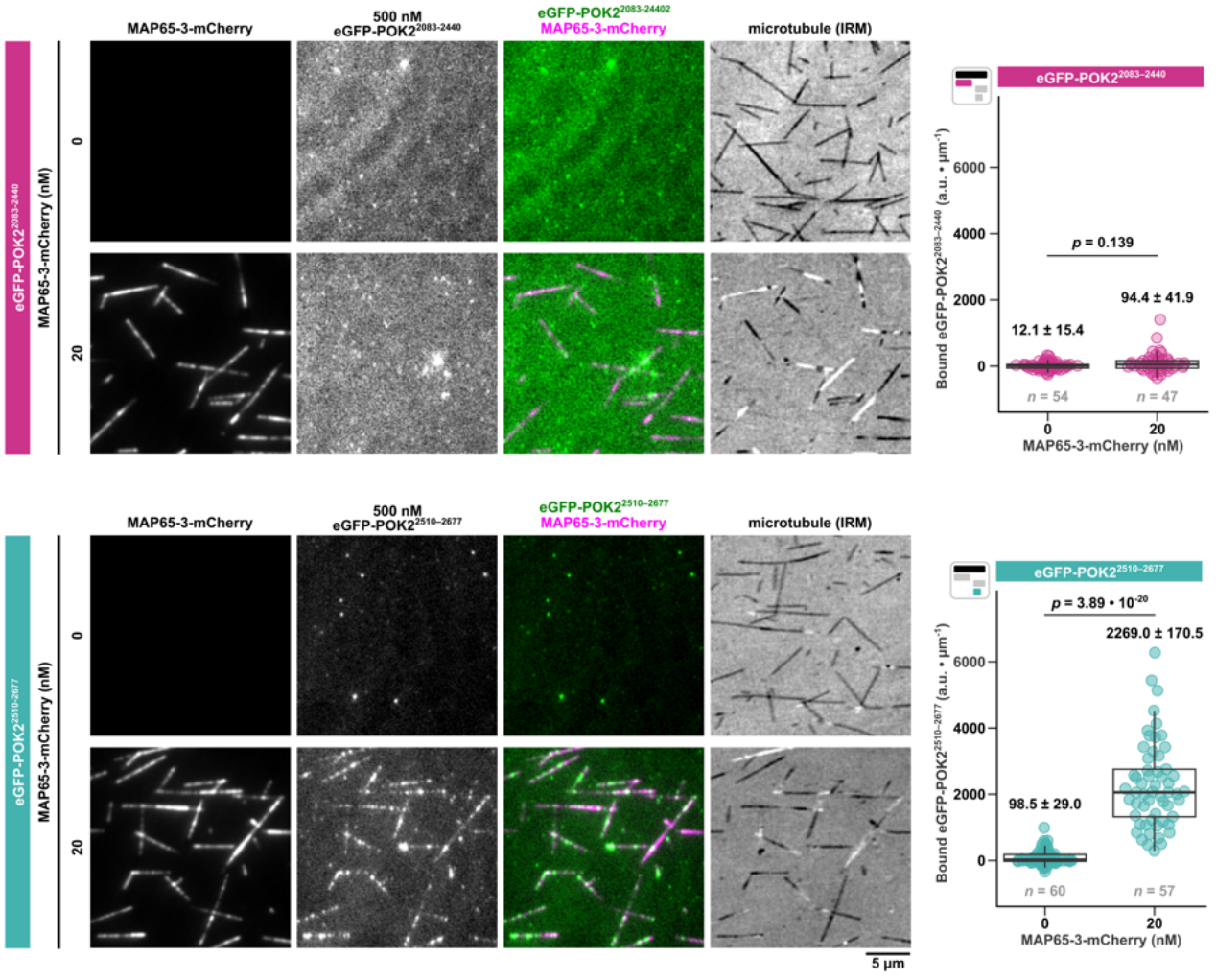

Figure 5.24: Shorter POK2 tail at high concentrations with MAP65-3.
500 nM eGFP-POK2$^{2083–2440}$ (dark pink) or 500 nM eGFP-POK2$^{2510–2677}$ (turqoise) were incubated with unlabelled double-stabilised microtubules in the presence of 0 or 20 nM MAP65-3-mCherry. On the right is quantification of the microtubule binding of the shorter POK2 tail constructs by using background subtracted eGFP signal intensity along the length of a microtubule. The ionic strength of the experiment here is also 170 mN. Box plot horizontal line, median; whiskers, 1.5 IQR; data points, individual microtubules measured, mean binding is given ± SE, *p*-values were calculated with Mann-Whitney-Wilcoxon test.

5.7 MAP65-3 and the POK2 tail do not interact at single molecule and low salt conditions.

To further investigate the mechanistic interaction between the POK2 tail and MAP65-3, *in vitro* microtubule binding assays at single molecule concentrations were performed. Since eGFP-POK2$^{2083\text{-}2771}$ purified with low concentrations and was stored in a high salt buffer, the influence of the high salt buffer in the final reaction mix for bulk microtubule binding assays have to be carefully controlled. For single molecule experiments, where only a very small volume of the original high salt buffer is used in the final reaction mix, the influence of the high salt buffer becomes negligible. For instance, using a final 1 nM eGFP-POK2$^{2083\text{-}2771}$ from a 500 nM stock in the final reaction mix results in a 500-fold dilution. Using PEM20 buffer without any additional salts, the final reaction mix with 1 nM eGFP-POK2$^{2083\text{-}2771}$ and 25 pM MAP65-3-mCherry for single molecule conditions has an ionic strength of ∼70 mN, which is a relatively low ionic strength. At this ionic strength, both 1 nM eGFP-POK2$^{2083\text{-}2771}$ and 25 pM MAP65-3-mCherry were able to interact with and diffuse on the microtubule (Fig. 5.25, *left*).

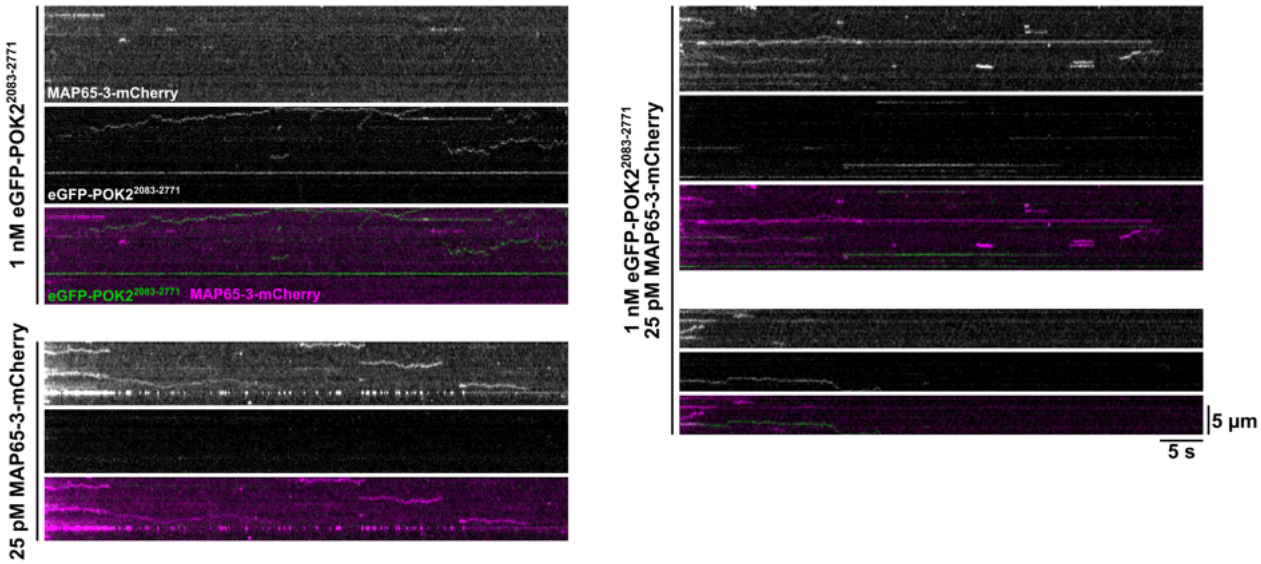

Figure 5.25: Single molecule MAP65-3 and single molecule POK2 tail do not interact in low salt conditions. Kymographs from TIRF time-lapse imaging sampled every 0.1 s of 1 nM eGFP-POK2$^{2083\text{-}2771}$ and 25 pM MAP65-3-mCherry at 70 mN ionic strength. Here, 10% power for the 561 nm was used in order to visualise single mCherry molecules with the caveat of increased photobleaching.

To investigate the interaction between single molecule POK2 tail and MAP65-3, 1 nM eGFP-POK2$^{2083\text{-}2771}$ and 25 pM MAP65-3-mCherry were mixed together in an *in vitro* microtubule binding assay (Fig. 5.25, *right*). Surprisingly, no interaction was observed between eGFP-POK2$^{2083\text{-}2771}$ and MAP65-3-mCherry. Considering that the microtubule consists of at least 13 protofilaments, the microtubule can be thought of as a 13-lane highway, where the POK2 tail and MAP65-3 would have one-in-thirteenth chance for an encounter. Hence, to account for this possibly, higher concentrations of MAP65-3-mCherry was used (Fig. 5.26). Nevertheless, interaction between the POK2 tail and MAP65-3 was not observed.

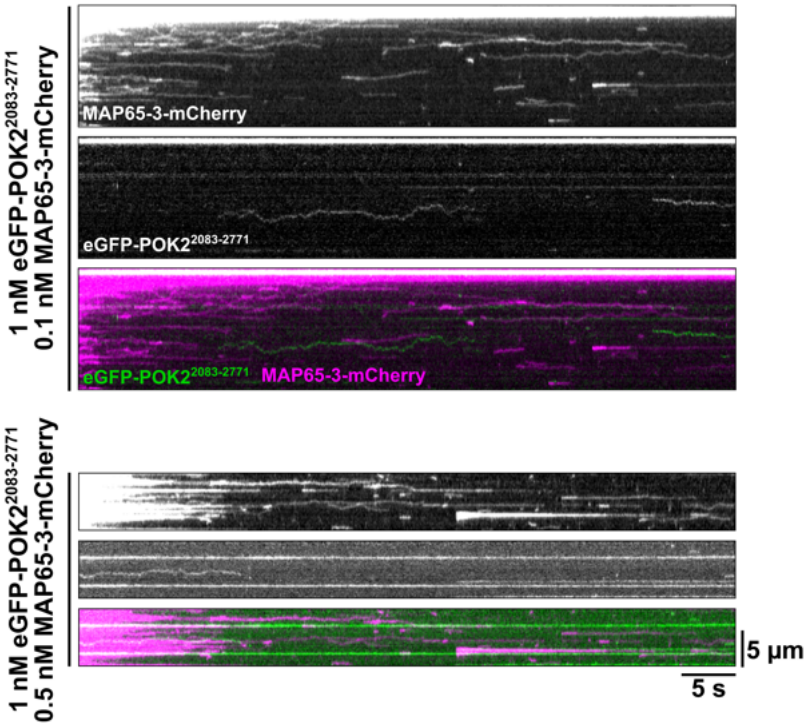

Figure 5.26: MAP65-3 and single molecule POK2 tail do not interact in low salt conditions. Kymographs from TIRF time-lapse imaging sampled every 0.1 s of 1 nM eGFP-POK2$^{2083-2771}$ and 0.1 and 0.5 nM MAP65-3-mCherry at 70 mN ionic strength. Here, 10% power for the 561 nm was used in order to visualise single mCherry molecules at the caveat of increased photobleaching.

A note on photobleaching of MAP65-3-mCherry

In all these assays, a higher laser power (10% 561 nm laser) was used to visualise the mCherry fluorescence for single molecule conditions. Previously, only 1% was used as MAP65-3-mCherry was used in saturating concentrations (20 nM). Even at 1% laser power, photobleaching occurred very quickly especially with high MAP65-3-mCherry concentrations. However, since 1% is not strong enough to visualise single molecule mCherry fluorescence, 10% laser power had to be used with the caveat of increased photobleaching.

5.8 MAP65-3 and the POK2 tail co-diffuse together at 160 mN ionic strength.

Previously, microtubule binding assays with shorter POK2 tail constructs revealed the importance of the final ∼100 residues for interaction with microtubules and also with MAP65-3-mCherry. As these final ∼100 residues contain a positively charged region, electrostatic interactions could possibly play a role in the interaction between the POK2 tail and MAP65-3 at the single molecule level, while being largely negligible in bulk conditions. To study the influence of electrostatic interactions on the POK2 tail and MAP65-3 interaction, *in vitro* microtubule binding assays at single molecule concentrations were performed with MAP65-3 and POK2 tail at varying ionic strengths. Again, considering that a

microtubule has at least 13 protofilaments, only the concentration of eGFP-POK2$^{2083\text{-}2771}$ was kept at 1 nM, whereas MAP65-3-mCherry was kept at 0.5 nM. The ionic strength of the final reaction mix (originally 70 mN ionic strength) was increased by introducing an additional 60, 90 and 120 mM KCl which results in 130, 160 and 190 mN ionic strengths respectively. Interestingly, interaction between eGFP-POK2$^{2083\text{-}2771}$ and MAP65-3-mCherry was observed at 130 and 160 mN ionic strengths, where both eGFP and mCherry signals could be seen to diffuse together (Fig. 5.27).

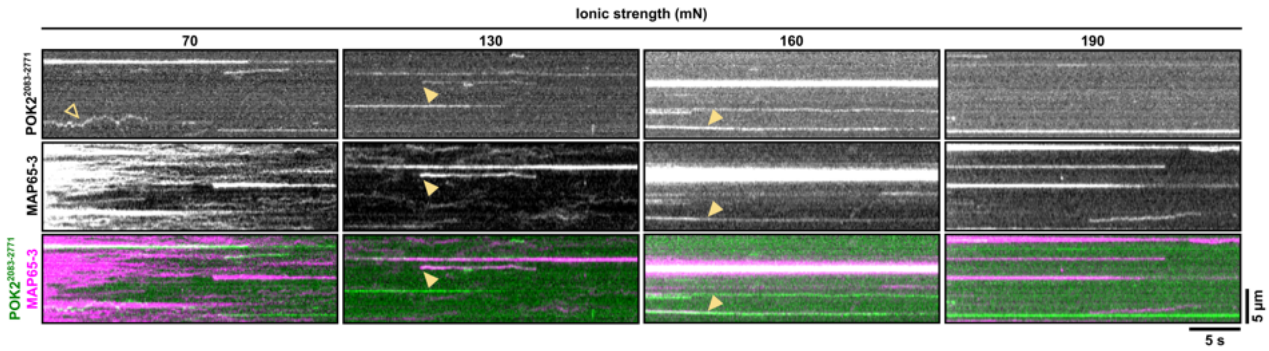

Figure 5.27: MAP65-3-mCherry and eGFP-POK2$^{2083\text{-}2771}$ both diffuse on the microtubule and occasionally co-diffuse.
Kymographs from TIRF time-lapse imaging sampled every 0.1 s of 1 nM eGFP-POK2$^{2083\text{-}2771}$ and 0.5 nM MAP65-3-mCherry at 70, 130, 160 and 190 mN ionic strengths. Note that MAP65-3 interaction with the microtubule decreased with increasing ionic strength and that MAP65-3 saturated the microtubule at 70 mN ionic strength and photobleached very quickly although only 1% 561 nm laser power was used. Open arrow heads, diffusive events where only eGFP-POK2$^{2083\text{-}2771}$ was visible; filled arrow heads; co-diffusive events where both eGFP-POK2$^{2083\text{-}2771}$ and MAP65-3-mCherry were visible.

5.8.1 Landing rate

Quantification of the landing rate of single diffusive eGFP signals and co-diffusive eGFP and mCherry signals revealed that interaction between eGFP-POK2$^{2083\text{-}2771}$ and MAP65-3-mCherry peaks at 160 mN ionic strength (Fig. 5.28A). Expectedly, eGFP-POK2$^{2083\text{-}2771}$ landing rate decreased with increasing ionic strength (Fig. 5.28A, *left*).

5.8.2 Landing sequence

To investigate whether the proteins require the microtubule for their interaction, the landing sequence of the co-diffusive traces were analysed by Dr. Hauke Drechsler. 54.5% of traces had eGFP and mCherry signals appear at the same time on the microtubule, whereas 16% and 20.5% had eGFP and mCherry signals appear first respectively (Fig. 5.28B). The results suggest that eGFP-POK2$^{2083\text{-}2771}$ and MAP65-3-mCherry very likely interacting in solution to land on the microtubule simultaneously but can also interact when they encounter each other on the microtubule.

5.8.3 Stochiometry

Dr. Hauke Drechsler analysed the intensities of mCherry signals and eGFP signals from eGFP-POK2$^{2083\text{-}2771}$ of the co-diffusive traces in hopes of revealing a stochiometric trend (Fig. 5.29). For easier visualisation, lines connecting mCherry and eGFP signal values from the same co-diffusing trace

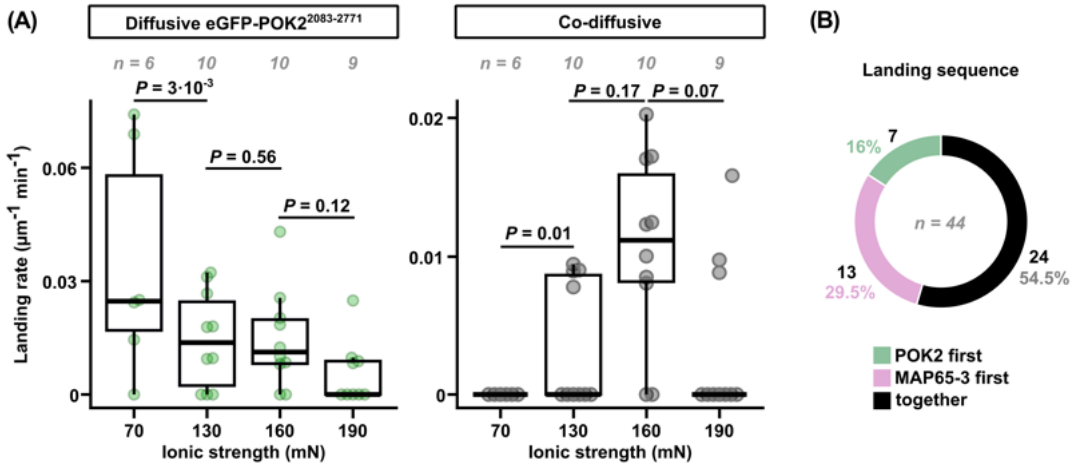

Figure 5.28: Landing rate and landing sequence of diffusive and co-diffusive molecules.
(A) Landing rate of diffusive eGFP-POK2$^{2083-2771}$ molecules alone (left) or co-diffusing with MAP65-3-mCherry (right). The landing rate of eGFP-POK2$^{2083-2771}$ molecules decreases with increasing ionic strength. However, the landing rate of co-diffusive eGFP-POK2$^{2083-2771}$ and MAP65-3-mCherry traces peak at 160 mN ionic strength. Box plots are IQR; whiskers are 1.5 IQR; lines in box plots are medians; *p*-values were calculated from a Mann-Whitney-Wilcoxon test. **(B)** Landing sequence of co-diffusive eGFP-POK2$^{2083-2771}$ and MAP65-3-mCherry traces based on the appearance of a eGFP or mCherry signal in a diffusive trace.

were drawn. In principle, if there was a trend in stochiometry between the two proteins, the connecting lines would form a bias. Unfortunately no significant trend in stochiometry could be observed. One possibility for the lack of a clear stochiometric pattern is the presence of untagged MAP65-3 without mCherry (Fig. 5.20). As MAP65-3 purifies as a dimer, it is not possible to purify MAP65-3-mCherry without the untagged species, even with size exclusion chromatography [123]. Hence, with the data at hand, it is not possible to reliably conclude whether or not there is a stochiometric relationship between MAP65-3 and the POK2 tail for co-diffusing on microtubules.

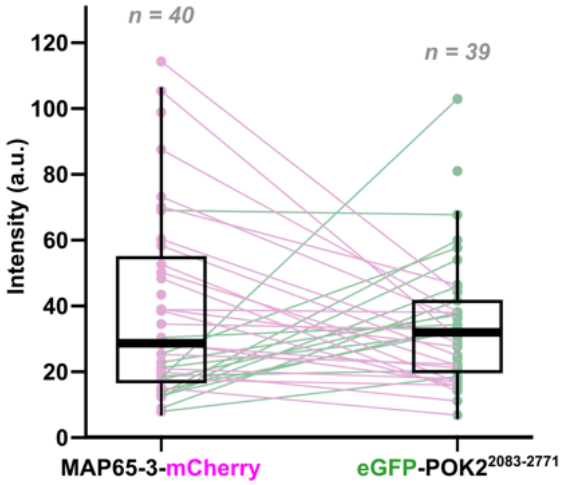

Figure 5.29: POK2 tail and MAP65-3 interact on the microtubule without specific stochiometry
Background subtracted intensity along a co-diffusive trace for MAP65-3-mCherry and eGFP-POK2$^{2083-2771}$. Lines connect signals measured from the same co-diffusive trace. Pink lines indicate when the MAP65-3-mCherry signal was higher, green lines indicate when the eGFP-POK2$^{2083-2771}$ signal was higher.

A note on photobleaching

One thing of concern was the weakness of the mCherry signals. Using 10% 561 nm laser power allowed visualisation of single molecule MAP65-3-mCherry (perhaps monomeric, or dimeric with one tagged and one untagged protein) with the caveat of photobleaching. However, using lower laser power means that single molecule species could not be visualised. Hence, it was possible that there were more co-diffusive traces than could be visualised. To check if this could be true, the same *in vitro* microtubule binding assay using 1 nM eGFP-POK2$^{2083\text{-}2771}$ and 0.5 nM MAP65-3-mCherry at 160 mN ionic strength was repeated using 10% laser power (Fig. 5.30). Interestingly, although 10% laser power revealed more short-interacting MAP65-3-mCherry traces, only very bright and long-interacting traces were observed to interact with eGFP-POK2$^{2083\text{-}2771}$. This suggests that for imaging co-diffusive MAP65-3-mCherry and eGFP-POK2$^{2083\text{-}2661}$ traces, the conservative 1% laser power was sufficient.

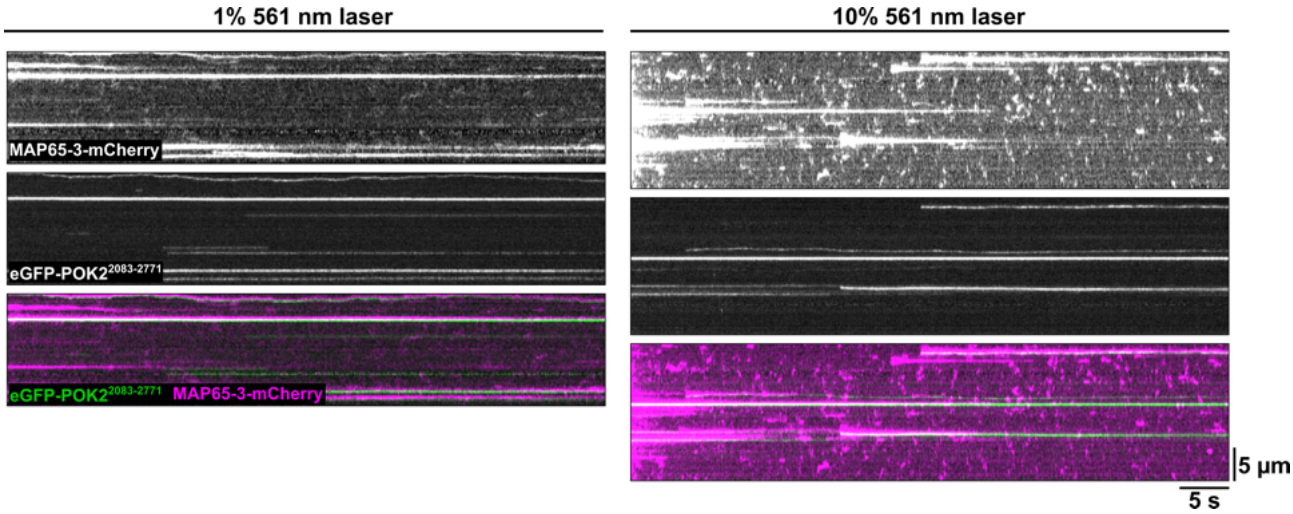

Figure 5.30: Kymographs of POK2 tail and MAP65-3 at 160 mN ionic strength with different 561 nm laser power.
Kymographs from TIRF time-lapse imaging sampled every 0.1 s of 1 nM eGFP-POK2$^{2083\text{-}2771}$ and 0.5 nM MAP65-3-mCherry at 160 and 190 mN ionic strength taken with 1% and 10% 561 nm laser power on the Shenlong setup. Brightness and contrast values for both sets of kymographs are the same.

5.8.4 Diffusion coefficient

To characterise the diffusive activity of the co-diffusive traces, FIESTA [259] was used to automatically track the traces to obtain (x,y) coordinates for each time point of the traces. As with the diffusion coefficient analysis for single eGFP-POK2$^{2083\text{-}2771}$ traces, displacement steps for different lag times, τ = 0.1 to 1.0 s were calculated and plotted as a distribution. Similarly, the Akaike and Bayesian information criteria (AIC, BIC) were used to decide on the number of Gaussians to fit the diplacement step distributions. The largest decrease in IC values was from one to two Gaussians, indicating that two Gaussians were sufficient to describe the displacement step data (Fig. 5.31A). The displacement step distributions were thus fitted with two Gaussians (Fig. 5.31B, 7.4). The variances of the Gaussians were then plotted against their respective lag times, τ and were separated based on their magnitude (Fig. 5.31C). With the assumption of two-dimensional diffusion along a straight line, the variances were fitted with a regression line, where $variance = 2D\tau + \varepsilon^2$ describes the line. As before, D is the diffusion coefficient and ε is the tracking precision. The half-slope of the regression lines gives two diffusion coefficients describing two non-stationary species, $D = 0.011 \pm 0.001$ $\mu m^2 \cdot s^{-1}$ and 0.0013

$\pm$ 0.0000 $\mu m^2 \cdot s^{-1}$. These values reveal that the co-diffusive species are three-fold and one order of magnitude slower than the diffusive eGFP-POK2$^{2083\text{-}2771}$ species alone (Fig. 5.12C).

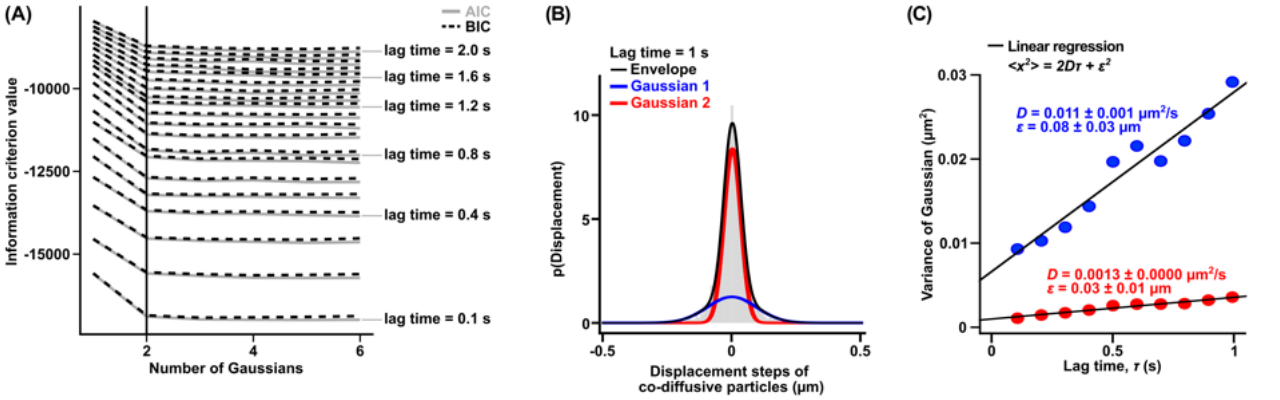

Figure 5.31: Diffusion coefficient of co-diffusve eGFP-POK2$^{2083\text{-}2771}$-8xHis and MAP65-3-mCherry traces. **(A)** Graph of Akaike and Bayesian information criterions (AIC, BIC) versus number of Gaussians fitted for displacement step distributions like in (B) for different lag times, τ = 0.1 to 2.0 s for every 0.1 s. The largest reduction in ICs is from one to two Gaussians (black vertical line). **(B)** Distribution of displacement steps of a representative lag time, τ = 1.0 s fitted with two Gaussians. **(C)** Graph of the variance, i.e. the squared standard deviation of each Gaussian versus lag time, τ. Here, two diffusion coefficients, D, are obtained. Lines are regression fits to the data from 0.1 to 1.0 s with the equation $variance = 2D\tau + \varepsilon^2$ which assumes two-dimensional diffusive. D and tracking precision, ε are given $\pm$ SE.

5.9 The POK2 tail binds lipids directly.

In vivo, initial recruitment of the POK2 tail to the CDZ is PPB microtubule-dependent. However, as the cell enters mitosis, the PPB is disassembled while the POK2 tail remains at the CDZ until the end of cytokinesis. Initial CDZ recruitment via the PPB has been suggested to previously depend on MAP65-3 [118]. Earlier in this thesis, direct microtubule binding of the POK2 tail presents another possible method in which the POK2 tail can be recruited to the PPB. However, both MAP65-3 binding and microtubule binding of the POK2 tail does not explain how it remains at the CDZ after PPB disassembly, especially since MAP65-3 is also delocalised from the CDZ upon mitotic entry [64, 66, 214, 268, 289, 330].

On the other hand, there are other known CDZ-resident proteins that are localised here throughout mitosis and cytokinesis (see Table 2.1). POK2 CDZ residence could be maintained through interactions with one or several CDZ-resident proteins. Alternatively, several kinesins have been shown to directly bind lipids, as kinesin cargoes are often membrane encapsulated (see Section 3.1.2.4). Although the POK2 tail does not possess lipid binding motifs such as the pleckstrin homology (PH) or phox homology (PX) motifs, it was possible that POK2 tail could directly interact with plasma membrane through unknown binding domains unique to plants.

To test if the POK2 tail could interact with lipids, a lipid blot assay with eGFP-POK2$^{2083\text{-}2771}$ as well as with the three shorter constructs were performed. eGFP-POK2$^{2083\text{-}2771}$ bound a variety of anionic lipids, such as phosphatidic acid (PA), cardiolipin (CL) and the phosphoinositol phosphates (PIPs)

PI(4)P, PI(4,5)P_2 and PI(3,4,5)P_3 but not phosphatidylserine (PS) (Fig. 5.32). These results indicate that eGFP-POK2$^{2083\text{-}2771}$ binds phospholipids directly.

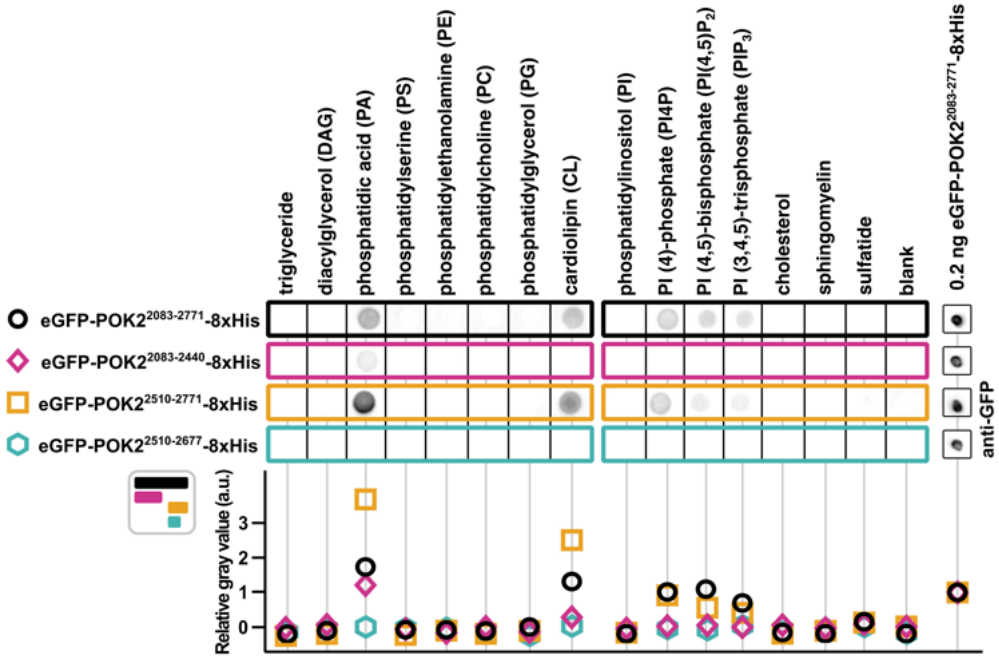

Figure 5.32: Lipid blot assay with eGFP-POK2 C-terminus constructs.
0.2 ng eGFP-POK2$^{2083\text{-}2771}$ (far right boxes) was spotted at the bottom of each PIP strip and used to normalise the signals on each lipid spot. The relative grey values of each spot was measured with FIJI and plotted below the lipid strips.

Two of the shorter POK2 tail constructs did not bind to the lipid strips very well, i.e. eGFP-POK2$^{2083\text{-}2440}$ and eGFP-POK2$^{2510\text{-}2677}$. Meanwhile, eGFP-POK2$^{2510\text{-}2771}$ retained the same lipid binding as the eGFP-POK2$^{2083\text{-}2771}$ construct and actually had increased binding to PA and CL comparatively. This suggests that the final ∼100 residues (aa2678–2771) are crucial for association with lipids, likely due to the highly charged residues in this region (see Fig. 3.5).

To confirm the lipid binding in a more physiological setting, giant unilamellar vesicles of different lipid compositions were prepared by PVA-swelling and mixed with 20 nM eGFP-POK$^{2083\text{-}2771}$ in a PEM20-based buffer. To visualise the GUVs and protein binding I used HILO and bright-field microscopy. The assay successfully recapitulated the results from the lipid blot assays, as eGFP-POK2$^{2083\text{-}2771}$ could bind to 75-100% PA GUVs (Fig. 5.33) and 50–100% CL GUVs (Fig. 5.34). Altogether, the data suggests that the POK2 tail is able to bind lipids directly.

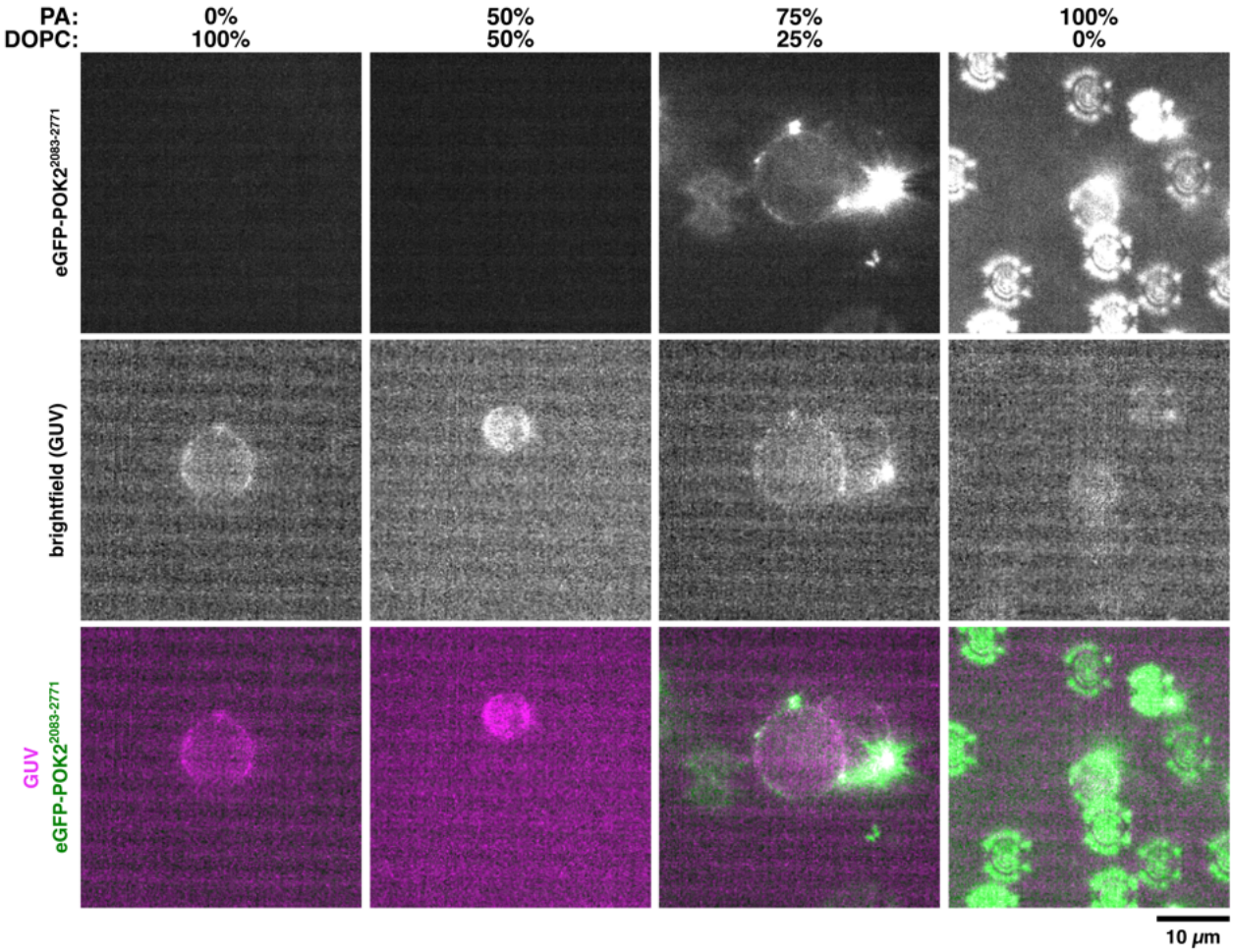

Figure 5.33: eGFP-POK2$^{2083-2771}$ bound PA GUVs.
20 nM eGFP-POK2$^{2083-2771}$ were mixed with GUVs with different % of phosphatidic acid (PA)/dipalmitoylphosphatidylcholine (DOPC) and imaged by HILO and bright-field microscopy. GUVs were unlabelled and illuminated by reflections off fluorescent contaminations in the 561 nm channel.

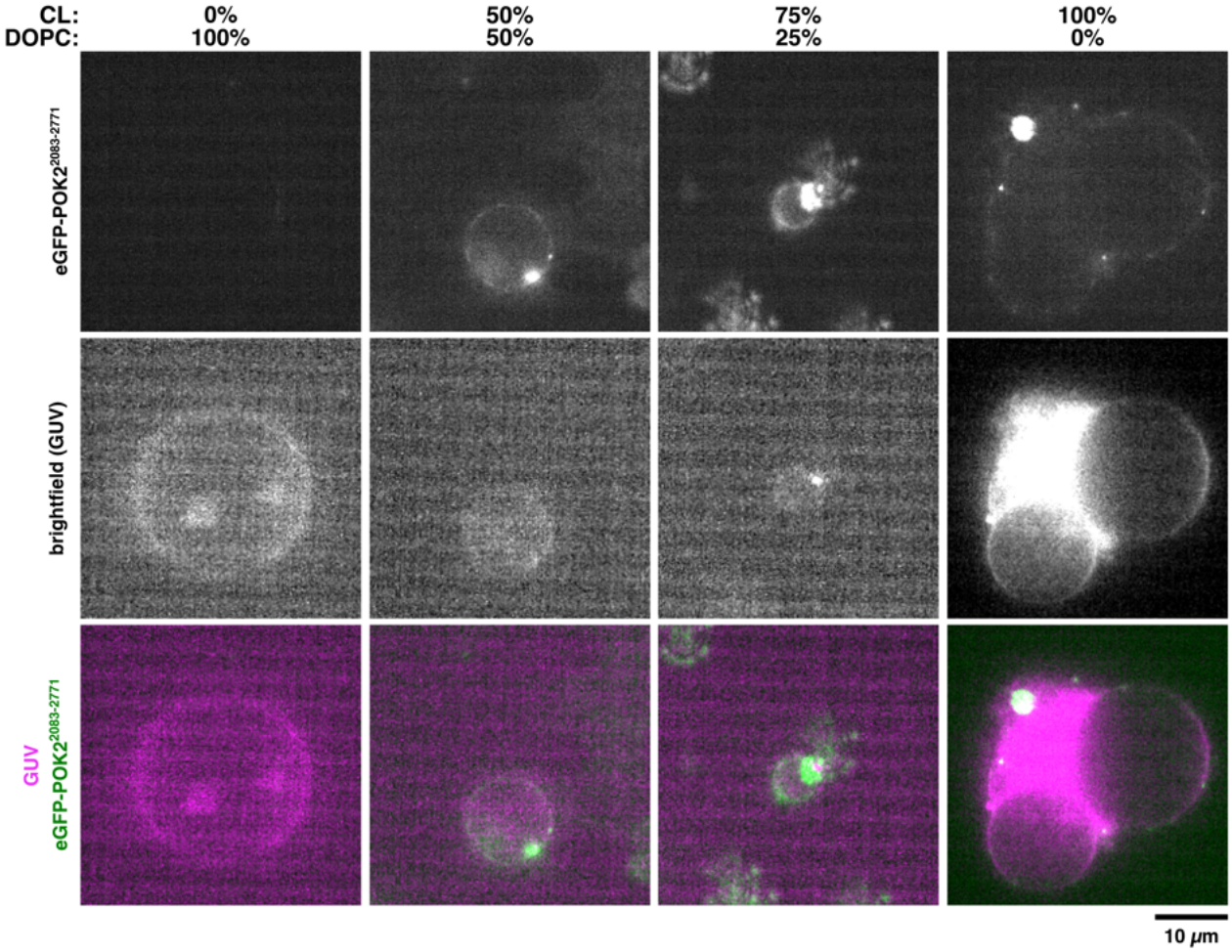

Figure 5.34: eGFP-POK2$^{2083-2771}$ bound CL GUVs.
20 nM eGFP-POK2$^{2083-2771}$ were mixed with GUVs with different % of cardiolipin (CL)/dipalmitoylphosphatidylcholine (DOPC) and imaged by HILO and bright-field microscopy. GUVs were unlabelled and illuminated by reflections off fluorescent contaminations in the 561 nm channel.

Altogether, the results from this thesis presents the POK2 tail as a versatile region of the POK2 protein, capable of multiple interactions with different structures and proteins. In this thesis, the POK2 tail was shown to bind both microtubules and lipids on its own, likely via its positively charged final $\sim$100 amino acids. The POK2 tail was also shown to interact with MAP65-3, where MAP65-3 could enhance the POK2 tail's microtubule binding. Moreover, single molecule experiments with the POK2 tail and MAP65-3 identified the POK2 tail-MAP65-3 co-diffusing species, which had expectedly reduced diffusion, potentiating a mechanism that could exploited *in vivo* to regulate POK2 activity.

5.10 MAP65-3 reduces microtubule binding of the POK2 motor.

In addition to the POK2 tail, MAP65-3 has also been shown to interact with the aa1–589 region of POK2, which contains the kinesin motor domain [118]. In *ple-2* mutants deficient in functional MAP65-3, POK2$^{1–589}$ still binds to the phragmoplast but is no longer restricted to the midzone [118]. The interaction between MAP65-3 and the POK2 motor is likely via its N-terminal unstructured region, as the POK2$^{1\text{-}189}$ construct is recruited to microtubules in transient expression in *N. benthamiana* [118]. However, how the MAP65-3 directly affects the motor activity is unclear.

To investigate if MAP65-3 is able to enhance the binding of the POK2 motor (aa1–589) to the microtubule as it does for the POK2 tail, *in vitro* TIRF microtubule assays were performed with POK2$^{1\text{-}589}$-eGFP-6xHis (hereafter POK2$^{1–589}$-eGFP), which was purifed previously by Dr. Mayank Chugh [54]. As a first look, POK2$^{1–589}$-eGFP at 1 nM, which is at non-single molecule conditions, was mixed with 0 or 20 nM MAP65-3-mCherry into a flow cell with immobilised double-stabilised microtubules. The fluorescent proteins were imaged with TIRF microscopy, while the unlabelled microtubules were imaged with IRM. As expected, POK2$^{1–589}$-eGFP bound microtubules (Fig. 5.35 *top*) in the absence of MAP65-3-mCherry. Surprisingly, when saturating concentrations of MAP65-3-mCherry was used, POK2$^{1—589}$-eGFP bound microtubules less (Fig. 5.35 *bottom*, 5.36). This suggests that despite MAP65-3 being able to bind POK2 via its N-terminal unstructured domain [118], the microtubule binding of the POK2 motor and MAP65-3 are mutually exclusive.

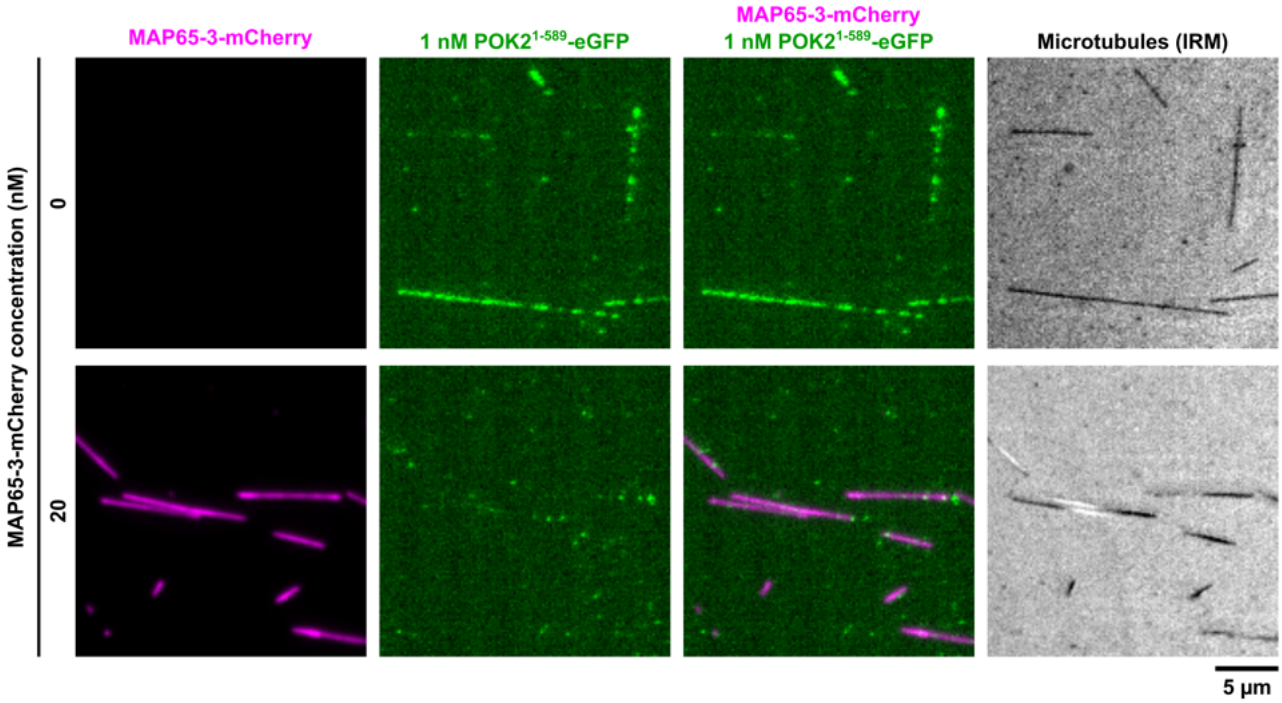

Figure 5.35: MAP65-3 reduces the microtubule binding of the POK2 motor.
Images of 1 nM POK2$^{1–589}$-eGFP binding double-stabilised microtubules in the presence of 0 or 20 nM MAP65-3-mCherry taken with TIRF microscopy. Microtubules were imaged with IRM. The reduction in microtublue binding of non-single molecule POK2$^{1–589}$-eGFP was observed consistently in multiple experimental repeats.

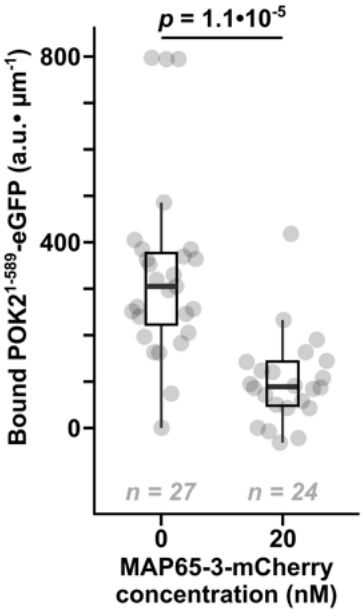

Figure 5.36: Quantification of POK2 motor microtubule binding in the absence or presence of MAP65-3. Background subtracted intensities of 1 nM POK2$^{1–589}$-eGFP along microtubules is plotted against 0 and 20 nM MAP65-3-mCherry. Intensities are obtained from single images such as Fig. 5.35. Box plot is IQR; whiskers are 1.5 IQR; each data point indicates data from one microtubule. Experimental repeats quantified = 1.

To further characterise this reduction in microtubule binding, single molecule conditions for POK2$^{1–589}$-eGFP were assayed with varying concentrations of MAP65-3, from single molecule (0.02 nM) to saturating conditions (20 nM) (Fig. 5.37). Overall, the reduction in microtubule binding of POK2$^{1–589}$-eGFP in the presence of 20 nM MAP65-3-mCherry was reproduced. In the presence of 20 nM MAP65-3-mCherry, POK2$^{1–589}$-eGFP signals on microtubules were no longer detectable even in maximum projections (Fig. 5.37). For a quick first look, the background subtracted eGFP intensities along the microtubule of the maximum projections were measured and plotted against the varying MAP65-3-mCherry concentrations assayed (Fig. 5.38). While there was a general tendency showing a reduction in intensity, the trend did not appear to be significant. This could be a result of the intensity quantification, which was less accurate than landing rate analysis, although it was faster to perform and sufficieintly robust for bulk binding experiments.

To obtain a quick impression of landing rates, kymographs along randomly chosen microtubules were drawn for the different 0.1 nM POK2$^{1–589}$-eGFP and varying MAP65-3-mCherry conditions (Fig. 5.39). From looking at the kymographs, it seems that landing rate of POK2$^{1–589}$-eGFP does not particularly reduce in the presence of 0.02–2 nM MAP65-3-mCherry, but drops off abruptly at 20 nM. More detailed assays using MAP65-3-mCherry concentrations between the 2 to 20 nM range would reveal more insights in the kinetics of MAP65-3 mediated inhibition of POK2 motor microtubule binding. Additionally, quantification of the landing rate would be more revealing of the nature of this inhibition.

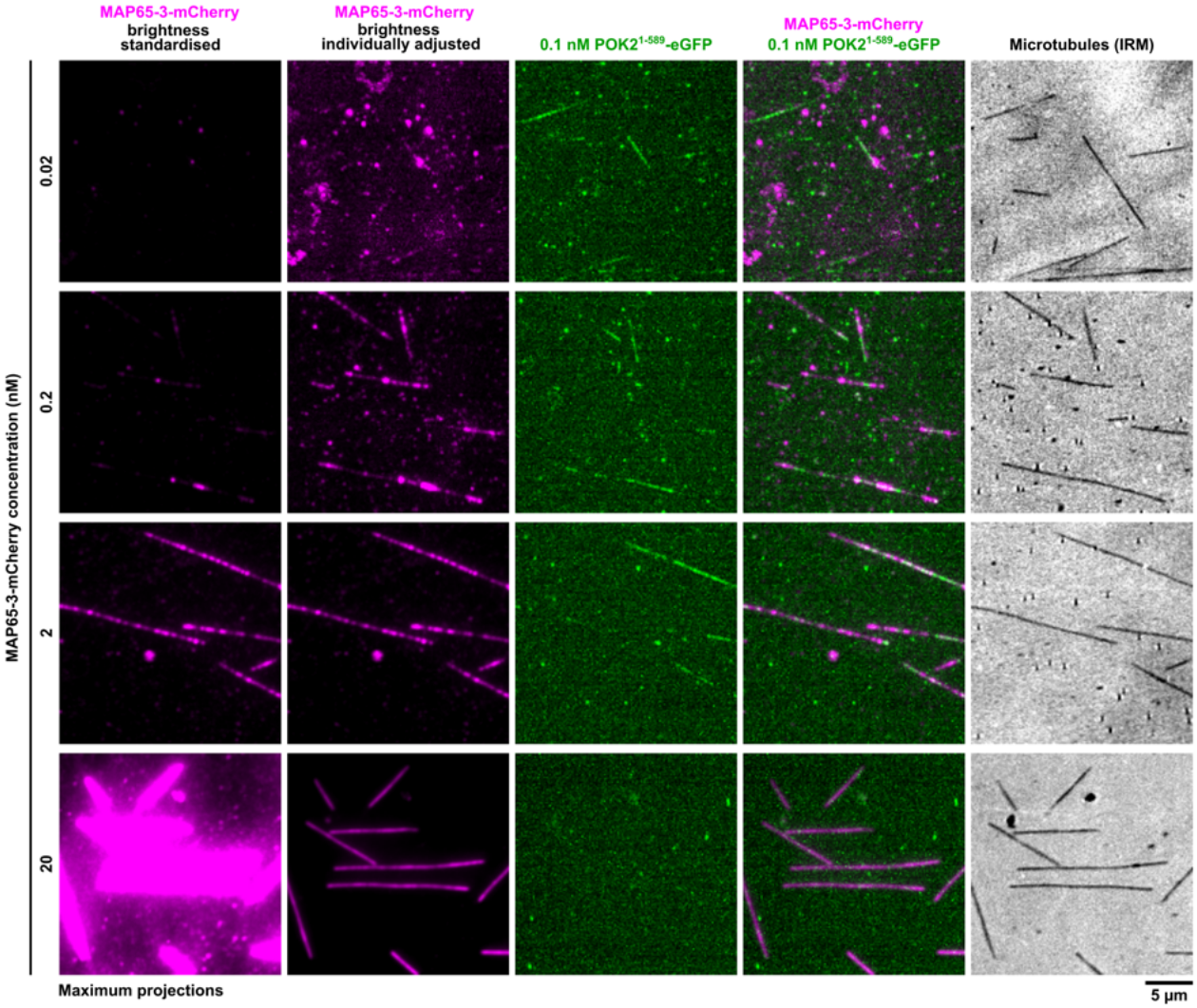

Figure 5.37: Microtubule binding of single molecule POK2 motor in the presence of varying MAP65-3 concentrations.
Maximum projections of TIRF time-lapse images (sampled at 100 ms intervals for 300 slices) of single molecule POK2$^{1–589}$-eGFP at 0.1 nM binding double-stabilised microtubules in the presence of 0.02, 0.2, 2, 20 nM MAP65-3-mCherry. Microtubules were imaged with IRM.

Interestingly, single molecule POK2$^{1–589}$-eGFP and single molecule MAP65-3-mCherry (i.e., 0.1 and 0.02 nM respectively) do not interact on the microtubule (Fig. 5.40). Since the POK2 motor purified well, there was no need to use PEM20 buffer to reduce the influence of salt from the protein's own storage buffer. Instead, PEM buffer was used, where both POK2$^{1–589}$-eGFP and MAP65-3-mCherry were diluted directly into Motility buffer. This means that the lack of interaction between the two proteins was observed at an ionic strength of 160 mN. Interestingly, this ionic strength is the equivalent ionic strength where interaction between the POK2 tail and MAP65-3-mCherry was observed (Fig. 5.27).

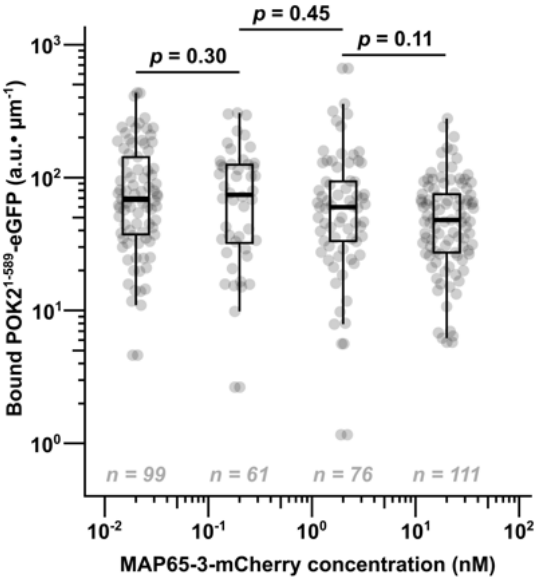

Figure 5.38: Quantification of single molecule POK2 motor microtubule binding in varying MAP65-3 concentrations.
Background subtracted intensities of 0.1 nM POK2$^{1–589}$-eGFP along microtubules is plotted against different MAP65-3-mCherry concentrations (0.02, 0.2, 2 and 2 nM). Intensities are obtained from maximum Fig. 5.37. Box plot is IQR; whiskers are 1.5 IQR; each data point indicates data from one microtubule. Experimental repeats = 2.

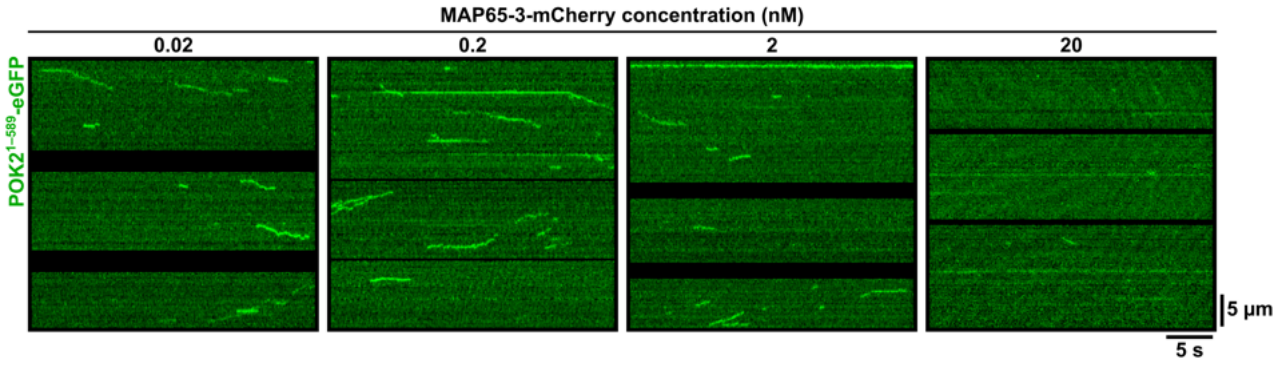

Figure 5.39: Kymographs of single molecule POK2 motor on microtubules in varying MAP65-3 concentrations.
Single molecule POK2$^{1–589}$-eGFP at 0.1 nM travelling along microtubules are visualised by generating kymographs drawn along the length of a microtubule from time-lapse movies acquired by TIRF. Varying concentrations of MAP65-3-mCherry (0.02, 0.2, 2 and 2 nM) were introduced together with the POK2 motor.

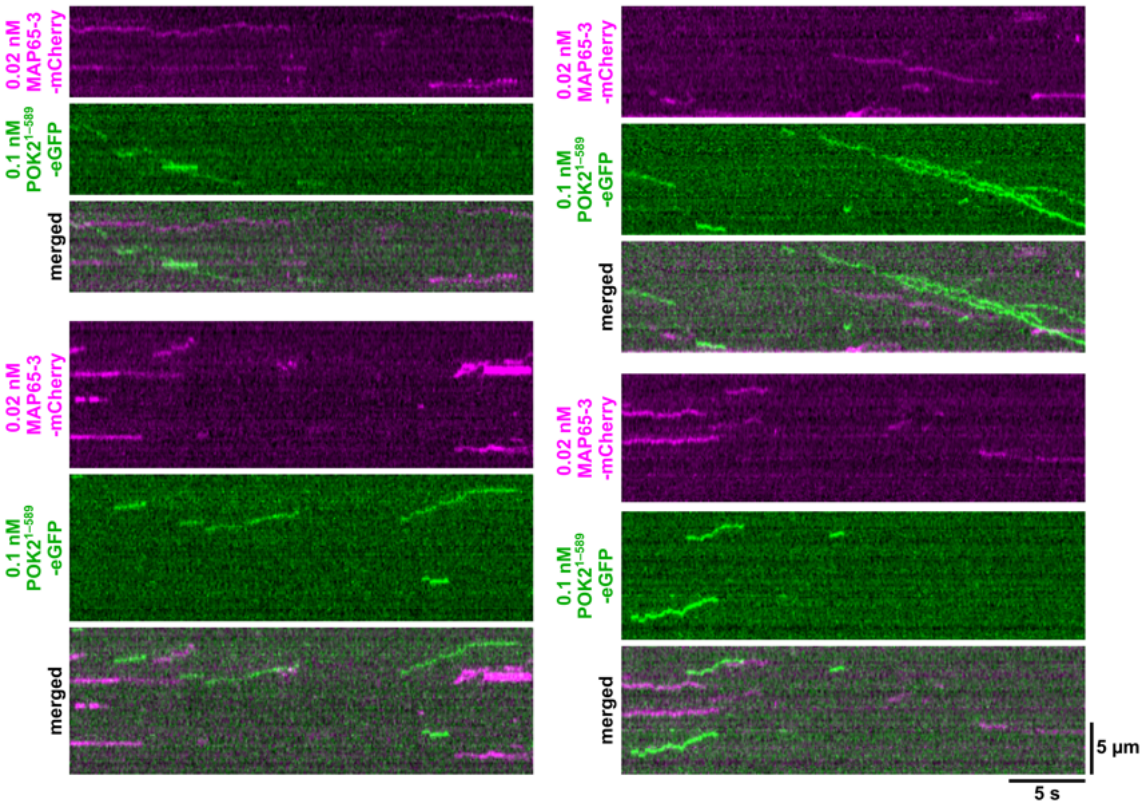

Figure 5.40: Kymographs of single molecule POK2 motor and single molecule MAP65-3.
Single molecule POK2$^{1-589}$-eGFP at 0.1 nM and single molecule MAP65-3-mCherry at 0.02 nM diffusing separately on the microtubule. Time-lapse were acquired with TIRF microscopy. Single molecules were not seen to co-translocate at these ionic concentrations (160 mN).

The data and results for the POK2 motor and MAP65-3-mCherry were preliminary. While the reduction in microtubule binding of the POK2 motor with saturating MAP65-3 concentrations was robust and reproducible, more experimental replicates and detailed analysis are required to draw reliable conclusions into the intricacies of this effect. Moreover, detailed analysis would be required to identify the effect of MAP65-3 on the landing rate, These analyses were not pursued as it extended beyond the scope of this thesis. Nevertheless, the preliminary results have provided interesting insights and would help to steer future experiments towards a promising direction.

Chapter 6

Discussion

The phragmoplast orienting kinesin 2 (POK2) is a division plane marker that localises to the cell division zone (CDZ) throughout plant cell division and guides the phragmoplast to the correct division plane for accurate positioning of a new cross wall. The ability of POK2 to localise to the CDZ is credited to the POK2 tail domain as a tail-only construct retains CDZ localisation *in vivo*. However the specific mechanism of CDZ localisation by the POK2 tail is unclear. In this thesis, I sought to answer this by *in vitro* microtubule and lipid assays with purified constructs of the POK2 tail. I purified eGFP-POK2$^{2083\text{-}2771}$ and showed that it could bind microtubules, increase microtubule binding in the presence of MAP65-3-mCherry and bind lipids. Additionally, I identified the final 2678-2771 residues as important for microtubule and lipid binding as well as MAP65-3-mCherry mediated microtubule binding.

6.1 The two microtubule binding domains of POK2

In this thesis, using *in vitro* total internal reflection fluorescence (TIRF) microscopy-based assays, the POK2 tail was shown to independently bind to and diffuse along microtubules. Additionally, *in vitro* bulk assays indicated that the contribution of the coiled-coil regions in the POK2 tail to microtubule binding is additive as all shorter constructs of the POK2 tail could bind microtubules but at reduced binding affinities. One of the shorter constructs (eGFP-POK2$^{2510-2771}$), however, had a higher microtubule binding affinity than the others, especially when compared to the construct lacking the final 94 residues (eGFP-POK2$^{2510-2677}$). This suggests that the final $\sim$100 residues are particularly important for microtubule binding. Within these $\sim$100 residues is a short stretch of positively charged residues (aa2726-2737, Fig. 3.5) which could mediate electrostatic interactions with the negatively charged E-hooks on the tubulin tails of the microtubules.

This finding is supported by a recent results on shorter POK2 tail constructs binding microtubules

in *N. benthamiana* transient expressions and *Arabidopsis thaliana* stable lines (communication from Dr. Pantelis Livanos and Dr. Sabine Müller), with some constructs even decorating spindle and phragmoplast microtubules. Dr. Livanos and Dr. Müller also identified the positively charge region in the POK2 tail, which they termed 'polybasic domain' but did not further study its interaction with microtubules. Taken together, the data in this thesis and of others strongly support the presence of a second bonafide microtubule binding domain (MBD) in the POK2 tail. Further experiments, such as with microtubules treated with substilisin to remove the E-hooks would be useful to address whether the microtubule binding is indeed via the hypothesised electrostatic interactions.

6.1.1 Details on POK2 tail microtubule interaction

The POK2 tail binds to and diffuses along microtubules and, based on fluorescence analysis, most likely as a dimer. An unbiased diffusion analysis (by analysing all traces that landed on the microtubule) revealed two populations, one stationary population (for traces that did not move) and one diffusive population with a diffusion coefficient, D = 0.03 $\pm$ 0.00 $\mu m^2 s^{-1}$. With this, the frictional drag coefficient can be estimated using Einstein's relation, $\gamma = \frac{k_B T}{D}$ [26], where γ is frictional drag coefficient, k_B is Boltzmann's constant, T is absolute temperature, and D is diffusion coefficient. This gives $\gamma = 8.90 \times 10^{-8}$ N·s·m^{-1}. Frictional force, $F_{friction}$ can then be calculated by $F_{friction} = \gamma \cdot v$, where v is velocity. Given that the kinesin motor-containing N-terminal POK2 construct was reported with a processive velocity of 0.43 $\pm$ 0.02 μm·s^{-1} [53], the resulting frictional force exerted by the POK2 tail would be 0.038 pN (Table 6.1). The N-terminal POK2 construct was reported to reach 0.34 $\pm$ 0.02 pN as single molecules and >1 pN as multimers [53] which are several folds greater than the estimated frictional force exerted by the POK2 tail. Thus, the POK2 tail interaction with microtubules would not be strong enough to impede movement of the POK2 kinesin motor.

Table 6.1: Frictional drag coefficient, γ and frictional force estimation, $F_{friction}$.
γ is estimated using Einstein's relation, $\gamma = \frac{k_B T}{D}$ [26], where k_B is Boltzmann's constant, T is absolute temperature, and D is diffusion coefficient. $F_{friction}$ is calculated by the equation $F_{friction} = \gamma \cdot v$, where v is velocity of the POK2 motor domain, 0.43 $\pm$ 0.02 μm·s^{-1} [53].

	Diffusion coefficient, D ($\mu m^2 s^{-1}$)	Temperature, T (K)	Frictional drag coefficient, γ (N·s·m^{-1})	Frictional force, $F_{friction}$ (pN)
Diffusive eGFP-POK2$^{2083-2771}$	0.031 $\pm$ 0.001	200	8.90×10^{-8}	0.038
Co-diffusive eGFP-POK2$^{2083-2771}$ and MAP65-3	0.011 $\pm$ 0.001 0.001 $\pm$ 0.000	203 203	2.55×10^{-7} 2.80×10^{-6}	0.11 1.20

More MBDs, more processive?

Having an additional microtubule binding domain (MBD) has been reported to increase processivity of motor proteins. For example, the p150 subunit of dynactin is required for dynein processivity [145]. Interestingly, the p150 subunit has two sequential MBD, a CAP-Gly domain which is commonly found in CLIP-170 microtubule binding proteins and a polybasic region [145]. The CAP-Gly domain binds microtubules strongly and actually inhibits dynein motility whereas the polybasic region increases microtubule affinity just enough to promote processivity [145]. Similarly, the second MBD in Kinesin-5/Eg5 and Kinesin-5/BimC was shown to increase microtubule affinity of the motor domain without

affecting motility [302, 346]. The positively charged region in the final ∼100 residues of POK2 could similarly potentiate processivity of the kinesin domain. Moreover, a highly basic MBD in the tail of kinesin-8/KIF18B was found to be inconsequential for processivity but was crucial for tethering the kinesin to microtubule plus-ends [188]. This highlights a potential for the POK2 tail to also function in end-targeting of the POK2 protein at the phragmoplast midzone. This would explain why the POK2 motor construct, POK2$^{1–589}$ decorates the phragmoplast midzone in a region broader than the full-length POK2 and a mini POK2 lacking only the middle domain (Δ590-2082) *in vivo* [118].

The C-terminal region was already suggested previously to aid kinesin motor processivity, as the POK2 motor-containing construct, POK2$^{1–589}$, binds microtubules and was processive towards the microtubule plus-end, although processivity was interrupted by bouts of diffusion [53]. Constructs without the unstructured region (aa1–189) upstream of the kinesin motor failed to increase processivity and instead resulted in a purely diffusve motor construct [53]. The N-terminal unstructured region (aa1–189), unlike the POK2 tail, is not predicted to have any positively charged regions. Instead, the N-terminal region of POK2 is predicted to contain only two polyampholytic stretches (aa1–13 and 40–54) and one polar region (aa118–131) (MobiDB [243]). Hence, it is unlikely to increase processivity by providing a second MBD like the POK2 tail. Speculatively, I would rather suggest that the N-terminal unstructured region would interact or dock on the kinesin motor to mediate certain conformational changes that improves bind-release coordination between the two motor heads of a functional POK2 dimer. Proving this would require detailed structural studies with techniques such as high-resolution cryo-electron microscopy or cross-linking mass spectrometry.

More MBDs, more microtubules?

The second MBD in the tail effectively makes another microtubule the 'cargo' which a kinesin transports. This results in microtubule bundling and sliding, which has been reported for kinesin-1 [111, 221, 275, 305] and kinesin-14 [91, 136, 137, 204, 219, 233, 318].

Plant kinesin-14s KCBP, KATB and KATC have all been proposed to function in arrangement of microtubule arrays such as the preprophase band (PPB), phragmoplast and cortical microtubule (CM) network. Like POK2, KCBP binds to the cell division zone (CDZ) and the phragmoplast [318]. However, other than a trichome morphogenesis defect, the *kcbp-1* mutant does not exhibit any cytokinetic defects [318]. Hence, it is unclear what KCBP does during cytokinesis and whether or not it has anything to do with its ability to bundle and/or slide microtubules.

Whether or not POK2 plays a role in microtubule bundling and sliding and thus function in organising the PPB and phragmoplast would require studying the full-length protein. Perhaps like its fellow family member human kinesin-12/15/KIF15, it would be able to tetramerise and bundle microtubules in a similar fashion [308]. Or perhaps the second MBD would help increase processivity when tetramerised like for kinesin-5/Eg5 [346]. A more important question is whether or not another microtubule

bundling protein is necessary at the PPB or phragmoplast, as in addition to KCBP, several MAP65s are also localised here (Table 2.2). If any, the type of microtubule bundling or sliding would have to be unique to POK2, either in microtubule selectivity, force generation or cross-bridge distance. Further experiments into different types of microtubule bundling would also shed light on potential events occuring in the PPB and phragmoplast.

Don't slide it, park it!

Increasing processivity of the kinesin motor or facilitating microtubule bundling may not be the only function of an additional MBD. Even for kinesin-1, which has been shown to bundle microtubules both *in vivo* and *in vitro* [111, 221, 275, 305], *in vivo* expression of kinesin-1 is diffuse and does not seem to promote microtubule bundling [41, 127]. Hence, perhaps in conjunction with cell type specificity, the second MBD was proposed to instead bind to the kinesin motor and microtubule tightly to 'park' inactive kinesins on the microtubule [70]. This model possibly extends to the CAP-Gly domain, which binds microtubules tightly, in the p150 subunit of Dynactin [145].

The POK2 tail is theoretically estimated to only generate 0.038 pN frictional forces (Table 6.1), something the POK2 motor which can generate up to 0.34 pN can easily overcome [53]. Hence, it is more likely that the POK2 tail increases processivity of the kinesin motor rather than inhibit its motility. However, the smaller diffusion coefficient of the MAP65-3 and POK2 tail heterocomplexes estimates a frictional force of 1.20 pN (Table 6.1), suggesting that a combination of the POK2 tail and MAP65 could easily 'park' the POK2 motor in place. This is consistent with the POK2 N-terminal domain construct decorating a wider area of the phragmoplast midzone compared to the full-length protein *in vivo* [118]. Upstream of the POK2 motor domain is the short unstructured domain that also binds MAP65-3 [118], which preliminary data in this thesis suggests is to some extent mutually exclusive with POK2 motor binding on the microtubule. A reduction in microtubule binding with saturating concentrations of MAP65-3 reduced microtubule binding of the POK2 motor construct, POK2$^{1\text{-}589}$-eGFP, whereas microtubule binding was seemingly unaffected at lower MAP65-3 concentrations. Single molecule interactions between the POK2 motor and MAP65-3 were not observed. Hence, whether or not MAP65-3 could affect POK2 motility via its upstream N-terminal region is not entirely clear and would be interesting to investigate in the future.

A valuable construct to obtain would be the full-length POK2, which has been difficult to clone [118]. Even *in vivo* expression of the GFP-tagged protein required a chimeric construct that had contained intron sequences [118]. Since the full-length protein would be difficult to obtain, the next best thing would be a POK2 without the central domain, POK2$^{\Delta 590\text{–}2082}$, which has been shown to localise to both the phragmoplast midzone and CDZ *in vivo* [118]. Initial attempts to obtain this construct and a construct with only N-terminal unstructured region and the POK2 tail, POK2$^{\Delta 190\text{–}2771}$ were unsuccessful as the protein did not express well (Table 7.3). The POK2$^{1\text{–}589}$ and POK2$^{190\text{–}589}$ expresses and purifies well from insect cells. Hence the difficulty to express the minimal POK2 constructs is likely due to the presence of the POK2 tail. Nevertheless, in light of the results from this

thesis, even more minimal constructs could be designed in the future, such as constructs containing only the final ∼100 residues, which might be easier to express and purify.

6.2 Interaction with MAP65-3

The data in this thesis adds to the existing knowledge regarding interaction between the POK2 and MAP65-3. Firstly, the interaction between the POK2 tail and MAP65-3 was successfully reconstituted *in vitro*. Additionally, the POK2 tail region that interacts with MAP65-3 was narrowed down to aa2510-2771, with the final 94 residues being necessary for robust microtubule recruitment in the presence of MAP65-3.

Secondly, direct interaction between MAP65-3 and the POK2 tail was visualised as co-diffusing single heterocomplexes. This interaction is salt sensitive and was most abundant at 160 mN ionic strength. This is interesting, because data from this thesis suggests that both the POK2 tail and MAP65-3 interacts individually with microtubules in an electrostatic manner. This posits local ionic strength as a possible regulator for the interaction between the proteins and microtubules and also with each other.

Thirdly, detailed analysis of the single co-diffusing heterocomplexes provides novel insights into the interaction between the POK2 tail and MAP65-3 with microtubules and with each other. Interestingly, stochiometric analysis of eGFP and mCherry fluorescence of co-diffusive heterocomplexes did not identify a particular trend. This suggests that the interaction between the POK2 tail and MAP65-3 is not specific to a binding pocket in a sense, but rather through multivalent interactions. The specific stochiometry might also be obscured due to the ability of both proteins to interact with the microtubule by themselves, again adding more multivalent interactions into the mix. As expected, the heterocomplexes also diffuse slower compared to the POK2 tail alone, indicative of a stronger interaction with the microtubule.

Fourthly, preliminary experiments with MAP65-3 and the POK2 motor revealed that saturating amounts of MAP65-3 reduced microtubule binding of the POK2 motor. At non-saturating amounts of MAP65-3, microtubule binding of the POK2 motor is unaffected. This can be explained by the lack of single molecule interaction observed between MAP65-3 and the POK2 motor, even at equivalent ionic strengths where single molecule POK2 tail interacted with single molecule MAP65-3. This posits that MAP65-3 and the POK2 motor compete for the same binding site on the microtubule and stands in contrast to results from others that MAP65-3 directly interacts with the aa1–189 unstructured region [118] and results in this thesis that MAP65-3 interacts with the POK2 tail.

6.2.1 In the context of the CDZ

POK2 is characterised by its dimorphic localisation during the cell cycle, giving rise two spatiotemporally distinct populations: a CDZ-localised and a phragmoplast midzone-localised population. The

former and latter are attributed to the C- and N-terminal domains of POK2 respectively. When expressed *in vivo*, the POK2 tail localises only to the CDZ. The POK2 tail has thus only two opportunities to encounter MAP65-3: (1) at the PPB and (2) at the CDZ during late telophase when the phragmoplast finally reaches the cell plate fusion site.

(1) PPB-localised MAP65-3 meets PPB/CDZ-localised POK2

The PPB acts as a recruitment platform through which many CDZ-resident proteins are initiially gathered. Eventhough MAP65-3 is essential for phragmoplast integrity [44, 123, 214], its function in the PPB has not been elucidated. A phenotype for the PPB in MAP65-3 *dyc283* and *ple-2* mutants has never been reported. If we take this to mean that PPB morphology is MAP65-3 independent, then MAP65-3 does not play any role in PPB establishment or structural maintenance despite its microtubule bundling activity [123]. This leaves open the possibility of MAP65-3 as a recruitment hub for CDZ-proteins itself. While most CDZ-resident proteins have their own MBDs, MAP65-3 could enhance intrinsic microtubule binding like for the POK2 tail to increase specificity and sensitivity of the PPB recruitment system.

(2) phragmoplast midzone-localised MAP65-3 meets CDZ-localised POK2

The second encounter possibility of CDZ-localised POK2 and MAP65-3 is during late telophase when the phragmoplast reaches the CDZ at the CPFS. Here, as the PPB is long gone, the POK2 tail localises to the CDZ either by direct lipid binding as shown in this thesis or by binding other CDZ-resident proteins such as IQD8 [153]. While the specific region in the POK2 tail which binds IQD8 is not yet elucidated, the aa2678-2771 region in the POK2 tail was shown in this thesis to be important for both lipid binding and MAP65-3 mediated microtubule binding enhancement. While further experiments are required to prove or negate the possibility of any interaction between the two POK2 and MAP65-3 populations, the current available data does not favour the hypothesis that the CDZ-localised POK2 population and the phragmoplast midzone-localised MAP65-3 population would interact.

6.2.2 In the context of the phragmoplast midzone

While the POK2 tail does not localise to the phragmoplast midzone *in vivo* [118], it does have an effect on midzone retention of the full protein as the POK2$^{1–589}$ has a wider localisation to the midzone compared to the full-length POK2 and the POK2$^{\Delta 590–2082}$ construct [118]. The POK2 tail is unlikely to play a significant role, as it does not localise to the phragmoplast midzone in the *pok1 pok2* mutant background where MAP65-3 is present at the midzone [118]. However, preliminary *in vitro* results show that saturating amounts of MAP65-3 outcompetes the POK2 motor for microtubule binding. These preliminary results thus raises the possbility of the POK2 tail as necessary to tether the entire POK2 protein to the phragmoplast midzone via its interaction with MAP65-3.

6.2.3 In the context of full-length POK2

MAP65-3 has been shown to interact with both the N- and C-terminal domains of POK2, each of which has a distinct localisation *in vivo*. Interestingly, MAP65-3 localisation overlaps with both, but does not cross-recruit the terminal domains (i.e., the C-terminal domain to the phragmoplast midzone or the N-terminal domain to the PPB). Seeing as the absence of one or the other terminal domain does not result in abnormal recruitment by MAP65-3, it is unlikely that the N- and C-terminal domains compete for the same binding site on MAP65-3. If they do, there would be an upstream regulatory element that prevents aberrant attachment by the undesired POK2 terminal domain. This could be local ionic strengths or accessory proteins, but is at the moment unclear. To further understand the interaction between MAP65-3 and the terminal domains of POK2, three-colour *in vitro* competition assays with all three constructs would be very helpful.

6.2.4 Limitations and future directions

The diffusion coefficient analysis suggests that the MAP65-3-POK2-tail heterocomplexes exist in two populations - a slower and a faster diffusing population. However, the stochiometric analysis is not reflective of this. A significant limitation of these analyses is the sample size (number of traces <50). This was also the reason why interaction times were not analysed, as there were huge variations given the small sample size.

Moreover, purification of MAP65-3-mCherry is tricky, unlike the purification of tagged MAP65-1 [182]. The attachment of a fluorophore to the N-terminus (as previously reported [123]) or C-terminus (as in this thesis) is not robust, and a significant portion of the purified protein lacks the mCherry fluorophore. Further purification by size exclusion chromatography ([123]) is unable to alleviate this issue as MAP65-3 dimerises as double-tagged, single-tagged and untagged dimers[1]. These species and the tagged and untagged monomers were also observed with mass photometry (Fig. 7.3). Hence, we cannot completely rule out the presence of more co-diffusive traces or the possibility of different and specific stochiometries in the MAP65-3 and POK2 tail heterocomplexes.

Another reason why the analysis was difficult was the mCherry fluorophore on the MAP65-3. At the time of construction, mCherry was the best fluorophore available for excitation in the $\sim$550–600 nm range. However, mCherry is two-fold less bright compared to eGFP and also less photostable (Table 6.2), meaning it photobleaches more quickly. Hence, optimal imaging conditions were a trade-off between photostability and imaging quality. Since then, other fluorophores have been identified and could be used instead of mCherry, such as mRuby3 which is four-fold brighter than mCherry although less photostable (Table 6.2). Since it is more fluorescent, lower laser power and shorter exposure times and/or longer sampling intervals could potentially circumvent the increased photobleaching probability. Switching the fluorophore might also have a positive effect on protein stability and yield. As such, MAP65-3 full-length and truncations constructs for the future have been prepared with mRuby3 or

[1] This is in contrast to MAP65-1 and MAP65-5 which have been reported to be monomeric in solution [98].

mNeonGreen (which is brighter than eGFP and similarly photostable (Table 6.2), but with reduced propensity to dimerise spontaneously) (Fig. 7.5).

Table 6.2: Fluorophore properties.
Excitation and emission wavelength, brightness, pKa, maturation and photostability half-life of fluorophores of interest. Data is taken from FPbase (https://www.fpbase.org/) unless cited otherwise, except for photostability of which references are listed directly in the table.

Fluorophore	Ex (nm)	Em (nm)	Brightness	pKa	Maturation (min)	Photostability, $t_{\frac{1}{2}}$ (s)
eGFP	488	507	33.54	6.0	25	150 [14]
mCherry	587	610	15.84	4.5	15	104 ± 23 [74]
mNeonGreen	506	517	92.8	5.7	10	158 [14]
mRuby3	558	592	57.6	4.8	136.5	12 ± 1 [74]

6.3 CDZ deposition

POK2 initially localises to the cell division zone (CDZ) by directly binding microtubules of the preprophase band (PPB) via its motor and non-motor microtubule binding domain (MBD)s, enhanced by its interaction with MAP65-3. However, upon entry into mitosis, the PPB disassembles, with POK2 continuing to mark the CDZ. In this thesis, the POK2 tail which is responsible for POK2 localisation to the CDZ [118], was shown to bind directly the several anionic lipids in lipid blot and giant unilamellar vesicle (GUV) assays. These results highlight the possibility of CDZ residency mediated by direct binding to local lipids by the POK2 tail.

Only the eGFP-POK2$^{2083-2771}$ and eGFP-POK2$^{2510-2771}$ constructs bound with high affinity to phosphatidic acid (PA), cardiolipin (CL) and phosphoinositol phosphates (PIPs) PI4P, PI(4,5)P_2 and PI(3,4,5)P_3 in the lipid blot assay. Remarkably, eGFP-POK2$^{2510-2677}$ did not bind well to any of the lipids, which implicates the final $\sim$100 residues, in addition to microtubule binding and MAP65-3 interaction, also in lipid binding. As PA, CL and the PIPs are anionic, this raises the possibility of lipid binding via the positively charged region previously mentioned (Fig. 6.1). In line with this, communication with Dr. Pantelis Livanos and Dr. Sabine Müller have revealed that this same region was found to bind anionic lipids in their assays as well.

Despite evidence for interaction to lipids via electrostatic charges, the POK2 tail does not seem to interact ubiquitously with all anionic lipids. In the lipid blot assay, the POK2 tail does not bind phosphatidylserine (PS), phosphatidylglycerol (PG), phosphoinositol (PI) or sulfatide (Fig. 5.32). It does not seem to be a distingushable steric or chemical feature shared between anionic lipids that bind or do not bind the POK2 tail (Fig. 6.2). Hence, it is unclear why the POK2 tail has a preference over some lipids than others.

Of the anionic lipids that interacted with the POK2 tail, CL is not known to localise to the plasma membrane in plant cells, and are only found in plastid membranes [24]. Meanwhile, neither PA nor any

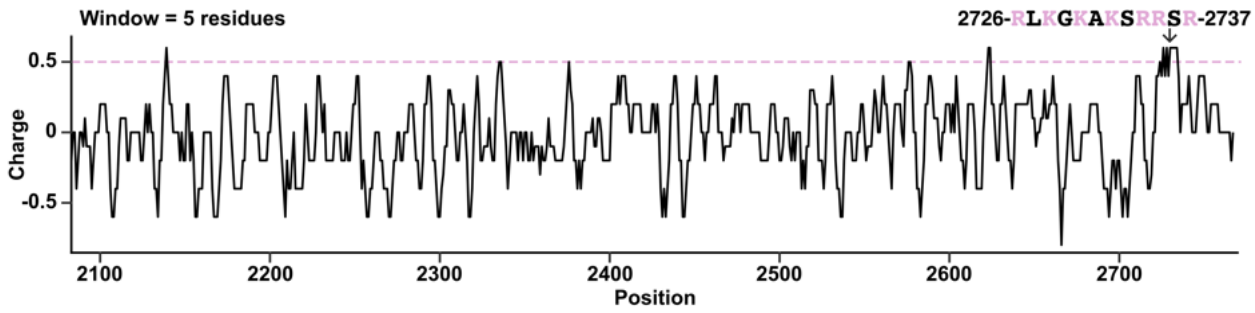

Figure 6.1: Positively charged region at the end of the POK2 sequence.
Charge calculation for the final ~800 residues of POK2 based on a window size of 5 residues, calculated with EMBOSS Charge. A particularly positively charged region, aa2726-2737 is highlighted where basic residues (positively charged) are labelled pink.

of the PIPs specficially demarcate the plasma membrane at the division zone [43, 287] (although PI4P and PI(4,5)P_2 specifically bind the cell plate from anaphase and late telophase respectively [286, 287]). This is in contrast to the plasma membrane enrichment of PA, PS and phosphatidylethanolamine (PE) and depletion of PI(4,5)P_2 at the division plane in animal and fungal cells [43, 69, 90, 151]. Hence, while the POK2 tail may be sufficient to reside POK2 to the plasma membrane, restriction to the CDZ would occur via a different mechanism and not simply through lipid binding.

6.3.1 *We're all in this together*

Recent publications have noted that many CDZ-resident proteins cross-interact with one another [62, 153]. POK2 itself interacts with TANGLED [215, 339], RanGAP1, IQD proteins [153], PHGAP1/2 and MAP65-3 [118]. Consequently, a model in which CDZ proteins scaffold themselves at the CDZ was proposed [62].

CDZ proteins, (self-)assemble!

The scaffold in question was proposed to be the IQD proteins [62], of which 43, 58, 84% of the IQD6, 7, and 8 protein sequences consists of intrinsically disordered regions (IDRs) respectively (Fig. 6.3). IDRs are flexible protein regions, often charged and of variable sequence, capable of mediating multivalent interactions [191]. The multivalency of IDRs allows IDR-containing proteins to act as platforms for protein interactions, providing a wider range of interactions in contrast to ordered domains which mediate 'lock-and-key' associations. In line with this, IDRs are also hallmarks of proteins capable of undergoing phase transition into membraneless compartments [191].

Coincidentally, several other CDZ proteins also carry IDRs (Fig. 6.3). Characteristically and reminiscent of nanodomains, POK2 [118], TANGLED [339], KCBP [40], PHGAPs [303], MAP65-4 [163] and IQD proteins [153] decorate the division plane as punctae. The punctate localisation of these proteins to the CDZ could be evidence of IDR-mediated self-assembly. Even so, the purpose of nanodomain-like localisation to the CDZ is not yet experimentally investigated.

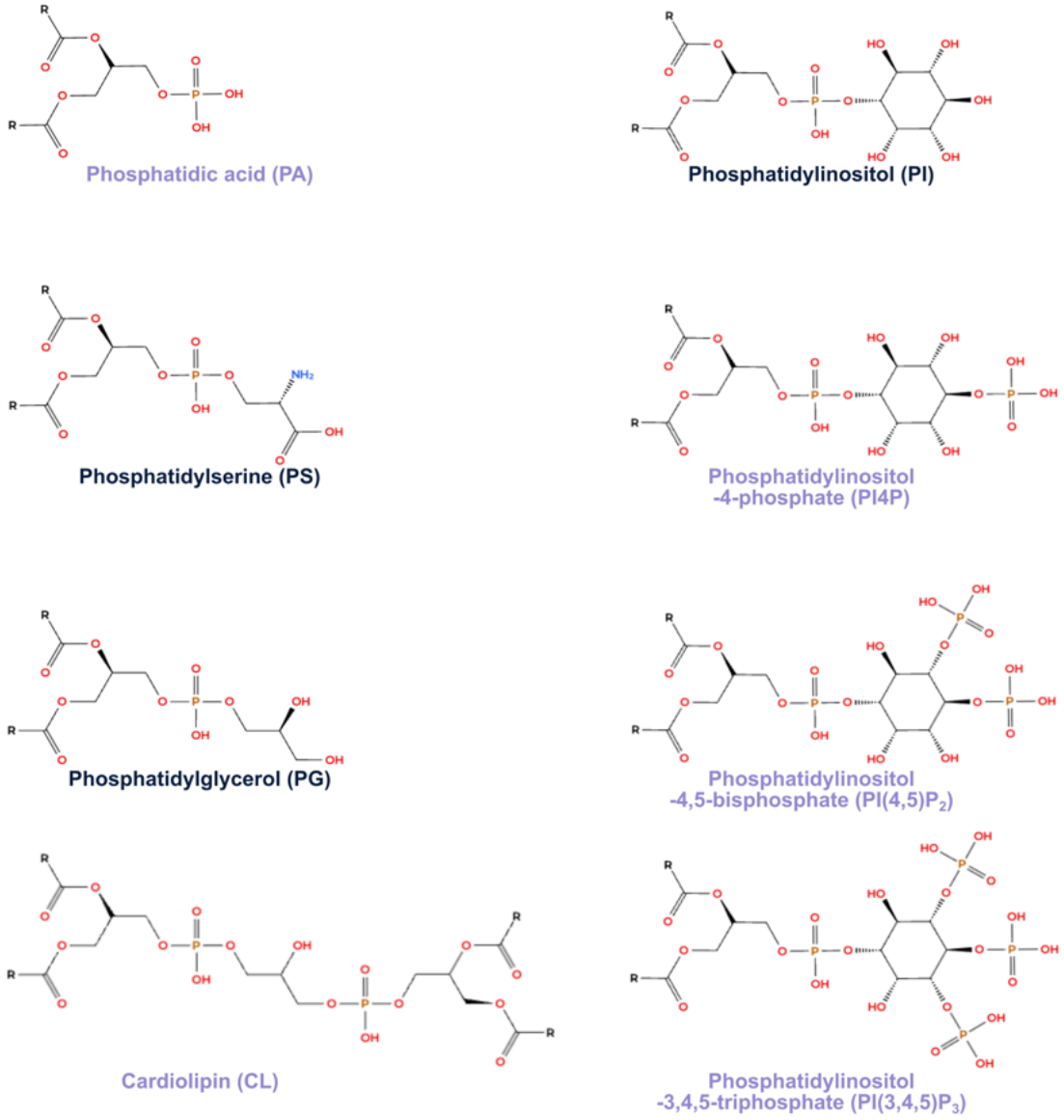

Figure 6.2: Chemical structure of anionic lipids of interest.
Chemical structures were drawn using MolView (https://app.molview.com/ [278]). Names in lavender indicate lipids that interacted with POK2 tail in lipid blot assays.

Interestingly, IDRs themselves have been implicated in membrane association since they share with lipid binding modules a prevalence of charged amino acids in their sequences [59]. In the case of POK2, the positively charged region that binds lipids (Fig. 5.32, [171]) is located within one of its IDRs. Accordingly, 15% of intrinsically disordered proteins are said to be lipid-binding proteins [67, 95]. Membrane association of IDR-containing proteins was proposed to even mediate a disorder-to-order transition [59]. Consequently, IDR-containing transmembrane receptors are noted to transduce intracellular signalling via their cytoplasmic IDRs [200, 284] by triggering self-oligomerisation into higher assemblies or by acting as signalling hubs.

The pervasiveness of IDRs in CDZ proteins, mutlivalency, membrane binding potential, disorder-

to-order promotion of IDRs all attractively point to support the previously proposed scaffolding model [62]. The multivalency provided by not only IQD proteins, but other CDZ proteins themselves additionally, could interconnect the CDZ proteins to prevent dissociation and diffusion. The presence and function of IDRs in plant transcription factors and receptors are well characterised [129], and invites comparison to CDZ proteins. However, more targeted experiments would be required to directly ascertain what the role of IDRs would be at the CDZ.

Clustering of POK2: aggregates or condensates?

The purification of the POK2 tail was challenging as most of the protein remained in the insoluble fraction after lysis and centrifugation. Despite doubling the amount of cell culture used in the purification, the final protein yield did not significantly increase. At the mid-nanomolar range, large clusters of the POK2 tail was seen to bind microtubules

The fact that not all the protein sedimented out in the sedimentation assay and that the yield of the protein did not increase, lend themselves to the possibility that the solubility of the POK2 tail was not a simple issue of protein aggregation. Several proteins with a propensity to undergo phase separation by way of their IDRs also tend to aggregate [12]. In the same vein, the POK2 tail, of which IDRs constitute 31% (Fig. 6.3), could have existed in an equilibrium between its free proteins and phase separated droplets, where a portion of phase separated droplets already transitioned irreversibly into aggregates. Hence, the inclination towards aggregation could be simply characteristic of the protein. Substantiating this is the punctate decoration of POK2 at the CDZ and the localisation of *in vivo* transiently expressed POK2 tail in *N. benthamiana* as cytoplasmic foci [118]. As with other CDZ proteins, the ability of POK2 to self-oligomerise into larger assemblies, perhaps by way of its IDRs, may be important for its function in marking the CDZ. Determining whether or not the POK2 tail truly phase separates into droplets would require more refined experiments such as fluorescent recovery after photobleaching (FRAP) or disruption by 1,6-hexanediol.

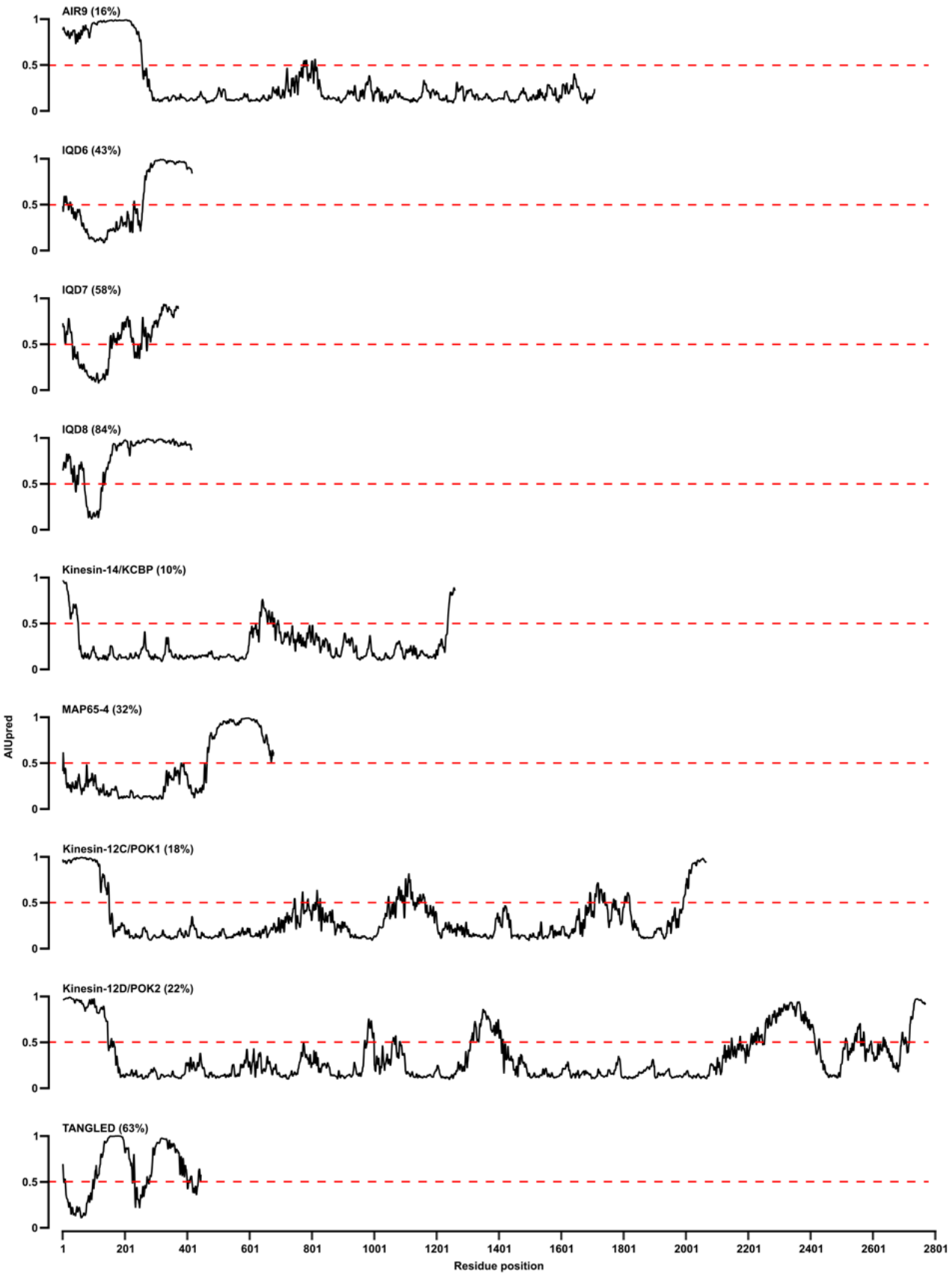

Figure 6.3: Disorder prediction of CDZ resident proteins.
Predictions were performed using AIUpred [82] for whole protein sequences from *Arabidopsis thaliana*. Red dashed line indicates cutoff at 0.5. Numbered percentages in brackets indicate percent amino acid sequence predicted to be disordered.

6.4 Gathering all the cookie crumbs...

The results in this thesis point towards a versatile POK2 tail, capable of binding microtubules, lipids and MAP65-3. All these interactions seem to be largely mediated through the final ∼100 residues, which houses a short positively charged region. While the interactions with microtubules and lipids are mostly likely electrostatic and would potentially be mutually exclusive, the MAP65-3 interaction might not necessarily be solely due to charge. Even though microtubule binding of the POK2 tail and MAP65-3 individually are salt dependent, MAP65-3 is able to enhance POK2 tail microtubule binding across different ionic strengths (Fig. 5.27). That is not to say that the positively charged region does not affect microtubule binding enhancement by MAP65-3 at all, as MAP65-3 enhances eGFP-POK2$^{2510\text{-}2677}$ microtubule binding much less than for eGFP-POK2$^{2510\text{-}2771}$ (Fig. 5.23). Hence, the possibility for mutual exclusivity is still present, but to what degree is unclear.

6.4.1 *POKtopus: grabbing its way to the CDZ*

Together with key events during the cell cycle, the knowledge that the POK2 tail interacts microtubules, lipids and MAP65-3 has allowed for a sequential, multilevel and robust model for CDZ deposition of POK2. Firstly, the PPB is assembled in part through microtubule cross-linking by MAP65s which localises to the PPB microtubules. With the PPB set up, POK2 binds PPB microtubules via their motor and non-motor microtubule binding domains (MBDs) (Fig. 6.4, *Step (1)*). Several binding modes are possible: (a) binding through the kinesin motor domain which is processive and diffusive, but overall plus-end directed [53], (b) simultaneous binding of both MBDs to the same microtubule, which possibly increases processivity for more efficient plus-end directed movement, and (c) simultaneous binding of both MBDs to different microtubules, effectively cross-linking the microtubules bound (Fig. 6.4, *Step (1, a–c)*). The aforementioned binding modes are within the realm of possibilities, but whether or not they actually take place *in vivo* on the PPB is still inconclusive. For one, the plus-end directed motility of POK2 is necessary for plus-end accumulation at the phragmoplast midzone, but end accumulation might not be necessary at the PPB.

Meanwhile, MAP65-3 on the PPB would enhance POK2 microtubule binding (Fig. 6.4, *Step (2)*), either by directly interacting with POK2 via its tail or N-terminal unstructured domain or by locally modifying the microtubule environment that would encourage POK2 binding. This step may occur simultaneously as and help facilitate *Step (1)* and would locally concentrate POK2 to the cell cortex.

The enrichment of POK2 on the PPB might encourage formation of large multivalent complexes, perhaps phase separated condensates (not depicted in Fig. 6.4), such that a POK2 cluster would simultaneously bind PPB microtubules, the plasma membrane and other PPB-/CDZ-resident proteins (Fig. 6.4, *Step (3)*). In this step, POK2 may or may not be still bound to MAP65-3. Nevertheless, MAP65-3 would be phosphorylated upon entry into mitosis, which inactivates its microtubule binding, and thus disassembling the PPB. POK2s that are already bound to the plasma membrane would be unaffected by PPB disassembly and remain bound at the CDZ. POK2s which were only associated

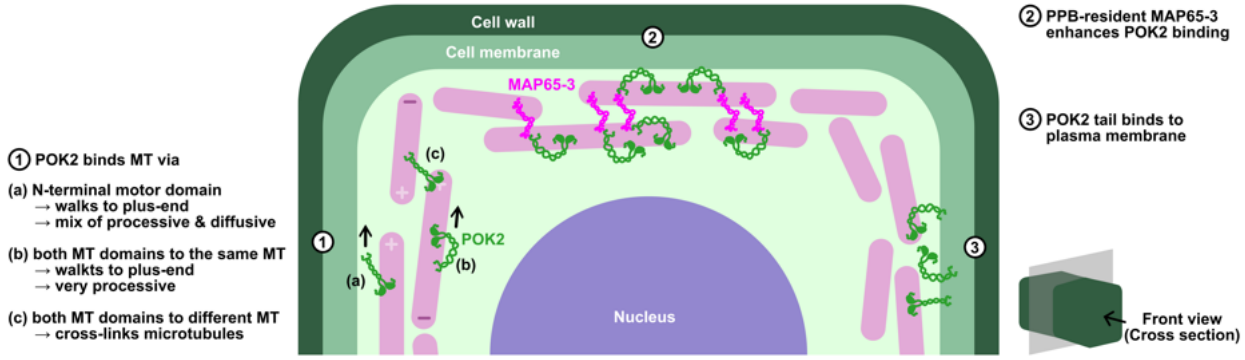

Figure 6.4: Proposed model of POK2 deposition at the CDZ.
Cartoon with a simplified depiction of preprophase in a cell. The cross-section is viewed perpendicular to the division plane. Representative microtubules (pink) are arranged cortically to resemble the PPB. The proposed steps in which POK2 takes to deposit at the CDZ is depicted sequentially from left to right (circled numbers, 1–3). In *Step (1)*, POK2 binds to PPB microtubules by its motor and non-motor microtubule binding domains in its N- and C-terminal regions respectively. In *Step (2)*, POK2 localisation to the PPB is enhanced by PPB-resident MAP65-3. In *Step (3)*, POK2 deposits at the plasma membrane that lies in proximity to the PPB microtubules. *Step (3)*, however, occurs through a mechanism that has yet to be clearly defined.

with PPB microtubules would be released and positioned near the plasma membrane, priming them for binding. Thus, the multifaceted POK2 tail serves as a versatile interface that facilitates its robust recruitment and residence at the CDZ.

6.4.2 *POK2MON, gotta catch 'em all!*

Once deposited at the CDZ, POK2 would remain here either by direct lipid binding through its tail or through interactions with other CDZ-resident proteins. Previously, I discussed how cross-interactions between CDZ-resident proteins could prevent their dispersal around the plasma membrane, as there was no enrichment of specific lipids at the CDZ [43, 287]. While the role of the POK2 motor in microtubule plus-end directed motility for initial CDZ deposition remains unclear, its function in late cytokinesis is well-defined [53, 118]. Attached to the plasma membrane via its tail, the POK2 motor is free to capture incoming microtubules extending out from the growing phragmoplast (Fig. 6.5, *Step (1)*). The POK2 would walk itself towards the plus-end of the microtubule, causing the microtubule to slide outwards. This would point the plus-ends directly at the CDZ, and in doing so, guide the midline of the phragmoplast to the CDZ. As the phragmoplast continues expanding centrifugally, it pushes against the POK2s which are in turn walking themselves to the microtubule plus-ends (Fig. 6.5, *Step (2)*). The push from the POK2s walking to the plus-ends and the push back from the phragmoplast inadvertantly focusses the POK2s into a finer division plane (Fig. 6.5, *Step (3)*), while cross-interactions of POK2 and other CDZ-resident proteins would prevent potential overfocussing. The focussing has been proposed to be the basis of the narrowing of the CDZ into the finely defined CPFS [53].

The population of end-accumulated POK2s and MAP65-3s already present on phragmoplast microtubules would encounter the POK2 population at the CDZ. Whether or not the MAP65-3s interact

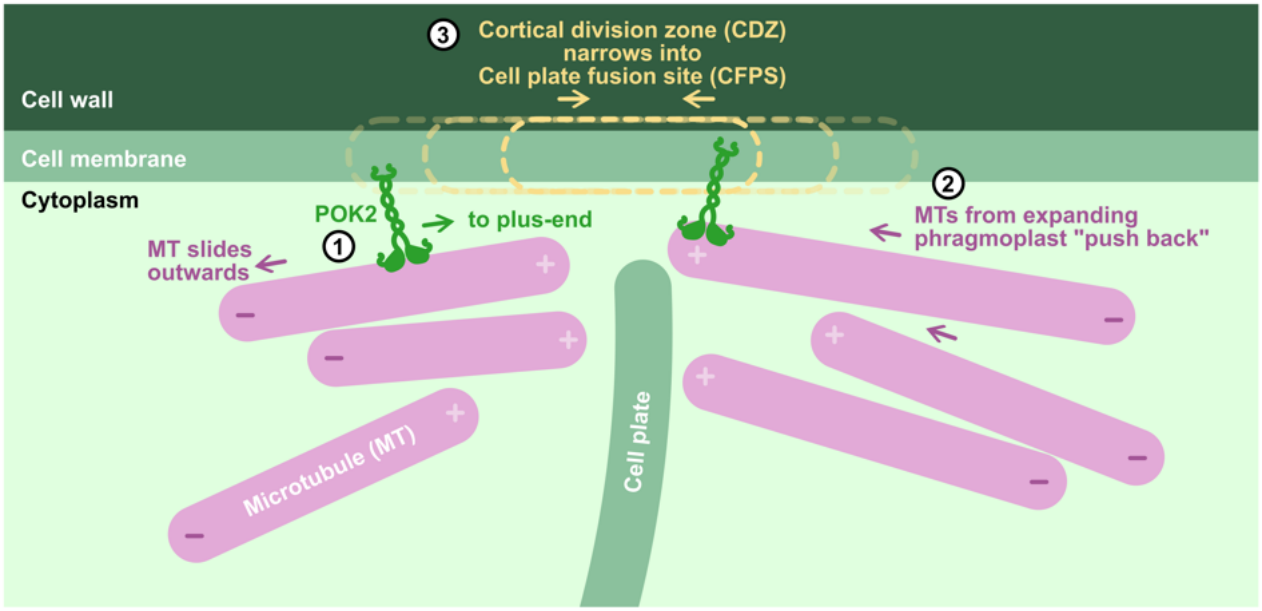

Figure 6.5: POK2 microtubule plus-end motion and phragmoplast expansion focusses the CDZ into the CPFS.
Simplified cartoon depicting key steps (circled numbers, 1–2) of POK2 capturing microtubules from the expanding phragmoplast in late cytokinesis. The cross-section is viewed along the division plane. In *Step (1)*, POK2 at the cell division zone (CDZ) binds to microtubules from the expanding phragmoplast and walks towards the plus-end. For now, if we take POK2's position as static, the microtubule would slide outwards, leaving the microtubule to face end-on towards the POK2 as in *Step (2)*. However, POK2 is not anchored to a fixed position, and as it pushes the microtubule away by its plus-end motility, the phragmoplast pushes back via its microtubules as it expands towards the CDZ. This causes the POK2 at the cell membrane to bunch together, thus focussing the CDZ into the defined cell plate fusion site (CPFS) (*Step (3)*).

with CDZ-resident POK2s is at the moment unclear. Whereas phargmoplast midzone-resident POK2s, having fulfilled their role in stabilising the phragmoplast [118, 167], might simply dissociate. On the other hand, being in close proximity and at high local concentrations, the two POK2 populations could phase separate into condensates. If true, POK2 condensation would render the capturing of phragmoplast microtubules even more efficient and robust.

Altogether the results of this thesis revealed and characterised the binding capabilities of the POK2 tail to microtubules, lipids and MAP65-3. These findings contributed to the development of a model for sequential and multiplex binding of the POK2 tail during CDZ deposition and refined previous understandings of its role at the phragmoplast midzone and in CDZ focussing. Nevertheless, further research into aspects such as interaction exclusivity, phase separation potential, salt dependency, etc., is required to explore the new concepts introduced in this work. Overall, this doctoral research has further expanded on the current understanding of underlying mechanisms behind division plane positioning, a process essential in cell patterning and, ultimately, organism morphology of plants.

Part IV

Appendix

Chapter 7

Supplementary data

7.1 Supplementary Figures

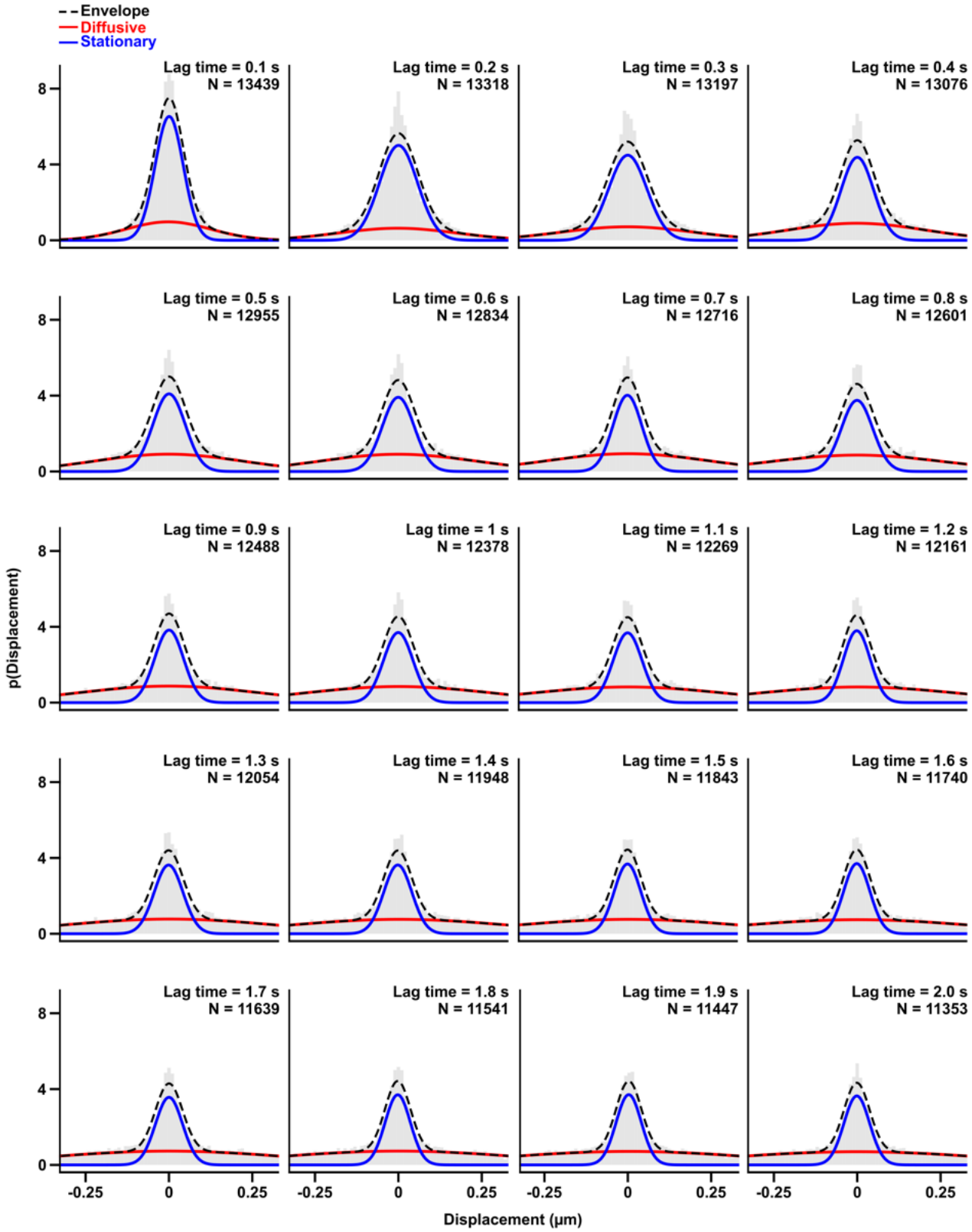

Figure 7.1: Distributions of POK2 tail displacement steps at different lag times.
Distributions for traces that landed on the microtubule of eGFP-POK2$^{2083–2771}$ displacement steps for lag times, τ = 0.1–2.0 s, for every 0.1 s. Data is fitted with two Gaussians (red and blue lines) of which envelope, which is the sum of the two Gaussians, is shown (black dashed line). The red and blue lines correspond to diffusive and stationary traces respectively, and follows Fig. 5.12.

Figure 7.2: All POK2 tail constructs generated including those not assayed in this thesis.
Highlighted in red are constructs that were not used in this thesis. The degree to which the constructs were expressed, purified or assayed is indicated. Numbers in brackets indicate plasmid i.d. number used in the lab. See Table 7.3 for details.

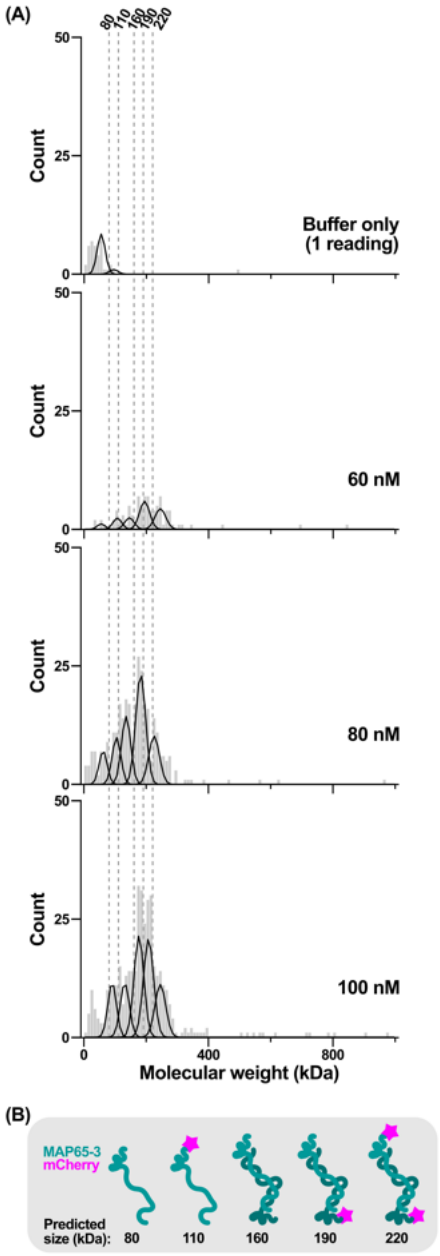

Figure 7.3: Mass photometry measurements with purified MAP65-3-mCherry.
(A) Mass photometry measurements with 0, 60, 80, and 100 nM MAP65-3-mCherry in PEM buffer. MAP65-3-mCherry was pre-diluted in MAP65-3 Desalting Buffer before mixing with PEM buffer in a 1:1 ratio to the final concentrations listed. Three individual measurements with MAP65-3-mCherry were performed for each concentration and counts from all three readings are plotted in the graphs above. Only the control measurement with no MAP65-3-mCherry and just the MAP65-3 Desalting Buffer buffer mixed with PEM buffer was taken with a single reading and shown here. The peaks of MAP65-3-mCherry roughly correspond to the predicted size of expected oligomeric species in (B). As a reference, the predicted sizes are marked as dashed vertical lines. Note that these do not directly overlap with the peaks of the distributions. **(B)** Cartoon depicted predicted oligomeric species of MAP65-3-mCherry. Since MAP65-3-mCherry purifies as a dimer and is contaminated with its untagged version, five oligomeric species are expected as shown with their predicted sizes listed.

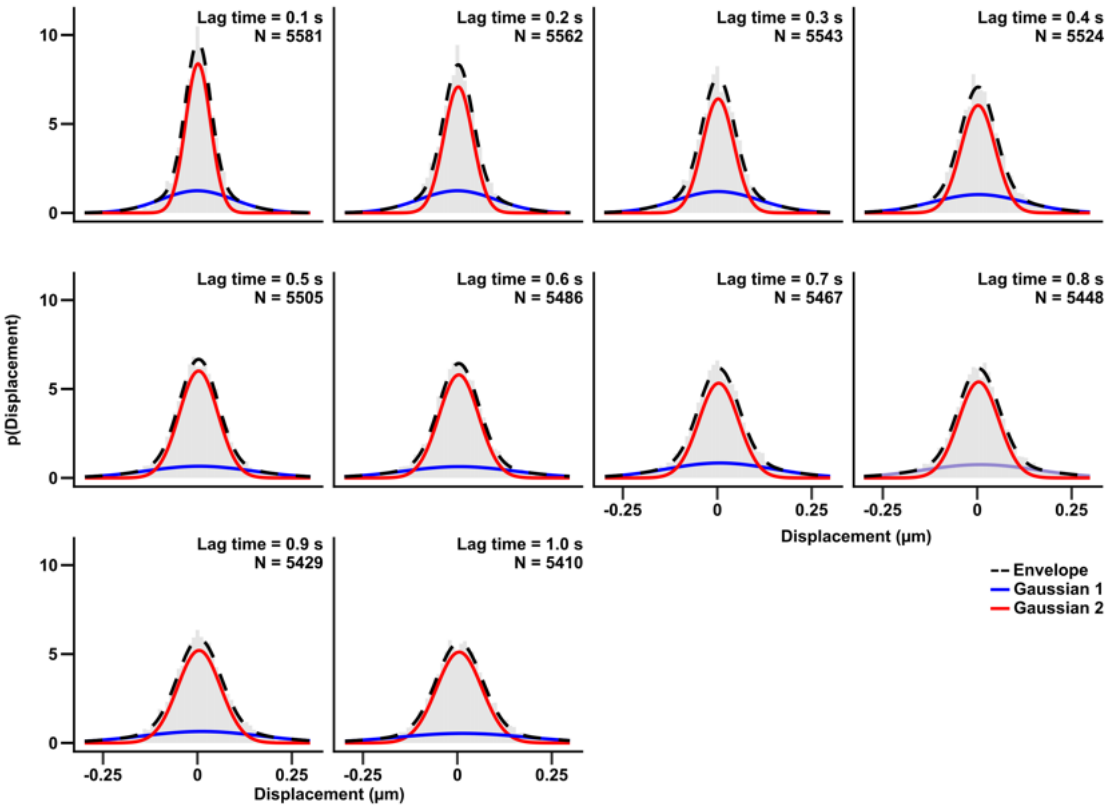

Figure 7.4: Distributions of co-diffusive MAP65-3-mCherry-8xHis and eGFP-POK2$^{2083\text{-}2771}$-8xHis displacement steps at lag times = 0.1 to 1.0 s.
Distributions for co-diffusive traces of eGFP-POK2$^{2083–2771}$ and MAP65-3-mCherrry displacement steps for lag times, τ = 0.1–1.0 s, for every 0.1 s. Data is fitted with two Gaussians (red and blue lines) of which envelope, which is the sum of the two Gaussians, is shown (black dashed line). The red and blue lines correspond to two differently diffusing states, and follows Fig. 5.31.

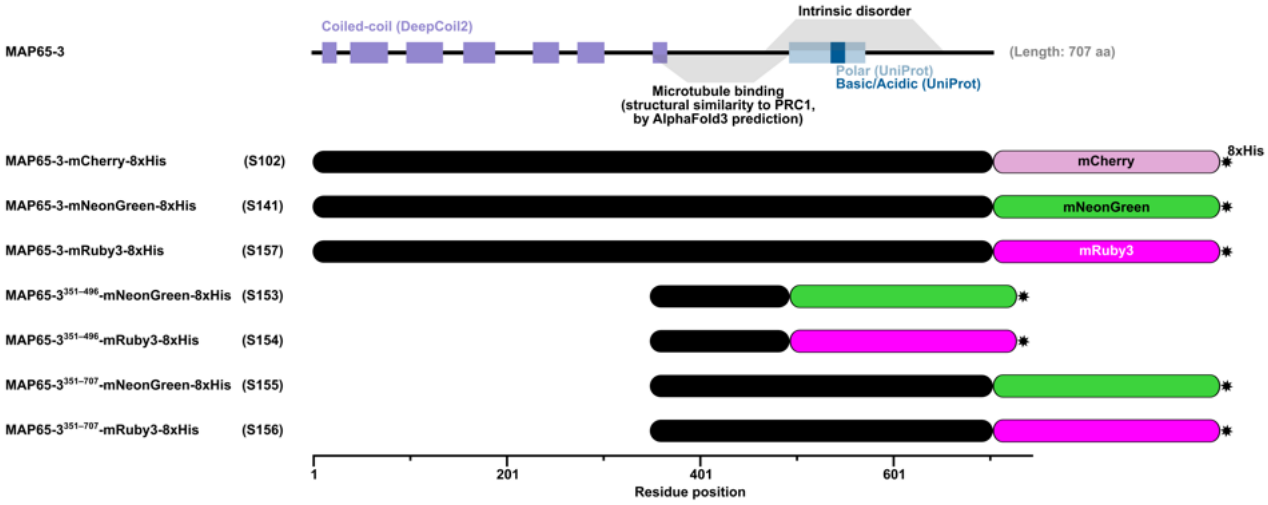

Figure 7.5: Additional MAP65-3 constructs with mNeonGreen or mRuby3 tags.
S102 indicates MAP65-3-mCherry construct used in this thesis. Additional constructs were prepare with mNeonGreen or mRuby3 tagged at the C-terminus. Numbers in brackets indicate plasmid i.d. number used in the lab. See Table 7.3 for details.

7.2 Supplementary Tables

Table 7.1: Accession numbers for relevant proteins mentioned in this thesis in the UniProt database and *Arabidopsis* (TAIR) database.
Organisms are represented by their acronyms, which are: *At, Arabidopsis thaliana; Pp, Physcomitrella patens; Hs, Homo sapiens.*

Protein	UniProt ID-Nr.	TAIR ID-Nr.	Organism
Kinesin-12A/PAKRP1	Q9LDN0	At4g14150	*At*
Kinesin-12B/PAKRP1L	Q8L7Y8	At3g23670	*At*
Kinesin-12C/POK1	Q27IK7	At3g17360	*At*
Kinesin-12D/POK2	Q27IK6	At3g19050	*At*
Kinesin-12E	F4J1U4	At3g44050	*At*
Kinesin-12F	F4JDI6	At3g20150	*At*
KINID1a	B2DFV1	-	*Pp*
KINID1b	B2DFV2	-	*Pp*
KIF15	Q9NS87	-	*Hs*
MAP65-3	Q9FHM4	At5g51600	*At*
PRC1	O43663	-	*Hs*

Table 7.2: Primers used in this thesis. Here are the primers that were used to clone plasmids #S59, 62, 64 and 66 which were expression plasmids for their respective proteins (see Table 7.3) used extensively in this thesis.

Purpose	Primer ID-Nr.	Sequence (5'→ 3')
S59 HiFi assembly	SP108	GACAAGAAAGATGAAACAAAGGAAATCATGGTTCATGTTG
S59 HiFi assembly	SP109	TTTGTTTCATCTTTCTTGTCGCCAGAACCAGCAGCGGAGCCAGCG
S59 HiFi assembly	SP165	GGAAGCGGATCTGGATCTGGACATC
S59 HiFi assembly	SP167	CCAGATCCAGATCCGCTTCCCCTGTCTAAAGAAGAGAAAAAAGGAACCTG
S62 HiFi assembly	SP108	GACAAGAAAGATGAAACAAAGGAAATCATGGTTCATGTTG
S62 HiFi assembly	SP109	TTTGTTTCATCTTTCTTGTCGCCAGAACCAGCAGCGGAGCCAGCG
S62 HiFi assembly	SP165	GGAAGCGGATCTGGATCTGGACATC
S62 HiFi assembly	SP169	CCAGATCCAGATCCGCTTCCCCTTGCAGCAGCAAGCTCCTCGTCC
S64 HiFi assembly	SP173	GCTCCGCTGCTGGTTCTGGCGATTCACGAGAAAGGGATCTTGAAGTCTCT
S64 HiFi assembly	SP107	GCCAGAACCAGCAGCGGAGCCAGCGGATCCCGGCGCGCCCTTGTACAGCTCGTCCATGCCGAGA
S64 HiFi assembly	SP165	GGAAGCGGATCTGGATCTGGACATC
S64 HiFi assembly	SP167	CCAGATCCAGATCCGCTTCCCCTGTCTAAAGAAGAGAAAAAAGGAACCTG
S66 HiFi assembly	SP173	GCTCCGCTGCTGGTTCTGGCGATTCACGAGAAAGGGATCTTGAAGTCTCT
S64 HiFi assembly	SP107	GCCAGAACCAGCAGCGGAGCCAGCGGATCCCGGCGCGCCCTTGTACAGCTCGTCCATGCCGAGA
S66 HiFi assembly	SP165	GGAAGCGGATCTGGATCTGGACATC
S66 HiFi assembly	SP172	CCAGATCCAGATCCGCTTCCCTCCTGAGCAAGCTGCATTCTATCC

Table 7.3: Plasmids used in this thesis.
Abbreviations: Amp, ampicilin.

Plasmid ID-Nr.	Descripion	*E. coli* Resistance	Source
pFastBac1	final destination vector for insect cell protein expression	Amp	ExpiSf Protein Production kit
S42	6xHis-eGFP-POK2$^{2083–2771}$ in pFastBac1	Amp	cloned in this thesis
S50	6xHis-eGFP-POK2$^{\Delta 590–2082}$ in pFastBac1	Amp	cloned in this thesis
S51	6xHis-eGFP-POK2$^{\Delta 190–2082}$ in pFastBac1	Amp	cloned in this thesis
S59	eGFP-POK2$^{2083–2771}$-8xHis in pFastBac1	Amp	cloned in this thesis
S60	eGFP-POK2$^{2083–2690}$-8xHis in pFastBac1	Amp	cloned in this thesis
S61	eGFP-POK2$^{2083–2509}$-8xHis in pFastBac1	Amp	cloned in this thesis
S62	eGFP-POK2$^{2083–2440}$-8xHis in pFastBac1	Amp	cloned in this thesis
S63	eGFP-POK2$^{2083–2402}$-8xHis in pFastBac1	Amp	cloned in this thesis
S64	eGFP-POK2$^{2510–2771}$-8xHis in pFastBac1	Amp	cloned in this thesis
S65	eGFP-POK2$^{2510–2690}$-8xHis in pFastBac1	Amp	cloned in this thesis
S66	eGFP-POK2$^{2510–2677}$-8xHis in pFastBac1	Amp	cloned in this thesis
S102	MAP65-3-mCherry-8xHis in pFastBac1	Amp	ordered from GenScript
S141	MAP65-3-mNeonGreen-8xHis in pFastBac1	Amp	cloned in this thesis
S153	MAP65-3$^{351–496}$-mNeonGreen-8xHis in pFastBac1	Amp	cloned in this thesis
S154	MAP65-3$^{351–496}$-mRuby3-8xHis in pFastBac1	Amp	cloned in this thesis
S155	MAP65-3$^{351–707}$-mNeonGreen-8xHis in pFastBac1	Amp	cloned in this thesis
S156	MAP65-3$^{351–707}$-mRuby3-8xHis in pFastBac1	Amp	cloned in this thesis
S157	MAP65-3-mRuby3-8xHis in pFastBac1	Amp	cloned in this thesis

Table 7.4: Software used in this thesis.

Software	Description/Purpose
SnapGene	Cloning design
Aekta Unicorn™	Controlling pumps for protein purification, chromatogram analysis
AcquireMP & DiscoverMP	Mass photometry data acquisition & analysis
Python	Coding language, for custom scripts
R	Coding language, for custom scripts
MicroManager [78]	Image acquisition
FIJI [271]	Image analysis
FIESTA [259]	MATLAB-based software for single particle tracking (Ruhnnow et al., 2016)
LabVIEW	Microscope control
Origin (Pro)	Graphing and statistics

Chapter 8

Contributions

The POK2 protein coding sequence in a plasmid was a kind gift from Dr. Pantelis Livanos and Dr. Sabine Müller. The analysis for POK2 tail intensities and for POK2 tail-MAP65-3 intensities and landing sequence of the POK2 tail-MAP65-3 co-diffusive traces were performed by Dr. Hauke Drechsler. The Python script used to perform multi-Gaussian fittings for the displacement steps of diffusive POK2 tail and co-diffusive POK2 tail-MAP65-3 molecules were written by Laura Muras. The fittings for two-term exponentials for POK2 interaction times were performed by Dr. Serapion Pyrpassopoulos. Purification of the shorter POK2 tail constructs were performed by Anastasia Gurskaya while under my supervision. Preliminary lipid blot assays were performed by Sehee Jang while under my supervision. Mass spectrometry and subsequent analysis was performed by Dr. Katharina Zittlau. Scripts to analyse mass photometry data were written by Dr. Maria Kharlamova.

All other experiments and data analyses were performed by me. Macros to measure and analyse the data were written directly in FIJI in the built-in java-based macro language, and exported for post-processing and analysis with either R or Python. GUV assays were performed by me with the help and advice of Yannic Lurz. The direction of this doctoral benefited greatly from discussions and advice from fellow lab members, in particular - Dr. Erik Schäffer, Dr. Hauke Drechsler, Benedikt Fischer, Dr. Serapion Pyrpassopoulos, Yannic Lurz and Dr. Maria Kharlamova.

Chapter 9

Lists

List of Publications

During this doctoral work (2019-2025)

- **The plant kinesin-12 POK2 tail is a versatile connectivity hub**
  Shu Yao Leong, Laura Muras, Benedikt S. J. Fischer, Sehee Jang, Anastasia Gurskaya, Mayank Chugh, Serapion Pyrpassopoulos, Hauke Drechsler, Erik Schäffer
  Journal of Cell Science, **2025** *(In revision)*

- **Plant Kinesins: from single molecules to function** (Review)
  Shu Yao Leong, Hauke Drechsler, Erik Schäffer
  (in preparation)

- ***In vitro* characterisation of the *Arabidopsis thaliana* Kinesin-8B motor**
  Shu Yao Leong, Maria A. Kharlamova, Erin S. Ritchie, Aleksandr V. Kostarev, Hauke Drechsler, Erik Schäffer
  (in preparation)

Before beginning this doctoral work (2017-2019)

- **Kinesin-13 and Kinesin-8 Function during Cell Growth and Division in the Moss *Physcomitrella patens***
  Shu Yao Leong, Tomoya Edzuka, Gohta Goshima, Moe Yamada
  The Plant Cell, **2020**

- **SPIRAL2 stabilises endoplasmic microtubule minus ends in the moss *Physcomitrella patens***
  Shu Yao Leong, Moe Yamada, Naoki Yanagisawa, Gohta Goshima
  Cell Structure and Function, **2018**

List of Figures

List of Tables

Materials

0.22 μm MCE filter membrane Millipore, GSWP02500.

0.8 μm cellulose acetate membrane Whatman, FP30/0.8 10462240.

18 x 18 mm glass cover slip #1.5 Menzel Glaeser, 630-1842.

22 x 22 mm glass cover slip #1.5 Marienfeld Superior, 0102052.

Aekta pure chromatography system Cytiva.

Agar-agar Sigma Aldrich, A7002.

Amicon Ultra-15 Centrifugal Filter Units Merck, UFC910008.

anti-β-tubulin mouse antibody Sigma Aldrich, T7816.

anti-GFP mouse antibody Roche, 11814460001.

anti-His mouse antibody Invitrogen, MA1-21315.

anti-RFP mouse antibody Chromotek, 6g6-100.

Benzonase nuclease Sigma Aldrich, E1014.

Bovine serum albumin (BSA) Carl Roth, 0052.2.

Bovine serum albumin (BSA) standard Thermo Scientific, 23210.

cardiolipin (CL) Avanti, 840012P.

Cell Free Protein Expression System: ALiCE for Research Kit LenioBio, AL00000001.

Chloroform Sigma Aldrich, 288306.

DH10Bac *E. coli* Gibco, 10361012.

DH5a *E. coli* NEB, C2987H.

DOPC Avanti, 850375.

double-sided waterproof sticky tape KlebeShop24, KS DC 3702-9.

Epishear 6.4 mm sonicator probe Active Motif, 53057.

ExpiSf Protein Production kit Gibco, 15829126.

FastDigest DpnI Fisher Scientific, 10819410.

Fusion Fx7 Imaging System Vilber.

Gentamycin Gibco, 15750-060.

Gibco ExpiSf CD Medium Gibco, 15889116.

GMPCPP Jena Bioscience, NU-405S.

HiFi assembly NEB, E2621L.

HisTrap HP column Cytiva, 17524701.

HiTrap Desalting Sephadex G-25 columns Cytiva, 29048684.

HiTrap TALON crude column Cytiva, 28953766.

Imperial protein stain Thermo Scientific, 24615.

IPTG Sigma Aldrich, I5502-10G.

Kanamycin Gibco, 15160-054.

LB Broth Carl Roth, X968.2.

Membrane lipid strips Echelon Biosciences, P-6001/P-6002.

microscope slide with reaction wells Marienfeld Superior, 1216333.

Mini-PROTEAN TGX Precast protein gel Bio-Rad, 4561035.

Monarch Gel Extraction Kit NEB, T1120.

Monarch Spin Miniprep Kit NEB, T1110S.

Mucasol Carl Roth, 1A3L.2.

NanoDrop Spectrophotometer Peqlab, ND-1000.

NHS-rhodamine Thermo Fisher Scientific, 46406.

OneMP system Refeyn Inc..

Phosphate Buffered Saline (PBS) Sigma Aldrich, P5493.

Pluronic F-127 Sigma Aldrich, P2443.

polyvinvyl alcohol (PVA) Sigma Aldrich, 341584.

Prestained broad range protein ladder New England Biolabs, P7719S.

Protein loading dye New England Biolabs, B7703S.

reusable CultureWell gaskets Grace Bio-Labs, 103250.

SuperSignal West Pico mouse Fast Western kit Pierce, 35060.

Tetracyclin Sigma Aldrich, T7660.

tilt/roller mixer Phoenix Instruments, RS-TR05.

TLA-55 fixed angle rotor Beckman Coulter.

Trans-Blot Turbo Mini 0.2 μm 7 x 8.5 cm PVDF Transfer Packs Bio-Rad, 1704156.

Trans-Blot Turbo Transfer System Bio-Rad, 1704150.

trichloroacetic acid (TCA) Sigma Aldrich, T8657.

Trypan Blue Gibco, 15250-061.

Typhoon Scanner GE Healthcare, FLA 9500.

X-Gal Invitrogen, 15520034.

Buffers

2x Polymerisation buffer 2x PEM, 30% glycerol, 1 mM GTP, 4 mM $MgCl_2$.

Depolymerisation buffer 50 mM MES [pH 6.6], 1 mM $CaCl_2$.

HMPB buffer high-molarity PIPES buffer: 1 M PIPES [pH 6.9], 10 mM $MgCl_2$, 20 mM EGTA.

MAP65-3 Desalting Buffer Lysis Buffer, but without PMSF or Triton X-100 and with 5% glycerol.

MAP65-3 Lysis Buffer 50 mM sodium phosphate buffer [pH 7.5], 100 mM NaCl, 0.5% Triton X-100, 30 mM imidazole, 0.1 mM ATP, 5 mM β-mercaptoethanol, 1 mM PMSF (Thermo Scientific, 36978), 1x cOmplete EDTA-free Protease Inhibitor Cocktail (Roche, 5056489001), 25 U/ml Universal Nuclease for Cell Lysis (Thermo Scientific, 88700).

MAP65-3 Wash Buffer Lysis Buffer, but without PMSF or Triton X-100.

Motility buffer 0.16 mg/ml casein, 20 mM D-glucose, 20 μg/ml glucose oxidase, 8 μg/ml catalase, 1 mM ATP, 5 mM DTT in PEM20.

PEM buffer 80 mM PIPES [pH 6.9], 1 mM EGTA, and 1 mM $MgCl_2$.

PEM-Tx buffer 10 μ paclitaxel in PEM buffer.

PEM20 buffer PEM buffer but with 20 mM PIPES instead.

POK2 Desalting Buffer POK2 Lysis Buffer, but without PMSF, protein inhibitors, nuclease.

POK2 Lysis Buffer 50 mM sodium phosphate buffer [pH 7.5], 300 mM KCl, 1 mM $MgCl_2$, 10% glycerol, 0.1 mM ATP, 5 mM β-mercaptoethanol, 1 mM PMSF (Thermo Scientific, 36978), 1x cOmplete EDTA-free Protease Inhibitor Cocktail (Roche, 5056489001), 25 U/ml Universal Nuclease for Cell Lysis (Thermo Scientific, 88700).

POK2 Storage Buffer is whatever POK2 is stored in as –80° stocks, in this case, it is the POK2 Desalting Buffer.

POK2 Wash Buffer POK2 Lysis Buffer, but without nuclease.

SOB media 2% (w/v) tryptone, 0.5% (w/v) yeast extract, 8.56 mM NaCl, 2.5 mM KCl, 10 mM $MgCl_2$, 10 mM $MgSO_4$, 20 mM glucose.

Acronyms

ACD asymmetric cell division.

BF bright field.

CBB Coomassie Brilliant Blue.

CC coiled-coil.

CD cell division.

CDK cyclin-dependent kinase.

CDZ cell division zone.

CFPE cell free protein expression.

CL cardiolipin.

CM cortical microtubule.

CP cell plate.

CPAM cell plate assembly matrix.

CPFS cell plate fusion site.

DMSO dimethylsulphoxide.

DOPC dipalmitoylphosphatidylcholine.

DTT dithiothreitol.

EMS ethyl methanesulfonate.

GMPCPP non-hydrolysable analog of GTP.

GUV giant unilamellar vesicle.

HCl hydrochloric acid.

HILO highly inclined and laminated optical sheet.

HMDS hexamethyldisilane.

HRP horse radish peroxidase.

IDR intrinsically disordered region.

IQD IQ67-domain.

IRM interference reflection microscopy.

k-fiber kinetochore-fiber.

kc kinetochore.

LINC linker of nucleoskeleton and cytoskeleton.

MAP microtubule associated protein.

MAP65 microtubule associated protein 65 kDa.

MAPK mitogen-activated protein kinase.

MBD microtubule binding domain.

PA phosphatidic acid.

PCR polymerase chain reaction.

PDMS polydimethylsilane.

PE phosphatidylethanolamine.

PIP phosphoinositol phosphate.

POK1 phragmoplast orienting kinesin 1.

POK2 phragmoplast orienting kinesin 2.

POK2-FL full-length POK2.

PPB preprophase band.

PS phosphatidylserine.

PVA polyvinyl alcohol.

PVDF polyvinylidene fluoride.

Rho rhodamine.

ROI region of interest.

RT room temperature.

SCD symmetric cell division.

SDS sodium dodecyl sulfate.

SDS-PAGE sodium dodecyl sulfate-polyacrylamide gel electrophoresis.

TIRF total internal reflection fluorescence.

Bibliography

1. Alghamdi, H. M. & Friel, C. T. in *The Kinesin Superfamily Handbook* 155–160 (CRC Press, 2020).
2. Allen, R. D., Metuzals, J., Tasaki, I., Brady, S. T. & Gilbert, S. P. Fast axonal transport in squid giant axon. *Science* **218,** 1127–1129. ISSN: 0036-8075 (1982).
3. Almeida, A. C. & Maiato, H. Chromokinesins. *Current Biology* **28,** R1131–R1135. ISSN: 0960-9822 (2018).
4. Almgren, F. J. & Taylor, J. E. The geometry of soap films and soap bubbles. *Scientific American* **235,** 82–93. ISSN: 0036-8733 (1976).
5. Ambrose, J. C., Li, W., Marcus, A., Ma, H. & Cyr, R. A minus-end–directed kinesin with plus-end tracking protein activity is involved in spindle morphogenesis. *Molecular biology of the cell* **16,** 1584–1592. ISSN: 1059-1524 (2005).
6. Ambrose, J. C., Shoji, T., Kotzer, A. M., Pighin, J. A. & Wasteneys, G. O. The Arabidopsis CLASP gene encodes a microtubule-associated protein involved in cell expansion and division. *The Plant Cell* **19,** 2763–2775. ISSN: 1532-298X (2007).
7. Andrieu, G., Quaranta, M., Leprince, C. & Hatzoglou, A. The GTPase Gem and its partner Kif9 are required for chromosome alignment, spindle length control, and mitotic progression. *The FASEB Journal* **26,** 5025–5034. ISSN: 0892-6638 (2012).
8. Anton, Z. *et al.* Molecular mechanism for kinesin-1 direct membrane recognition. *Science Advances* **7.** ISSN: 2375-2548 (Electronic) 2375-2548 (Linking) (2021).
9. Asenjo, A. B., Weinberg, Y. & Sosa, H. Nucleotide binding and hydrolysis induces a disorder-order transition in the kinesin neck-linker region. *Nature structural molecular biology* **13,** 648–654. ISSN: 1545-9993 (2006).
10. Ashraf, M. A., Liu, L. & Facette, M. R. A polarized nuclear position specifies the correct division plane during maize stomatal development. *Plant Physiology* **193,** 125–139. ISSN: 0032-0889 (2023).
11. Austin, J. R., Seguí-Simarro, J. M. & Staehelin, L. A. Quantitative analysis of changes in spatial distribution and plus-end geometry of microtubules involved in plant-cell cytokinesis. *Journal of cell science* **118,** 3895–3903. ISSN: 1477-9137 (2005).

12. Babinchak, W. M. & Surewicz, W. K. Liquid–liquid phase separation and its mechanistic role in pathological protein aggregation. *Journal of molecular biology* **432,** 1910–1925. ISSN: 0022-2836 (2020).
13. Bai, Z. *et al.* The impact and origin of copy number variations in the Oryza species. *BMC genomics* **17,** 1–12 (2016).
14. Bajar, B. T. *et al.* Improving brightness and photostability of green and red fluorescent proteins for live cell imaging and FRET reporting. *Scientific reports* **6,** 20889. ISSN: 2045-2322 (2016).
15. Bakhuizen, R., Van Spronsen, P., Sluiman-den Hertog, F., Venverloo, C. & Goosen-de Roo, L. Nuclear envelope radiating microtubules in plant cells during interphase mitosis transition. *Protoplasma* **128,** 43–51. ISSN: 0033-183X (1985).
16. Bannigan, A. *et al.* A conserved role for kinesin-5 in plant mitosis. *Journal of cell science* **120,** 2819–2827. ISSN: 1477-9137 (2007).
17. Beck, M., Komis, G., Müller, J., Menzel, D. & Šamaj, J. Arabidopsis homologs of nucleus-and phragmoplast-localized kinase 2 and 3 and mitogen-activated protein kinase 4 are essential for microtubule organization. *The Plant Cell* **22,** 755–771. ISSN: 1532-298X (2010).
18. Bernstein, M., Beech, P. L., Katz, S. G. & Rosenbaum, J. L. A new kinesin-like protein (Klp1) localized to a single microtubule of the Chlamydomonas flagellum. *The Journal of cell biology* **125,** 1313–1326. ISSN: 0021-9525 (1994).
19. Berthold, G. *Studien über protoplasmamechanik* (Arthur Felix Verlag (Leipzig), 1886).
20. Besson, S. & Dumais, J. Universal rule for the symmetric division of plant cells. *Proceedings of the National Academy of Sciences* **108,** 6294–6299. ISSN: 0027-8424 (2011).
21. Besson, S. & Dumais, J. *Stochasticity in the symmetric division of plant cells: when the exceptions are the rule* Generic. 2014.
22. Bisgrove, S. R., Lee, Y.-R. J., Liu, B., Peters, N. T. & Kropf, D. L. The microtubule plus-end binding protein EB1 functions in root responses to touch and gravity signals in Arabidopsis. *The Plant Cell* **20,** 396–410. ISSN: 1532-298X (2008).
23. Blatner, N. R. *et al.* The structural basis of novel endosome anchoring activity of KIF16B kinesin. *The EMBO Journal* **26,** 3709–3719. ISSN: 0261-4189 (2007).
24. Bligny, R. & Douce, R. A precise localization of cardiolipin in plant cells. *Biochimica et biophysica acta* **617,** 254–263. ISSN: 0006-3002 (1980).
25. Boban, Z., Mardešić, I., Subczynski, W. K. & Raguz, M. Giant unilamellar vesicle electroformation: What to use, what to avoid, and how to quantify the results. *Membranes* **11,** 860. ISSN: 2077-0375 (2021).
26. Bormuth, V., Varga, V., Howard, J. & Schäffer, E. Protein friction limits diffusive and directed movements of kinesin motors on microtubules. *science* **325,** 870–873. ISSN: 0036-8075 (2009).
27. Boruc, J. *et al.* Phosphorylation of MAP65-1 by Arabidopsis Aurora kinases is required for efficient cell cycle progression. *Plant physiology* **173,** 582–599. ISSN: 1532-2548 (2017).
28. Boruc, J. *et al.* TPX2-LIKE PROTEIN3 is the primary activator of α-aurora kinases and is essential for embryogenesis. *Plant physiology* **180,** 1389–1405. ISSN: 1532-2548 (2019).

29. Bowser, J. & Reddy, A. Localization of a kinesin-like calmodulin-binding protein in dividing cells of Arabidopsis and tobacco. *The Plant Journal* **12,** 1429–1437. ISSN: 0960-7412 (1997).
30. Brady, S. T. A novel brain ATPase with properties expected for the fast axonal transport motor. *Nature* **317,** 73–75. ISSN: 0028-0836 (1985).
31. Braun, M., Diez, S. & Lansky, Z. in *The Kinesin Superfamily Handbook* 115–134 (CRC Press, 2020).
32. Breviario, D., Gianì, S. & Morello, L. Multiple tubulins: evolutionary aspects and biological implications. *The Plant Journal* **75,** 202–218. ISSN: 0960-7412 (2013).
33. Britto, M. *et al.* Schizosaccharomyces pombe kinesin-5 switches direction using a steric blocking mechanism. *Proceedings of the National Academy of Sciences* **113,** E7483–E7489. ISSN: 0027-8424 (2016).
34. Brown, R. & Lemmon, B. E. The cytoskeleton and spatial control of cytokinesis in the plant life cycle. *Protoplasma* **215,** 35–49. ISSN: 0033-183X (2001).
35. Burbank, K. S. & Mitchison, T. J. Microtubule dynamic instability. *Current Biology* **16,** R516–R517. ISSN: 0960-9822 (2006).
36. Burkart, G. M. & Dixit, R. Microtubule bundling by MAP65-1 protects against severing by inhibiting the binding of katanin. *Molecular biology of the cell* **30,** 1587–1597. ISSN: 1059-1524 (2019).
37. Buschmann, H. & Müller, S. Update on plant cytokinesis: rule and divide. *Current opinion in plant biology* **52,** 97–105. ISSN: 1369-5266 (2019).
38. Buschmann, H. & Zachgo, S. The evolution of cell division: from streptophyte algae to land plants. *Trends in Plant Science* **21,** 872–883. ISSN: 1360-1385 (2016).
39. Buschmann, H. *et al.* Microtubule-associated AIR9 recognizes the cortical division site at preprophase and cell-plate insertion. *Current Biology* **16,** 1938–1943. ISSN: 0960-9822 (2006).
40. Buschmann, H. *et al.* Arabidopsis KCBP interacts with AIR9 but stays in the cortical division zone throughout mitosis via its MyTH4-FERM domain. *Journal of Cell Science* **128,** 2033–2046. ISSN: 1477-9137 (2015).
41. Cai, D., Verhey, K. J. & Meyhöfer, E. Tracking single Kinesin molecules in the cytoplasm of mammalian cells. *Biophysical journal* **92,** 4137–4144. ISSN: 0006-3495 (2007).
42. Cai, Q. & Tammineni, P. Alterations in mitochondrial quality control in Alzheimer's disease. *Frontiers in cellular neuroscience* **10,** 24. ISSN: 1662-5102 (2016).
43. Caillaud, M.-C. Anionic Lipids: A Pipeline Connecting Key Players of Plant Cell Division. *Frontiers in Plant Science* **10.** ISSN: 1664-462X (2019).
44. Caillaud, M.-C. *et al.* MAP65-3 microtubule-associated protein is essential for nematode-induced giant cell ontogenesis in Arabidopsis. *The Plant Cell* **20,** 423–437. ISSN: 1532-298X (2008).
45. Camlin, N. J., McLaughlin, E. A. & Holt, J. E. Motoring through: the role of kinesin superfamily proteins in female meiosis. *Human Reproduction Update* **23,** 409–420. ISSN: 1355-4786 (2017).

46. Case, R. B., Rice, S., Hart, C. L., Ly, B. & Vale, R. D. Role of the kinesin neck linker and catalytic core in microtubule-based motility. *Current Biology* **10,** 157–160. ISSN: 0960-9822 (2000).
47. Chaaban, S. & Brouhard, G. J. A microtubule bestiary: structural diversity in tubulin polymers. *Molecular biology of the cell* **28,** 2924–2931. ISSN: 1059-1524 (2017).
48. Chauhan, P. *et al.* Ionic strength alters crosslinker-driven self-organization of microtubules. *Cytoskeleton.* ISSN: 1949-3584 (2024).
49. Chen, C. *et al.* The Arabidopsis ATK1 gene is required for spindle morphogenesis in male meiosis. ISSN: 1477-9129 (2002).
50. Chen, Y. *et al.* MOR1/MAP215 acts synergistically with katanin to control cell division and anisotropic cell elongation in Arabidopsis. *The Plant Cell* **34,** 3006–3027. ISSN: 1040-4651 (2022).
51. Chial, H., Thompson, H. & Splittgerber, A. A spectral study of the charge forms of Coomassie Blue G. *Analytical biochemistry* **209,** 258–266. ISSN: 0003-2697 (1993).
52. Chrétien, D. & Wade, R. H. New data on the microtubule surface lattice. *Biology of the Cell* **71,** 161–174. ISSN: 0248-4900 (1991).
53. Chugh, M. *et al.* Phragmoplast Orienting Kinesin 2 Is a Weak Motor Switching between Processive and Diffusive Modes. *Biophys J* **115,** 375–385 (2018).
54. Chugh, M. *Single-molecule investigations into how plant kinesin-12 motor proteins accurately align the cell division plane* Thesis (2021).
55. Cleary, A. L. & Smith, L. G. The Tangled1 gene is required for spatial control of cytoskeletal arrays associated with cell division during maize leaf development. *The Plant Cell* **10,** 1875–1888. ISSN: 1532-298X (1998).
56. Cleary, A. L. F-actin redistributions at the division site in living Tradescantia stomatal complexes as revealed by microinjection of rhodamine-phalloidin. *Protoplasma* **185,** 152–165. ISSN: 0033-183X (1995).
57. Colasanti, J., Cho, S.-O., Wick, S. & Sundaresan, V. Localization of the functional p34cdc2 homolog of maize in root tip and stomatal complex cells: association with predicted division sites. *The Plant Cell* **5,** 1101–1111. ISSN: 1532-298X (1993).
58. Cornfine, S. *et al.* The kinesin KIF9 and reggie/flotillin proteins regulate matrix degradation by macrophage podosomes. *Molecular biology of the cell* **22,** 202–215. ISSN: 1059-1524 (2011).
59. Cornish, J., Chamberlain, S. G., Owen, D. & Mott, H. R. Intrinsically disordered proteins and membranes: a marriage of convenience for cell signalling? *Biochemical Society Transactions* **48,** 2669–2689. ISSN: 0300-5127 (2020).
60. Croom, H. B., Correia, J. J. & Williams Jr, R. C. The effects of elevated pH and high salt concentrations on tubulin. *Archives of biochemistry and biophysics* **249,** 397–406. ISSN: 0003-9861 (1986).
61. Cyr, R. J. Microtubules in plant morphogenesis: role of the cortical array. *Annual Review of Cell Biology* **10,** 153–180. ISSN: 0743-4634 (1994).

62. Dahiya, P. & Bürstenbinder, K. The making of a ring: Assembly and regulation of microtubule-associated proteins during preprophase band formation and division plane set-up. *Current Opinion in Plant Biology* **73,** 102366. ISSN: 1369-5266 (2023).
63. Dambournet, D. *et al.* Rab35 GTPase and OCRL phosphatase remodel lipids and F-actin for successful cytokinesis. *Nature cell biology* **13,** 981–988. ISSN: 1465-7392 (2011).
64. Damme, D. V., Bouget, F.-Y., Poucke, K. V., Inzé, D. & Geelen, D. Molecular dissection of plant cytokinesis and phragmoplast structure: a survey of GFP-tagged proteins. *The Plant Journal* **40,** 386–398. ISSN: 0960-7412 (2004).
65. Day, I. S., Miller, C., Golovkin, M. & Reddy, A. Interaction of a kinesin-like calmodulin-binding protein with a protein kinase. *Journal of Biological Chemistry* **275,** 13737–13745. ISSN: 0021-9258 (2000).
66. Deng, X., Xiao, Y., Tang, X., Liu, B. & Lin, H. Arabidopsis α-Aurora kinase plays a role in cytokinesis through regulating MAP65-3 association with microtubules at phragmoplast midzone. *Nature Communications* **15,** 3779. ISSN: 2041-1723 (2024).
67. Deryusheva, E. *et al.* Does intrinsic disorder in proteins favor their interaction with lipids? *Proteomics* **19,** 1800098. ISSN: 1615-9853 (2019).
68. Dhonukshe, P., Laxalt, A. M., Goedhart, J., Gadella, T. W. & Munnik, T. Phospholipase D activation correlates with microtubule reorganization in living plant cells. *The Plant Cell* **15,** 2666–2679. ISSN: 1532-298X (2003).
69. Di Paolo, G. & De Camilli, P. Phosphoinositides in cell regulation and membrane dynamics. *Nature* **443,** 651–657. ISSN: 1476-4687 (2006).
70. Dietrich, K. A. *et al.* The kinesin-1 motor protein is regulated by a direct interaction of its head and tail. *Proceedings of the National Academy of Sciences* **105,** 8938–8943. ISSN: 0027-8424 (2008).
71. Drechsler, H., Grewal, J. S. & McAinsh, A. D. in *The Kinesin Superfamily Handbook* 135–154 (CRC Press, 2020).
72. Drechsler, H. & McAinsh, A. D. Kinesin-12 motors cooperate to suppress microtubule catastrophes and drive the formation of parallel microtubule bundles. *Proceedings of the National Academy of Sciences* **113,** E1635–E1644. ISSN: 0027-8424 (2016).
73. Drechsler, H., McHugh, T., Singleton, M. R., Carter, N. J. & McAinsh, A. D. The Kinesin-12 Kif15 is a processive track-switching tetramer. *Elife* **3,** e01724. ISSN: 2050-084X (2014).
74. Dunsing, V. *et al.* Optimal fluorescent protein tags for quantifying protein oligomerization in living cells. *Scientific reports* **8,** 10634. ISSN: 2045-2322 (2018).
75. Durairajan, S. S. K. *et al.* Unraveling the interplay of kinesin-1, tau, and microtubules in neurodegeneration associated with Alzheimer's disease. *Frontiers in Cellular Neuroscience* **18,** 1432002. ISSN: 1662-5102 (2024).
76. Duroc, Y., Bouchez, D. & Pastuglia, M. The preprophase band and division site determination in land plants. *The plant cytoskeleton,* 145–185. ISSN: 1441909869 (2011).
77. Edamatsu, M. Bidirectional motility of the fission yeast kinesin-5, Cut7. *Biochemical and biophysical research communications* **446,** 231–234. ISSN: 0006-291X (2014).

78. Edelstein, A. D. *et al.* Advanced methods of microscope control using Manager software. *Journal of biological methods* **1,** e10 (2014).
79. Endow, S. A. & Higuchi, H. A mutant of the motor protein kinesin that moves in both directions on microtubules. *Nature* **406,** 913–916. ISSN: 0028-0836 (2000).
80. Eng, R. C. & Wasteneys, G. O. The microtubule plus-end tracking protein ARMADILLO-REPEAT KINESIN1 promotes microtubule catastrophe in Arabidopsis. *The Plant Cell* **26,** 3372–3386. ISSN: 1532-298X (2014).
81. Engelke, M. F. *et al.* Engineered kinesin motor proteins amenable to small-molecule inhibition. *Nature Communications* **7,** 11159. ISSN: 2041-1723 (2016).
82. Erdős, G. & Dosztányi, Z. AIUPred: combining energy estimation with deep learning for the enhanced prediction of protein disorder. *Nucleic Acids Research,* gkae385. ISSN: 0305-1048 (2024).
83. Errera, L. Sur une condition fondamentale d'équilibre des cellules vivantes. *Ann. Soc. Belge Microscopie* **103,** 822 (1886).
84. Errera, L. Uber zellformen und seifenblasen. *Bot. Centralbl.* **34,** 395–398 (1888).
85. Esmaeeli Nieh, S. *et al.* De novo mutations in KIF1A cause progressive encephalopathy and brain atrophy. *Annals of clinical and translational neurology* **2,** 623–635. ISSN: 2328-9503 (2015).
86. Euteneuer, U., Jackson, W. & McIntosh, J. Polarity of spindle microtubules in Haemanthus endosperm. *The Journal of cell biology* **94,** 644–653. ISSN: 0021-9525 (1982).
87. Euteneuer, U. & McIntosh, J. R. Polarity of midbody and phragmoplast microtubules. *The Journal of cell biology* **87,** 509–515. ISSN: 0021-9525 (1980).
88. Fache, V. *et al.* Arabidopsis kinetochore fiber-associated MAP65-4 cross-links microtubules and promotes microtubule bundle elongation. *The Plant Cell* **22,** 3804–3815. ISSN: 1532-298X (2010).
89. Farmer, V. J. & Zanic, M. TOG-domain proteins. *Current Biology* **31,** R499–R501. ISSN: 0960-9822 (2021).
90. Field, S. J. *et al.* PtdIns(4,5)P2 functions at the cleavage furrow during cytokinesis. *Current Biology* **15,** 1407–12. ISSN: 0960-9822 (Print) 0960-9822 (2005).
91. Fink, G. *et al.* The mitotic kinesin-14 Ncd drives directional microtubule–microtubule sliding. *Nature cell biology* **11,** 717–723. ISSN: 1465-7392 (2009).
92. Flanders, D. J., Rawlins, D. J., Shaw, P. J. & Lloyd, C. W. Nucleus-associated microtubules help determine the division plane of plant epidermal cells: avoidance of four-way junctions and the role of cell geometry. *The Journal of cell biology* **110,** 1111–1122. ISSN: 0021-9525 (1990).
93. Fridman, V. *et al.* Kinesin-5 Kip1 is a bi-directional motor that stabilizes microtubules and tracks their plus-ends in vivo. *Journal of cell science* **126,** 4147–4159. ISSN: 1477-9137 (2013).
94. Friel, C. T. *The Kinesin Superfamily Handbook: Transporter, Creator, Destroyer* ISBN: 0429958242 (CRC Press, 2020).
95. Fuglebakk, E. & Reuter, N. A model for hydrophobic protrusions on peripheral membrane proteins. *PLoS computational biology* **14,** e1006325. ISSN: 1553-734X (2018).

96. Fygenson, D. K., Needleman, D. J. & Sneppen, K. Variability-based sequence alignment identifies residues responsible for functional differences in and tubulin. *Protein Science* **13,** 25–31. ISSN: 0961-8368 (2004).
97. Gabrych, D. R., Lau, V. Z., Niwa, S. & Silverman, M. A. Going too far is the same as falling short†: Kinesin-3 family members in hereditary spastic paraplegia. *Frontiers in Cellular Neuroscience* **13,** 419. ISSN: 1662-5102 (2019).
98. Gaillard, J. *et al.* Two microtubule-associated proteins of Arabidopsis MAP65s promote antiparallel microtubule bundling. *Molecular biology of the cell* **19,** 4534–4544. ISSN: 1059-1524 (2008).
99. Galindo-Trigo, S., Grand, T. M., Voigt, C. A. & Smith, L. M. A malectin domain kinesin functions in pollen and seed development in Arabidopsis. *Journal of Experimental Botany* **71,** 1828–1841. ISSN: 0022-0957 (2020).
100. Galva, C. *et al.* The Microtubule Plus-End Tracking Proteins SPR1 and EB1b Interact to Maintain Polar Cell Elongation and Directional Organ Growth in Arabidopsis. *The Plant Cell* **26,** 4409–4425. ISSN: 1040-4651 (2014).
101. Gerson-Gurwitz, A. *et al.* Directionality of individual kinesin-5 Cin8 motors is modulated by loop 8, ionic strength and microtubule geometry. *The EMBO journal* **30,** 4942–4954. ISSN: 1460-2075 (2011).
102. Giannoutsou, E., Galatis, B., Zachariadis, M. & Apostolakos, P. Formation of an endoplasmic reticulum ring associated with acetylated microtubules in the angiosperm preprophase band. *Cytoskeleton* **69,** 252–265. ISSN: 1949-3584 (2012).
103. Gicking, A. M., Swentowsky, K. W., Dawe, R. K. & Qiu, W. Functional diversification of the kinesin-14 family in land plants. *FEBS letters* **592,** 1918–1928. ISSN: 0014-5793 (2018).
104. Gittes, F., Mickey, B., Nettleton, J. & Howard, J. Flexural rigidity of microtubules and actin filaments measured from thermal fluctuations in shape. *The Journal of cell biology* **120,** 923–934. ISSN: 0021-9525 (1993).
105. Goldstein, L. S. & Gunawardena, S. Flying through the Drosophila cytoskeletal genome. *The Journal of cell biology* **150,** F63–F68. ISSN: 0021-9525 (2000).
106. Goodbody, K. C., Venverloo, C. J. & Lloyd, C. W. Laser microsurgery demonstrates that cytoplasmic strands anchoring the nucleus across the vacuole of premitotic plant cells are under tension. Implications for division plane alignment. *Development* **113,** 931–939. ISSN: 0950-1991 (1991).
107. Gunning, B., Hardham, A. & Hughes, J. Pre-prophase bands of microtubules in all categories of formative and proliferative cell division in Azolla roots. *Planta* **143,** 145–160. ISSN: 0032-0935 (1978).
108. Guo, L. *et al.* Evaluating the microtubule cytoskeleton and its interacting proteins in monocots by mining the rice genome. *Annals of botany* **103,** 387–402. ISSN: 1095-8290 (2009).
109. Guo, M., Kim, P., Li, G., Elowsky, C. G. & Alfano, J. R. A bacterial effector co-opts calmodulin to target the plant microtubule network. *Cell host microbe* **19,** 67–78. ISSN: 1931-3128 (2016).

110. Guo, X. *et al.* An Arabidopsis Kinesin-14D motor is associated with midzone microtubules for spindle morphogenesis. *Current Biology* **34,** 3747–3762. e6. ISSN: 0960-9822 (2024).
111. Hackney, D. D. & Stock, M. F. Kinesin's IAK tail domain inhibits initial microtubule-stimulated ADP release. *Nature cell biology* **2,** 257–260. ISSN: 1476-4679 (2000).
112. Hahne, G. & Hoffmann, F. The effect of laser microsurgery on cytoplasmic strands and cytoplasmic streaming in isolated plant protoplasts. *European journal of cell biology* **33,** 175–179. ISSN: 0171-9335 (1984).
113. Hamant, O. *et al.* Developmental patterning by mechanical signals in Arabidopsis. *science* **322,** 1650–1655. ISSN: 0036-8075 (2008).
114. Hancock, W. O. in *The Kinesin Superfamily Handbook* 33–40 (CRC Press, 2020).
115. Hanke, J. H. *et al.* Discovery of a Novel, Potent, and Src Family-selective Tyrosine Kinase Inhibitor. *Journal of Biological Chemistry* **271.** doi: 10.1074/jbc.271.2.695, 695–701. ISSN: 0021-9258 (1996).
116. Hepler, P. K. & Jackson, W. T. Microtubules and early stages of cell-plate formation in the endosperm of Haemanthus katherinae Baker. *The Journal of Cell Biology* **38,** 437–446. ISSN: 1540-8140 (1968).
117. Hermsdorf, G. *Optical tweezers combined with fluorescence microscopy and a heating laser for the study of model lipid bilayer systems and membrane proteins* Thesis (2021).
118. Herrmann, A. *et al.* Dual localized kinesin-12 POK2 plays multiple roles during cell division and interacts with MAP65-3. *EMBO Rep* **19.** ISSN: 1469-3178 (Electronic) 1469-221X (Print) (2018).
119. Herrmann, A. *et al.* KINESIN-12E regulates metaphase spindle flux and helps control spindle size in Arabidopsis. *The Plant Cell* **33,** 27–43. ISSN: 1532-298X (2021).
120. Higuchi, H. & Endow, S. A. Directionality and processivity of molecular motors. *Current opinion in cell biology* **14,** 50–57. ISSN: 0955-0674 (2002).
121. Hirokawa, N. Kinesin and dynein superfamily proteins and the mechanism of organelle transport. *Science* **279,** 519–526. ISSN: 1095-9203 (1998).
122. Hiwatashi, Y. *et al.* Kinesins are indispensable for interdigitation of phragmoplast microtubules in the moss Physcomitrella patens. *The Plant Cell* **20,** 3094–3106. ISSN: 1532-298X (2008).
123. Ho, C.-M. K. *et al.* Interaction of antiparallel microtubules in the phragmoplast is mediated by the microtubule-associated protein MAP65-3 in Arabidopsis. *The Plant Cell* **23,** 2909–2923. ISSN: 1532-298X (2011).
124. Hoepfner, S. *et al.* Modulation of Receptor Recycling and Degradation by the Endosomal Kinesin KIF16B. *Cell* **121,** 437–450. ISSN: 0092-8674 (2005).
125. Hoeprich, G. J., Thompson, A. R., McVicker, D. P., Hancock, W. O. & Berger, C. L. Kinesin's neck-linker determines its ability to navigate obstacles on the microtubule surface. *Biophysical journal* **106,** 1691–1700. ISSN: 0006-3495 (2014).
126. Hofmeister, W. Zusatze und Berichtigungen zu den 1851 veroffentlichen Untersuchungen der Entwicklung hoherer Kryptogamen. *Jahrb. Wiss. Bot.* **3** (1863).

127. Hollenbeck, P. J. The distribution, abundance and subcellular localization of kinesin. *The Journal of cell biology* **108,** 2335–2342. ISSN: 0021-9525 (1989).
128. Hotta, T., Lee, Y.-R. J., Higaki, T., Hashimoto, T. & Liu, B. Two kinesin-14A motors oligomerize to drive poleward microtubule convergence for acentrosomal spindle morphogenesis in arabidopsis thaliana. *Frontiers in Cell and Developmental Biology* **10,** 949345. ISSN: 2296-634X (2022).
129. Hsiao, A.-S. Plant protein disorder: Spatial regulation, broad specificity, switch of signaling and physiological status. *Frontiers in Plant Science* **13,** 904446. ISSN: 1664-462X (2022).
130. Hülskamp, M., Miséra, S. & Jürgens, G. Genetic dissection of trichome cell development in Arabidopsis. *Cell* **76.** doi: 10.1016/0092-8674(94)90118-X, 555–566. ISSN: 0092-8674 (1994).
131. Hussain, H. *Structural organisation of the human kinesin-12 Kif15* Thesis (2018).
132. Hussey, P. J. & Gull, K. Multiple isotypes of α-and β-tubulin in the plant Phaseolus vulgaris. *FEBS letters* **181,** 113–118. ISSN: 0014-5793 (1985).
133. Inoue, D. *et al.* Sensing surface mechanical deformation using active probes driven by motor proteins. *Nature communications* **7,** 12557. ISSN: 2041-1723 (2016).
134. Ionita-Laza, I., Lange, C. & M. Laird, N. Estimating the number of unseen variants in the human genome. *Proceedings of the National Academy of Sciences* **106,** 5008–5013. ISSN: 0027-8424 (2009).
135. Itoh, R., Fujiwara, M. & Yoshida, S. Kinesin-related proteins with a mitochondrial targeting signal. *Plant physiology* **127,** 724–726. ISSN: 1532-2548 (2001).
136. Jiang, S., Li, M., Xu, T., Ren, D. & Liu, G. Two kinesins from Arabidopsis, KatB and KatC, have a second microtubule-binding site in the tail domain. *BMB Reports* **40,** 44–52. ISSN: 1976-670X (2007).
137. Kao, Y.-L., Deavours, B., Phelps, K., Walker, R. & Reddy, A. Bundling of microtubules by motor and tail domains of a kinesin-like calmodulin-binding protein from Arabidopsis: regulation by Ca2+/calmodulin. *Biochemical and biophysical research communications* **267,** 201–207. ISSN: 0006-291X (2000).
138. Karahara, I. *et al.* The preprophase band is a localized center of clathrin-mediated endocytosis in late prophase cells of the onion cotyledon epidermis. *The Plant Journal* **57,** 819–831. ISSN: 0960-7412 (2009).
139. Kawabe, A. *et al.* Characterization of plant Aurora kinases during mitosis. *Plant molecular biology* **58,** 1–13. ISSN: 0167-4412 (2005).
140. Kawamura, E. *et al.* MICROTUBULE ORGANIZATION 1 regulates structure and function of microtubule arrays during mitosis and cytokinesis in the Arabidopsis root. *Plant physiology* **140,** 102–114. ISSN: 1532-2548 (2006).
141. Kharlamova, M. *RAD52-mediated single-strand DNA annealing: a single-molecule approach* Thesis (2024).
142. Kharlamova, M. A. *et al.* Monomers and short oligomers of human RAD52 promote single-strand annealing. *Proceedings of the National Academy of Sciences of the United States of America* **122,** e2420771122. ISSN: 1091-6490 (2025).

143. Kim, Y., Heuser, J. E., Waterman, C. M. & Cleveland, D. W. CENP-E combines a slow, processive motor and a flexible coiled coil to produce an essential motile kinetochore tether. *The Journal of cell biology* **181,** 411–419. ISSN: 1540-8140 (2008).
144. Kimata, Y. *et al.* Novel inhibitors of microtubule organization and phragmoplast formation in diverse plant species. *Life Science Alliance* **6.** ISSN: 2575-1077 (2023).
145. Kincaid, M. M. & King, S. J. Motors and their tethers: the role of secondary binding sites in processive motility. *Cell Cycle* **5,** 2733–2737. ISSN: 1538-4101 (2006).
146. Klopfenstein, D. R. & Vale, R. D. The lipid binding pleckstrin homology domain in UNC-104 kinesin is necessary for synaptic vesicle transport in Caenorhabditis elegans. *Mol Biol Cell* **15,** 3729–39. ISSN: 1059-1524 (Print) 1059-1524 (2004).
147. Komaki, S. *et al.* Nuclear-localized subtype of end-binding 1 protein regulates spindle organization in Arabidopsis. *J Cell Sci* **123,** 451–9. ISSN: 0021-9533 (2010).
148. Komis, G. *et al.* Katanin Effects on Dynamics of Cortical Microtubules and Mitotic Arrays in Arabidopsis thaliana Revealed by Advanced Live-Cell Imaging. *Front Plant Sci* **8,** 866. ISSN: 1664-462X (Print) 1664-462x (2017).
149. Kosetsu, K., de Keijzer, J., Janson, M. E. & Goshima, G. MICROTUBULE-ASSOCIATED PROTEIN65 is essential for maintenance of phragmoplast bipolarity and formation of the cell plate in Physcomitrella patens. *The Plant Cell* **25,** 4479–4492. ISSN: 1532-298X (2013).
150. Kosetsu, K. *et al.* The MAP kinase MPK4 is required for cytokinesis in Arabidopsis thaliana. *The Plant Cell* **22,** 3778–3790. ISSN: 1532-298X (2010).
151. Kouranti, I., Sachse, M., Arouche, N., Goud, B. & Echard, A. Rab35 regulates an endocytic recycling pathway essential for the terminal steps of cytokinesis. *Current Biology* **16,** 1719–25. ISSN: 0960-9822 (Print) 0960-9822 (2006).
152. Krysan, P. J., Jester, P. J., Gottwald, J. R. & Sussman, M. R. An Arabidopsis mitogen-activated protein kinase kinase kinase gene family encodes essential positive regulators of cytokinesis. *The Plant Cell* **14,** 1109–1120. ISSN: 1532-298X (2002).
153. Kumari, P. *et al.* IQ67 DOMAIN proteins facilitate preprophase band formation and division-plane orientation. *Nature plants* **7,** 739–747. ISSN: 2055-0278 (2021).
154. Lan, M., Kang, E., Liu, X., Fu, Y. & Zhu, L. Stable ARMADILLO REPEAT KINESIN 2 in light inhibits hypocotyl elongation and facilitates light-induced cortical microtubule reorientation in Arabidopsis. *Journal of experimental botany* **74,** 800–816. ISSN: 0022-0957 (2023).
155. Lan, M., Liu, X., Kang, E., Fu, Y. & Zhu, L. ARK2 stabilizes the plus-end of microtubules and promotes microtubule bundling in Arabidopsis. *Journal of Integrative Plant Biology* **65,** 100–116. ISSN: 1672-9072 (2023).
156. Lawrence, C. J. *et al.* A standardized kinesin nomenclature. *J Cell Biol* **167,** 19–22. ISSN: 0021-9525 (Print) 1540-8140 (Electronic) 0021-9525 (Linking) (2004).
157. Lebecq, A. *et al.* The phosphoinositide signature guides the final step of plant cytokinesis. *Science advances* **9,** eadf7532. ISSN: 2375-2548 (2023).
158. Lee, K.-H., Utku, A., Qi, L. & Wang, H. The α-Aurora kinases function in vascular development in Arabidopsis. *Plant and Cell Physiology* **60,** 188–201. ISSN: 0032-0781 (2019).

159. Lee, Y.-R. J., Giang, H. M. & Liu, B. A novel plant kinesin-related protein specifically associates with the phragmoplast organelles. *The Plant Cell* **13,** 2427–2439. ISSN: 1532-298X (2001).
160. Lee, Y. R. J. & Liu, B. Identification of a phragmoplast-associated kinesin-related protein in higher plants. *Current Biology* **10.** doi: 10.1016/S0960-9822(00)00564-9, 797–800. ISSN: 0960-9822 (2000).
161. Lee, Y.-R. J., Li, Y. & Liu, B. Two Arabidopsis phragmoplast-associated kinesins play a critical role in cytokinesis during male gametogenesis. *The Plant Cell* **19,** 2595–2605. ISSN: 1532-298X (2007).
162. Levan, A. & Steinegger, E. The resistance of colchicum and bulbocodium to the c-mitotic action of colchicine. *Hereditas* **33,** 552–66. ISSN: 0018-0661 (Print) 0018-0661 (1947).
163. Li, H. *et al.* Arabidopsis MAP 65-4 plays a role in phragmoplast microtubule organization and marks the cortical cell division site. *New Phytologist* **215,** 187–201. ISSN: 0028-646X (2017).
164. Li, H. *et al.* Arabidopsis microtubule-associated protein AtMAP65-2 acts as a microtubule stabilizer. *Plant Molecular Biology* **69,** 313–324. ISSN: 0167-4412 (2009).
165. Lin, F. *et al.* A dual role for cell plate-associated PI4K in endocytosis and phragmoplast dynamics during plant somatic cytokinesis. *The EMBO journal* **38,** e100303. ISSN: 1460-2075 (2019).
166. Lipka, E., Herrmann, A. & Mueller, S. Mechanisms of plant cell division. *Wiley Interdisciplinary Reviews: Developmental Biology* **4,** 391–405. ISSN: 1759-7684 (2015).
167. Lipka, E. *et al.* The phragmoplast-orienting kinesin-12 class proteins translate the positional information of the preprophase band to establish the cortical division zone in Arabidopsis thaliana. *The Plant Cell* **26,** 2617–2632. ISSN: 1532-298X (2014).
168. Liu, B., Cyr, R. J. & Palevitz, B. A. A kinesin-like protein, KatAp, in the cells of arabidopsis and other plants. *The Plant Cell* **8,** 119–132. ISSN: 1532-298X (1996).
169. Liu, H.-L., Pemble IV, C. W. & Endow, S. A. Neck-motor interactions trigger rotation of the kinesin stalk. *Scientific Reports* **2,** 236. ISSN: 2045-2322 (2012).
170. Liu, T., Peña, A., Shilliday, F. & Moores, C. A. in *The Kinesin Superfamily Handbook* 87–100 (CRC Press, 2020).
171. Livanos, P., Kriechbaum, C., Hermann, A. & Müller, S. Kinesin-12 POK2 polarization is a prerequisite for a fully functional division site and aids cell plate positioning. *unpublished* (2024).
172. Livanos, P. & Müller, S. Division plane establishment and cytokinesis. *Annual review of plant biology* **70,** 239–267. ISSN: 1543-5008 (2019).
173. Löwe, J. & Amos, L. A. Crystal structure of the bacterial cell-division protein FtsZ. *Nature* **391,** 203–206. ISSN: 0028-0836 (1998).
174. Lu, L., Lee, Y.-R. J., Pan, R., Maloof, J. N. & Liu, B. An internal motor kinesin is associated with the Golgi apparatus and plays a role in trichome morphogenesis in Arabidopsis. *Molecular Biology of the Cell* **16,** 811–823. ISSN: 1059-1524 (2005).
175. Lucas, J. R. & Shaw, S. L. Overlapping Localization of MAP65-2, -6, and -7 in Arabidopsis Hypocotyl Cells. *MicroPublications BIology* **2023.** ISSN: 2578-9430 (2023).

176. Lucas, J. & Geisler, M. Plant Kinesin Repertoires Expand with New Domain Architecture and Contract with the Loss of Flagella. *Journal of Molecular Evolution,* 1–21. ISSN: 0022-2844 (2024).
177. Lucas, J. R. & Shaw, S. L. MAP65-1 and MAP65-2 promote cell proliferation and axial growth in Arabidopsis roots. *The Plant Journal* **71,** 454–463. ISSN: 0960-7412 (2012).
178. Lucas, J. R. *et al.* Microtubule-associated proteins MAP65-1 and MAP65-2 positively regulate axial cell growth in etiolated Arabidopsis hypocotyls. *The Plant Cell* **23,** 1889–1903. ISSN: 1532-298X (2011).
179. Madeira, F. *et al.* The EMBL-EBI Job Dispatcher sequence analysis tools framework in 2024. *Nucleic Acids Research,* gkae241. ISSN: 0305-1048 (2024).
180. Malcos, J. L. & Cyr, R. J. *Domain complexity of plant kinesins* Conference Paper. 2008.
181. Malcos, J. L. & Cyr, R. J. An ungrouped plant kinesin accumulates at the preprophase band in a cell cycle-dependent manner. *Cytoskeleton* **68,** 247–258. ISSN: 1949-3584 (2011).
182. Mao, T., Jin, L., Li, H., Liu, B. & Yuan, M. Two microtubule-associated proteins of the Arabidopsis MAP65 family function differently on microtubules. *Plant physiology* **138,** 654–662. ISSN: 1532-2548 (2005).
183. Marcus, A. I., Li, W., Ma, H. & Cyr, R. J. A kinesin mutant with an atypical bipolar spindle undergoes normal mitosis. *Molecular biology of the cell* **14,** 1717–1726. ISSN: 1059-1524 (2003).
184. Martin, A. *et al.* Targeted gene knockouts reveal overlapping functions of the five Physcomitrella patens FtsZ isoforms in chloroplast division, chloroplast shaping, cell patterning, plant development, and gravity sensing. *Molecular plant* **2,** 1359–1372. ISSN: 1674-2052 (2009).
185. Martinez, P., Luo, A., Sylvester, A. & Rasmussen, C. G. Proper division plane orientation and mitotic progression together allow normal growth of maize. *Proceedings of the National Academy of Sciences* **114,** 2759–2764. ISSN: 0027-8424 (2017).
186. Marx, A., Hoenger, A. & Mandelkow, E. Structures of kinesin motor proteins. *Cell Motility and the Cytoskeleton* **66,** 958–966. ISSN: 0886-1544 (2009).
187. Mathur, J. & Chua, N.-H. Microtubule stabilization leads to growth reorientation in Arabidopsis trichomes. *The Plant Cell* **12,** 465–477. ISSN: 1532-298X (2000).
188. McHugh, T., Gluszek, A. A. & Welburn, J. P. Microtubule end tethering of a processive kinesin-8 motor Kif18b is required for spindle positioning. *Journal of Cell Biology* **217,** 2403–2416. ISSN: 0021-9525 (2018).
189. McMichael, C. M. & Bednarek, S. Y. Cytoskeletal and membrane dynamics during higher plant cytokinesis. *New Phytologist* **197,** 1039–1057. ISSN: 0028-646X (2013).
190. Meurer-Grob, P., Kasparian, J. & Wade, R. H. Microtubule structure at improved resolution. *Biochemistry* **40,** 8000–8008. ISSN: 0006-2960 (2001).
191. Miao, J. & Chong, S. Roles of intrinsically disordered protein regions in transcriptional regulation and genome organization. *Current Opinion in Genetics Development* **90,** 102285. ISSN: 0959-437X (2025).

192. Miki, H., Okada, Y. & Hirokawa, N. Analysis of the kinesin superfamily: insights into structure and function. *Trends in cell biology* **15,** 467–476. ISSN: 0962-8924 (2005).
193. Miki, H., Setou, M., Kaneshiro, K. & Hirokawa, N. All kinesin superfamily protein, KIF, genes in mouse and human. *Proceedings of the National Academy of Sciences* **98,** 7004–7011. ISSN: 0027-8424 (2001).
194. Miki, T., Naito, H., Nishina, M. & Goshima, G. Endogenous localizome identifies 43 mitotic kinesins in a plant cell. *Proceedings of the National Academy of Sciences* **111,** E1053–E1061. ISSN: 0027-8424 (2014).
195. Mills, A. M., Morris, V. H. & Rasmussen, C. G. The localization of PHRAGMOPLAST ORIENTING KINESIN1 at the division site depends on the microtubule-binding proteins TANGLED1 and AUXIN-INDUCED IN ROOT CULTURES9 in Arabidopsis. *The Plant Cell* **34,** 4583–4599. ISSN: 1040-4651 (2022).
196. Mineyuki, Y. & Gunning, B. A role for preprophase bands of microtubules in maturation of new cell walls, and a general proposal on the function of preprophase band sites in cell division in higher plants. *Journal of Cell Science* **97,** 527–537. ISSN: 0021-9533 (1990).
197. Mineyuki, Y., Yamashita, M. & Nagahama, Y. p 34 cdc2 kinase homologue in the preprophase band. *Protoplasma* **162,** 182–186. ISSN: 0033-183X (1991).
198. Mineyuki, Y. in *International review of cytology* 1–49 (Elsevier, 1999). ISBN: 0074-7696.
199. Mineyuki, Y. & Furuya, M. Involvement of colchicine-sensitive cytoplasmic element in premitotic nuclear positioning of Adiantum protonemata. *Protoplasma* **130,** 83–90. ISSN: 0033-183X (1986).
200. Minezaki, Y., Homma, K. & Nishikawa, K. Intrinsically disordered regions of human plasma membrane proteins preferentially occur in the cytoplasmic segment. *Journal of molecular biology* **368,** 902–913. ISSN: 0022-2836 (2007).
201. Minoura, I. *et al.* Overexpression, purification, and functional analysis of recombinant human tubulin dimer. *FEBS letters* **587,** 3450–3455. ISSN: 0014-5793 (2013).
202. Mir, R., Morris, V. H., Buschmann, H. & Rasmussen, C. G. Division plane orientation defects revealed by a synthetic double mutant phenotype. *Plant Physiology* **176,** 418–431. ISSN: 1532-2548 (2018).
203. Mitsui, H., Yamaguchi-Shinozaki, K., Shinozaki, K., Nishikawa, K. & Takahashi, H. Identification of a gene family (kat) encoding kinesin-like proteins in Arabidopsis thaliana and the characterization of secondary structure of KatA. *Molecular and General Genetics* **238,** 362–368. ISSN: 0026-8925 (1993).
204. Molodtsov, M. I. *et al.* A force-induced directional switch of a molecular motor enables parallel microtubule bundle formation. *Cell* **167,** 539–552. e14. ISSN: 0092-8674 (2016).
205. Moore, R. C., Zhang, M., Cassimeris, L. & Cyr, R. J. In vitro assembled plant microtubules exhibit a high state of dynamic instability. *Cell Motility* **38,** 278–286. ISSN: 0886-1544 (1997).
206. Morales-Penningston, N. F. *et al.* GUV preparation and imaging: minimizing artifacts. *Biochimica et Biophysica Acta (BBA)-Biomembranes* **1798,** 1324–1332. ISSN: 0005-2736 (2010).

207. Morejohn, L. C., Bureau, T. E., Tocchi, L. P. & Fosket, D. E. Tubulins from different higher plant species are immunologically nonidentical and bind colchicine differentially. *Proceedings of the National Academy of Sciences* **81,** 1440–1444. ISSN: 0027-8424 (1984).

208. Morejohn, L. C. & Fosket, D. E. Higher plant tubulin identified by self-assembly into microtubules in vitro. *Nature* **297,** 426–428. ISSN: 0028-0836 (1982).

209. Morejohn, L. C. & Fosket, D. E. The biochemistry of compounds with anti-microtubule activity in plant cells. *Pharmacology Therapeutics* **51,** 217–230. ISSN: 0163-7258 (1991).

210. Moschou, P. N., Gutierrez-Beltran, E., Bozhkov, P. V. & Smertenko, A. Separase promotes microtubule polymerization by activating CENP-E-related kinesin Kin7. *Developmental cell* **37,** 350–361. ISSN: 1534-5807 (2016).

211. Mozafari, M., Mazaheri, E. & Dormiani, K. Simple equations pertaining to the particle number and surface area of metallic, polymeric, lipidic and vesicular nanocarriers. *Scientia pharmaceutica* **89,** 15. ISSN: 2218-0532 (2021).

212. Mueller, S. & Juergens, G. *Plant cytokinesis—no ring, no constriction but centrifugal construction of the partitioning membrane* in *Seminars in cell developmental biology* **53** (Elsevier), 10–18. ISBN: 1084-9521.

213. Muller, S. & Livanos, P. Plant Kinesin-12: Localization Heterogeneity and Functional Implications. *Int J Mol Sci* **20.** ISSN: 1422-0067 (Electronic) 1422-0067 (Linking) (2019).

214. Müller, S. *et al.* The plant microtubule-associated protein AtMAP65-3/PLE is essential for cytokinetic phragmoplast function. *Curr Biol* **14,** 412–7. ISSN: 0960-9822 (Print) 0960-9822 (2004).

215. Müller, S., Han, S. & Smith, L. G. Two kinesins are involved in the spatial control of cytokinesis in Arabidopsis thaliana. *Current Biology* **16,** 888–894. ISSN: 0960-9822 (2006).

216. Müller, S. *et al.* Two new loci, PLEIADE and HYADE, implicate organ-specific regulation of cytokinesis in Arabidopsis. *Plant physiology* **130,** 312–324. ISSN: 1532-2548 (2002).

217. Murata, T. & Wada, M. Effects of centrifugation on preprophase-band formation in Adiantum protonemata. *Planta* **183,** 391–398. ISSN: 0032-0935 (1991).

218. Murata, T. *et al.* Mechanism of microtubule array expansion in the cytokinetic phragmoplast. *Nature communications* **4,** 1967. ISSN: 2041-1723 (2013).

219. Narasimhulu, S. B. & Reddy, A. S. Characterization of microtubule binding domains in the Arabidopsis kinesin-like calmodulin binding protein. *The Plant Cell* **10,** 957–965. ISSN: 1532-298X (1998).

220. Naren, P. *et al.* Microtubule acetylation dyshomeostasis in Parkinson's disease. *Translational Neurodegeneration* **12,** 20. ISSN: 2047-9158 (2023).

221. Navone, F. *et al.* Cloning and expression of a human kinesin heavy chain gene: interaction of the COOH-terminal domain with cytoplasmic microtubules in transfected CV-1 cells. *The Journal of cell biology* **117,** 1263–1275. ISSN: 0021-9525 (1992).

222. Nebenführ, A. & Dixit, R. Kinesins and myosins: molecular motors that coordinate cellular functions in plants. *Annual Review of Plant Biology* **69,** 329–361. ISSN: 1543-5008 (2018).

223. Ni, C. Z., Wang, H. Q., Xu, T., Qu, Z. & Liu, G. Q. AtKP1, a kinesin-like protein, mainly localizes to mitochondria in Arabidopsis thaliana. *Cell Research* **15,** 725–733. ISSN: 1748-7838 (2005).
224. Nicolas, A. *et al.* Genome-wide analyses identify KIF5A as a novel ALS gene. *Neuron* **97,** 1267–1288. ISSN: 0896-6273 (2018).
225. Nishihama, R., Banno, H., Kawahara, E., Irie, K. & Machida, Y. Possible involvement of differential splicing in regulation of the activity of Arabidopsis ANP1 that is related to mitogen-activated protein kinase kinase kinases (MAPKKKs). *The Plant Journal* **12,** 39–48. ISSN: 0960-7412 (1997).
226. Nishihama, R. *et al.* The NPK1 mitogen-activated protein kinase kinase kinase is a regulator of cell-plate formation in plant cytokinesis. *Genes Development* **15,** 352–363. ISSN: 0890-9369 (2001).
227. Nishihama, R. *et al.* Expansion of the cell plate in plant cytokinesis requires a kinesin-like protein/MAPKKK complex. *Cell* **109,** 87–99. ISSN: 0092-8674 (2002).
228. Oda, Y. & Fukuda, H. Rho of plant GTPase signaling regulates the behavior of Arabidopsis kinesin-13A to establish secondary cell wall patterns. *The Plant Cell* **25,** 4439–4450. ISSN: 1532-298X (2013).
229. Oh, S. A., Bourdon, V., Dickinson, H. G., Twell, D. & Park, S. K. Arabidopsis Fused kinase TWO-IN-ONE dominantly inhibits male meiotic cytokinesis. *Plant reproduction* **27,** 7–17. ISSN: 2194-7953 (2014).
230. Oh, S. A. *et al.* A divergent cellular role for the FUSED kinase family in the plant-specific cytokinetic phragmoplast. *Current Biology* **15,** 2107–2111. ISSN: 0960-9822 (2005).
231. Oh, S. A. *et al.* Arabidopsis Fused kinase and the Kinesin-12 subfamily constitute a signalling module required for phragmoplast expansion. *The Plant Journal* **72,** 308–319. ISSN: 0960-7412 (2012).
232. Oh, S.-A., Lee, S. J., Kim, J. H., Twell, D. & Park, S. K. Overexpression of TWO-IN-ONE domains inhibits cytokinesis in Arabidopsis. *Journal of Plant Biology* **65,** 331–340. ISSN: 1226-9239 (2022).
233. Oladipo, A., Cowan, A. & Rodionov, V. Microtubule motor Ncd induces sliding of microtubules in vivo. *Molecular biology of the cell* **18,** 3601–3606. ISSN: 1059-1524 (2007).
234. Oppenheimer, D. G. *et al.* Essential role of a kinesin-like protein in Arabidopsis trichome morphogenesis. *Proceedings of the National Academy of Sciences* **94,** 6261–6266. ISSN: 0027-8424 (1997).
235. Otegui, M. S. & Staehelin, L. A. Electron tomographic analysis of post-meiotic cytokinesis during pollen development in Arabidopsis thaliana. *Planta* **218,** 501–515. ISSN: 0032-0935 (2004).
236. Pan, R., Lee, Y.-R. J. & Liu, B. Localization of two homologous Arabidopsis kinesin-related proteins in the phragmoplast. *Planta* **220,** 156–164. ISSN: 0032-0935 (2004).

237. Panteris, E., Adamakis, I. D., Voulgari, G. & Papadopoulou, G. A role for katanin in plant cell division: microtubule organization in dividing root cells of fra2 and lue1Arabidopsis thaliana mutants. *Cytoskeleton (Hoboken)* **68,** 401–13. ISSN: 1949-3592 (2011).
238. Parigoris, E. *et al.* Facile generation of giant unilamellar vesicles using polyacrylamide gels. *Scientific reports* **10,** 4824. ISSN: 2045-2322 (2020).
239. Peters, C. *et al.* Insight into the molecular mechanism of the multitasking kinesin-8 motor. *The EMBO journal* **29,** 3437–3447. ISSN: 1460-2075 (2010).
240. Phillips, R. K., Peter, L. G., Gilbert, S. P. & Rayment, I. Family-specific kinesin structures reveal neck-linker length based on initiation of the coiled-coil. *Journal of Biological Chemistry* **291,** 20372–20386. ISSN: 0021-9258 (2016).
241. Pickett-Heaps, J. & Northcote, D. Cell division in the formation of the stomatal complex of the young leaves of wheat. *Journal of Cell Science* **1,** 121–128. ISSN: 0021-9533 (1966).
242. Pinto, I. M., Rubinstein, B. & Li, R. Force to divide: structural and mechanical requirements for actomyosin ring contraction. *Biophysical journal* **105,** 547–554. ISSN: 0006-3495 (2013).
243. Piovesan, D. *et al.* MOBIDB in 2025: integrating ensemble properties and function annotations for intrinsically disordered proteins. *Nucleic Acids Research* **53,** D495–D503. ISSN: 0305-1048 (2025).
244. Plateau, J. A. F. *Statique expérimentale et théorique des liquides soumis aux seules forces moléculaires: Tome premier* (Gauthier-Villars, 1873).
245. Pleskot, R., Li, J., Žárský, V., Potocký, M. & Staiger, C. J. Regulation of cytoskeletal dynamics by phospholipase D and phosphatidic acid. *Trends in plant science* **18,** 496–504. ISSN: 1360-1385 (2013).
246. Poirier, K. *et al.* Mutations in TUBG1, DYNC1H1, KIF5C and KIF2A cause malformations of cortical development and microcephaly. *Nature genetics* **45,** 639–647. ISSN: 1546-1718 (2013).
247. Portran, D. *et al.* MAP65/Ase1 promote microtubule flexibility. *Molecular biology of the cell* **24,** 1964–1973. ISSN: 1059-1524 (2013).
248. Pringle, J. *et al.* Microtubule organization by kinesin motors and microtubule crosslinking protein MAP65. *Journal of Physics: Condensed Matter* **25,** 374103. ISSN: 0953-8984 (2013).
249. Quan, L. *et al.* Functional divergence of the duplicated AtKIN14a and AtKIN14b genes: critical roles in Arabidopsis meiosis and gametophyte development. *The Plant Journal* **53,** 1013–1026. ISSN: 0960-7412 (2008).
250. Rappaport, R. Cell division: direct measurement of maximum tension exerted by furrow of echinoderm eggs. *Science* **156,** 1241–1243. ISSN: 0036-8075 (1967).
251. Reddy, A. S. & Day, I. S. Kinesins in the Arabidopsis genome: a comparative analysis among eukaryotes. *BMC genomics* **2,** 1–13 (2001).
252. Reddy, A., Safadi, F., Narasimhulu, S. B., Golovkin, M. & Hu, X. A Novel Plant Calmodulin-binding Protein with a Kinesin Heavy Chain Motor Domain. *Journal of Biological Chemistry* **271,** 7052–7060. ISSN: 0021-9258 (1996).
253. Reski, R. Rings and networks: the amazing complexity of FtsZ in chloroplasts. *Trends in plant science* **7,** 103–105. ISSN: 1360-1385 (2002).

254. Rice, S. *et al.* A structural change in the kinesin motor protein that drives motility. *Nature* **402,** 778–784. ISSN: 0028-0836 (1999).
255. Richardson, D. N., Simmons, M. P. & Reddy, A. S. Comprehensive comparative analysis of kinesins in photosynthetic eukaryotes. *BMC genomics* **7,** 1–37 (2006).
256. Río-Bergé, C., Cong, Y. & Reggiori, F. Getting on the right track: Interactions between viruses and the cytoskeletal motor proteins. *Traffic* **24,** 114–130. ISSN: 1398-9219 (2023).
257. Robinson, D. *et al.* Gene-by-environment interactions influence the fitness cost of gene copy-number variation in yeast. *G3: Genes, Genomes, Genetics* **13,** jkad159. ISSN: 2160-1836 (2023).
258. Roostalu, J. *et al.* Directional switching of the kinesin Cin8 through motor coupling. *Science* **332,** 94–99. ISSN: 0036-8075 (2011).
259. Ruhnow, F., Zwicker, D. & Diez, S. Tracking Single Particles and Elongated Filaments with Nanometer Precision. *Biophysical Journal* **100.** doi: 10.1016/j.bpj.2011.04.023, 2820–2828. ISSN: 0006-3495 (2011).
260. Sablin, E. P. *et al.* Direction determination in the minus-end-directed kinesin motor ncd. *Nature* **395,** 813–816. ISSN: 0028-0836 (1998).
261. Sachs, J. Uber die Anordnung der Zellen in jungsten Pflanzentheilen. *Arb. Bot. Inst. Wurzburg* **2,** 46–104 (1878).
262. Sakai, T. *et al.* Armadillo repeat-containing kinesins and a NIMA-related kinase are required for epidermal-cell morphogenesis in Arabidopsis. *The Plant Journal* **53,** 157–171. ISSN: 0960-7412 (2008).
263. Sasabe, M. *et al.* The NACK-PQR MAP kinase cascade controls plant cytokinesis. *Tobacco BY-2 Cells: From Cellular Dynamics to Omics,* 79–94. ISSN: 3540326731 (2006).
264. Sasabe, M., Kosetsu, K., Hidaka, M., Murase, A. & Machida, Y. Arabidopsis thaliana MAP65-1 and MAP65-2 function redundantly with MAP65-3/PLEIADE in cytokinesis downstream of MPK4. *Plant signaling behavior* **6,** 743–747. ISSN: 1559-2324 (2011).
265. Sasabe, M. & Machida, Y. MAP65: a bridge linking a MAP kinase to microtubule turnover. *Current Opinion in Plant Biology* **9,** 563–570. ISSN: 1369-5266 (2006).
266. Sasabe, M. & Machida, Y. Regulation of organization and function of microtubules by the mitogen-activated protein kinase cascade during plant cytokinesis. *Cytoskeleton* **69,** 913–918. ISSN: 1949-3584 (2012).
267. Sasabe, M. *et al.* Phosphorylation of NtMAP65-1 by a MAP kinase down-regulates its activity of microtubule bundling and stimulates progression of cytokinesis of tobacco cells. *Genes development* **20,** 1004–1014. ISSN: 0890-9369 (2006).
268. Sasabe, M. *et al.* Phosphorylation of a mitotic kinesin-like protein and a MAPKKK by cyclin-dependent kinases (CDKs) is involved in the transition to cytokinesis in plants. *Proceedings of the National Academy of Sciences* **108,** 17844–17849. ISSN: 0027-8424 (2011).
269. Schaefer, E. *et al.* The preprophase band of microtubules controls the robustness of division orientation in plants. *Science* **356,** 186–189 (2017).

270. Schellhaus, A. K. *et al.* Developmentally Regulated GTP binding protein 1 (DRG1) controls microtubule dynamics. *Scientific Reports* **7,** 9996. ISSN: 2045-2322. https://doi.org/10.1038/s41598-017-10088-5 (2017).
271. Schindelin, J. *et al.* Fiji: an open-source platform for biological-image analysis. *Nature Methods* **9,** 676–682. ISSN: 1548-7105 (2012).
272. Schmidt, S. & Smertenko, A. Identification and characterization of the land-plant-specific microtubule nucleation factor MACET4. *J Cell Sci* **132.** ISSN: 0021-9533 (2019).
273. Schneider, R. & Persson, S. Connecting two arrays: the emerging role of actin-microtubule cross-linking motor proteins. *Frontiers in plant science* **6,** 415. ISSN: 1664-462X (2015).
274. Sedbrook, J. C., Ehrhardt, D. W., Fisher, S. E., Scheible, W.-R. & Somerville, C. R. The Arabidopsis SKU6/SPIRAL1 Gene Encodes a Plus End–Localized Microtubule-Interacting Protein Involved in Directional Cell Expansion[W]. *The Plant Cell* **16,** 1506–1520. ISSN: 1040-4651 (2004).
275. Seeger, M. A. & Rice, S. E. Microtubule-associated protein-like binding of the kinesin-1 tail to microtubules. *Journal of Biological Chemistry* **285,** 8155–8162. ISSN: 0021-9258 (2010).
276. Segui-Simarro, J., Austin, J., White, E. A. & Staehelin, L. A. Electron tomographic analysis of somatic cell plate formation in meristematic cells of Arabidopsis preserved by high-pressure freezing. *Plant Cell* **16,** 836–856 (2004).
277. Segui-Simarro, J. M., Otegui, M. S., Austin II, J. R. & Staehelin, L. A. Plant cytokinesis–insights gained from electron tomography studies. *Cell division control in plants,* 251–287. ISSN: 3540734864 (2008).
278. Sehnal, D. *et al.* Mol* Viewer: modern web app for 3D visualization and analysis of large biomolecular structures. *Nucleic acids research* **49,** W431–W437. ISSN: 0305-1048 (2021).
279. Shaner, N. C., Steinbach, P. A. & Tsien, R. Y. A guide to choosing fluorescent proteins. *Nature methods* **2,** 905–909. ISSN: 1548-7091 (2005).
280. Shastry, S. & Hancock, W. O. Neck linker length determines the degree of processivity in kinesin-1 and kinesin-2 motors. *Current Biology* **20,** 939–943. ISSN: 0960-9822 (2010).
281. Shaw, S. L., Kamyar, R. & Ehrhardt, D. W. Sustained microtubule treadmilling in Arabidopsis cortical arrays. *Science* **300,** 1715–1718. ISSN: 0036-8075 (2003).
282. Shemesh, A. *et al.* Effect of tubulin self-association on GTP hydrolysis and nucleotide exchange reactions. *Biochimica et Biophysica Acta (BBA)-Proteins and Proteomics* **1871,** 140869. ISSN: 1570-9639 (2023).
283. Siddiqui, S. S. Metazoan motor models: kinesin Superfamily inC. elegans. *Traffic* **3,** 20–28. ISSN: 1398-9219 (2002).
284. Sigalov, A. B. & Uversky, V. N. Differential occurrence of protein intrinsic disorder in the cytoplasmic signaling domains of cell receptors. *Self/nonself* **2,** 55–72. ISSN: 1938-2030 (2011).
285. Simmert, S., Abdosamadi, M. K., Hermsdorf, G. & Schäffer, E. LED-based interference-reflection microscopy combined with optical tweezers for quantitative three-dimensional microtubule imaging. *Optics Express* **26,** 14499–14513. https://opg.optica.org/oe/abstract.cfm?URI=oe-26-11-14499 (2018).

286. Simon, M. L. A. *et al.* A multi-colour/multi-affinity marker set to visualize phosphoinositide dynamics in A rabidopsis. *The Plant Journal* **77,** 322–337. ISSN: 0960-7412 (2014).
287. Simon, M. L. A. *et al.* A PtdIns(4)P-driven electrostatic field controls cell membrane identity and signalling in plants. *Nature Plants* **2,** 16089. ISSN: 2055-0278 (2016).
288. Sinnott, E. W. & Bloch, R. Cytoplasmic behavior during division of vacuolate plant cells. *Proceedings of the National Academy of Sciences* **26,** 223–227. ISSN: 0027-8424 (1940).
289. Smertenko, A. P. *et al.* The C-terminal variable region specifies the dynamic properties of Arabidopsis microtubule-associated protein MAP65 isotypes. *Plant Cell* **20,** 3346–58. ISSN: 1040-4651 (Print) 1040-4651 (2008).
290. Smertenko, A. *et al.* Plant cytokinesis: terminology for structures and processes. *Trends in cell biology* **27,** 885–894. ISSN: 0962-8924 (2017).
291. Smertenko, A. *et al.* Phragmoplast microtubule dynamics–a game of zones. *Journal of cell science* **131,** jcs203331. ISSN: 1477-9137 (2018).
292. Smertenko, A. P. *et al.* The Arabidopsis microtubule-associated protein AtMAP65-1: molecular analysis of its microtubule bundling activity. *The Plant Cell* **16,** 2035–2047. ISSN: 1532-298X (2004).
293. Smertenko, A. P. *et al.* Control of the AtMAP65-1 interaction with microtubules through the cell cycle. *Journal of Cell Science* **119,** 3227–3237. ISSN: 1477-9137 (2006).
294. Smith, L. G., Gerttula, S. M., Han, S. & Levy, J. Tangled1: a microtubule binding protein required for the spatial control of cytokinesis in maize. *The Journal of cell biology* **152,** 231–236. ISSN: 0021-9525 (2001).
295. Smith, L. G., Hake, S. & Sylvester, A. W. The tangled-1 mutation alters cell division orientations throughout maize leaf development without altering leaf shape. *Development* **122,** 481–489. ISSN: 0950-1991 (1996).
296. Sofroni, K. *et al.* CDKD-dependent activation of CDKA;1 controls microtubule dynamics and cytokinesis during meiosis. *J Cell Biol* **219.** ISSN: 0021-9525 (Print) 0021-9525 (2020).
297. Soga, K., Wakabayashi, K. & Hoson, T. Growth and cortical microtubule dynamics in shoot organs under microgravity and hypergravity conditions. *Plant signaling behavior* **13,** 135–144. ISSN: 1559-2324 (2018).
298. Song, H., Golovkin, M., Reddy, A. & Endow, S. A. In vitro motility of AtKCBP, a calmodulin-binding kinesin protein of Arabidopsis. *Proceedings of the National Academy of Sciences* **94,** 322–327. ISSN: 0027-8424 (1997).
299. Soyano, T., Nishihama, R., Morikiyo, K., Ishikawa, M. & Machida, Y. NQK1/NtMEK1 is a MAPKK that acts in the NPK1 MAPKKK-mediated MAPK cascade and is required for plant cytokinesis. *Genes development* **17,** 1055–1067. ISSN: 0890-9369 (2003).
300. Spiegelman, Z., Lee, C.-M. & Gallagher, K. L. KinG is a plant-specific kinesin that regulates both intra-and intercellular movement of SHORT-ROOT. *Plant Physiology* **176,** 392–405. ISSN: 1532-2548 (2018).
301. Steiner, A. *et al.* Cell cycle-regulated PLEIADE/At MAP 65-3 links membrane and microtubule dynamics during plant cytokinesis. *The Plant Journal* **88,** 531–541. ISSN: 0960-7412 (2016).

302. Stock, M. F., Chu, J. & Hackney, D. D. The kinesin family member BimC contains a second microtubule binding region attached to the N terminus of the motor domain. *Journal of Biological Chemistry* **278,** 52315–52322. ISSN: 0021-9258 (2003).
303. Stockle, D. *et al.* Putative RopGAPs impact division plane selection and interact with kinesin-12 POK1. *Nat Plants* **2,** 16120. ISSN: 2055-0278 (Electronic) 2055-0278 (Linking) (2016).
304. Stoppin-Mellet, V., Fache, V., Portran, D., Martiel, J.-L. & Vantard, M. MAP65 coordinate microtubule growth during bundle formation. *PloS one* **8,** e56808. ISSN: 1932-6203 (2013).
305. Straube, A., Hause, G., Fink, G. & Steinberg, G. Conventional kinesin mediates microtubule-microtubule interactions in vivo. *Molecular biology of the cell* **17,** 907–916. ISSN: 1059-1524 (2006).
306. Strauß, T., Schattner, S., Hoth, S. & Walter, W. J. The Arabidopsis thaliana kinesin-5 AtKRP125b is a processive, microtubule-sliding motor protein with putative plant-specific functions. *International journal of molecular sciences* **22,** 11361. ISSN: 1422-0067 (2021).
307. Strompen, G. *et al.* The Arabidopsis HINKEL gene encodes a kinesin-related protein involved in cytokinesis and is expressed in a cell cycle-dependent manner. *Current Biology* **12,** 153–158. ISSN: 0960-9822 (2002).
308. Sturgill, E. G. *et al.* Kinesin-12 Kif15 targets kinetochore fibers through an intrinsic two-step mechanism. *Current Biology* **24,** 2307–2313. ISSN: 0960-9822 (2014).
309. Suetsugu, N. *et al.* Two kinesin-like proteins mediate actin-based chloroplast movement in Arabidopsis thaliana. *Proceedings of the National Academy of Sciences* **107,** 8860–8865. ISSN: 0027-8424 (2010).
310. Takahashi, Y., Soyano, T., Kosetsu, K., Sasabe, M. & Machida, Y. HINKEL kinesin, ANP MAPKKKs and MKK6/ANQ MAPKK, which phosphorylates and activates MPK4 MAPK, constitute a pathway that is required for cytokinesis in Arabidopsis thaliana. *Plant and cell physiology* **51,** 1766–1776. ISSN: 1471-9053 (2010).
311. Takahashi, Y., Soyano, T., Sasabe, M. & Machida, Y. A MAP kinase cascade that controls plant cytokinesis. *Journal of biochemistry* **136,** 127–132. ISSN: 1756-2651 (2004).
312. Takeuchi, M. *et al.* Single microfilaments mediate the early steps of microtubule bundling during preprophase band formation in onion cotyledon epidermal cells. *Molecular biology of the cell* **27,** 1809–1820. ISSN: 1059-1524 (2016).
313. Tan, Z. *et al.* Autoinhibited kinesin-1 adopts a hierarchical folding pattern. *Elife* **12,** RP86776. ISSN: 2050-084X (2023).
314. Tanaka, H. *et al.* The AtNACK1/HINKEL and STUD/TETRASPORE/AtNACK2 genes, which encode functionally redundant kinesins, are essential for cytokinesis in Arabidopsis. *Genes to Cells* **9,** 1199–1211. ISSN: 1356-9597 (2004).
315. Tang, X. *et al.* A kinetochore-associated kinesin-7 motor cooperates with BUB3.3 to regulate mitotic chromosome congression in Arabidopsis thaliana. *Nature Plants.* ISSN: 2055-0278 (2024).

316. Ti, S.-C. Reconstituting Microtubules: A Decades-Long Effort From Building Block Identification to the Generation of Recombinant /-Tubulin. *Frontiers in Cell and Developmental Biology* **10,** 861648. ISSN: 2296-634X (2022).
317. Ti, S.-C., Wieczorek, M. & Kapoor, T. M. Purification of affinity tag-free recombinant tubulin from insect cells. *STAR protocols* **1,** 100011. ISSN: 2666-1667 (2020).
318. Tian, J. *et al.* Orchestration of microtubules and the actin cytoskeleton in trichome cell shape determination by a plant-unique kinesin. *Elife* **4,** e09351. ISSN: 2050-084X (2015).
319. Torres, J. Z. *et al.* The STARD9/Kif16a kinesin associates with mitotic microtubules and regulates spindle pole assembly. *Cell* **147,** 1309–23. ISSN: 0092-8674 (Print) 0092-8674 (2011).
320. Traas, J. A. *et al.* An actin network is present in the cytoplasm throughout the cell cycle of carrot cells and associates with the dividing nucleus. *The Journal of cell biology* **105,** 387–395. ISSN: 0021-9525 (1987).
321. Tulin, A., McClerklin, S., Huang, Y. & Dixit, R. Single-molecule analysis of the microtubule cross-linking protein MAP65-1 reveals a molecular mechanism for contact-angle-dependent microtubule bundling. *Biophysical journal* **102,** 802–809. ISSN: 0006-3495 (2012).
322. Vale, R. D., Coppin, C. M., Malik, F., Kull, F. J. & Milligan, R. A. Tubulin GTP hydrolysis influences the structure, mechanical properties, and kinesin-driven transport of microtubules. *Journal of Biological Chemistry* **269,** 23769–23775. ISSN: 0021-9258 (1994).
323. Vale, R. D. & Fletterick, R. J. The design plan of kinesin motors. *Annual review of cell and developmental biology* **13,** 745–777. ISSN: 1081-0706 (1997).
324. Vale, R. D., Reese, T. S. & Sheetz, M. P. Identification of a novel force-generating protein, kinesin, involved in microtubule-based motility. *Cell* **42,** 39–50. ISSN: 0092-8674 (1985).
325. Van Damme, D., Vanstraelen, M. & Geelen, D. Cortical division zone establishment in plant cells. *Trends in plant science* **12,** 458–464. ISSN: 1360-1385 (2007).
326. Van Damme, D. *et al.* Arabidopsis α Aurora kinases function in formative cell division plane orientation. *The Plant Cell* **23,** 4013–4024. ISSN: 1532-298X (2011).
327. Van Oostende-Triplet, C. *et al.* Vesicle dynamics during plant cell cytokinesis reveals distinct developmental phases. *Plant physiology* **174,** 1544–1558. ISSN: 1532-2548 (2017).
328. Vanstraelen, M., Torres Acosta, J. A., De Veylder, L., Inzé, D. & Geelen, D. A plant-specific subclass of C-terminal kinesins contains a conserved a-type cyclin-dependent kinase site implicated in folding and dimerization. *Plant Physiology* **135,** 1417–1429. ISSN: 1532-2548 (2004).
329. Vanstraelen, M. *et al.* Cell cycle-dependent targeting of a kinesin at the plasma membrane demarcates the division site in plant cells. *Current Biology* **16,** 308–314. ISSN: 0960-9822 (2006).
330. Vavrdová, T. *et al.* Multicolour three dimensional structured illumination microscopy of immunolabeled plant microtubules and associated proteins. *Plant Methods* **15,** 1–17 (2019).
331. Vemu, A., Garnham, C. P., Lee, D.-Y. & Roll-Mecak, A. in *Methods in enzymology* 149–166 (Elsevier, 2014). ISBN: 0076-6879.
332. Verhey, K. J. & Hammond, J. W. Traffic control: regulation of kinesin motors. *Nature reviews Molecular cell biology* **10,** 765–777. ISSN: 1471-0072 (2009).

333. Vermeer, J. E. *et al.* Imaging phosphatidylinositol 4-phosphate dynamics in living plant cells. *The Plant Journal* **57,** 356–372. ISSN: 0960-7412 (2009).
334. Vicinanza, M., D'angelo, G., Di Campli, A. & De Matteis, M. A. Function and dysfunction of the PI system in membrane trafficking. *The EMBO journal* **27,** 2457–2470. ISSN: 1460-2075 (2008).
335. Vos, J. W., Dogterom, M. & Emons, A. M. C. Microtubules become more dynamic but not shorter during preprophase band formation: a possible "search-and-capture" mechanism for microtubule translocation. *Cell motility and the cytoskeleton* **57,** 246–258. ISSN: 0886-1544 (2004).
336. Vos, J. W., Safadi, F., Reddy, A. S. & Hepler, P. K. The kinesin-like calmodulin binding protein is differentially involved in cell division. *The Plant Cell* **12,** 979–990. ISSN: 1532-298X (2000).
337. Wade, R. H., Chrétien, D. & Job, D. Characterization of microtubule protofilament numbers: how does the surface lattice accommodate? *Journal of molecular biology* **212,** 775–786. ISSN: 0022-2836 (1990).
338. Wakeel, A., Wang, L. & Xu, M. SPEECHLESS and MUTE mediate feedback Regulation of Signal Transduction during Stomatal Development. *Plants* **10,** 432. ISSN: 2223-7747 (2021).
339. Walker, K. L., Müller, S., Moss, D., Ehrhardt, D. W. & Smith, L. G. Arabidopsis TANGLED identifies the division plane throughout mitosis and cytokinesis. *Current Biology* **17,** 1827–1836. ISSN: 0960-9822 (2007).
340. Wang, H. *et al.* The Arabidopsis kinesin gene AtKin-1 plays a role in the nuclear division process during megagametogenesis. *Plant cell reports* **33,** 819–828. ISSN: 0721-7714 (2014).
341. Wang, S., Chin, H. F., Karatekin, E., Pollard, T. D. & O'Shaughnessy, B. Two Isoforms of Myosin-II Account for the Tension of the Fission Yeast Cytokinetic Ring. *Biophysical Journal* **110,** 618a. ISSN: 0006-3495 (2016).
342. Wang, Y. *et al.* Plant Kinesin: from Microtubule Arrays to Physiological Regulation. *Chinese Bulletin of Botany* **57,** 358. ISSN: 1674-3466 (2022).
343. Wang, Z. *et al.* Binding of PLD2-Generated Phosphatidic Acid to KIF5B Promotes MT1-MMP Surface Trafficking and Lung Metastasis of Mouse Breast Cancer Cells. *Dev Cell* **43,** 186–197.e7. ISSN: 1534-5807 (Print) 1534-5807 (2017).
344. Wardlaw, C. in *Commémoration Léo Errera: Université Libre de Bruxelles* 210 (Imprimerie Gutenberg, 1960).
345. Weinberger, A. *et al.* Gel-assisted formation of giant unilamellar vesicles. *Biophysical journal* **105,** 154–164. ISSN: 0006-3495 (2013).
346. Weinger, J. S., Qiu, M., Yang, G. & Kapoor, T. M. A nonmotor microtubule binding site in kinesin-5 is required for filament crosslinking and sliding. *Current Biology* **21,** 154–160. ISSN: 0960-9822 (2011).
347. Welburn, J. P. & Friel, C. T. in *The Kinesin Superfamily Handbook* 101–114 (CRC Press, 2020).
348. Wickstead, B. & Gull, K. A "holistic" kinesin phylogeny reveals new kinesin families and predicts protein functions. *Molecular biology of the cell* **17,** 1734–1743. ISSN: 1059-1524 (2006).

349. Wickstead, B., Gull, K. & Richards, T. A. Patterns of kinesin evolution reveal a complex ancestral eukaryote with a multifunctional cytoskeleton. *BMC evolutionary biology* **10,** 1–12 (2010).
350. Widlund, P. O. *et al.* One-step purification of assembly-competent tubulin from diverse eukaryotic sources. *Molecular biology of the cell* **23,** 4393–4401. ISSN: 1059-1524 (2012).
351. Wiedemeier, A. M. *et al.* Mutant alleles of Arabidopsis RADIALLY SWOLLEN 4 and 7 reduce growth anisotropy without altering the transverse orientation of cortical microtubules or cellulose microfibrils. ISSN: 1477-9129 (2002).
352. Williamson, R. E. in *International review of cytology* 135–206 (Elsevier, 1991). ISBN: 0074-7696.
353. Xu, X. M. *et al.* RanGAP1 is a continuous marker of the Arabidopsis cell division plane. *Proceedings of the National Academy of Sciences* **105,** 18637–18642. ISSN: 0027-8424 (2008).
354. Xue, X., Jaulin, F., Espenel, C. & Kreitzer, G. PH-domain-dependent selective transport of p75 by kinesin-3 family motors in non-polarized MDCK cells. *J Cell Sci* **123,** 1732–41. ISSN: 0021-9533 (Print) 0021-9533 (2010).
355. Yamada, M., Tanaka-Takiguchi, Y., Hayashi, M., Nishina, M. & Goshima, G. Multiple kinesin-14 family members drive microtubule minus end–directed transport in plant cells. *Journal of Cell Biology* **216,** 1705–1714. ISSN: 0021-9525 (2017).
356. Yang, C.-Y. *et al.* TETRASPORE encodes a kinesin required for male meiotic cytokinesis in Arabidopsis. *The Plant Journal* **34,** 229–240. ISSN: 0960-7412 (2003).
357. Yang, X.-Y. *et al.* Arabidopsis kinesin KP1 specifically interacts with VDAC3, a mitochondrial protein, and regulates respiration during seed germination at low temperature. *The Plant Cell* **23,** 1093–1106. ISSN: 1532-298X (2011).
358. Yi, P. & Goshima, G. Division site determination during asymmetric cell division in plants. *The Plant Cell* **34,** 2120–2139. ISSN: 1040-4651 (2022).
359. Zhang, Q. *et al.* Phosphatidic acid regulates microtubule organization by interacting with MAP65-1 in response to salt stress in Arabidopsis. *The Plant Cell* **24,** 4555–4576. ISSN: 1532-298X (2012).
360. Zhong, R., Burk, D. H., Morrison III, W. H. & Ye, Z.-H. A kinesin-like protein is essential for oriented deposition of cellulose microfibrils and cell wall strength. *The plant cell* **14,** 3101–3117. ISSN: 1532-298X (2002).
361. Zhou, S., Chen, Q., Li, X. & Li, Y. MAP65-1 is required for the depolymerization and reorganization of cortical microtubules in the response to salt stress in Arabidopsis. *Plant Science* **264,** 112–121. ISSN: 0168-9452 (2017).
362. Zhu, C. & Dixit, R. Functions of the Arabidopsis kinesin superfamily of microtubule-based motor proteins. *Protoplasma* **249,** 887–899. ISSN: 0033-183X (2012).

Acknowledgements

This is where I go through my very long list of people I am grateful for, whom without, this thesis would not have been written and I would not have stayed sane all these years. Firstly, to Erik, thank you for accepting me into your lab where you gave me all the freedom to 'play with microtubules' to my heart's content. Thank you also for the support and supervision that allowed me to grow and mature into an independent scientist, for teaching me many lessons outside just the science, which are invaluable whether or not I stay in academia, for putting up with me as I evolved through the years and for always being open to communicating, no matter how difficult and awkward I get.

To Hauke, who I drove up the wall with my flowery and inaccurate scientific language and use of inkscape (sorry I am poor), thank you for agreeing to writing all my manuscripts with me despite the aforementioned flowery language and lack of a proper illustrator software. I promise I will use a different (poor person) illustration tool for our next publication. Jokes aside, thank you very much for teaching me a lot of biochemistry and biology in the lab and for allowing me to pose all my stupid questions at you. Thank you also for showing me what amazing scientific writing is like. I still can't do it, but at least I now know what it looks like. After all, I have the before and after versions of our paper. Hah. Also for the social side, thanks for all the conversations on every imaginable topic. I particularly enjoy the ones on tea, funny things your little ones do and deep social commentary on the declining state of human society. ;)

To Ionas, Carolina, Anita, Rahul and Alexandra, thank you for being people I could always turn to for career and life advice. Thank you also for pushing me to do things I otherwise would not have done. Thank you to Ionas, for pushing me to try new experiments and methods and for encouraging me to go to conferences and to network. Thank you also to Rahul, for always taking the time to explain all the physic stuff whenever I don't understand something. Thank you to Alexandra, for being the science-y older sister I never knew I needed and for showing me that you can stay happy, optimistic and fun in something as competitive as academia. Thank you to Carolina and Anita, for the company, the comiseration (haha gossip), and also for the important pieces of advice and insight here and there.

To my fellow PhDs, Dr. Viktoria Charlotte Wedler, Dr. Maria A. Kharlamova (hard earned doctorates

have to be mentioned in full, eh?), Benedikt Sebastian Jakob Fischer (in case the other Benedikt Fischers get confused), Aleksandr V. Kostarev and Yannic Lurz, thank you for everything. You guys are the people I spend more time with than anybody else. Thank you for being the people I could go to for absolutely anything, life / science / genshin tedtalks / video game nights we said we'd do but never did (at least you guys never invited me!) / moving house, etc. I'm so grateful to have met all of you in this life and have 0 regrets for having walked down this path, as I got to meet all of you. You know how you have too much to say, and so you instead get overwhelmed and then say nothing? That's happening right now. I could write whole pages for each of you, for how you've invariably changed me. Thank you for accepting me, as crazy and half-depressed but also half-hyper with the memory of an ADHD squirrel as I am. I truly hope we can continue our friendship into the future, and know that you all always have a place with me.

To the poor guinea pigs I mentored - Steffen, Stace, Sehee and Layla, sorry you had to have me supervise you when I was still learning myself how to science. Thank you for being great students, for putting up with me and for succeeding in your paths.

To all the students who have come through the lab through the years, in particular, Laura, Steven, Freddy, Nicolas, Alex, Brent, Ole, Tobi, Leo and well as our new PhDs Emanuel and Viktor, thank you for showing me that learning comes from all directions. Coming from very hierarchical parts of asia, it wasn't easy to shed the deep-rooted senior-junior relationships, but it was made much easier with wonderful students like you guys, who didn't see status and were all amazingly brilliant and contributive. Thank you for always being a breath of fresh air in the lab. Thank you also specifically to Laura, for being so brilliant I could go to you for absolutely anything (science, code, math, german, physics, life, poetry, etc.). Thank you for also just turning in my friend, and for being there for me even when I was not there myself. Thank you to Steven, for movie nights (!!!) and for all the music recommendations. Thanks for also being my seat-mate, where I could see all of your cool data before anyone else did, and for all the chats we've had while analysing data and refusing to go down to beer hour. Thank you to Freddy, for being adorable and for having your head screwed on right ;)

Thank you to my fellow floor mates at one point or another, particularly (in alphabetical order) Charlotte, Danalyn, Dennis (you're part of AG Lahaye, right?), Erin, Harin, Haseong, Kaltra, Kyrylo, Mariam, Michelle, Nan, Nga, Niels, Theresa, Trang, Paloma, Paul, Riëtte, Stefan and Zac (who basically belongs partially in the ZMBP, right?). Thanks for being lovely people, for the conversations we would randomly have and for letting me bug you guys for help and stuff I need. Thank you specifically also to Dennis and Erin. Dennis, for always being real and just your chill friendship in general. Erin. Oh Erin. Thank you so much, for being amazing, for being sane, for being not only a wonderful person, but for also being an amazing example of a brilliant scientist who can do it all. Thank you also to Thomas, Gabriella, Jessica, Julien and Isabel, for being in a sense, academic aunts and uncles I could go to for advice and insights into the careers further down the line. Thank you also to Klaus, for agreeing to a speeeeeeedy review of this thesis. Thank you for just being cool people,

that made me forget I come from a country full of top-down hierarchies (it's not completely eradicated in me, hence the weird 'academic uncles and aunties'). Thank you also to Annett, Robert, Angela, Natalie, Markus, Joachim, Edda and Petra whom I bugged constantly as well for science-y stuff, and for also being cool people. Thank you also to Sandra, Sven and Natalie, who helped me so much with the FCS and FCCS experiments, you guys were always so nice and kind to explain everything to me and answer all my silly questions. Thank you also to Charley, Ute, Kevin, Silvia and Anne, for all the administrative things you do for all of us and also for me in particular. Thank you also for not just being 'the administrative' people, but just being lovely people to chat with.

Thank you also to Sibylle and Ale, whom really helped to drag me across the finish line. Knowing that I could always run to the PhD office really helps to lift the weight off. Thank you to my IMPRS batch mates, Anupaum, Patrizia, Michael, Lisa, Yimin, Alexander, Katya and Veysi. We were such an anti-social batch, thanks to COVID, but it was always nice to see each other and find a comforting presence in all the MPI events we had. Thank you also to Caroline and Pin-Jou for your friendship and conversations. I promise we will finally get that coffee / lunch we keep planning to!

Thank you to Akari, for always being there, for your friendship and for your listening ear. Life is hard, but it is much better with you in my life to enjoy gohōbi and jōshi-kai together. Thank you also to Alice and Bene (Jia Zhi!), who supported me through my early-to mid PhD days, with our weekly updates on our life-ongoings. Thanks to you both, my german got to such a level where I comfortably switch to it when I need to. But more importantly, thank you for the friendship that was a constant throughout my PhD.

To my parents and sister, thank you for the unwavering support in me. Thank you for always being home for me, for being people that I could always turn to. To my dear Eugene, my new family, thank you for your love and support, for taking care of me and reminding me to take care me when I forget to, for showing me how to prioritise what matters, for reminding me that there is life outside lab and for providing me with the security, safety and strength to march forward.

Statement of Authorship

Statement of authorship
I here by certify that

- I have composed this thesis myself,
- all references and verbatim extracts have been quoted, and all sources of information have been specfically acknowledged,
- this thesis has not been accepted in any previous application for a degree, neither in total nor in substantial parts.

Eidesstattlicher Versicherung
Ich versichere hermit, dass ich

- die vorliegende Arbeit selbstständig verfasst habe,
- keine anderen als die angegebene Quellen benutzt und alle wörtlich oder sinngemäß aus anderen Werken übernommenen Aussagen als solche gekennzeichnet habe,
- und die eingereichte Arbeit weder vollständig noch in wesentlichen Teilen Gegenstand eines anderen Prüfungsverfahrens gewesen ist.

....

Ort, Datum — Unterschrift / Signature

Place, Date — Shu Yao Leong